JAERI-Conf--98-006

JAERI-Conf
98-006

JP9804030

PROCEEDINGS OF THE SIXTH INTERNATIONAL WORKSHOP ON CERAMIC BREEDER BLANKET INTERACTIONS OCTOBER 22-24, 1997, MITO CITY, JAPAN

March 1998

(Ed.) Kenji NODA

日本原子力研究所
Japan Atomic Energy Research Institute

本レポートは，日本原子力研究所が不定期に公刊している研究報告書です。
入手の問合わせは，日本原子力研究所研究情報部研究情報課（〒319-1195　茨城県那珂郡東海村）あて，お申し越しください。なお，このほかに財団法人原子力弘済会資料センター〒319-1195　茨城県那珂郡東海村日本原子力研究所内）で複写による実費領布をおこなっております。

This report is issued irregularly.
Inquiries about availability of the reports should be addressed to Research Information Division, Department of Intellectual Resources, Japan Atomic Energy Research Institure, Tokai-mura, Naka-gun, Ibaraki-ken 319-1195, Japan.

編集兼発行　日本原子力研究所
印　　刷　㈱原子力資料サービス

JAERI-Conf 98-006

International Energy Agency Specialists' Workshop
and
Japan-Us Workshop 97FT4-01

Proceedings of the Sixth International Workshop on Ceramic Breeder Blanket Interactions

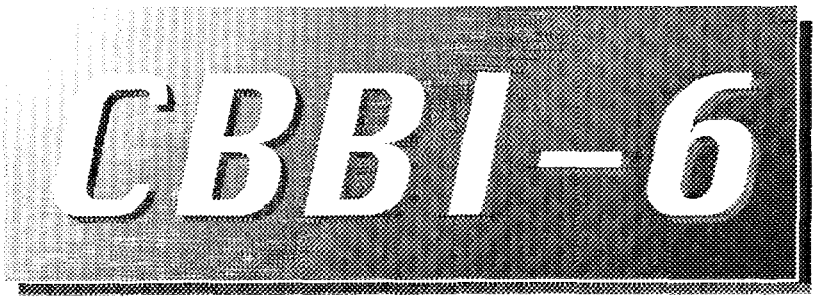

Mito, October 22-24, 1997

Editor
Kenji Noda
JAERI-Japan

Co-chairs:	K. Noda (JAERI) M. Yamawaki (Univ. of Tokyo)
Regional Co-chairs:	C. E. Johnson (ANL) N. Roux (CE/Saclay)

Sixth International Workshop on Ceramic Breeder Blanket Interactions
Oct. 22-24, 1997, Mito, Japan

JAERI－Conf 98－006

Proceedings of the Sixth International Workshop on Ceramic Breeder Blanket Interactions
October 22-24, 1997, Mito City, Japan

(Ed.) Kenji NODA

Department of Materials Science and Engineering
Tokai Research Establishment
Japan Atomic Energy Research Institute
Tokai-mura, Naka-gun, Ibaraki-ken

(Received February 12, 1998)

This report is the Proceedings of "the Sixth International Workshop on Ceramic Breeder Blanket Interactions" which was held as a workshop on ceramic breeders under Annex II of IEA Implementing Agreement on a Programme of Research and Development on Fusion Materials, and Japan-US Workshop 97FT4-01. This workshop was held in Mito city, Japan on October 22-24, 1997. About forty experts from EU, Japan, USA, and Chile attended the workshop. The scope of the workshop included the following: 1) fabrication and characterization of ceramic breeders, 2) properties data for ceramic breeders, 3) tritium release characteristics, 4) modeling of tritium behavior, 5) irradiation effects on performance behavior, 6) blanket design and R&D requirements, 7) hydrogen behavior in materials, and 8) blanket system technology and structural materials. In the workshop, information exchange was performed for fabrication technology of ceramic breeder pebbles in EU and Japan, data of various properties of Li_2TiO_3, tritium release behavior of Li_2TiO_3 and Li_2ZrO_3 including tritium diffusion, modeling of tritium release from Li_2ZrO_3 in ITER condition, helium release behavior from Li_2O, results of tritium release irradiation tests of Li_4SiO_4 pebbles in EXOTIC-7, R&D issues for ceramic breeders for ITER and DEMO blankets, etc.

Keywords: Ceramic Breeder, Fabrication, Properties, Tritium Release, Modeling, Irradiation Effects, Blanket Design, R&D Issues

第６回セラミック増殖材ブランケット相互作用国際ワークショップ報文集
1997年10月22～24日、水戸市

日本原子力研究所東海研究所材料研究部
（編）野田　健治

（1998年２月12日受理）

本報文集は「ＩＥＡ核融合材料研究開発に関する実施取決め」付属書Ⅱに基づくセラミック増殖材に関するワークショップ及び日米ワークショップ97FT4-01として開催された「第６回セラミック増殖材ブランケット相互作用」国際ワークショップの報文をまとめたものである。本ワークショップは1997年10月22日から24日にかけて、水戸市で開催され、EU、日本、米国、チリより約40名の専門家が出席した。

本ワークショップでは，1)セラミック増殖材の製造及びキャラクタリゼーション、2)諸特性、3)トリチウム放出性能、4)トリチウム挙動のモデリング、5)照射挙動、6)ブランケット設計と材料研究開発課題、7)材料中の水素挙動、8)ブランケットシステム技術等についての発表と討論が行われた。この中で、EU及び日本におけるセラミック増殖材のペブル製造技術、Li_2TiO_3等の諸特性のデータ現状、Li_2TiO_3及びLi_2ZrO_3等のトリチウム放出挙動及びその拡散挙動，ITER条件におけるLi_2ZrO_3からのトリチウム放出モデリング、Li_2Oからのヘリウム放出挙動、EXOTIC-7におけるLi_4SiO_4ペブルのトリチウム放出照射試験結果、ITER及びDEMO炉用セラミック増殖材についての研究開発課題等についての情報交換が行われた。

東海研究所：〒319－1195　茨城県那珂郡東海村白方白根２－４

Contents

Summary of The 6th International Workshop on Ceramic Breeder Blanket Interactions

The 6th International Workshop on Ceramic Breeder Blanket Interaction was held in Mito, Japan on October 22-24, 1997. About forty experts from EU, Japan, USA, and Chile attended the workshop. The scope of the workshop included the following: 1) fabrication and characterization of ceramic breeders, 2) properties data for ceramic breeders, 3) tritium release characteristics, 4) modeling of tritium behavior, 5) irradiation effects on performance behavior, 6) blanket design and R&D requirements, 7) hydrogen behavior in materials, and 8) blanket system technology and structural materials.

(1) Fabrication and characterization of ceramic breeders.

At CEA, Li_2ZrO_3 and Li_2TiO_3 pebbles were fabricated by two methods, the extrusion method and the agglomeration method. Characterization of the first batches of pebbles from each method indicates that both methods are suitable for production of pebbles meeting the required specifications with respect to pebble size, pebble density and grain size.

Optimization in the preparation of Li_2TiO_3 pebbles by the sol-gel method was reported. The conditions for improvement in fabrication of Li_2TiO_3 pebbles focused on aging conditions and sintering temperatures. The resulting optimization has yielded high-density pebbles in the range of 80-85 % T.D.

(2) Properties data for ceramic breeders.

Thermodynamic analysis of the Li_4SiO_4/H_2O system indicates that the system exhibits positive deviations from ideal behavior meaning that protium is easily released from lithium orthosilicate. Also, the system exhibits an anomalous solubility above 973K. Further testing of the thermodynamics must be performed.

A work function method was applied to study the effects of sweep gas composition on the surface properties of Li_4SiO_4. The formation of the oxygen deficient layer near surface occurred when H_2 was added to the sweep gas in small concentrations. The experimental data were used for evaluation of the tritium release mechanism.

Examination of surface electronic properties of Li_2O suggested that the Fermi energy of the system increases with oxygen vacancy increases.

The properties data base for Li_2TiO_3 was recently expanded through additional measurements and compilation efforts. The compilation includes stability of Li_2TiO_3, specific heat, thermal diffusivity, linear thermal expansion, thermal creep, and interaction with water and acids.

Insight into lithium loss mechanism from ceramic breeder surface was provided.

(3) Tritium release behavior from ceramic breeders.

The tritium diffusion coefficient has been measured for single crystal Li_2TiO_3 in postirradiation annealing tests. The tritium release in the temperature range from 623 to 1373 K seems to be controlled by diffusion within the crystals. The activation energy of tritium diffusion coefficient was estimated to be 104 kJ/mol. The tritium diffusion coefficients over the temperature range of 623-1373 K is expressed by $D_r = 0.1\exp(-104/RT)$.

The tritium release from Li_2TiO_3 pellets and pebbles was studied by postirradiation annealing at CCHEN, Chile. The experimental results indicated that the tritium release is controlled by first order desorption.

The isotope exchange reactions on the surface of candidate ceramic breeder materials and its effect on tritium inventory in the materials, was reported. In particular, the tritium inventory in Li_2ZrO_3, under steady state condition, was estimated by considering the process of diffusion in the grain, adsorption at the grain surface and two isotope exchange reactions between H_2 or H_2O and tritium on the grain surface.

(4) Modeling of tritium release behavior from ceramic breeders.

The attempts made to model tritium release behavior in Li_2ZrO_3 in the low temperature regime of ITER conditions emphasized the need for additional relevant ceramic breeder properties measurements. Currently, one has to make estimates of the needed properties and this generally makes the process more tedious and the result less reliable.

Quantum chemical models were used to examine ceramic breeder surface characteristics during tritium release. It was stressed that the surface hydroxyl group plays a key role in the release process.

As a group, those involved in the modeling studies stated their belief that a greater attention need to be given to modeling to enable better blanket performance evaluations.

(5) Irradiation effects on ceramic breeder performance.

Irradiation effects in ceramic breeders may have strong impact on ceramics characteristics. The helium release characteristics appear to strongly depend on the nature of examined materials. Helium release from Li_2O single crystal proceeds through the processes of bulk diffusion with trapping by irradiation defects such as defect clusters.

The analysis of the tritium release performance from Li_4SiO_4 pebbles in EXOTIC-7 experiment provided direct evidence that the mixing of Be/Li_4SiO_4 pebbles is not recommended. The Li_4SiO_4 pebbles (Li-burnup 13% and 18%), that were in contact with Be released tritium at about 1073K. However, for material free of contact with Be, tritium is released at about 673 K from the Li_4SiO_4 pebbles (Li-burnup 10%). It is not clear if this shift of tritium release peak temperature from low to high temperature is due to contact with Be or caused by higher Li-burnup.

The irradiation program of several ceramic breeders was presented. The irradiation behavior of Li_4SiO_4, Li_2ZrO_3 and Li_2TiO_3 pebbles is under investigation in EXOTIC-8 experiment at High Flux Reactor (HFR) in Petten. The tritium release measuring station at HFR has been revised and affords greater operating flexibility with ease of capsule removal at any time.

(6) Blanket design and materials R&D requirements.

The ITER blanket design was changed from the concept of the breeding blanket with Be block to that with Be binary pebble-bed. Furthermore, the breeder blanket design configuration has been altered from a radial layer to a toroidal layer. Li_2ZrO_2 and Li_2TiO_3 pebbles were selected as reference and alternative materials for the breeding blanket, respectively. The design team identified deficiencies in the properties data base for tritium release at low temperatures, tritium behavior on the materials surface, modeling tritium behavior, the development of low cost fabrication method, a more complete tabulation of fabricated material properties, and irradiation behavior, etc. DEMO blanket design concepts for each party and R&D issues of ceramic breeders for the DEMO blankets were also shown.

(7) Hydrogen behavior in materials.

Studies of counter-diffusion and permeation of hydrogen and deuterium in metals was reported. These data were related to breeder blanket performance where the potential for hydrogen moving from the water coolant side to the blanket side due to cooling-tube corrosion is potentially quite troublesome. A new experimental system in which deuterium and hydrogen permeate in opposite direction was used to study their permeation characteristics.

Dynamic behavior of hydrogen and deuterium in $ScCe_{0.95}Yb_{0.25}O_3$ during annealing and anomalous exchange of deuterium implanted in the materials by hydrogen in air-vapor was investigated by an elastic recoil detection method.

A brief explanation of the operational characteristics of an experimental loop at ENEA for compatibility and hydrogen permeation studies was provided.

(8) Blanket system technology and structural materials.

Investigation of regeneration operation of cryogenic molecular sieve bed for tritium recovery system and corrosion fatigue studies on low activation ferritic steel (F82H) in reducing water coolant environments were presented.

Through the workshop, information exchange of status of R&D of ceramic breeders and the related technology in each party and discussion to define R&D issues of ceramic breeders were performed. A good consensus among the workshop participants was presented for further communication between designer and materials community.

A proposal from ECN Petten to host the next workshop was accepted by the Workshop and is scheduled for September 1998 in Petten, The Netherlands.

SESSION 1

Ceramic Breeder Properties (1)

Thermodynamics of the Li_4SiO_4/H_2O System

C. Alvani ENEA, Cassaccia Italy

S. Casadio ENEA, Cassaccia Italy

C. Johnson ANL, Argonne USA

Abstract

The chemical interaction of He or He + 0.1%H_2 purge gase with Li_4SiO_4 pebbles has been examined as a function temperature and partial pressure of water vapor by Temperature Programmed Reduction (TPR) and Temperature Programmed Desorption (TPD) measurements. The experimental conditions were selected to be representative of those envisaged occurring in the HCPB blanket. At constant partial pressure of moisture, water adsorption on Li_4SiO_4 decreases with increasing temperature up to 973K. Above that temperature water absorption increases due of the increasing water solubility of lithium hydroxide with temperature. Using these data, thermodynamic calculations have been carried out to evaluate the behavior of lithium orthosilicate in a moisture-containing environment. The evaluation was done over the 773 to 1173K temperature range. In general, the behavior of lithium orthosilicate was similar to earlier studies on lithium oxide except that the orthosilicate is not as strong in its deviations from ideality as the oxide.

Introduction

Of the many areas of research that are important to the development of tritium breeder ceramics blankets, the recovery of tritium from the lithium containing ceramic breeder blanket is one that involves considerable chemical thermodynamic analysis. Thermodynamics provides a unique approach to analysis of materials behavior. In this paper we examine the equilibrium thermodynamics of candidate ceramic breeder material. Previously [1], an analysis of the Li_2O/H_2O system was carried out and proved to be extremely beneficial to understanding the behavior of tritium in ceramic breeder materials and its release to the purge gas. The lithium oxide system exhibited positive deviation from ideal behavior suggesting that tritium release would be much easier than anticipated. A similar study is currently in progress for the ternary Li_4SiO_4/H_2O system.

Experimental Approach

Two carrier gases were used in these experiments [2]. The "reference" gas mixture was He + 0.1% H_2 and the alternate gas mixture was He + 30 vpm O_2. The moisture level in these gases varied from 10 to 250 vpm and was quantitatively measured. A modified Micrometrics TPD/TPR 2900 apparatus was employed in order to control:

i) the surface cleaning of the specimen with the dried purge gases,
ii) the reaching of the steady-state equilibrium of water adsorption at the experimental temperatures (500-1100K) and at various vapor partial pressures,
iii) the quantitative determination of the adsorbed water.

Preliminary experiments were performed on "as received" Li_4SiO_4 pebbles (dia. ~150 um, surface area 0.1m2/g) coming from FZK. The total water content in equilibrium with the He purge gas was measured at temperatures from 500 to 1100K. The total adsorbed water was measured by quantitative analysis of the desorbed water under linear temperature scanning from the equilibrium temperature up to 1100K and by adding the residual water measured at this temperature by a final purging with dry gas. However, this last quantity of water was found to be negligible in most of the examined cases.

On the basis of the moisture evolved or absorbed with time and a knowledge of the purge gas flow rate, the quantity of moisture evolved or absorbed in the sample can be determined. Recognize that this quantity represents the amount of LiOH (or hydrogen) adsorbed on or in solid solution in the orthosilicate matrix. It is also assumed that the LiOH formed during the heating cycle is representative of a reversible reaction that exists between water vapor, lithium orthosilicate and lithium hydroxide. The order of magnitude of the water uptake from Li_4SiO_4 around 500 to 773K depends on surface area. However, above 873K important differences appear. Interaction with moisture at 773-973K has contributions form both surface and bulk. Above 973K bulk contributions are dominant. Assumed that water was released from system.

The experimental results of the solubility measurements at 773 to 1173K and various partial pressures of water are listed in Table I. At each of the five temperatures a broad range of moisture partial pressure was selected for examination at each temperature to ensure that the full range of conditions expected in blanket operation were included. To better show the quality and range of the data, a plot of log pH2O versus log X was compiled. Figure 1 displays the relationship between the mole fraction of hydroxide formed as a function of temperature. Here one can see that the precision of the data are excellent and the expected slopes were obtained. The data show an interesting behavior in that the hydroxide concentration decreases with temperature from 773 to 973K and then increases thereafter. This is unusual behavior and could be the result of a dramatic change in the manner in which moisture is adsorbed or absorbed into the sample. Above 973K the increase in solubility of lithium hydroxide into the sample is expected.

Table I

Solubility of H_2O(LiOH, mole fraction) in Li_4SiO_4 as a function of temperature and partial pressure of water vapor.

Temp, K	pH_2O, Pa	pH_2O, atm	mol fract, X	log pH_2O	log X
773.15	0.729	7.198E-06	1.633E-05	-5.1428	-4.7870
773.15	9.360	9.238E-05	4.210E-05	-4.0344	-4.3757
773.15	29.499	2.911E-04	6.652E-05	-3.5359	-4.1771
773.15	1.904	1.880E-05	2.690E-05	-4.7259	-4.5703
773.15	15.742	1.554E-04	6.007E-05	-3.8087	-4.2214
773.15	11.042	1.090E-04	4.870E-05	-3.9627	-4.3125
873.15	1.398	1.380E-05	1.061E-05	-4.8602	-4.9744
873.15	2.897	2.859E-05	1.472E-05	-4.5437	-4.8322
873.15	9.542	9.418E-05	2.357E-05	-4.0261	-4.6276
873.15	28.881	2.850E-04	4.124E-05	-3.5451	-4.3847
873.15	1.793	1.770E-05	1.276E-05	-4.7521	-4.8943
873.15	17.322	1.710E-04	3.282E-05	-3.7671	-4.4838
873.15	10.470	1.033E-04	2.455E-05	-3.9858	-4.6099
973.15	0.750	7.398E-06	2.374E-06	-5.1309	-5.6245
973.15	2.958	2.919E-05	4.980E-06	-4.5347	-5.3028
973.15	11.376	1.123E-04	1.069E-05	-3.9497	-4.9711
973.15	28.546	2.817E-04	1.828E-05	-3.5502	-4.7379
973.15	4.255	4.199E-05	6.780E-06	-4.3769	-5.1688
973.15	14.020	1.384E-04	1.277E-05	-3.8590	-4.8937
973.15	16.167	1.596E-04	1.341E-05	-3.7971	-4.8726
973.15	83.471	8.238E-04	3.482E-05	-3.0842	-4.4582
973.15	10.700	1.056E-04	1.073E-05	-3.9763	-4.9693
1073.15	0.750	7.402E-06	3.308E-06	-5.1307	-5.4804
1073.15	1.965	1.939E-05	5.140E-06	-4.7124	-5.2890
1073.15	3.120	3.079E-05	7.001E-06	-4.5116	-5.1548
1073.15	28.792	2.842E-04	1.908E-05	-3.5464	-4.7193
1073.15	4.579	4.519E-05	8.482E-06	-4.3449	-5.0715
1073.15	12.946	1.278E-04	1.299E-05	-3.8936	-4.8863
1073.15	21.111	2.083E-04	1.805E-05	-3.6812	-4.7436
1073.15	78.305	7.728E-04	3.602E-05	-3.1119	-4.4435
1173.15	1.803	1.779E-05	5.964E-06	-4.7497	-5.2245
1173.15	5.723	5.648E-05	1.084E-05	-4.2481	-4.9649
1173.15	15.175	1.498E-04	1.824E-05	-3.8246	-4.7389
1173.15	21.749	2.146E-04	1.958E-05	-3.6683	-4.7082
1173.15	83.066	8.198E-04	3.867E-05	-3.0863	-4.4126

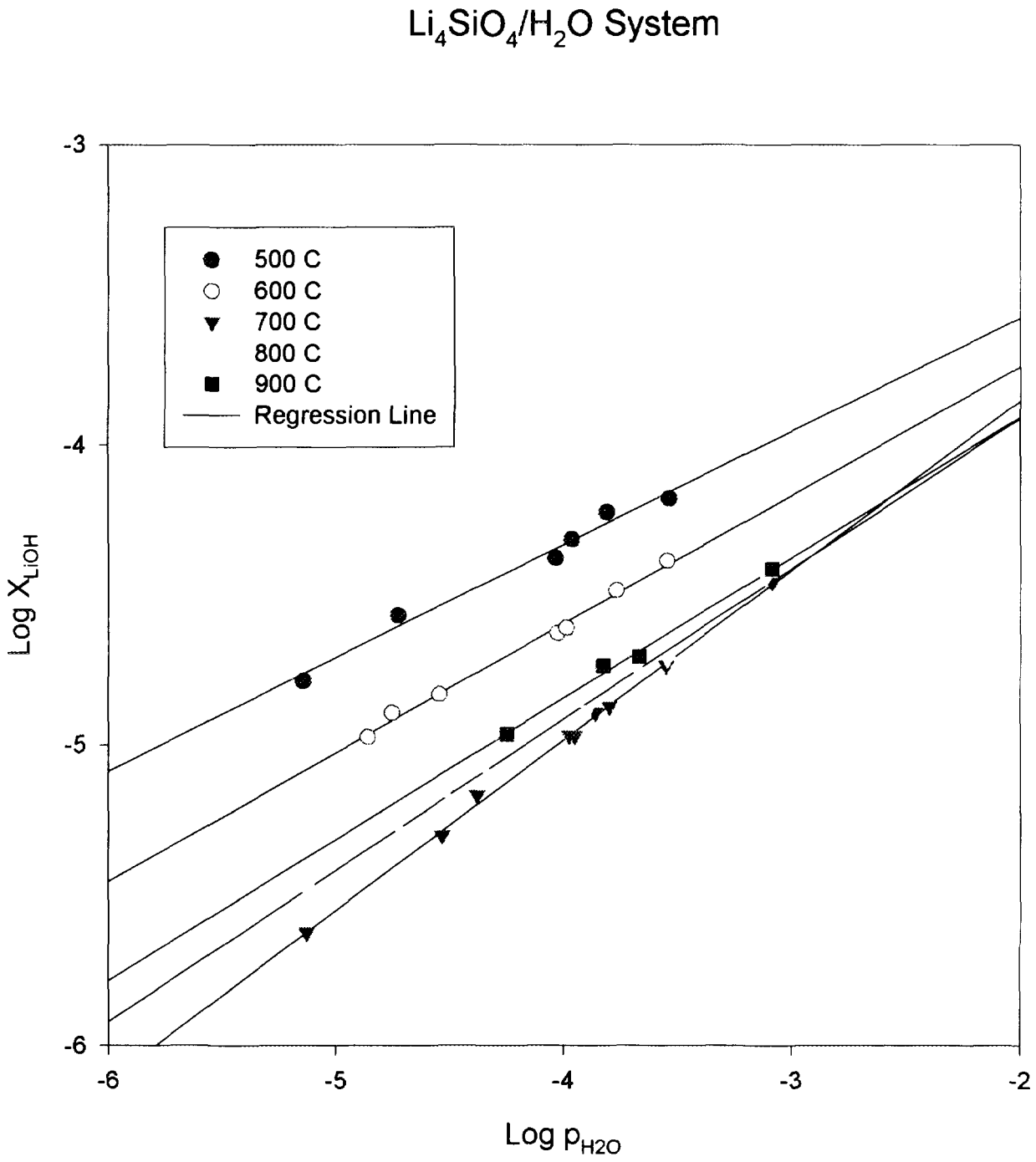

Figure 1. Plot of the concentration of LiOH in Li_4SiO_4 at various temperatures as a function of the partial pressure of water vapor in helium purge gas.

Discussion

Experimental data on the solubility of water vapor in lithium orthosilicate were collected as a function of temperature and partial pressure of water and are shown in Table I. As a first step in attempting to understand the processes taking place when lithium orthosilicate is in contact with moisture, the reaction shown in equation (1) has been assumed:

$$Li_4SiO_4 + H_2O(g) = 2LiOH + Li_2SiO_3 \qquad (1)$$

As written, the reaction suggests the formation of lithium hydroxide and lithium metasilicate. There is every expectation that lithium hydroxide forms and, at these low moisture concentrations, may be present as a solid solution. It has not been substantiated that the metasilicate forms, but if LiOH forms there are not many other choices as a reaction product. A reaction product involving SiO_2 is not reasonable because of the inherent stability of the metasilicate and the probable slow kinetics of the overall reaction.

The thermodynamic analysis proceeded on the basis of equation (1) and the data in Table I. The principal tool used for the thermodynamic analysis was the SOLGAS computer program [3], which employs a minimization routine to identify the most stable system. These efforts demonstrated the need to consider the formation of a solid solution between the product lithium hydroxide, and the reactant lithium orthosilicate. While the inclusion of a solid solution appeared to help the analysis, there was never any indication that the inclusion of the metasilicate contributed to a clearer understanding of the orthosilicate-moisture system. Also, as these calculations did not seem to be improving our understanding of the water-orthosilicate system, we decided to temporarily abandon the use of SOLGAS in favor of a simpler approach.

Further, the thermodynamic analysis does not, in reality, take into account the solubility of H_2O in Li_4SiO_4, but simply relates the behavior of the solute to pure LiOH, whatever the exact chemistry of the solute might be. Consequently, in speaking of the solubility of lithium hydroxide, we do so without implying that a molecular species "LiOH" is in solution. The exact nature of this species is an interesting issue external to the present thermodynamic inquiry. It is an unresolved question whether, in solid Li_4SiO_4, the hydroxide is an OH^- ion or a labile proton transiently associated with a succession of O^{2-} ions in the lattice.

The alternative approach selected for analysis was to rewrite the reaction in a simpler form, in which attention is given only to the reactants and products and the involvement of silicon is ignored. Also, in choosing the simpler form of reaction, one can more easily compare equilibrium constants to obtain a value for the activity coefficients for the principal reaction. The simpler form of the reaction is shown as Eqn. (2), with the reaction written in equilibrium-constant form in Eqn. (3):

$$H_2O(g) + Li_2O(ortho) = 2LiOH \qquad (2)$$

$$(a_{LiOHi})^2 / (pH_2O\ aLi_2O) = K_{exp} \qquad \text{and in reduced form,}$$

$$x^2/pH_2O = K_{exp} \qquad (3)$$

Equilibrium constants, K_{exp}, were calculated for each temperature (every 100 degrees between 773 and 1173 K) using a roughly constant partial pressure of moisture of 29 Pa (~2.8E-4 atm). These data are tabulated in column two of Table III and provides a form for comparison with tabulated data for the equilibrium constant for the formation of lithium hydroxide. The latter equilibrium constant data were taken from Barin [3] and are shown in Table II for the temperature range of 773 to 1173 K.

Table II

Tabulated Thermodynamic Data for $H_2O(g) + Li_2O = 2LiOH$

Temp, K	ΔH, kJ	ΔS, J	ΔG, kJ	K_a
773.15	-76.208	-64.199	-26.573	6.24E+1
873.15	-71.035	-57.902	-20.478	1.68E+1
973.15	-66.228	-52.687	-14.956	6.35E+0
1073.15	-61.771	-48.324	-9.912	3.04E+0
1173.15	-57.650	-44.650	-5.269	1.72E+0

If the orthosilicate system exhibits behavior similar to that of the oxide system, then one needs to determine the activity coefficient for LiOH. This is accomplished by comparing the ratio of the experimental equilibrium constant, K_{exp}, to the tabulated equilibrium constant, K_a obtained from the free energy of formation. This is shown in Eqn. (4).

$$K_{exp} / K_a = 1/(\gamma_{LiOH})^2 \qquad (4)$$

Using this approach one can determine the activity coefficient, γ, for LiOH. The activity coefficient data obtained are given in column four of Table III

Table III

Equilibrium Constants u8sed for Calculation of LiOH Activity Coefficient

Temp, K	$X^2/pH_2O = K_{exp}$	K_{exp}/K_a	γ
773.15	1.52E-5	2.45E-7	2026
873.15	5.97E-6	3.55E-7	1678
973.15	1.19E-6	1.87E-7	2313
1073.15	1.28E-6	4.22E-7	1540
1173.15	1.78E-6	1.04E-6	981

The activity coefficients for the temperature range 773 to 1073 K are in fair agreement. The low value for 1173 K may be due to the much lower moisture concentration in this series. Assuming the lower moisture content in the purge gas is the contributing factor, we estimated the activity constant to be 1308, still somewhat lower than one would expect from the data at the other temperatures. An average value for the activity coefficient is 1889.

Summary

The results of the present study show that the H_2O/Li_4SiO_4 system is thermodynamically non-ideal with substantial positive deviations from ideality. In accord with such deviations, the solubility of H_2O(LiOH) in Li_4SiO_4 is less than that calculated from an ideal solution model and increases with temperature at constant partial pressure of water vapor. Thus, the solubility of tritium as LiOT in a ceramic breeder blanket of Li_4SiO_4 is expected to be low under anticipated fusion reactor environments.

While the thermodynamic analysis may need some additional study, the work that has been completed has been informative in that these initial results indicate positive deviations from ideal behavior for the Li_4SiO_4/H_2O system similar to that for Li_2O/H_2O. The difference between the two systems is one of degree, with the oxide system showing lesser tendency to retain tritium than the orthosilicate system. Another more interesting difference in that the orthosilicate system exhibits an anomaly above 973 K, where the activity coefficient drops by about a factor of two. With such a large spread in the data, the reason for this abrupt change is not clear, as there is strong indication that the laboratory work is of high precision. However, what is certain is that further testing of the thermodynamic analysis must be made.

References

[1] M. Tetenbaum, A. K. Fischer, and C. E. Johnson, Fusion Tech. 7 (1985) 53.

[2] C. Alvani, P.L. Carconi, M.R. Mancini, A. Maouro, F. Pierdominici, A. Masci, and S. casadio, European Fusion Technology Programme Helium Cooled Pebble-Bed Blanket, Sub-Task B3-2.1, 1996 Activity Report

[3] T. M. Bessmann, SOLGASMIX-PV, Oak Ridge National Laboratory Report ORNL/TM-5575, April 1977.

[4] I. Barin, Thermochemical Data of Pure Substances, VCH Press, D-6940 Weinheim, Germany 1993.

Study on the Sweep Gas Effect on the Surface of Li_4SiO_4 by means of Work Function Measurement

Atsushi Suzuki, Kenji Yamaguchi and Michio Yamawaki

Graduate School of Quantum Engineering and Systems Science, Faculty of Engineering, The Univ. of Tokyo.

Abstract

In the establishment of fuel cycle of tritium, it is important to make research on how the sweep gas composition affects the surface properties of breeder materials and the release of tritium from the surface of them. In this study, the change of contact potential difference (CPD) between Li4SiO4 and Pt was measured in various gas compositions with a high temperature Kelvin probe. The work function change of Li4SiO4 was obtained from the measured CPD and the work function change of Pt which was estimated from blank tests. ¿From the results, the effect of oxygen deficient layer near the surface of Li4SiO4 was observed, and the effect of OH^- at the surface of Li_4SiO_4 was considered.

Study on the Sweep Gas Effect on the Surface of Li_4SiO_4 by means of Work Function Measurement

Atsushi SUZUKI, Kenji YAMAGUCHI, Michio YAMAWAKI

Graduate School of Quantum Engineering and Systems Science, Faculty of Engineering, The Univ. of Tokyo.

Research Activity for Blanket Materials in Yamawaki Lab.

- **H-T mass spectrometry**

  Vapor pressure measurement with D_2 / D_2O addition.

  Li_4SiO_4, $LiAlO_2$, Li_2TiO_3, Li_2ZrO_3.

  → Mr. Tonegawa

  Possibility of non-stoichiometry?
  Tritium recovery process ?

- **H-T Kelvin Probe**

  Work function measurement

  → This presentation

  Quantitative analysis

- **Ab initio calculation**

  Relationship between defects and Fermi-level, etc.

  → Mr. Matsuura

JAERI—Conf 98—006

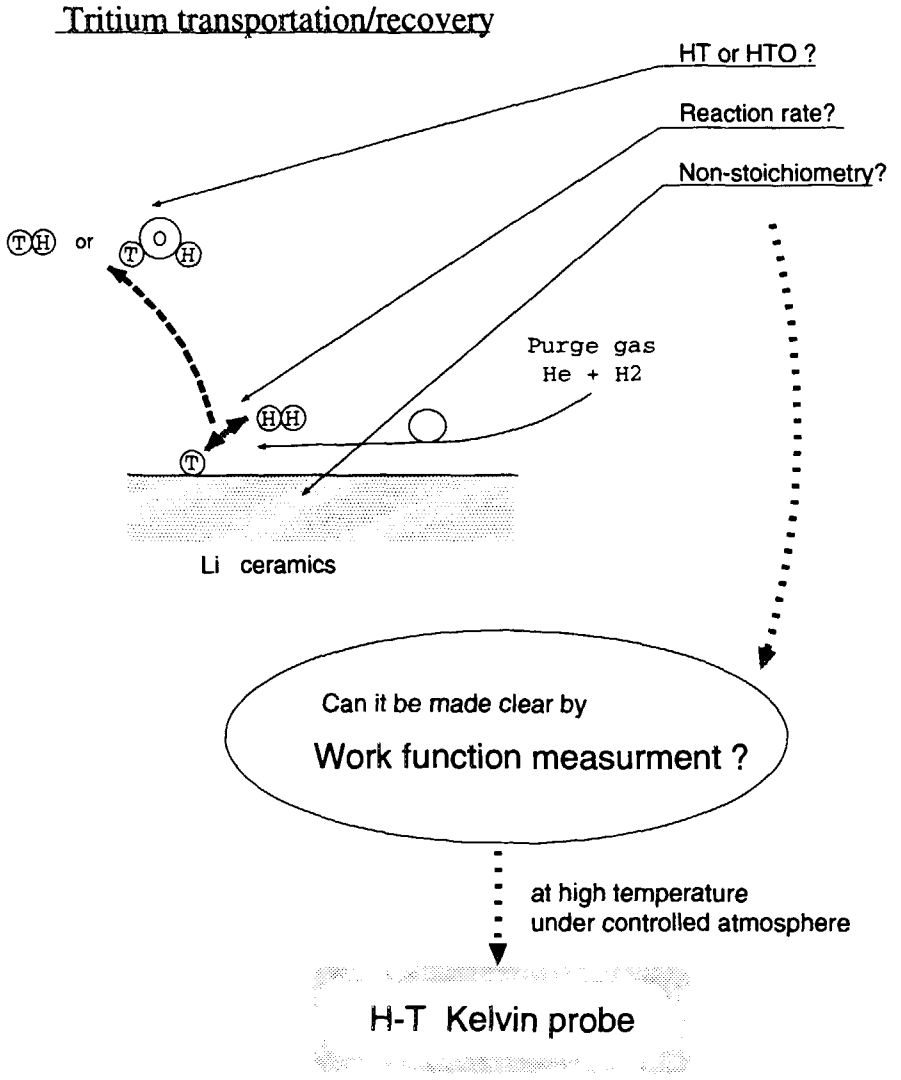

Aim

- To discuss about the following phenomena in the system of H_2 - Li_4SiO_4,
  - the formation of vacancies at/near the surface of Li_4SiO_4
  - adsorption/desorption processes

  by work function measurement.

Method

- High temperature Kelvin probe, which is based on CPD (Contact Potential Difference) measurement, was used. CPD is expressed as the difference between the work function of the sample and that of reference electrode.

Principle of Kelvin method

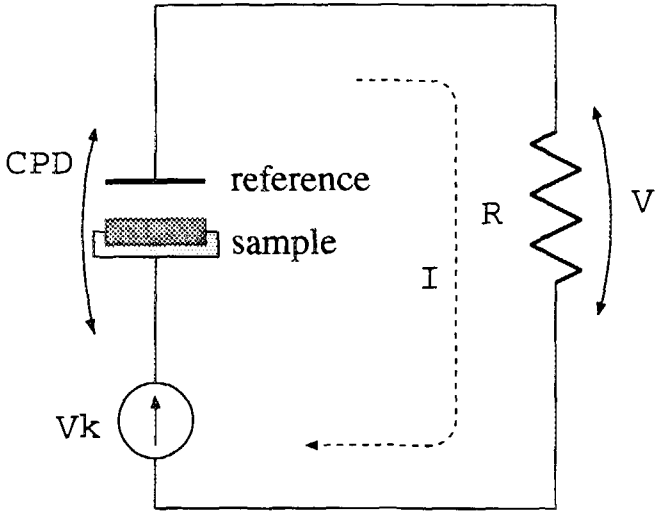

$$\mathbf{CPD} = \phi_{\mathbf{sample}} - \phi_{\mathbf{ref.}} \tag{1}$$

$$\mathbf{R}\frac{\mathbf{d}}{\mathbf{dt}}[\mathbf{C}(\mathbf{CPD} + \mathbf{V_k} + \mathbf{V})] + \mathbf{V} = \mathbf{0} \tag{2}$$

If one assumes

$$\mathbf{C(t)} = \mathbf{C_0}(\mathbf{1} + \mathbf{m}\sin(\omega\mathbf{t})), \tag{3}$$

the first term of V_1 of V(t) in Fourier expansion form becomes

$$\mathbf{V_1} = \mathbf{m}\omega\mathbf{RC_0}(\mathbf{V_k} + \mathbf{U})(\mathbf{1} + \mathbf{RC_0})^{-\mathbf{2}} \tag{4}$$

so that $V_1 = 0$ when $U = -V_k$.

Device Configuration

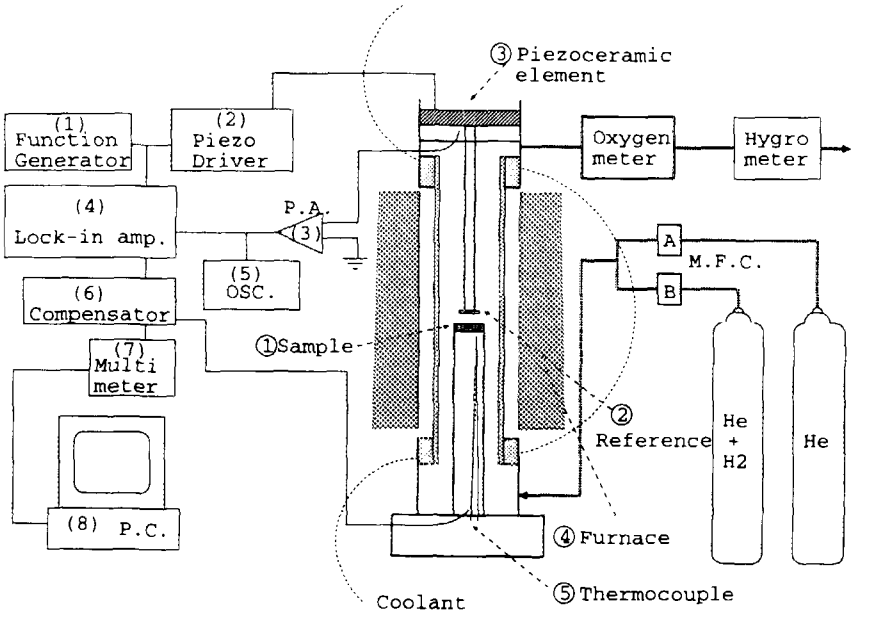

- **Sample: Li_4SiO_4 pellet**
  Reference : Pt

$$\mathbf{CPD} = \phi_{\mathbf{Li_4SiO_4}} - \phi_{\mathbf{Pt}}$$

- **Sample support : Pt**
- **Purge gas : He ↔ He + H_2 (100cc/min., 200cc/min.)**
- **Temp. : 973 K**
- **Integral feedback system**

The change of ϕ_{Pt} ?

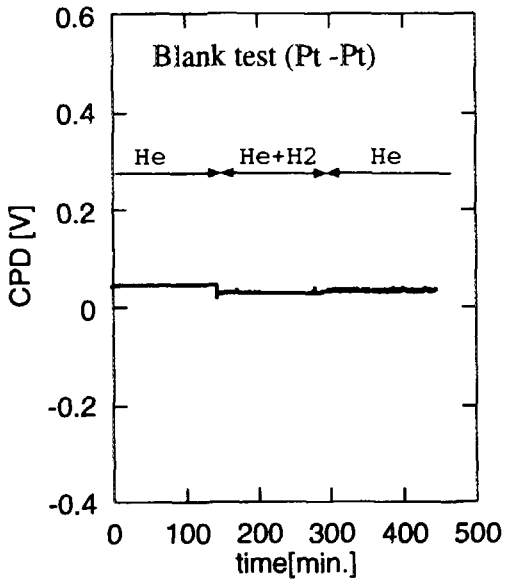

fig. CPD between Pt reference electrode and Pt sample support. (Blank test)

- From the measurement of CPD between ZrO_2 and Pt in the purge gas of He $\leftrightarrow$ H_2, the change of ϕ_{Pt} was considered to be negligible.

$\Rightarrow$ The change of ϕ_{Pt} can be negligible in the system of He $\leftrightarrow$ H_2.

Results (Li_4SiO_4 - Pt)

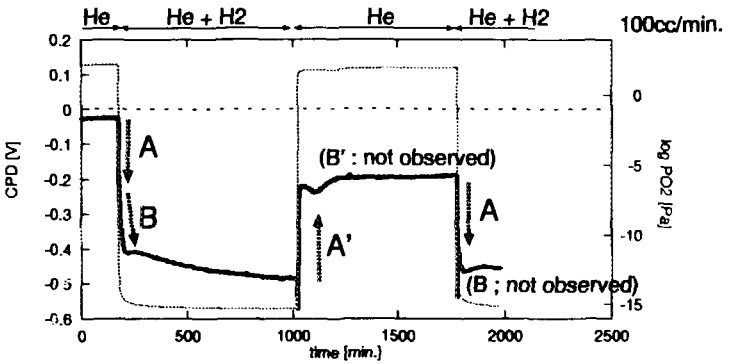

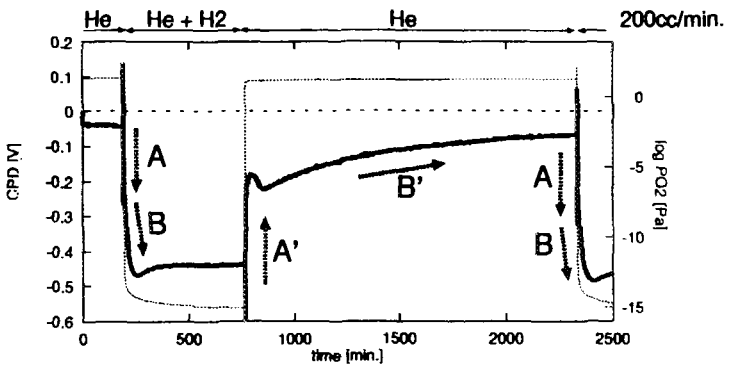

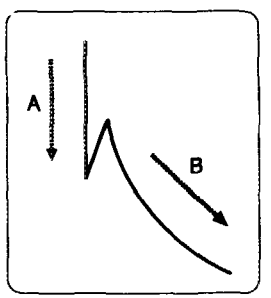

Change A - A'

Change B - B'

What is the reaction ?

About the change A

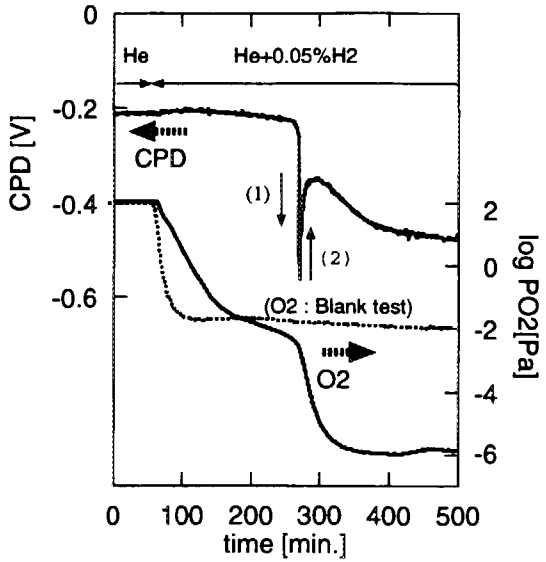

Fig. The work function change caused by an addition of H_2.

- Small amount of H_2 was added. → P_{O_2} was changed slowly.
- P_{O_2} was decreased when CPD was changed.
- The CPD change (1) and (2) are caused by

$$2OH^- \rightarrow H_2O(g) + O^{2-} + V_O \qquad (1)$$

$$2e^- + V_O + \tfrac{1}{2}O_2(g) \rightarrow O^{2-} \qquad (2)$$

- The change A is related to the formation of oxygen vacancies.

Possible processes

- He ⇒ H_2

$$H_2(g)+2O^{2-} \rightarrow 2OH^- + 2e^- \qquad (a)$$
$$H_2O(g)+V_O+O^{2-} \rightarrow 2OH^- \qquad (b)$$
$$2OH^- + 2e^- \rightarrow H_2(g)+2O^{2-} \qquad (c)$$
$$2OH^- \rightarrow H_2O(g)+V_O+O^{2-} \qquad (d)$$

- H_2 ⇒ He

$$2OH^- + 2e^- + 2V_O \rightarrow H_2(g)+2O^{2-} \qquad (c)$$
$$2OH^- \rightarrow H_2O(g)+V_O+O^{2-} \qquad (d)$$
$$2e^- + V_O + \tfrac{1}{2}O_2(g) \rightarrow O^{2-} \qquad (e)$$

- V_O formation : decrease of $\phi_{Li_4SiO_4}$ (electronegativity of oxygen is large)
- OH^- formation : decrease of $\phi_{Li_4SiO_4}$ (electric field is formed from H^+ to O^-)

* Change A : $H_2(g)+O^{2-} \rightarrow H_2O(g)+V_O+2e^-$
* Change A' : $2OH^- + 2e^- + 2V_O \rightarrow H_2(g)+2O^{2-}$
$2e^- + V_O + \frac{1}{2}O_2(g) \rightarrow O^{2-}$

- Change B and B' depend on the flow rate of the purge gas

* Change B : $H_2(g)+2O^{2-} \rightarrow 2OH^- + 2e^-$
* Change B': $2OH^- + 2e^- \rightarrow H_2(g)+2O^{2-}$

The relationship between $\Delta\phi_{Li_4SiO_4}$ and P_{O_2}

– based on the defect equilibria

– quasi-equilibrium between near surface layer of Li_4SiO_4 and O_2 in the gas phase

- **Defect production**

$$\frac{1}{2}O_2 + V_O^{\cdot\cdot} + 2e^- \rightleftharpoons O_O^{\times} \tag{5}$$

$$K = [V_O^{\cdot\cdot}][e^-]^2 P_{O_2}^{1/2} \tag{6}$$

- **Condition of electrical neutrality**

$$2[V_O^{\cdot\cdot}] = [e^-] \tag{7}$$

- **From eq.(6) and eq.(7),**

$$[e^-] = \text{const.} P_{O_2}^{-1/6} \tag{8}$$

- **Fermi-Dirac distribution function**

$$\frac{[e^-]}{N} = \left(\exp\left(\frac{\epsilon - E_F}{kT}\right) + 1\right)^{-1} \tag{9}$$

$V_O^{\cdot\cdot}$	:	doubly charged oxygen vacancy
K	:	the equilibrium constant
[ ]	:	concentration
N	:	density of state
ϵ	:	energy of the produced electron

- **When $\epsilon - E_F \gg kT$, according to Maxwell - Boltzmann statistics,**

$$\frac{[e^-]}{N} = \exp\left(\frac{-(\epsilon - E_F)}{kT}\right) \tag{10}$$

(Maxwell-Boltzmann statistics)

- **From the eqs. (8) and (10),**

$$\frac{E_F - \epsilon}{kT} = -\frac{1}{6}\ln P_{O_2} + \ln N + C \tag{11}$$

- **Assuming that ϵ and N are independent on P_{O_2},**

$$\frac{1}{kT}\left[\frac{\partial(\phi)}{\partial \ln P_{O_2}}\right] = \frac{1}{n}, \quad n = 6, \quad (\Delta E_F = -\Delta\phi) \tag{12}$$

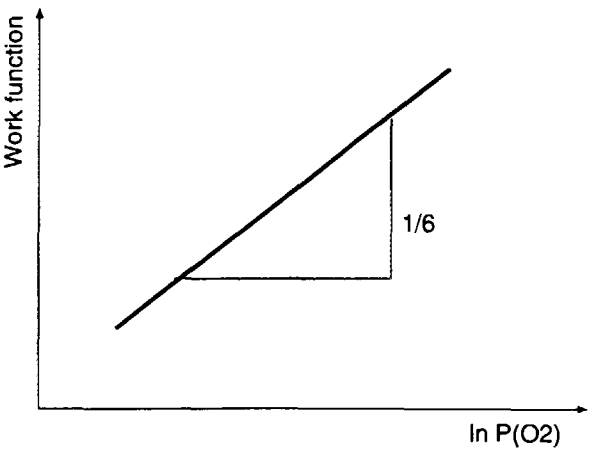

fig. $\ln P_{O_2}$ vs. Work function

$\ln P_{O_2}$ vs. ϕ plot from the experimental data

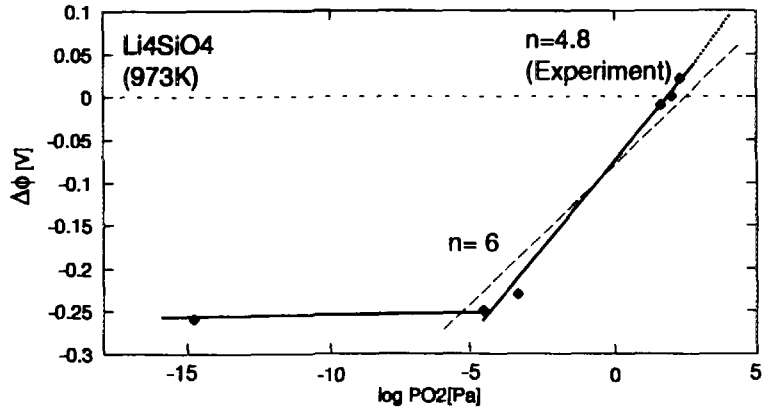

fig. $\Delta\phi_{Li_4SiO_4}$ **vs.** $\log P_{O_2}$. **CPD of** $P_{O_2} = 100$Pa **was put as zero point.**

- **The obtained value of** n **was 4.8.**
- **The dependence was observed in the range of** $P_{O_2} > 10^{-5}$Pa.

In the case of YSZ (Y_2O_3 doped ZrO_2)

- $[V_{\ddot{O}}]$ is determined by $[Y'_{Zr}]$. $[V_{\ddot{O}}]$ in mass action law is constant.

$$K = [V_{\ddot{O}}][e^-]^2 P_{O_2}^{1/2} \tag{13}$$

- The P_{O_2} dependence of ϕ is as follows,

$$\frac{1}{kT}\left[\frac{\partial(\Phi)}{\partial \ln P_{O_2}}\right] = \frac{1}{4} \tag{14}$$

From the experimental data in the following table,

$$\frac{1}{kT}\left[\frac{\partial(\Phi)}{\partial \ln P_{O_2}}\right] = \frac{1}{4.1 \pm 0.4} \tag{15}$$

run	1	2	3	4	5	6	7	8	9
$\Delta\Phi_{YSZ}$mV	60	46	50	59	58	49	58	63	63
n	3.8	4.9	4.5	3.9	3.9	4.6	3.9	3.6	3.6

⇓

Reliability of eq.(12)

$\phi_{Li_4SiO_4}$ - OH^- (Change B, B')

The work function ($\phi_{Li_4SiO_4}$) is considered to decrease by OH^- adsorption.

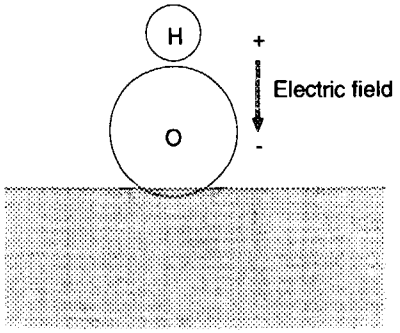

- Behavior of OH^-

$$H_2(g)+2O^{2-} \rightarrow \underline{2OH^-} + 2e^-$$

  - desorption as H_2O (Change A)
  - remain as OH^- (Change B)

⇒ 2 or several types of OH^- adsorption site ??

Summary

1. The change of $\phi_{Li_4SiO_4}$ caused by the change of composition of the purge gas was measured with a high temperature Kelvin probe.
2. $\Delta\phi_{Li_4SiO_4}$ was divided into 2 steps, one is related to oxygen deficient layer and the other is OH^- adsorption.
3. The value of n in the relationship between P_{O_2} and ϕ was obtained to be 4.8. The predicted value is 6.
4. The transition of the nonstoichiometric composition in near surface layer of Li_4SiO_4 was observed in the P_{O_2} range of $10^{-5}Pa < P_{O_2}$.

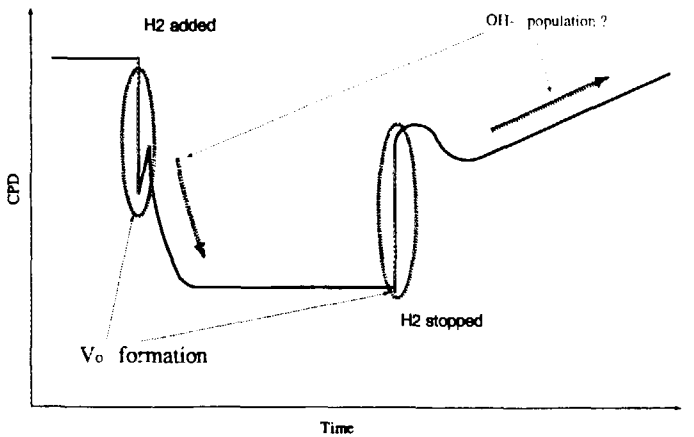

PROGRESS IN THE DEVELOPMENT OF Li_2ZrO_3 and Li_2TiO_3 PEBBLES

Jean-Daniel LULEWICZ , Nicole ROUX

COMMISSARIAT A L'ENERGIE ATOMIQUE - Centre de SACLAY
DTA/CEREM/CE2M/LECMA
91191 - GIF/SUR/YVETTE Cédex - France

ABSTRACT

Li_2ZrO_3 and Li_2TiO_3 pebbles are being developed as ceramic breeder for the European Helium-cooled pebble bed DEMO blanket concept. Status is given of the fabrication work, and of the properties characteristics determination

1 - INTRODUCTION

Li_2ZrO_3 and Li_2TiO_3 are recognized as attractive tritium breeding materials for fusion reactor blankets. Li_2ZrO_3 shows an excellent irradiation and tritium release behaviour up to lithium burn-ups in excess of 10%. Activation of zirconium under irradiation may be a concern although it is small in comparison to that of current blanket structural materials. Li_2TiO_3 exhibits good tritium release behaviour to low temperatures and its activation under neutron irradiation is low. Whereas the pebble bed option is currently selected for ceramic blanket concepts, data on pebble beds behaviour are still limited for Li_2ZrO_3 and almost unexistent for Li_2TiO_3.

Current focus at CEA is placed on the development of Li_2ZrO_3 and Li_2TiO_3 pebbles as ceramic breeders for the E.U helium-cooled pebble bed DEMO blanket concept (HCPB) [1]. In this framework ENEA is developing Li_2TiO_3 pebbles too, using a different fabrication route.

In order to assess the capability of the Li_2ZrO_3 and Li_2TiO_3 ceramics to fulfill the HCPB concept requirements, critical issues are being addressed :

- fabrication of the pebbles
- thermal and mechanical behaviour of pebble beds
- irradiation and tritium release behaviour of pebble beds.

2 - FABRICATION OF Li_2ZrO_3 and Li_2TiO_3 PEBBLES

Each of the processes available to produce pebbles has its own range of applicability. At CEA the choice of the fabrication process of Li_2ZrO_3 and Li_2TiO_3 pebbles followed two guidelines:

- the simplicity of the process and its scalability to requisite quantities, and
- the capability of the process to fulfill the specifications of the pebbles. Based on the HCPB blanket concept requirements the specifications of the pebbles were initially established as follows

  . shape, as spherical as practicable

  . diameter, ~ 1 mm

  . density, ≥ 85% of theoretical density (T.D)

  . grain size, ~ 1 μm

These characteristics are expected to ensure a sufficient Tritium Breeding Ratio (TBR), and an adequate thermal and mechanical behaviour while allowing a good tritium release behaviour. As a result, two processes are being evaluated : 1) extrusion/spheronization/sintering, and 2) agglomeration/sintering. Both processes make use of conventional techniques of powder technology and can be scaled up to industrial quantities.

2.1 - Fabrication of Li_2ZrO_3 pebbles using extrusion

Preparation of the Li_2ZrO_3 powder

The Li_2ZrO_3 powder was prepared by solid state reaction of a mixture of Li_2CO_3 and Hafnium-free ZrO_2 powders in proportions leading to the composition 0.95 Li_2ZrO_3, 0.05 ZrO_2. This procedure was previously worked out in the development of Li_2ZrO_3 pellets at CEA [2]. Specific surface area of the Li_2ZrO_3 powder is 5 m^2g^{-1}.

Shaping of green Li_2ZrO_3 pebbles using extrusion and spheronization

A paste is prepared by mixing the Li_2ZrO_3 powder a binder and a plasticizer. Whereas in the first batch manufactured [3] the binder content was in the order of 30% which resulted in too low a density (~30%) of the sintered pebbles, in the next batches the binder content was decreased to ~ 8%. The paste is extrused in 1.5 mm diameter cylinders. The latter are rounded in a specially designed device and green pebbles are obtained.

Sintering of the Li_2ZrO_3 green pebbles

The green pebbles are sintered in air in the 1050°C-1100°C range during 2 hours.

2.2 - Fabrication of Li_2TiO_3 pebbles using agglomeration

Batches of Li_2TiO_3 pebbles were produced at 7.5% ^6Li and 51.5% ^6Li content. 51.5% ^6Li enriched pebbles were prepared with the aim to achieve a lithium burn-up representative of DEMO end-of-life conditions in the EXOTIC 8 in-situ tritium release experiment in HFR.

Preparation of the Li_2TiO_3 powder

The Li_2TiO_3 powder was prepared by solid state reaction of Li_2CO_3 powder and TiO_2 powder in proportions leading to the composition 0.95 Li_2TiO_3, 0.05 TiO_2 [2]. The Li_2CO_3 powder at 51.5% ^6Li was prepared by mixing in appropriate proportions the Li_2CO_3 powder at 7.5% ^6Li

and the Li_2CO_3 powder at 95% ^6Li. The specific surface area of the Li_2TiO_3 powders is ~ 10 m^2g^{-1}.

Shaping of Li_2TiO_3 green pebbles using agglomeration.

Li_2TiO_3 nuclei are made from the Li_2TiO_3 powder and are subsequently rotated in an ad-hoc equipment while Li_2TiO_3 powder is fed and a binder is sprayed. Granules are grown through this rotation/agglomeration process.

Sintering of the Li_2TiO_3 green pebbles

The Li_2TiO_3 green pebbles are sintered under varying temperature and time conditions in order to identify those allowing to meet the goals for microstructural characteristics, i.e., high density, small grain size. Typical temperature range is 1000-1200°C, time 15 minutes to 2 hours.

2.3 - Fabrication of Li_2TiO_3 pebbles using extrusion

Preparation of the Li_2TiO_3 powder

The preparation of the Li_2TiO_3 powder is identical to that described in section 2.2.

Shaping of the green Li_2TiO_3 pebbles using extrusion

A paste containing the Li_2TiO_3 powder, a binder, and a plasticizer is prepared as described in section 2.1. As a first trial, the paste was extruded through a die with holes 2 mm in diameter. Subsequently, cylinders 2 to 3 mm high are obtained and are rounded in an ad-hoc device into green pebbles.

Sintering of the Li_2TiO_3 green pebbles

The green pebbles are sintered in air under varying temperature and time conditions.

3 - PEBBLES CHARACTERISTICS AND PERFORMANCE

3.1 - Geometrical characteristics

Pebbles obtained by both processes are not perfectly spherical. Although it may not be critical, improvement is being attempted. Sizes of sintered pebbles range from 0.5 mm to 1.2 mm for agglomerated Li_2TiO_3 pebbles, 0.8 mm to 1.2 mm and 1.6 mm to 1.9 mm for extruded Li_2ZrO_3 and Li_2TiO_3 pebbles respectively. Obviously, an extruding die with smaller holes

should be used in order to meet the target of 1 mm for the Li_2TiO_3 pebbles size. Examples of pebbles are shown in Fig.1.

3.2 - Microstructural characteristics

As mentioned above, sintering conditions were varied in order to optimize microstructural characteristics. Small grain size altogether with high density is aimed at. Best sets of characteristics (grain size, density, specific surface area), and related sintering conditions are listed in Table 1 together with crush load and pebble bed density. One can see that densities in the 85% T.D-90% T.D range (which allow for acceptable TBR) can be obtained simultaneously with small grain size (which is advantageous for mechanical strength and tritium release behaviour). This is also true for the first Li_2TiO_3 pebbles produced by extrusion. Typical fracture micrographs are shown in Fig.2.

3.3 - Mechanical strength

The mechanical strength of the pebbles is evaluated from the compressive crush load for a single pebble (see Table 1). Values are the average of 20-30 measurements. The scatter in pebble size, non-sphericity of the pebble, and material heterogeneity are causes of the scatter in the crush load value. The average crush load value is a useful parameter to control pebbles quality and to guide fabrication. Results of crush load values obtained to-date indicate satisfactory mechanical strength.

3.4 - Annealing behaviour

Sintered products may undergo changes on long-time annealing. In order to check the long term stability of the pebbles, and hence to identify the maximum temperature ensuring no significant change of the original characteristics of the pebbles, the study of the annealing behaviour was initiated. The annealing behaviour at 800°C and 900°C, in air, of Li_2ZrO_3 pebbles (sintered at 1050°C during 2 hours), and of Li_2TiO_3 pebbles (sintered at 1050°C during 1 hour) was investigated. Post-annealing examination includes observation of grain size, and measurement of crush load.

No changes were observed after annealing at 800°C for pebbles of any of the ceramics. A very small increase in grain size is observed for the Li_2ZrO_3 pebbles after annealing at 900°C (see Fig.3.a) with no change in crush load (see Fig.4). A limited increase in grain size is observed for Li_2TiO_3 pebbles after annealing at 900°C (see Fig.3.b). Grain size of the annealed pebbles

remains small. Crush load of Li_2TiO_3 pebbles slightly decreases tending to a limit, i.e., 1.7 daN (see Fig.4).

Due to the limited grain size increase, and to the high temperature, the tritium release behaviour of the Li_2ZrO_3 pebbles and of the Li_2TiO_3 pebbles is unlikely to be modified This study will help define the sintering conditions of the pebbles allowing both adequate characteristics and stability of the characteristics at the highest possible temperature.

3.5 - Behaviour of the pebbles on air exposure

Weight gain of pebbles on air exposure was investigated. Weight gain is due to moisture uptake and carbonatation of the materials, both of which are deleterious to ceramic performance and therefore should be minimized. Precautions may be needed against moisture during fabrication, and storage of the pebbles not only at lab-scale but more critically at the industrial scale. Results of weight gain as a function of time for Li_2ZrO_3 and Li_2TiO_3 pebbles under relative humidity in the 40% to 60% range are displayed in Fig.5. One can observe that Li_2TiO_3 pebbles are totally insensitive to ambient atmosphere even after a one year exposure. This is a significant advantage with regards to fabrication and storage. Li_2ZrO_3 pebbles gain weight up to ~ 10%. However, new batches of Li_2ZrO_3 pebbles with a lower specific surface area exhibit a lower sensitivity.

3.6 - Tritium release behaviour.

The major part of the pebbles specimens fabricated to-date were tested in tritium release annealing tests. Results of isothermal tritium release, in He + 0.1% H_2 purge gas, for Li_2TiO_3 pebbles with 90% T.D, 1.5-2 μm grain size, and Li_2ZrO_3 87% T.D, 1-1.5 μm grain size are displayed in Fig.6. Good tritium release is observed at 225-250°C especially for Li_2ZrO_3 pebbles. In addition, the first batch of Li_2TiO_3 pebbles, namely, Li_2TiO_3 pebbles fabricated by the agglomeration method and sintered at 1050°C during 1 hour are being tested in the EXOTIC 8 in-situ tritium release experiment in HFR. Preliminary evaluation of temperature transients indicates good tritium release behaviour [4].

In order to investigate the effect of lithium burn-up on the irradiation performance of the Li_2TiO_3 pebbles, a 51.5% ^6Li enriched pebble specimen (see section 2.2) will be loaded in the next EXOTIC 8 insertion.

CONCLUDING SUMMARY

Two processes, i.e., extrusion and agglomeration, are being evaluated for the fabrication of Li_2ZrO_3 and Li_2TiO_3 pebbles fulfilling the requirements of the European HCPB blanket concept.

Characterization of the first batches of pebbles indicates that both processes can produce pebbles meeting the fixed specifications with respect to pebble size, pebble density, and grain size. Pebbles shape needs to be improved, eventhough there is no experimental evidence that it is a critical issue.

Mechanical strength of the pebbles, as estimated from the crush strength of single pebbles, appears to be adequate.

Annealing tests at 900°C indicate no significant change for Li_2ZrO_3 pebbles, and limited grain growth with limited decrease in strength for Li_2TiO_3 pebbles. As part of the optimization of the pebbles, adjustment of microstructural characteristics is in progress in order to ensure stability of the pebbles at the highest possible temperature.

Tritium release behaviour, as estimated from tritium release annealing tests, is quite satisfactory. Testing of the pebbles is in progress in the EXOTIC 8 in-situ tritium release experiment in HFR for a more thorough investigation.

REFERENCES

[1] M.Dalle Donne, G.Dell'Orco, S.Malang, J.Reimann, N.Roux, K.Schleisiek, Development of the E.U Helium-cooled pebble bed blanket. Presented at ISFNT 4 (1997) to be published in Fusion Engineering and Design.

[2] N.Roux, J.Avon, A.Floreancig, J.Mougin, B.Rasneur, S.Ravel, Low-temperature tritium releasing ceramics as potential materials for the ITER breeding blanket, J.Nucl.Mater. 233-237 (1996).

[3] J.D.Lulewicz, N.Roux, First results on the investigation of Li_2ZrO_3 and Li_2TiO_3 pebbles. Presented at ISFNT 4 (1997) to be published on Fusion Engineering and Design.

[4] J.van der Laan, R.Conrad, personal communication, September 1997.

Table 1

CHARACTERISTICS OF Li_2TiO_3 and Li_2ZrO_3 PEBBLES

Ref.	Material	Fabrication process	Sintering temperature (°C)	Pebble diameter (mm)	Specific surface area (m^2g^{-1})	Grain size (μm)	Density (% T.D.)	Crush load (daN)	Pebble bed density ($g.cm^{-3}$)
RP 3	Li_2TiO_3	Agglomeration	1050	0.7-0.85	0.16	1.5-2	90.8	2.8 (1.5-4.3)*	1.86
RP 3	Li_2TiO_3	Agglomeration	1200	0.7-0.85	0.10	over sintering	88.6	1.8 (1.1-2.5)*	
217	Li_2ZrO_3	Extrusion/Spheronization	1050	0.8-1	0.86	0.5-1	81	2.1 (1.1-3.9)*	2.06
217	Li_2ZrO_3	Extrusion/Spheronization	1100	0.8-1	0.75	1-1.5	87	2.8 (1.7-4.2)*	

* extreme values

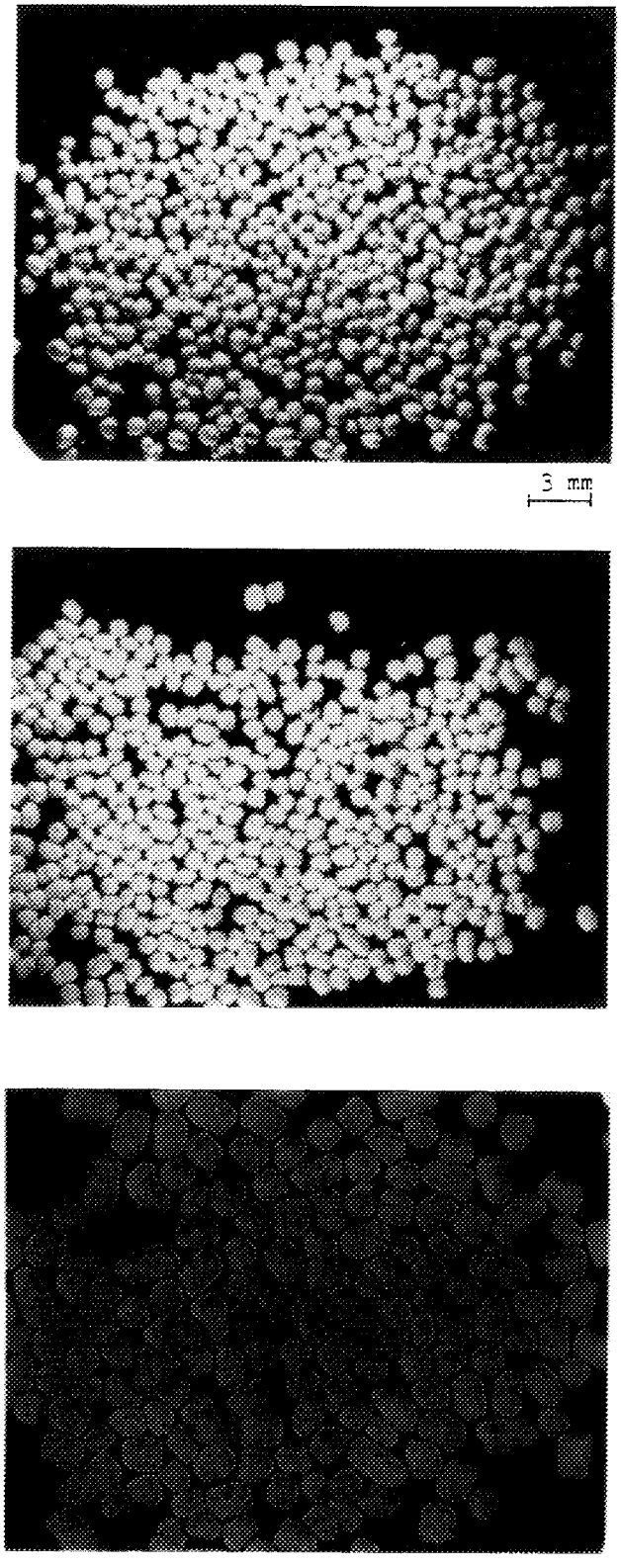

Figure 1

Top : Li_2TiO_3 pebbles (agglomeration), Middle : Li_2ZrO_3 pebbles (extrusion), Bottom : Li_2TiO_3 pebbles (extrusion)

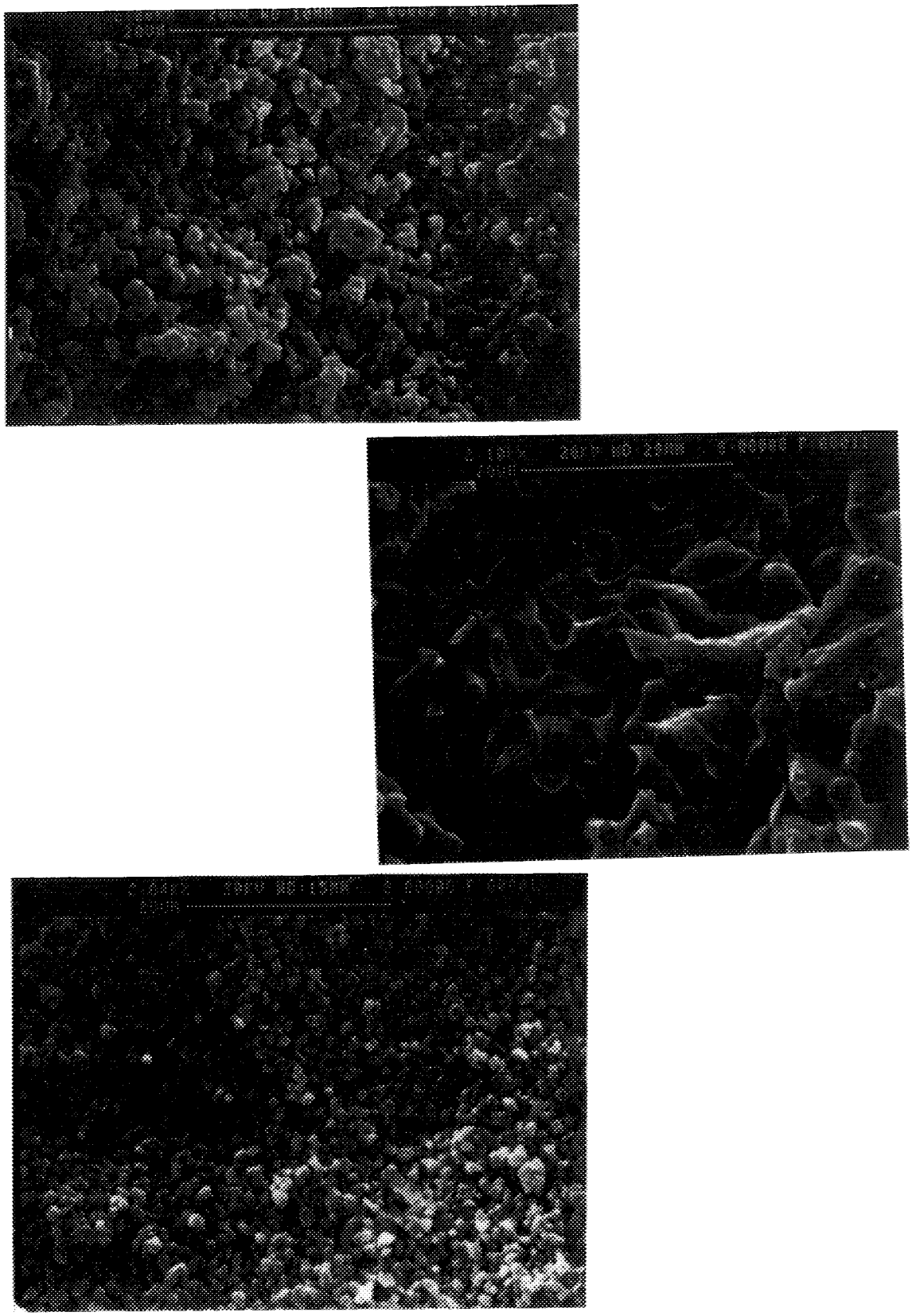

Figure 2
SEM micrographs of
Top : Li_2TiO_3 pebbles (agglomeration) sintered at 1050°C during 1 hour
Middle : Li_2TiO_3 pebbles (agglomeration) sintered at 1200°C during 2 hours
Bottom : Li_2ZrO_3 pebbles (extrusion) sintered at 1100°C during 2 hours

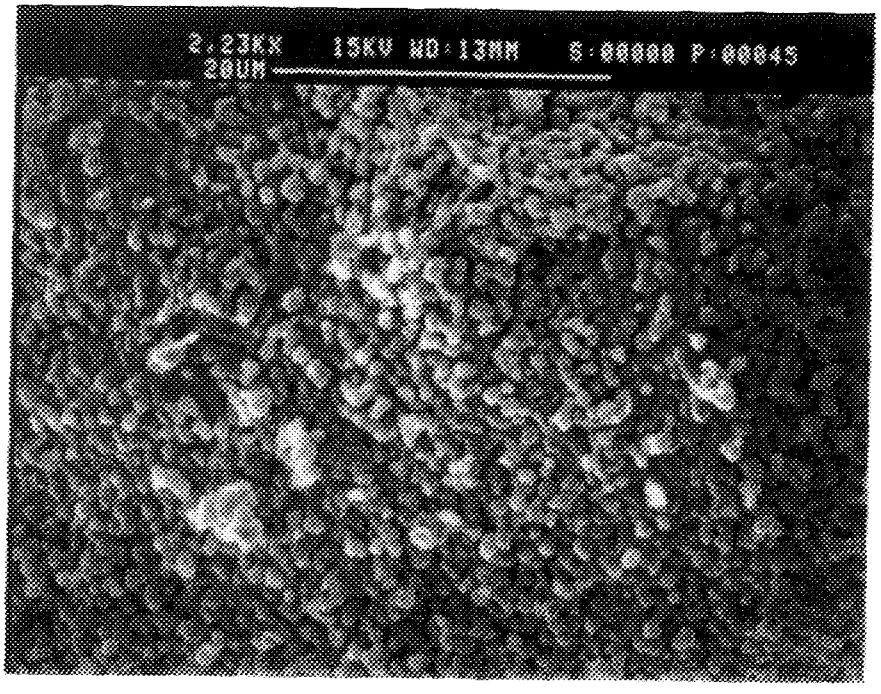

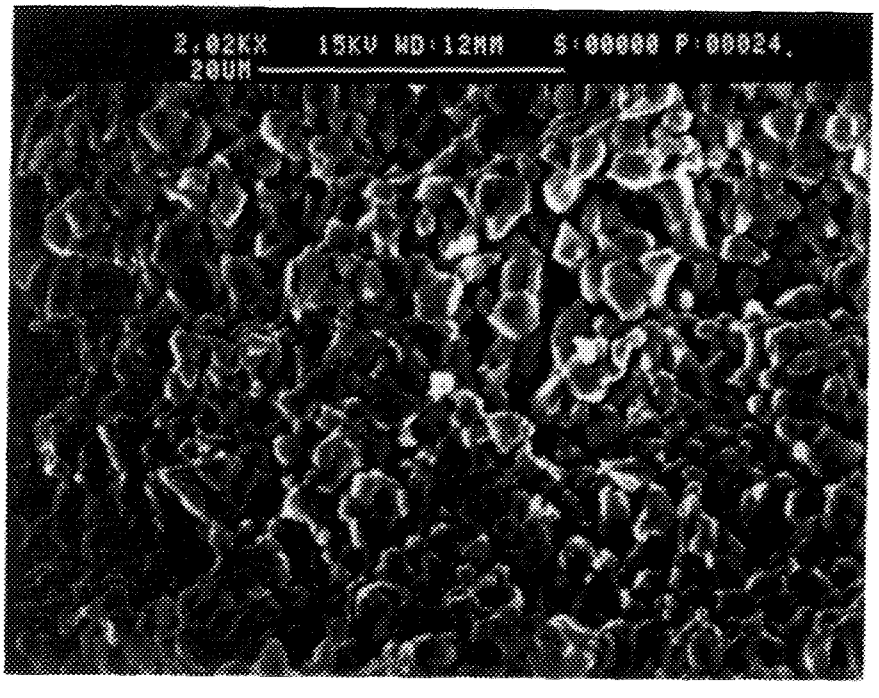

Figure 3.a

Li_2ZrO_3 annealed at 900°C during 15 days (top) and 75 days (bottom)

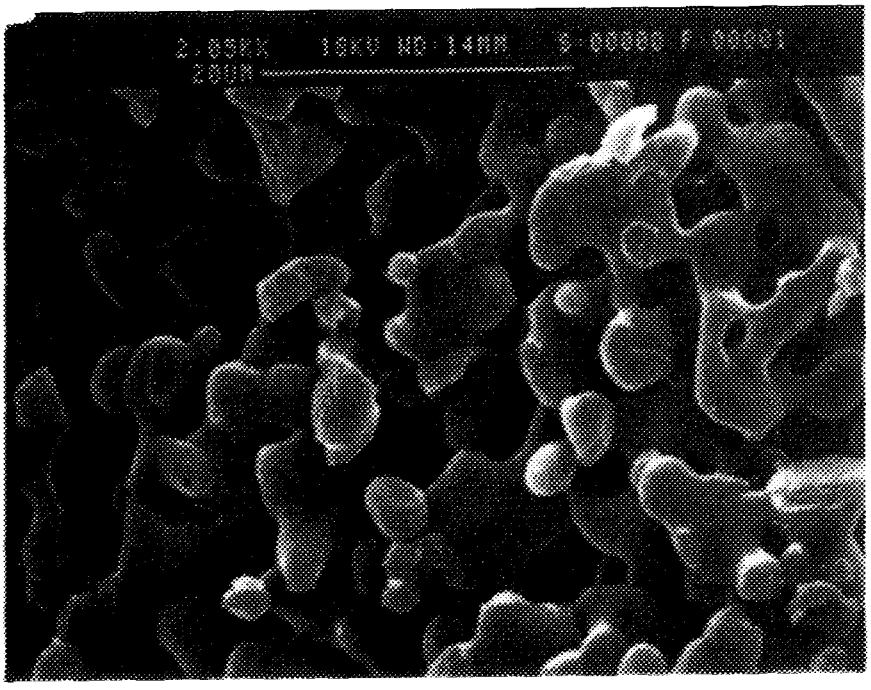

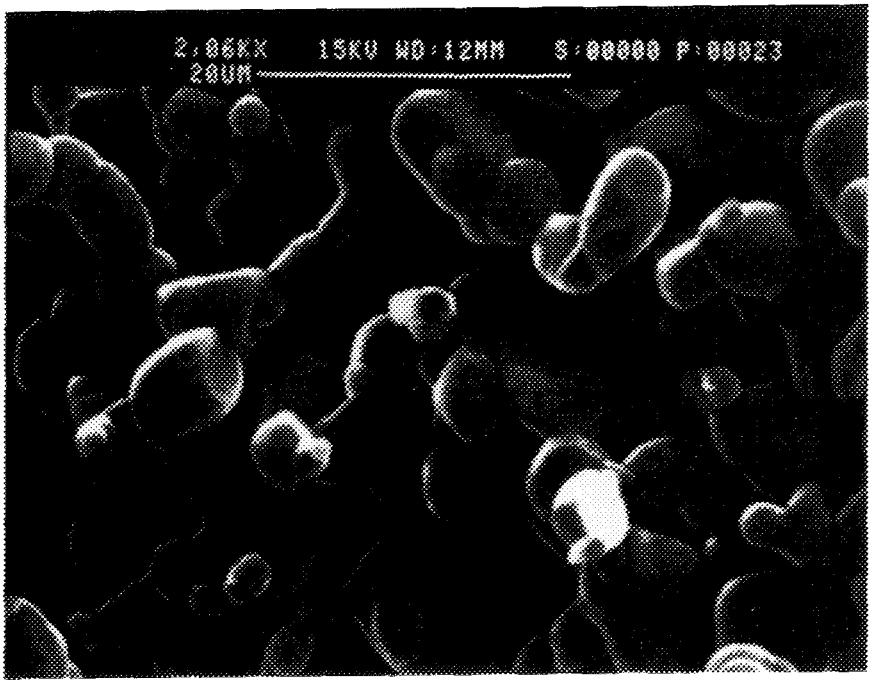

Figure 3.b

Li_2TiO_3 annealead at 900°C during 30 days (top) and 90 days (bottom)

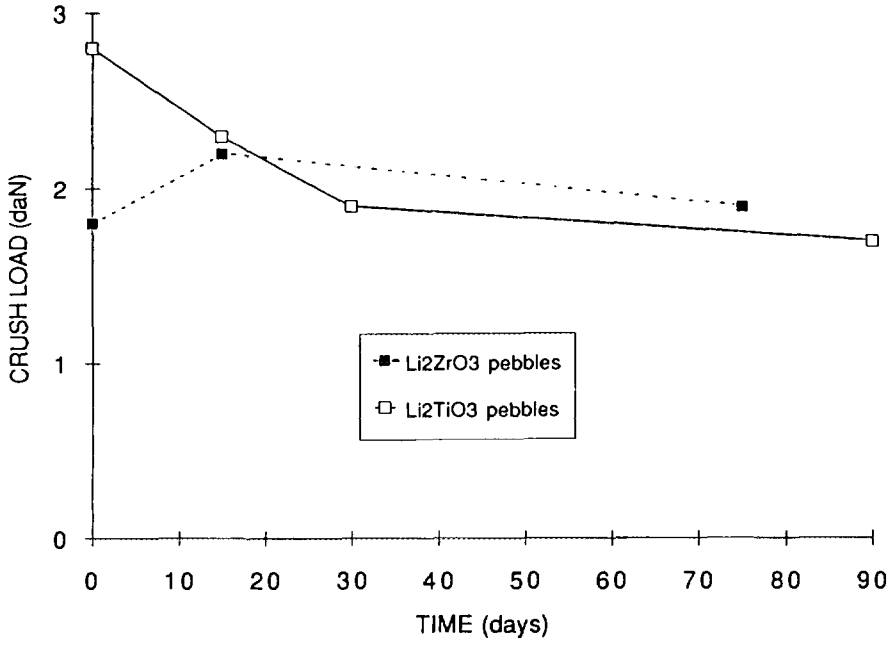

Figure 4

Crush load as a function of annealing time at 900°C for Li_2ZrO_3 and Li_2TiO_3 pebbles

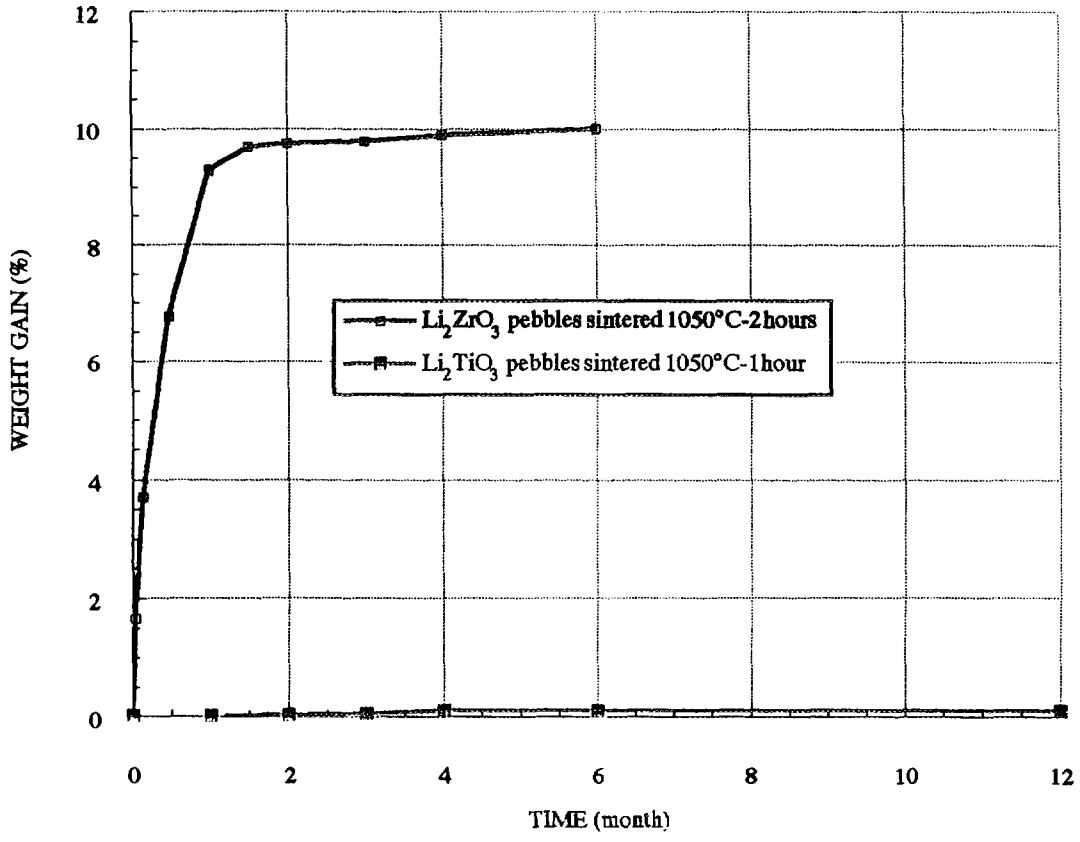

Figure 5

Weight gain of Li_2ZrO_3 and Li_2TiO_3 pebbles on air exposure

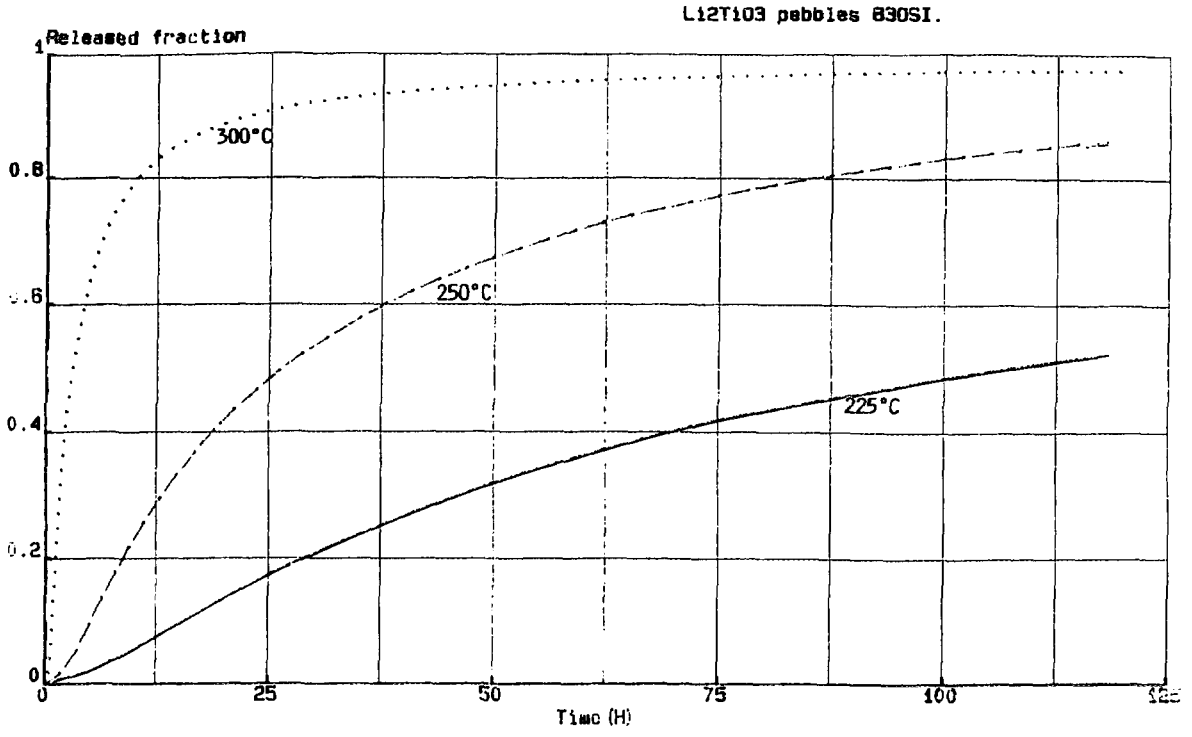

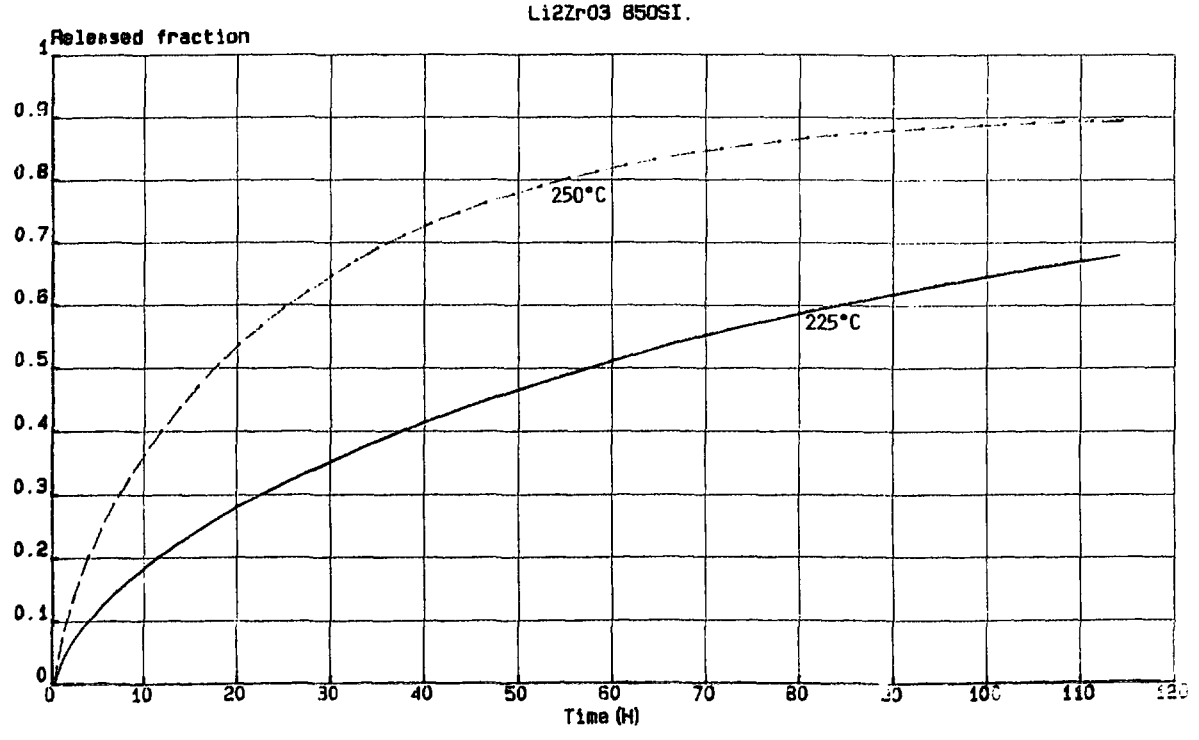

Figure 6

Tritium release from Li_2TiO_3 and Li_2ZrO_3 pebbles

Study on the surface electronic properties of Li-containing solids

Fumio Matsuura, Atsushi Suzuki, Kenji Yamaguchi and M. Yamawaki

Graduate School of Quantum Engineering and Systems Science, Faculty of Engineering, The Univ. of Tokyo.

The electronic state of Li_2O surface will be modified by absorption and/or desorption of chemically-active species, such as H_2 and H_2O. The reactions induced by these species will involve some point defects in the solid. Whereas the high temperature Kelvin probe has proven to be quite effective in obtaining information on the surface reactions between gas and solid, an attempt is being made to incorporate numerical calculation to obtain further information which may not be easily done by experiments.

The code employed in the present study is "CRYSTAL", which employs a self-consistent-field Hartree-Fock method. As a preliminary study, we tried to calculate the change of Fermi Energy as a function of the density of oxygen vacancy. The results revealed that the greater the density of oxygen vacancy, the larger the Fermi Energy of Li_2O, which was consistent with the experimental results obtained by high temperature Kelvin probe.

Study on the surface electronic properties of Li-containing solids

○ Fumio Matsuura, Atsushi Suzuki, Kenji Yamaguchi, M. Yamawaki

Graduate School of Quantum Engineering and Systems Science,
Faculty of Engineering, The Univ. of Tokyo.

6th International Workshop on Ceramic Breeder Blanket Interactions

Researches of surface reaction mechanisms

To clarify surface reaction mechanism in tritium recovery processes, surface-sensitive techniques have been employed.

Work Function measurement is expected to provide information on the surface electronic properties of ceramic breeders.

Change of oxygen potential due to H_2 admission induces defect formation described such as follows.

$$O_O^{\times} \rightleftharpoons V_O^{(n)} + ne' + \frac{1}{2}O_2 \qquad (1)$$

When O vacancies are formed, WF is considered to decrease.
Because,

- **the produced electrons have larger energy than those which are trapped to the ions**
- **electoronegativity of O is large compared with metal elements**

JAERI−Conf 98−006

J.Nowotny[1] et al, reported the qualitative relation between P_{O_2} and WF.

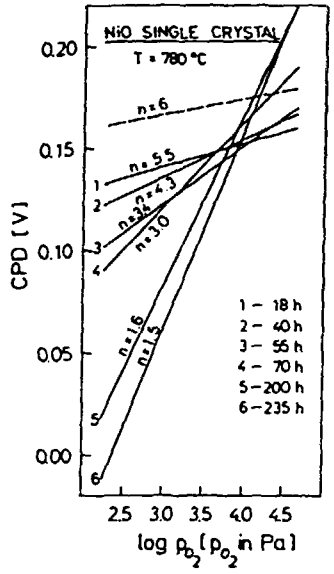

Fig.1 Changes in CPD vs log P_{O_2} for NiO single crystal (against Pt) at different of treatment time at 780 ℃.

$$\text{※ CPD} = \frac{WF[NiO] - WF[sample(Pt)]}{e}$$

The relationship between $\mathbf{WF}(\phi)$ and $\mathbf{P_{O_2}}$ based on the defect equilibria is described as follows

$$\mathbf{O_O^x \rightleftharpoons V_O^{(n)} + ne' + \frac{1}{2}O_2} \tag{2}$$

$$\mathbf{K = [V_O^{(n)}][e^-]^n P_{O_2}^{1/n}} \tag{3}$$

From the condition of electrical neutrality,

$$n[\mathbf{V_O^{(n)}}] = [\mathbf{e^-}] \tag{4}$$

When $\epsilon - E_F \gg kT$, according to Maxwell-Boltzmann distribution

$$\frac{[\mathbf{e^-}]}{\mathbf{N}} = \exp\left(\frac{-(\epsilon - \mathbf{E_F})}{\mathbf{kT}}\right) \tag{5}$$

(ϵ: energy of produced electron, N: density of state)

Assuming that ϵ and N are independent on P_{O_2},

$$\frac{1}{\mathbf{kT}}\left[\frac{\partial(\phi)}{\partial \ln \mathbf{P_{O_2}}}\right] = \frac{1}{\mathbf{n}} \tag{6}$$

In the case of NiO (Fig.1), n=1.5~6

[1]J.Nowotny et al, J. Am. Ceram. Soc., 72(1989) 564

In the case of YSZ (ZrO_2+3 % Y_2O_3), the relationship between WF and P_{O_2} have also been reported by Suzuki, Nowotny.

Similar to NiO, WF was increased with P_{O_2} increase.

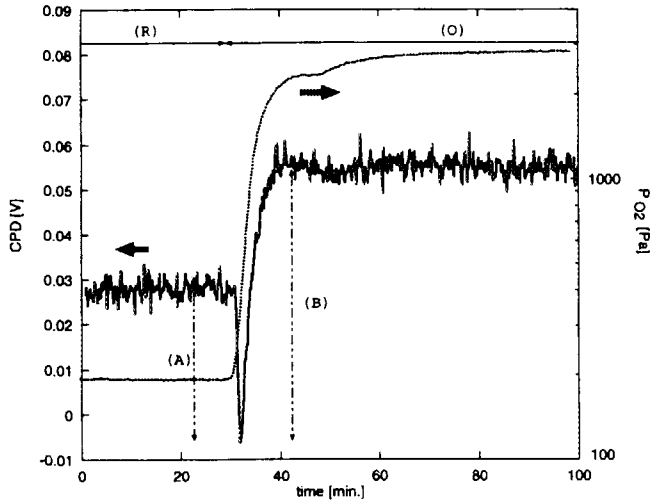

Fig.2 The change of WF of YSZ and P_{O_2} due to the change of the composition of the sweep gas

Suzuki et al. reported the "n" value is 4.1±0.4 where the theoretical value is 4

In this workshop, Suzuki reported the WF measurement result on the Li_4SiO_4.

When H_2 gas was admitted at 200 min,P_{O_2} was decreased and WF was also decreased.
At 800 min when the gas was changed to pure He, P_{O_2} and WF was increased.

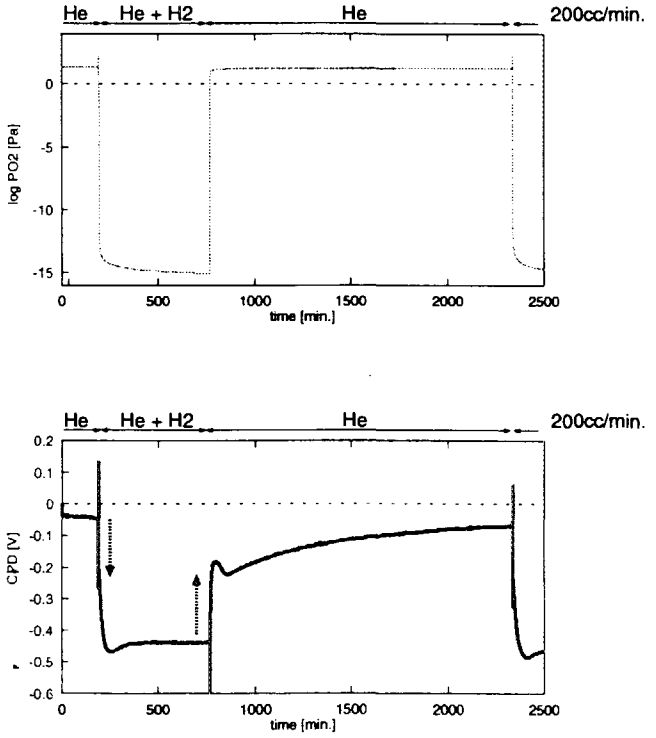

Fig.3 The change of WF of Li_4SiO_4 and P_{O_2} due to the change of the composition of the sweep gas

In all cases (NiO, ZrO_2+3 % Y_2O_3, Li_4SiO_4),the WF was incresed when P_{O_2} was increased.
(or, WF was decreased when P_{O_2} was decreased.)

i.e.

$$\frac{1}{kT}\left[\frac{\partial\phi}{\partial \ln P_{O_2}}\right] = \frac{1}{n} \quad > \mathbf{0} \qquad (7)$$

A Work Function measurement method explain surface phenomena with a value "n"

But, there is still question.
In equation (7),the ϵ and N are assumed constant. Is this really?
And, dose the equation really reflect the actual electronic properties of surface ?

For more detailed understanding of these microscopic phenomena, experimental techniques provide limited information.

⇓

It is recommended to employ computer simulation.

Method

Self-consistent-field Hartree-Fock method

This ab initio method, contains no ad hoc adjustable parameters and uses crystal orbitals (CO) instead of Molecular orbitals(MO).
and

Crystalline lattice is taken into account

CRYSTAL-95

This code can deal with crystalline structure by using finite number of atomic layers parallel to the crystal surface.

Li_2O structure

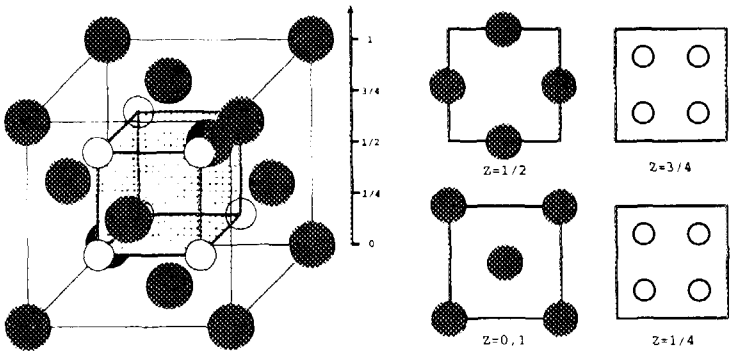

- anti-fluorite structure
- O: face centered cubic lattice
- Li: primitive cubic lattice
- Li-O=1.98 Å a_0=4.573 Å
- ionic bonding material

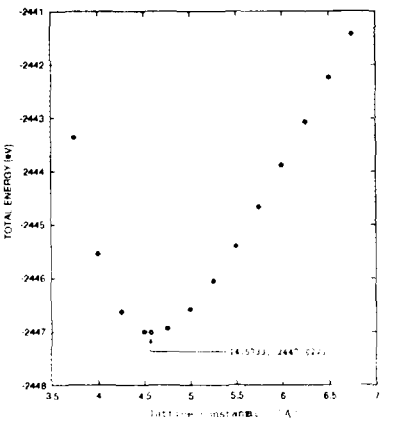

Fig.4 Li_2O Total Energy vs lattice constant a_0

Li_2O surface

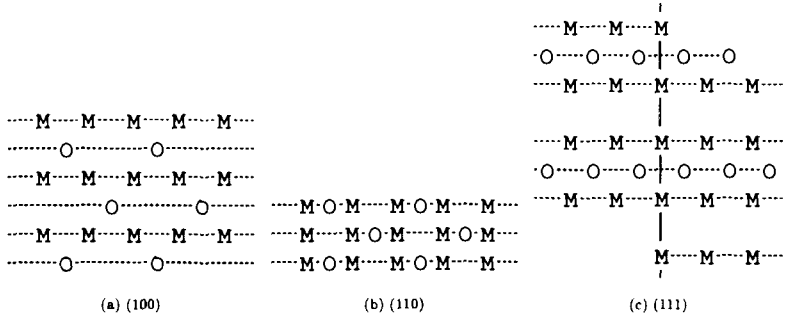

- Defect structure (Assumption)
  - Oxygen vacancy
  - 2 electrons are trapped at the vacancy

$$O_O \rightarrow 2e^- + V_O^{\cdot\cdot} + \frac{1}{2}O_2(g)$$

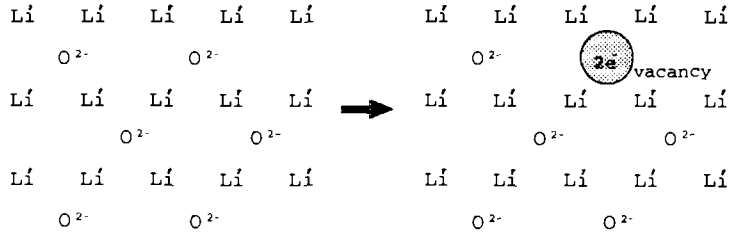

Calculated condition

Example of (110) surface

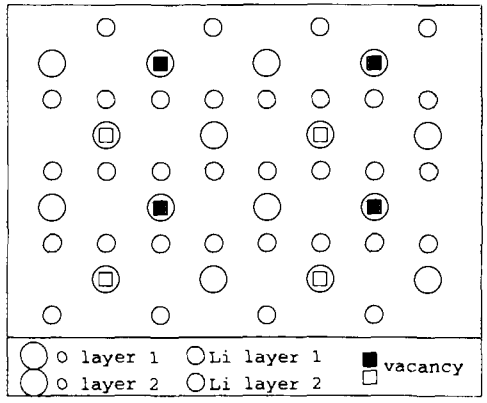

- **Parameter**—**the density of vacancies**
  - (A) No vacancy
  - (B) vacancy at ■
  - (C) vacancy at □
  - (D) vacancy at both ■ and □

Calculated results

Fermi Level of system

density of vacancy		(110)	(100)	(111)
small	(A)	-9.787eV	-5.785eV	-6.742eV
↓	(B)(C)	-3.506eV	-2.593eV	-2.720eV
large	(D)	-2.379eV	-1.687eV	-1.067eV

Calculated Fermi Energy was increased when density of vacancies was increased.

Discussion

When H_2 gas is admitted, oxygen potential decreases, which leads to increase of oxygen vacancy,

$$\mathbf{O_O \rightarrow 2e^- + V_O^{\cdot\cdot} + \frac{1}{2}O_2(g)} \quad (8)$$

Also, oxygen vacancy is formed as follows,

$$\mathbf{H_2(g) + O_O \rightarrow H_2O(g) + 2e^- + V_O^{\cdot\cdot}} \quad (9)$$

$$\mathbf{OH^- + H^+ \rightarrow H_2O(g) + 2e^- + V_O^{\cdot\cdot}} \quad (10)$$

The calculation results indicates that oxygen vacancy increase the Fermi Energy.
The relation between Fermi Energy($\mathbf{E_F}$) and WF(ϕ) is

$$\Delta E_F = -\Delta\phi$$

so, it is considered that **H_2 addition (i.e. decrease of P_{O_2}) would decrease Work Function.**
In turn, **increase of P_{O_2} would increase Work Function.**

⇓

same in agreement with WF measurement

And, What else causes WF change ?

- Adsorption

  Work Function changes as a function of sulfur coverage on Ni(001) surface after H_2S adsorption was reported.(CBBI-4)
  WF was increased when sulfur coverage was increased.

- The behavior of OH^-

$$\mathbf{H_2(g)+2O^{2-} \rightarrow \underline{2OH^-} + 2e^-}$$

  Adsorption of OH^- would form electron field at the surface, and change the surface electronic states.

Summary

- **With the Hartree-Fock method, Fermi Energy was calculated with for oxygen deficient system. The relationship between oxygen potential and Work Function was discussed.**

- **Adsorption effect should be included for more explanation of Work Function change in future calculation.**

  And also, defect structure would be complex. Various charges defect type should be included.

SESSION 2

Modeling of Tritium Release Behavior

Modeling Tritium Behavior in Li_2ZrO_3*

M. C. Billone
Energy Technology and Technology Development Divisions
Fusion Power Program
Argonne National Laboratory
9700 S. Cass Avenue
Argonne, IL 60439

Abstract

Lithium metazirconate (Li_2ZrO_3) is a promising tritium breeder material for fusion reactors because of its excellent tritium release characteristics. In particular, for water-cooled breeding blankets (e.g., ITER), Li_2ZrO_3 is appealing from a design perspective because of its good tritium release at low operating temperatures. The steady-state and transient tritium release/retention database for Li_2ZrO_3 is reviewed, along with conventional diffusion and first-order surface desorption models which have been used to match the database. A first-order surface desorption model is recommended in the current work both for best-estimate and conservative (i.e., inventory upper-bound) predictions. Model parameters are determined and validated for both types of predictions, although emphasis is placed on conservative design predictions. The effects on tritium retention of ceramic microstructure, protium partial pressure in the purge gas and purge gas flow rate are discussed, along with other mechanisms for tritium retention which may not be dominant in the experiments, but may be important in blanket design analyses. The proposed tritium retention/release model can be incorporated into a transient thermal performance code to enable whole-blanket predictions of tritium retention/release during cyclic reactor operation. Parameters for the ITER driver breeding blanket are used to generate a numerical set of model predictions for steady-state operation.

*Work supported by the United States Department of Energy/Office of Fusion Energy, under Contract No. W-31-109-Eng-38.

1. INTRODUCTION

Lithium metazirconate (Li_2ZrO_3) is considered an attractive tritium breeding material for fusion reactor blankets because of its excellent tritium release properties, even at relatively low temperatures (e.g., < 350°C). Several DEMO reactor designs[1,2] and the ITER driver blanket design[3] have specified the use of Li_2ZrO_3 in either sintered-product pellet form or pebble-bed form. The thermal and tritium performance properties of Li_2ZrO_3 and Li_2O have been compared by Billone in Ref. 4, along with approaches to modeling tritium transport in these two ceramic breeder materials.

The tritium retention/release database for Li_2ZrO_3 has undergone significant expansion during the past five years. The steady-state database comes from post-irradiation measurements of tritium inventory [I in weight parts per million (wppm)] in samples which have been irradiated in in-reactor purge-flow tests. Examples of such tests are the EXOTIC series (pebbles and pellets), BEATRIX-II Part II (pebbles), CRITIC-II (pebbles) and SIBELIUS (pellets). These data are generally normalized to the tritium generation rate (G in wppm/hour) to give a tritium residency time (τ = I/G in hours). The generation rate is taken from the last reactor cycle which is assumed to operate at a constant temperature profile and purge flow rate and composition for a time long enough to establish steady-state retention and release. Data from transient testing come from several methods: the difference between the transient release rate (R in wppm/hour) and the generation rate (G in wppm/hour) can be determined by integrating (G - R) in response to a sudden change in temperature or purge-protium-content to give the change in steady-state inventory (ΔI); the time-history of the release rate represents a detailed form of transient data; and the time-histories of the release data from post-irradiation isothermal anneal tests and/or temperature ramp tests represent a detailed form of transient data. In addition, data are also obtained from samples irradiated at very low temperature and subjected to a post-irradiation isothermal anneal and/or temperature ramp tests. Finally, laboratory tests have been used to characterize the response of unirradiated Li_2ZrO_3 to moisture and hydrogen isotopes in the gaseous form.

In terms of models used to interpret tritium retention/release data, diffusion, first-order surface desorption and diffusion-desorption models are generally used, although surface adsorption and second-phase precipitation models are also included in more detailed treatments.[5,6] The decision as to the degree of modeling sophistication required depends on the extent of the database and the application. MISTRAL[5] is an example of a fundamental first-principles code for analyzing both transient and steady-state performance of ceramic breeders. However, several possible draw-backs to using MISTRAL as a design code are: a) the database is not extensive and thorough enough to allow determination and fine-tuning of the many pre-exponential constants and activation energies incorporated into the models; b) MISTRAL, which performs the analysis for a local radial slice of solid breeder, does not have the internal capacity to repeat this calculation many times to account for poloidal, toroidal and radial variations in operating conditions in order to generate a "whole-blanket" result; and c) it is difficult to incorporate and/or couple MISTRAL to a whole-blanket code which generates time- and space-dependent distributions of tritium generation rates and temperatures. TIARA[6] is an example of a code with less-detailed, steady-state models for diffusion, first-order surface desorption, solubility and second-phase precipitation. Model parameters are determined from out-of-reactor testing of irradiated and unirradiated samples. Validation is performed by comparing code predictions to inventory data derived from post-irradiation data from samples which have been subjected to in-reactor purge-flow testing. However, several possible draw-backs to using TIARA as a design code are: a) to date, only model parameters for Li_2O have been determined and validated; b) the code is restricted in

application to steady-state operation; and c) separate calculations must be performed for each radial layer in a module and for each module in the poloidal direction with no internal means of integrating the results to obtain a whole-blanket result.

The objective of the current work is to generate a model for Li_2ZrO_3 tritium retention/release which reasonably matches, or at least bounds, the database, and yet is simple enough to incorporate into a whole-blanket code for design analysis of breeding blanket performance under steady and cyclic operation. Progress in model development is discussed in this current effort. Sample design calculations are presented for the case of the ITER driver blanket operating in a steady-state mode.

The effects on tritium retention of ceramic microstructure, protium partial pressure in the purge gas and purge gas flow rate are discussed, along with other mechanisms for tritium retention which may not be dominant in the experiments, but may be important in blanket design analyses. Additional test results, not included in the current work, are highlighted.

2. Diffusion vs. First Order Surface Desorption Models

Before the development of more sophisticated codes such as MISTRAL and TIARA, modeling of tritium behavior in lithium-based ceramics consisted of single mechanism (e.g., diffusion or desorption) or dual mechanism (e.g., diffusion and desorption) models. Both diffusion and first-order surface desorption models lead to the result that the steady-state tritium inventory [I in weight parts per million (wppm)] is linearly proportional to the tritium generation rate (G in wppm/hour) with the proportionality constant equal to the tritium residency time (τ = I/G, where τ is commonly expressed in units of hours). For a single spherical grain, the diffusional residency time is related to the geometry of the sample according to

$$\tau = a^2/(15\ D) \tag{1}$$

where a is the grain radius (in m) and D is the diffusion coefficient in m^2/hour. For the same geometry, the desorption residency time is related to the geometry of the sample according to

$$\tau = a/(3\ k) \tag{2}$$

where k is the desorption rate constant. For each mechanism, there are two constants which can be determined by matching predictions to data:

$$D = D_o \exp\left[-Q_{dif}/(R\ T)\right] \tag{3}$$

and

$$k = k_o \exp\left[-Q_{des}/(R\ T)\right] \tag{4}$$

where D_o and k_o are pre-exponential constants, Q_{dif} and Q_{des} are effective activation energies for the respective mechanisms, R is the universal gas constant [8.314 x 10^{-3} kJ/(mol•K)] and T is the absolute temperature in K.

For porous, polycrystalline samples, it is customary to assume spherical grains and to use Eq. 1 for the diffusional tritium residency time. However, in the case of the desorption residency time, the volume to surface-area ratio term (a/3) in Eq. 2 is replaced by $(a_s \rho_{th})^{-1}$, where a_s is the specific pore-solid interface area (in m^2/g) for interconnected porosity and ρ_{th} is the theoretical density of the ceramic in g/m^3. In addition, excess protium in the purge gas is assumed to enhance tritium release and to reduced tritium inventory. The adsoption of protium onto the surface of the ceramic is assumed to be proportional to the square root of the protium partial pressure[$(P_{H2})^{0.5}$, where P_{H2} is in Pa]. Thus, the surface desorption model predicts that the residency time for a porous solid purged by excess protium can be expressed as:

$$\tau = [a_s \rho_{th} k_o (P_{H2})^{0.5}]^{-1} \exp [Q_{des}/(R T)] \quad (5)$$

Based on steady-state data alone, it is difficult to determine which mechanism is rate limiting unless the sample microstructure and the operating conditions are varied in a controlled manner. Both mechanisms result in a linear dependence of inventory on generation rate and an exponential increase in inventory as the temperature is lowered. However, for a spherical single crystal, the diffusion inventory increases as a^2 while the desorption inventory increases as a. Also, for samples purged by He + H_2, the diffusional inventory is independent of the protium content in the purge while the desorption inventory varies inversely as the square root of the protium partial pressure. It is more common to use porous, polycrystalline samples to study tritium behavior. This often results in a complication in the interpretation of the data. As the grain size is increased, the porosity tends to decrease and the pore-solid surface area tends to decrease, resulting in an increase in both diffusion and desorption inventory. Special fabrication procedures are required to increase the grain size at a constant pore-solid surface area. Furthermore, changes in the sample microstructure and/or operating conditions during the in-reactor testing period may result in a change in the rate-limiting mechanism or a change into the transitional regime where both mechanisms are rate-limiting.

The mathematical solutions for transient diffusion vs. desorption appear to be quite different, but the numerical results are quite similar. Two examples are given in the following. In the first case, a spherical grain at uniform temperature T and zero initial tritium concentration experiences a step-function increase in generation rate from 0 to G. The release-rate fraction (F_{rr} = R/G) for a diffusion controlled mechanism is given by

$$F_{rr} = 1 - (6/\pi^2) \Sigma (1/n^2) \exp [-n^2 \pi^2 t/(15 \tau)] \quad (6)$$

where the sum in Eq. 6 is from 1 to ∞ and τ is defined by Eq. 1. For $F_{rr} < 0.2$ or $t/\tau < 0.015$, the short-time approximation to Eq. 6 may be used:

$$F_{rr} = 2.745874 (t/\tau)^{0.5} \quad (6a)$$

For longer times up to $F_{rr} = 0.95$ or $t/\tau = 5$, the intermediate-time solution to Eq. 6 may be used:

$$F_{rr} = 2.745874 (t/\tau)^{0.5} - 0.2 (t/\tau) \quad (6b)$$

The first-order desorption solution to the same problem is given by

$$F_{rr} = 1 - \exp(-t/\tau) \quad (7)$$

where τ is given by Eq. 2.

The two solutions (Eq. 6 and Eq. 7) are compared graphically in Fig. 1 for the same value of τ and, hence, the same steady-state inventory (time integration of G-R) and the same area under the fractional release rate curve. The diffusion solution initially rises more quickly from 0 to about 0.8 than does the desorption solution, but it approaches the steady-state solution of 1 more slowly. However, with experimental error in measuring tritium release, with generation rates that rise quickly (but not instantaneously) with time, and with temperature gradients generally associated with in-reactor test samples, the response time history is distorted and it is very difficult to determine diffusion-controlled release from desorption-controlled release based on the non-ideal, experimental release-rate history.

The second comparison example consists of the same spherical grain at the same steady generation rate. After steady-state release has been obtained, the temperature is increased instantaneously from T_1 to T_2 resulting in an increase in release rate fraction to above 1 and a decrease in steady-state inventory (ΔI). The corresponding decrease in residency time is from τ_1 to τ_2, which implies an increase in diffusion coefficient if diffusion is rate-limiting or an increase in the desorption-rate constant if desorption is rate-limiting. The mathematical solution to this problem for the diffusion-rate-limiting case is

$$F_{rr} = 1 + (\tau_1/\tau_2 - 1)(6/\pi^2) \Sigma (1/n^2) \exp[-n^2 \pi^2 t/(15 \tau_2)] \quad (8)$$

The mathematical solution to this problem for the desorption-rate-limiting case is

$$F_{rr} = 1 + (\tau_1/\tau_2 - 1) \exp(-t/\tau_2) \quad (9)$$

The two solutions are compared in Fig. 2 to experimental data from EXOTIC-6 transient #E0121208, which involved an increase in average breeder temperature from 368°C to 468°C.[7] In Ref. 7, based on a diffusion best-fit to the data, the residency times of τ_1 = 3.5 hours and τ_2 = 0.28 hours were determined. As shown in Fig. 2, using the same residency time value in the desorption model (Eq. 9) results in nearly identical results. With these residency times, both models give the same inventories at T_1 and T_2, as well as the same inventory change (ΔI). Based on tritium measurement errors, on possible distortion of the tritium release time history as the signal travels long distances in purge tubes form sample to monitoring instrumentation, on the effects of temperature gradients through the sample and on the non-instantaneous nature of the temperature increase, it is, again, very difficult to distinguish mechanisms based on these transient results. Both models give a step change in release-rate fraction of 12.5 for the specified residency value times, while the data gives a peak change of only 5.5. Both models give approximately the same asymptotic return to steady-state.

In summary, diffusion, diffusion/desorption, and desorption models have been used to interpret tritium release data and to predict tritium behavior in blanket designs. In terms of steady-state results, the diffusion and desorption models give the same predictions when the same residency time values are used. The time-dependent predictions from the two models are too close to allow a

distinction in rate-limiting mechanism based on most available transient data sets for Li_2ZrO_3. However, for other lithium-based ceramics, such as Li_2O, for which single-crystal lattice diffusivity has been measured, the calculated diffusion inventory is orders of magnitude lower than the inventory measured after in-reactor purge flow experiments.[6] The surface desorption rate constant determined for Li_2O from very controlled tests gives much better agreement with measured tritium inventories than does the diffusion coefficient. Thus, within the solid breeder analytical and experimental communities, there is general agreement that surface desorption is more rate-limiting than diffusivity for the microstructures which have been extensively tested and are recommended for design application. In general, of course, these are fine-grained samples with grain diameters on the order of 1 μm.

In the current work, the desorption model is selected over the diffusion model for detailed evaluation and validation because there are stronger physical arguments for it being more rate-limiting than diffusion and because it is simpler to apply to design problems for which there are large temperature gradients and, in some cases such as ITER, cyclic operation.

3. Tritium Retention/Release Database

3.1 Steady-state database

Direct measurements of tritium inventory in Li_2ZrO_3 cylindrical-pellet and pebble samples have been made following in-reactor purge flow tests. Tables 1 and 2 summarize the pertinent microstructural parameters and operating conditions for samples irradiated in the EXOTIC 3-6 tests (pellets and pebbles),[7] the BEATRIX-II Phase II test (pebbles),[8] the CRITIC-II test (pebbles),[9-11] and the SIBELIUS test (pellets).[12] For the pellet data, the tritium inventories are quite low (≤ 0.1 wppm) for average breeder temperatures ≥ 390°C and local temperatures ≥ 340°C. However, when scaled by the generation rate to give residency time, $\tau \leq 5.4$ hours under the same operating conditions. Figure 3 shows the variation in residency time for porous pellets with the volume averaged temperature. The variation in model parameters (e.g., grain size, pore-solid surface area, protium pressure) is not large enough and/or consistent enough to justify one model (e.g., surface desorption) over another (e.g., diffusion). These data do not scale very well with the square of the grain size, as would be suggested by a diffusion model. With the exception of the one SIBELIUS data point at 100 Pa protium pressure, the majority of the data are at the same protium pressure (300 Pa), making it difficult to justify surface desorption based on protium pressure. Normalizing the pore-solid surface area to 0.9 m^2/g, gives a variation of 0.44 to 1.67 in this surface-desorption parameter. The pore/solid surface area scaling gives results which have only marginally less scatter than the results with grain-size-squared scaling. For the most interesting case (EXOTIC-4, Capsule 16.1 with $\tau = 5.4$ hours), the pore-solid surface area is not given. Finally, it is difficult to determine an effective activation energy from Fig. 3, because of the insufficient number of data points, the scatter in the data points, and the temperature-gradient effects which are not included in the analysis. In principle, an upper-bound residency time correlation could be established for the given temperature regime, but there would be no confidence is assuming that the activation energy would be high enough to extrapolate the residency times to lower temperatures and still represent a lower bound.

The pebble bed data in Table 2 represent a large number of individual data points for individual pellets: 1 for EXOTIC-6, 38 for BEATRIX-II/Phase-II and 40 for CRITIC-II. However, there is a high degree of uncertainty in assigning a local temperature for each pebble and, hence, each data point. Table 2 summarizes the range of inventories measured for each region of the pebble bed and

the corresponding temperature range. The tritium residency times are plotted in Fig. 4 as a function of average sample temperature. The pebble grain sizes are about an order of magnitude higher than the pellet grain sizes. Specific pore/solid surface area is reported only for the CRITIC-II pebbles. The BEATRIX-II/Phase-II pebbles are expected to have a similar value. The 94% dense EXOTIC-6 pebbles are expected to have a significantly lower pore/solid surface area than the 80-85% dense pebbles for BEATRIX-II and CRITIC-II. If the results were normalized to a protium pressure of 300 Pa, then according to the surface desorption model the BEATRIX-II results would be multiplied by a factor of only 0.95 and the CRITIC-II results would be multiplied by a factor of 0.58. In general, tritium inventories are quite small (< 0.3 wppm) for T ≥ 400°C. Higher inventories are measured for the EXOTIC-II pebble bed (2.4 wppm at an average temperature of 360°C and local temperatures of 315 to 425°C) and the CRITIC-II pebble bed (6.3±4.6 wppm at an average temperature of 285°C and a local temperature range of 170 to 400°C). While these pebble results are quite good for validating models for tritium retention/release, they are not adequate for distinguishing between diffusion and desorption models or for determining an effective activation energy.

3.2 In-reactor transient tritium release data

For the EXOTIC-5, EXOTIC-6 and CRITIC-II tests, a number of transient tritium release curves were recorded following a change in temperature or protium content in the purge gas. For BEATRIX-II, transient release data are available only for changes in protium content in the purge. In Ref. 7, the data for EXOTIC temperature transients are tabulated in terms of the diffusional residency times which gave either the best fit to the inventory change (ΔI) and/or the time dependent release. The $\Delta\tau = \Delta I/G$ values are determined by integrating over time the transient release rate (R) minus the generation rate (G). The determination of $\Delta\tau$ in this manner results in values which are independent of models and, hence, can be used to determine model parameters for either a diffusion or a desorption model. The major uncertainty in this approach is associated with the long periods of time for which the final release rate is close, but not equal, to the generation rate. Following temperature increases, the release rate seems to come to a steady-state value which is slightly above the generation rate. The opposite occurs following a temperature decrease in that the apparent steady-state release rate is slightly below the generation rate. However, in the detailed tables in Ref. 7, it is not clear which residency times were determined by this method. It appears that most of the residency times in Ref. 7 were determined as values of τ which give a best-fit of the diffusion model to the measured transient release rate data vs. time. As shown in Fig. 2, a surface desorption approach would have led to essentially the same values of tritium residency time.

The values of residency time reported in Ref. 7 based on temperature-change data are shown in Fig. 5 (pellet data) and Fig. 6 (pebble-bed data) vs. the inverse of the average temperature in K. The scatter in the data is more than an order of magnitude for the pellet data (more samples with different microstructures) and less than an order of magnitude for the pebble data.

3.3 Transient data from postirradiation isothermal anneals and/or temperature ramps

In addition to the data described in the two previous subsections, data are also available in the literature for samples irradiated at low temperature and subjected to laboratory postirradiation isothermal annealing and or linear temperature ramp testing. Uncertainties associated with these data sets are: possible release of some of the tritium during irradiation; spatial distribution of tritium following irradiation, level of tritium remaining in the samples after testing. These data have not yet been used to validate the proposed surface desorption model.

4. Determination of Parameters for the First-Order Surface Desorption Model

4.1 Transient data for Li_2ZrO_3 EXOTIC-5,6 pellets

The motivation for separating the residency time data for cylindrical pellets (Fig. 5) from the residency time for pebble beds (Fig. 6) is the large difference in microstructures (grain sizes and specific pore/solid surface area) for the two types of samples. Both the larger grain size and the implicitly smaller pore/solid surface area of the pebble beds suggest that inventories and residency times should be higher for the pebbles. However, even with this separation of databases, the scatter in the data is too large to allow model parameters to be selected with confidence.

The authors of Ref. 7 suggest ways to filter and group the data. Residency times determined from the first reactor cycle (approximately 25 days) tended to be smaller than residency times determined from subsequent cycles. Residency times determined from temperature decrease transients tended to be smaller than residency times determined from temperature increase experiments. For design application, the main interest is in long-time behavior. For ITER application the long-time behavior at low temperature is of particular interest.

In Fig. 5, the pellet residency times have been determined from temperature increase and temperature decrease experiments at reference purge flow conditions (He+0.1%H_2, 0.3 MPa pressure, 100 ml/minute flow rate). The results of the first 25-day cycle of operation have been omitted from this plot. Also, the data are separated into temperature increase and temperature decrease values. While, for a specific sample, it may be true that temperature rise experiments lead to higher values of residency time than do temperature decrease experiments, the scatter of results from sample to sample appears to be greater than this effect for any one sample. Best fit correlations to the values of residency time data are:

Temperature rise experiments: $\tau = \exp(-12.569 + 8.309\times10^3/T)$, hours (10a)

Average of all data: $\tau = \exp(-12.068 + 7.911\times10^3/T)$, hours (10b)

Temperature decrease experiments: $\tau = \exp(-11.577 + 7.536\times10^3/T)$, hours (10c)

Because the scatter is so large for the residency times of these samples and the effective activation energies are relatively close (69 kJ/mole for Eq. 10a, 66 kJ/mole for Eq. 10b, and 63 kJ/mole for Eq. 10c), it is recommended that the best-fit correlation to all of the data (Eq. 10b) be used as a first estimate of the tritium residency time for pellets with microstructures and purge conditions within the range of those for EXOTIC-5 through -6 samples.

4.2 Transient data Li_2ZrO_3 EXOTIC-6 pebbles

In Fig. 6, tritium residency times are shown for temperature rise and temperature decrease experiments for the EXOTIC-6 Li_2ZrO_3 pebble bed. As expected, there is less scatter in the results, because all of the data come from the single pebble bed, whereas the pellet data came from samples with different microstructures. The data from the first reactor cycle have been omitted from this data set. The best-fit correlations to the temperature rise data (1), all the data (2) and the temperature decrease data (3) are:

Temperature rise experiments: $\tau = \exp(-18.7916 + 1.3291 \times 10^4/T)$, hours (11a)

Average of all data: $\tau = \exp(-15.328 + 1.1033 \times 10^4/T)$, hours (11b)

Temperature decrease experiments: $\tau = \exp(-13.237 + 9.609 \times 10^3/T)$, hours (11c)

4.3 Best-estimate and upper-bound correlations for pellets

It is assumed that the effective activation energy derived from the transient data is representative of the rate-limiting surface-desorption mechanism. The directly-measured tritium inventory data (normalized to the generation rate to give residency time) are used to determine the pre-exponential factor for best-fit and upper-bound correlations. Figure 7 shows the results of this exercise for the cylindrical pellets used in EXOTIC-3,4,5,6 and SIBELIUS. The SIBELIUS data point has been normalized to the EXOTIC protium level of 300 Pa, by assuming that the residency time for surface desorption varies inversely with the square root of the protium pressure for protium/tritium ratios >> 1. Eleven data points are shown in Fig. 7. Only ten are used in the analysis. The EXOTIC-3 residency time of 0.75 hours at an average temperature of 630°C appears to be unreasonable. The best fit correlation (τ_{bf} in hours) to the steady-state data is

$$\tau_{bf} = (300\ \text{Pa}/P_{H2})^{0.5} \exp(-12.222 + 7.911 \times 10^3/T) \quad (12)$$

The "reasonable" upper bound correlation (τ_{ub} in hours) is derived by matching the four highest residency times at a given temperature (see Tables 1 and 2): 2.4 hours for EXOTIC-3 sample at an average temperature of 405°C, 4.6 hours for EXOTIC-4 sample at an average temperature of 410°C, 5.4 hours for EXOTIC-4 sample at an average temperature of 360°C, and 0.34 hours scaled to 0.20 hours for SIBELIUS sample at an average temperature of 545°C. The results are:

$$\tau_{ub} = (300\ \text{Pa}/P_{H2})^{0.5} \exp(-10.644 + 7.911 \times 10^3/T) \quad (13)$$

The results from Eqs. 12 and 13 are shown in Fig. 7.

4.4 Best-estimate and upper-bound correlations for pebbles

The data in Fig. 4 have been normalized to a protium pressure of 300 Pa and replotted in Fig. 8. For the BEATRIX-II data, the residency times have been scaled by $(270/300)^{0.5} = 0.95$, which is a small correction. The CRITIC-II data have been scaled by $(100/300)^{0.5} = 0.577$. Although the CRITIC and BEATRIX data sets represent inventory measurements from a large number of pebbles, it is difficult to use the data for model improvement and validation because of the uncertainties in the temperature of each pebble. The horizontal lines in Fig. 8 represent the range of temperatures in the region in which the pebbles were selected. These ranges are quite large for BEATRIX and CRITIC samples. The vertical lines represent the average value and standard deviation of the data. However, plotting the average value vs. the average temperature is misleading. All of the pebbles within the temperature region would have to be measured in order to get a true average. This is particularly true of the CRITIC-II outer ring pebbles for which inventory values varied considerably. It is less important for the hotter inner rings (T > 400°C) where inventories are quite low. The EXOTIC-6 data point in Fig. 8 is a true average value

because the tritium in the whole sample was measured. Thus, it has a higher weighting value for correlation refinement and validation than do the low temperature CRITIC-II data.

Given the large uncertainties involved in interpreting the inventory data for pebbles, it was not possible to determine a best-fit and an upper-bound correlation for residency time. In considering tritium residency time correlations (Eq. 11a-c) determined from transient EXOTIC-6 data, it was observed that Eq. 11a is very consistent with the residency time derived from the post-irradiation measurement. Thus, with only a small modification, it is recommended for design calculations. For temperatures below ≈ 400°C, the correlation is believed to give an upper bound on the tritium residency time. This observation is certainly true for the CRITIC-II data from the 170-400°C region of the bed. For temperatures above ≈ 560°C, the correlation is a lower bound of the data. Thus, the correlation is arbitrarily limited to a residency time of 0.1 hours for T > 560°C.

$$\tau_{ub} = (300\ \text{Pa}/P_{H2})^{0.5} \exp(-18.259 + 1.329\text{x}10^4/T) \text{ for } T \leq 833\ \text{K} \quad (14a)$$

and

$$\tau_{ub} = 0.1\ (300\ \text{Pa}/P_{H2})^{0.5} \text{ for } T > 833\ \text{K} \quad (14b)$$

5. Design Application

Equations 12, 13 and 14 are used to calculate best-estimates and upper-bound estimates for the Li_2ZrO_3 breeder layers of the lowest-breeder-temperature ITER design described by Y. Gohar in Ref. 12. Table 3 gives the masses, tritium generation rate, minimum/maximum temperature, and calculated inventory for each layer, as well as the total. Calculations were performed by integrating the product of the generation rate and residency time, with the spatial variations in temperature and generation rate included in the calculation. The sintered product design is assumed to consist of fine-grained (~1 μm), low density (~70%) Li_2ZrO_3 cubes. The pebble bed design is assumed to consist of coarse grained (10-40 μm), high density (~94%) large pebbles with diameter of 0.5 mm (e.g., EXOTIC-6 pebbles) packed to ~ 60% packing fraction and smaller diameter pebbles with the same microstructure packed to about ~14% packing fraction.

The best-estimate of the tritium inventory in the sintered-product pellet design (SPBE) is only 12 g, even with a minimum temperature of 267°C. The upper-bound estimate for the sintered-product pellet design (SPUB) is 58 g, which is still reasonable from a design perspective. The pebble-bed upper-bound (PBUB) actually only applies to the EXOTIC-6 pebble microstructure and not to Li_2ZrO_3 pebble beds in general. The estimated inventory of 280 g is considered a significant amount by design standards. Most of the inventory is concentrated in the third layer (farthest from the plasma) of design configuration #3 which has the lowest values of T_{min}/T_{max}. Using data from BEATRIX-II/Phase-II and CRITIC-II type pebbles with smaller grain sizes (5-10 μm) and densities (80-85%) would lead to lower calculated inventories for the pebble bed design.

A major uncertainty in using the residency time approach to extrapolate to design conditions is the effect of the reduced protium-to-tritium ratio in the design. The data base for the correlations involves over-purged systems with protium-to-tritium ratios ranging from ~70 (CRITIC-II, end-of-life) to ~2200 (EXOTIC-4, Capsule 16.1). Currently, the proposed surface-desorption model considers the ratio of tritium to the square-root of the protium pressure in determining the tritium inventory. It remains to be demonstrated what minimum value of protium-to-tritium ratio is required in order for this model to be valid.

6. Discussion

The present work represents a first attempt to develop a simple model to be used in the extrapolation of transient and steady-state tritium release/retention data to design applications. The next stages in the model development involve:

a. normalizing the data to specific surface area -- used to determine the ratio of interconnected pore surface area to solid volume -- as well as to the square-root of the protium pressure;

b. exploring methods for reducing the scatter in the determination of residency time from the EXOTIC-5&6 transient data; Currently, some scatter reduction was achieved by eliminating data from the first 25 days of irradiation and separating the data into temperature rise vs. temperature decrease data. In the process of doing this, it has been observed that using only the residency times determined for the final temperature of a temperature change reduce the scatter significantly. There is certainly analytical justification for doing this;

c. exploring two-mechanism diffusion/desorption models to rationalize the difference in apparent activation energies between fine-grained/low-density pellets (66 kJ/mol) and large-grain/high-density pebbles (111 kJ/mol);

d. fine tuning the model parameters and validating the model by using it to integrate over the temperature distribution of the sample and comparing predicted inventory to measured inventory;

e. incorporating the laboratory data for tritium release during postirradiation annealing of the samples;

f. using laboratory data on surface adsorption/desorption and solubility of moisture and gaseous hydrogen isotopes to explore slower mechanisms of tritium retention/release than those observed in the over-purged, in-reactor experiments (e.g., see Ref. 14)

g. continue to test modeling assumptions and refine model parameters against data which are forthcoming (e.g., EXOTIC-7&8)

7. Conclusions

Progress in modeling the tritium retention/release behavior of Li_2ZrO_3 sintered-product pellets and pebbles has been reported. A surface desorption model, which includes the effects of specific surface area and protium pressure in the purge -- has been proposed and tested against available in-reactor tritium release data and post-irradiation measurements of tritium inventory. Transient, on-line data from the EXOTIC-5&6 experiments on low-density, fine-grained Li_2ZrO_3 cylindrical pellets have been used to determine an effective activation energy (66 kJ/mol) for surface desorption. The pre-exponential factor in the model has been adjusted to achieve both best-fit and upper-bound model parameters for extrapolation of data to blanket designs such as ITER. A similar approach was used to derive an upper-bound surface desorption effective energy (111 kJ/mol) and pre-exponential factor for the high-density, large-grain-size pebbles tested in the EXOTIC-6 experiments. The models were applied to the design conditions for a candidate ITER driver blanket to predict the distribution of tritium inventory is such a blanket design. Recommendations are made on how to improve the modeling effort by including more data sets and more sophisticated models.

References

1. N. Roux, J. Mouglin, B. Rasneur, E. Proust, L. Giancarli and J. F. Salavy, "Current Material and Design Studies in View of the Utilization of Li_2ZrO_3 in the BIT Blanket Concept," J. Nucl. Mater., 212-215 (1994) 862-867.

2. P. Lorenzetto, P. Gierszewski, S. Chiocchio, G. Federici, H. Gorenflo, M. Iseli, H. McIlwain, E. Salpietro and G. Williams, "A Driver Blanket for NET," Proc. 17th Symp. Fus. Tech. (SOFT-17), Rome, Sept. 14-18, 1992, 1414-1418.

3. Y. Gohar, M. Billone, A. Cardella, W. Dänner, K. Ioki, T. Kuroda, D. Lousteau, P. Lorenzetto, S. Majumdar, R. Mattas, R. Raffray, Y. Strebkov, H. Takatsu and E. Zolti, "ITER Breeding Blanket Design," Proc. Symp. Fus. Eng. (SOFE 95), Sept. 30-Oct. 5, 1995, pp. 410-417.

4. M. C. Billone, "Thermal and Tritium Transport in Li_2O and Li_2ZrO_3," J. Nucl. Mater. 233-237 (1996) 1462-1466.

5. A. R. Raffray, M. C. Billone, G. Federici and S. Tanaka, "Progress in Tritium Retention and Release Modeling for Ceramic Breeders," Fus. Eng. Des., 28 (1995) 240-251.

6. M. C. Billone, "TIARA Analysis of Tritium Inventory in Li_2O," Fus. Eng. Des. 28 (1995) 313-318.

7. H. Kwast, M. Stijel, R. Muis and R. Conrad, "EXOTIC: Development of Ceramic Tritium Breeding Materials for Fusion Reactor Blankets, The Behaviour of Tritium in: Lithium Aluminate, Lithium Oxide, Lithium Silicates, and Lithium Zirconates," Petten Report ECN-C--95-123, December, 1995.

8. O. D. Slagle and G. W. Hollenberg, "BEATRIX-II, Phase II: Data Summary Report," Pacific Northwest National Laboratory, Report No. PNNL-11148, May 1996.

9. J. M. Miller and R. A. Verrall, "Performance of a Li_2ZrO_3 Sphere-Pac Assembly in the CRITIC-II Irradiation Experiment," J. Nucl. Mater. 212-215 (1994) 897-901.

10. R. A. Verrall, J. M. Miller and L. K. Jones, "The CRITIC-II On-Line Irradiation of Lithium Zirconate Pebbles," Proc. Fifth International Workshop on Ceramic Breeder Blanket Interactions (CBBI-5), Rome, Sept. 23-25, 1996, ed. S. Casadio (ENEA), pp 117-129.

11. R. A. Verrall, J. M. Miller and L. K. Jones, "The CRITIC-II On-Line Irradiation of Lithium Zirconate Pebbles," AECL-11768, CFFTP-9637, March 1997.

12. J. P. Kopasz and C. E. Johnson, "Performance of Ceramic Breeder Materials in the SIBELIUS Experiment," J. Nucl. Mater. 219 (1995) 259

13. Y. Gohar, ITER/JCT-Garching, personal communication, Oct. 2, 1997
(material presented at the ITER Blanket Meeting, San Diego, Oct. 2-4, 1997)

14. C. Alvani, P.L. Carconi, M. R. Mancini, A. Moauro, F. Pierdominici, A. Masci and S. Casadio, "Purge Gas Interactions with Ceramic Breeder Pebbles," Sub-TASK B3-2.1 -- 1996 Activity Report, ENEA Document INN/NUMA/MATAV(97)1

Table 1. Summary of microstructure, operating conditions and measured tritium inventory following irradiation in EXOTIC-3, 4 and 5 in-reactor purge flow tests. Numbers in parentheses below the experiment number are the capsule number. All samples are solid or hollow cylindrical pellets. Operating conditions apply to last reactor cycle prior to shut-down.

Parameter	EX-3 (11.1)	EX-3 (12.1)	EX-4 (14.1)	EX-4 (14.2)	EX-4 (16.1)	EX-5 (17.1)	EX-5 (21.1)	EX-5 (18.1)
Mass, g	35.75	35.75	59.4	58.9	34.6	21.3	20.0	16.0
Density, %td	79	79	86	85	79	77.5	74.5	74
Open Porosity, %	20	20	14	15	21	19.5	25.5	26
Pore-Solid Surface Area, m^2/g	0.4	0.4	0.9	0.9	---	0.9	0.9	1.2
Grain Diam., μm	2.5	2.5	1.0	1.0	0.7	0.9	0.8	1.1
Protium Partial Pressure, Pa	300	300	300	300	300	300	300	300
Generation Rate, wppm/hour	0.0227	0.0241	0.0158	0.0191	0.0209	0.130	0.144	0.137
Temperature, °C Inner Average Outer	650 630 610	425 405 385	460 410 360	680 635 590	380 360 340	460 430 400	480 450 420	410 390 370
Li Burnup, at.%	0.1	0.1	0.13	0.13	0.13	1.8	2.05	1.9
Inventory, wppm	0.018	0.06	0.075	0.001	0.117	0.007	0.009	0.1
Residency Time, hours	0.75	2.4	4.6	0.05	5.4	0.05	0.06	0.73

Table 2. Summary of microstructure, operating conditions and measured tritium inventory following irradiation in EXOTIC-6, BEATRIX II (Phase II), CRITIC-II, and SIBELIUS in-reactor purge flow tests. All samples are solid or hollow cylindrical pellets. Operating conditions apply to last reactor cycle prior to shut-down.

Parameter	EX-6 (21.1)	EX-6 (21.2)	SIB.	EX-6 (24.2)	BEAT.-II Phase-II	CRITIC-II
Sample Form	Pellet	Pellet	Pellet	Pebble Bed	Pebble Bed	Pebble Bed
Mass, g	9.22	10.58	1.00	8.16	29.5	203
Density, %td	73	81	81	94 (peb) 52.5 (bed)	80-82 (peb) 53 (bed)	80-85 (peb) 53 (bed)
Open Porosity, %	27	19	19.5	6 (peb)	14-16 (peb)	14-16 (peb)
Pore-Solid Surface Area, m^2/g	1.5	0.8	---	---	(0.34±0.12)	0.34±0.12
Grain Diam., μm	1	2	1	10-40	10	5-10
Protium Partial Pressure, Pa	300	300	100	300	270	100
Generation Rate, wppm/hour	0.252	0.227	0.064	0.27	0.443	0.026
Temperature, °C Inner	485	495	550	425	985	900
Average	450	455	545	360	---	---
Outer	440	445	540	315	395	170
Li Burnup, at.%	3.01	3.02	0.8	3.11	3.1	0.5
Inventory, wppm	0.009	0.015	0.022	2.4	0.32±0.01 (395-770°C) 0.15±0.12 (770-945°C) 0.032±0.01 (945-1025°C)	6.3±4.6 (170-400°C) 0.009±0.009 (400-750°C) 0.002±0.002 (750-900°C)
Residency Time, hours	0.04	0.07	0.341	9.5	0.72±0.02 (395-770°C) 0.34±0.27 (770-945°C) 0.072±0.023 (945-1025°C)	244±178 (170-400°C) 0.4±0.5 (400-750°C) 0.078±0.116 (750-900°C)

Table 3. Summary of ITER Driver Blanket Design A Parameters for 100% Dense Beryllium Layers and 70% Dense Solid Breeder (Li_2ZrO_3) Layers. The design consists of 24 breeding modules in the poloidal direction. The inventory calculations are for sintered-product-best-estimate (SPBE) correlation, sintered-product-upper-bound (SPUB) correlation and pebble-bed-upper-bound (PBUB) correlation. The purge is assumed to be He at atmospheric pressure (0.1 MPa) with 0.1% H_2 and a flow rate giving a protium-to-tritium ratio > 10 locally and ~ 20 on the average.

Config./ Layer	Mass MT	Generation Rate, g/day	T_{min}/T_{max} ℃	I(SPBE) g	I(SPUB) g	I(PBUB) g
3/1	15.559	75.396	425/764	0.4	2.1	1.6
3/2	23.338	56.995	313/667	2.4	11.4	31.3
3/3	23.338	23.291	267/417	5.5	26.5	169
2/1	5.386	16.010	357/785	0.2	1.1	1.5
2/2	5.386	11.254	297/564	0.8	3.9	13.8
1/1	5.574	24.584	338/605	0.6	3.1	5.6
1/2	8.360	18.772	271/550	2.1	10.2	56.8
Total	87	226	267/785	12	58	280

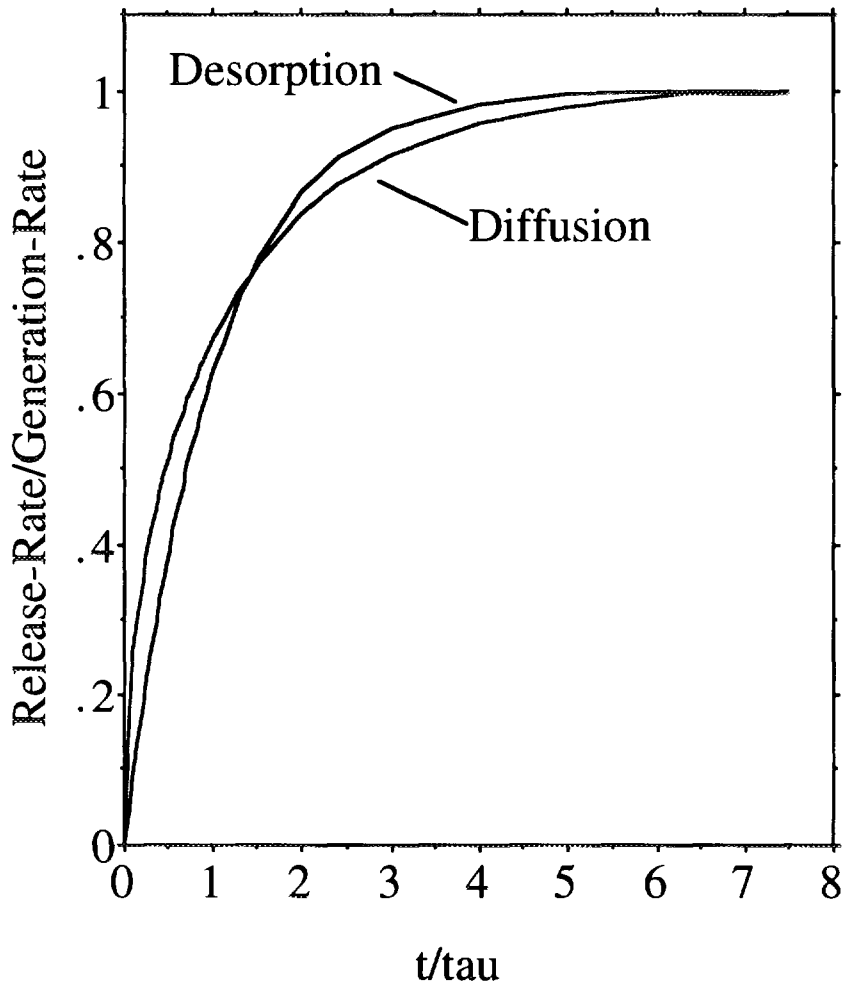

Fig. 1. Comparison of analytical solutions for first-order surface desorption and bulk diffusion for an isothermal spherical grain in response to an instantaneous increase in generation rate at time t = 0. Tau is the residency time and is equal to the steady-state inventory (I) divided by the generation rate (G): tau = I/G. Both models have the same steady-state inventory, but slightly different time dependence.

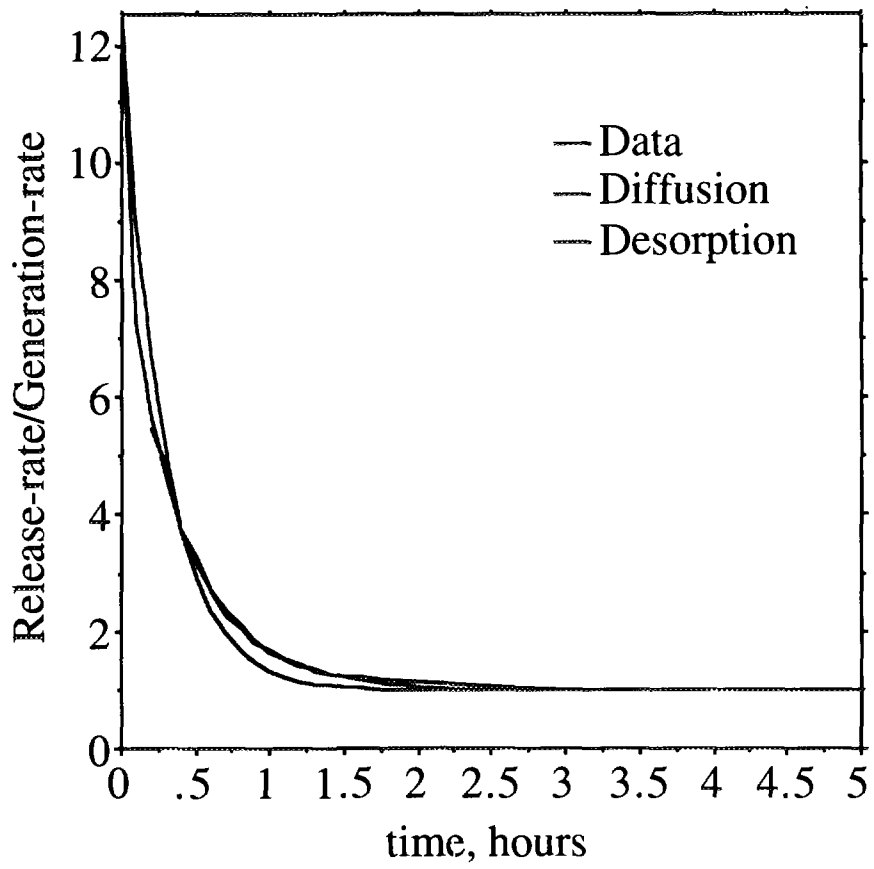

Fig. 2. Comparison of diffusion and desorption model predictions to the tritium release rate data (normalized to the generation rate) vs. time for the EXOTIC-6 transient E0121208 for Li_2ZrO_3 capsule 21.2 exposed to an increase in average temperature from 368°C to 468°C. Both models use the same tritium residency time and give the same long-time decrease in tritium inventory. The diffusion model prediction is essentially coincident with the data after 0.2 hours when the data are shifted by 0.2 hours. The desorption model predictions also give good agreement with the data.

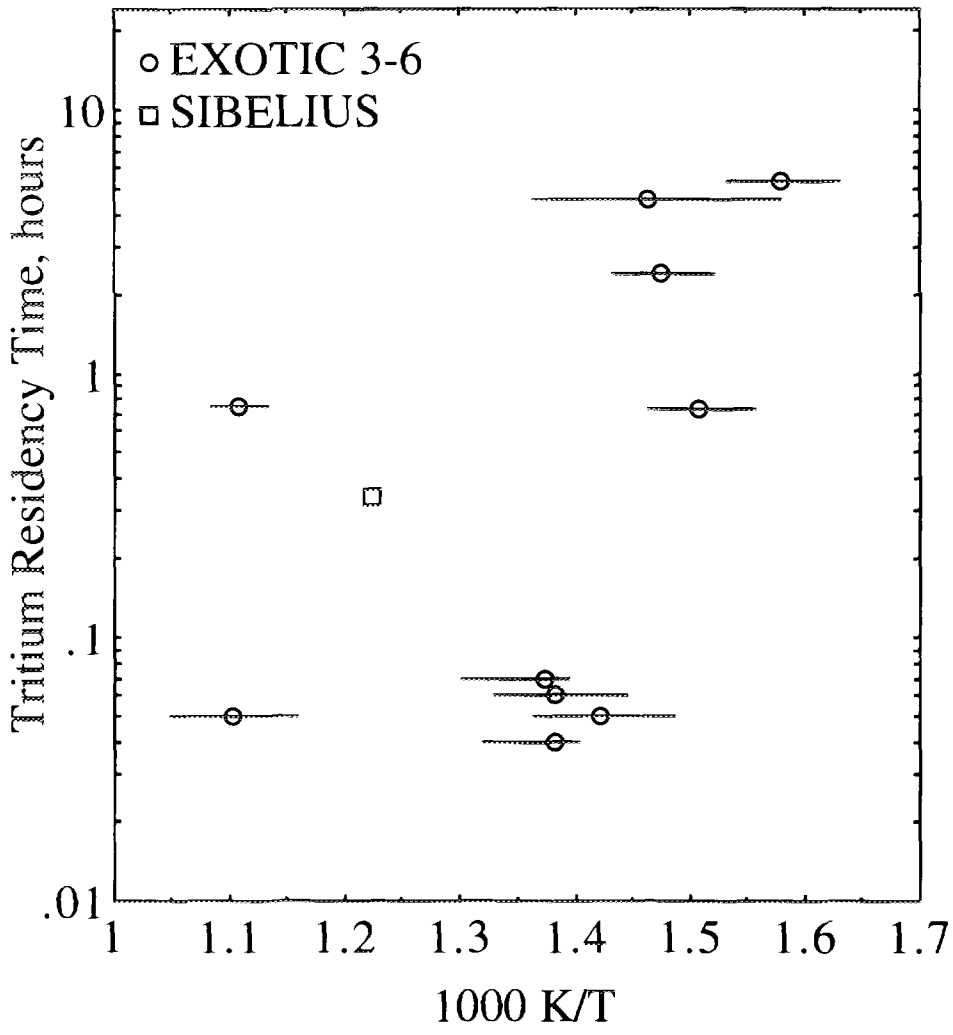

Fig. 3. Tritium residency time derived from EXOTIC-3 to -6 and SIBELIUS Li_2ZrO_3 cylindrical-pellet inventory data. The residency time is determined from postirradiation inventory data divided by the generation rate during the last cycle of irradiation. The average pellet temperature is used to derive 1000 K/T, where T is in K. Grain sizes range and densities range from 0.7 to 2.5 μm and 73-86%, respectively. The horizontal bands show the range of temperature from T_{min} to T_{max} for each sample. Temperature range is 315-680°C.

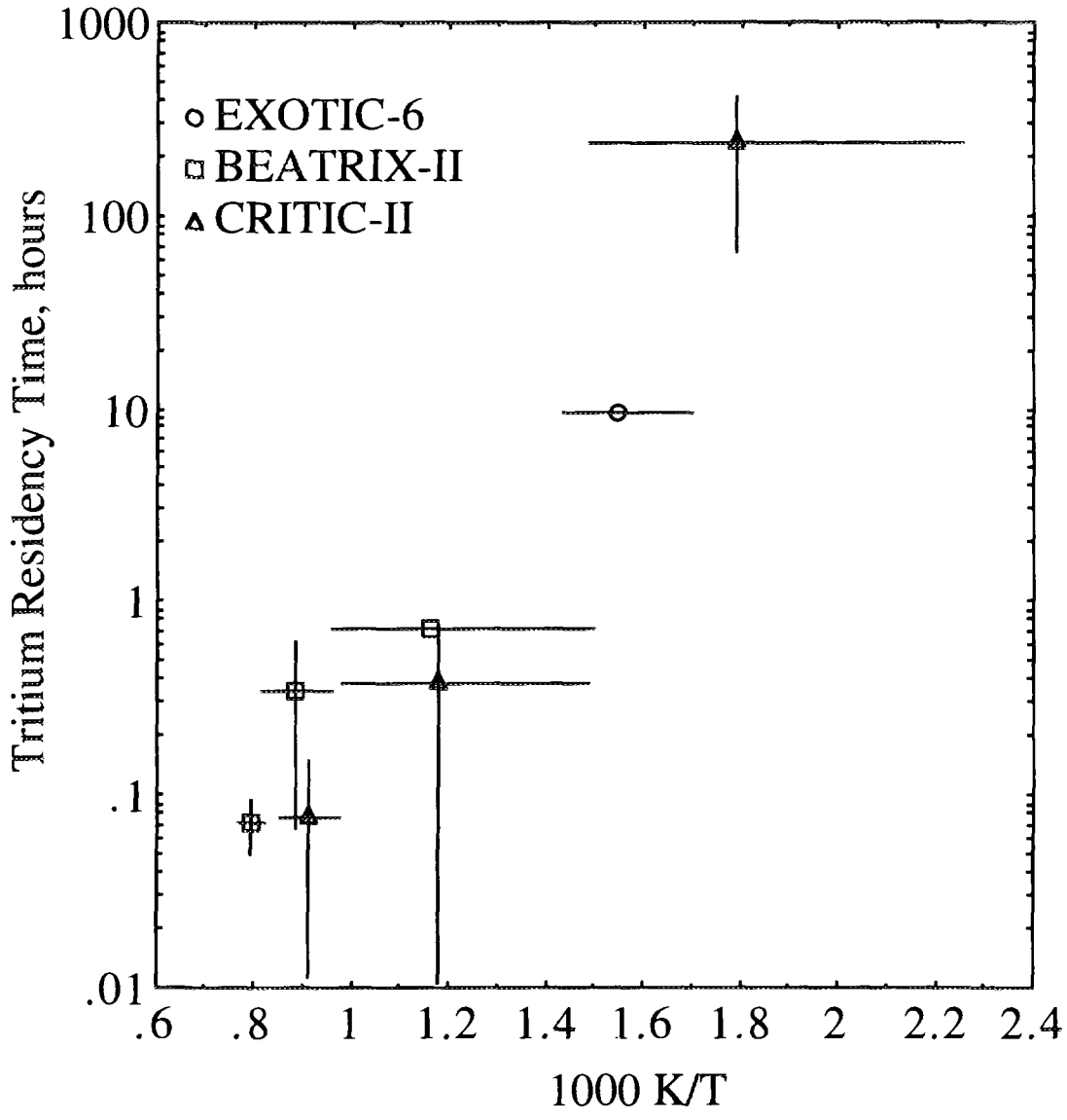

Fig. 4. Tritium residency time derived from EXOTIC-6, BEATRIX-II/Phase-II and CRITIC-II Li_2ZrO_3 pebble-bed inventory data. The residency time is determined from postirradiation inventory data divided by the generation rate during the last cycle. The average pebble-bed-region temperature is used to derive 1000 K/T, where T is in K. The horizontal lines show the temperature range for the pebbles examined. The vertical lines show the one-standard-deviation of the measurements. Temperature range is 170-1025°C.

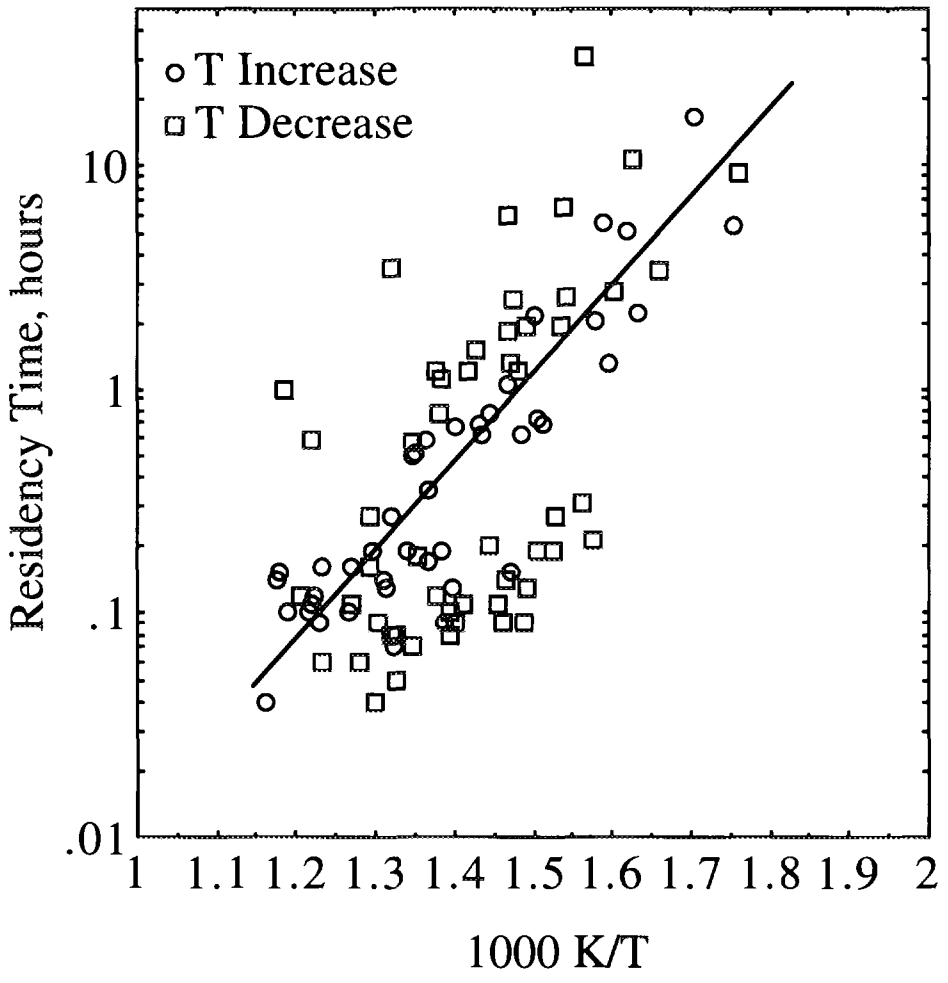

Fig. 5. Tritium residency time vs. the inverse of the average temperature (in K) for sintered-pellet Li_2ZrO_3 based on on-line EXOTIC-5 and EXOTIC-6 tritium release data in response to temperature transients. Pellet densities range from 73 to 81% of theoretical, grain sizes range from 0.8 to 2.0 μm and Li burnups range from 1.8 to 3.0 at.%. All tests were conducted in He + 0.1 vol.% H_2 purge at 100 ml/minute and 0.3 MPa. The line represents the best-fit correlation to the transient data for pellets: $\tau = \exp(-12.0684 + 7.911 \times 10^3/T)$, hours.

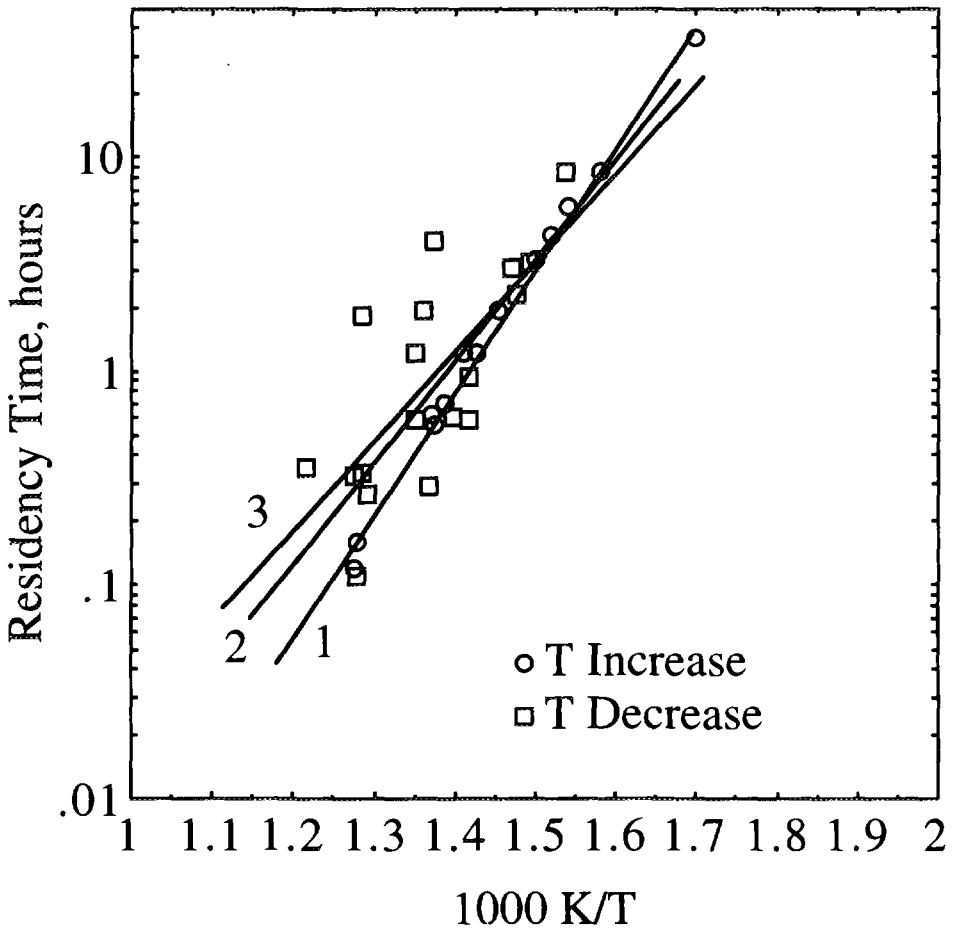

Fig. 6. Tritium residency time vs. the inverse of the average temperature (in K) for the EXOTIC-6 Li_2ZrO_3 pebble bed, based on on-line tritium release data in response to temperature transients. The 0.5-mm pebbles are 94% dense with 10-40 μm grain size and smear density of 52.5%. All tests were conducted in He + 0.1 vol.% H_2 purge at 100 ml/minute. The residency time correlations for the temperature increase data (1), the average of the data (2), and the temperature decrease data (3) are:

1. $\tau = \exp(-18.7916 + 1.3291 \times 10^4/T)$, hours

2. $\tau = \exp(-15.3278 + 1.1033 \times 10^4/T)$, hours

3. $\tau = \exp(-13.2369 + 9.609 \times 10^3/T)$, hours

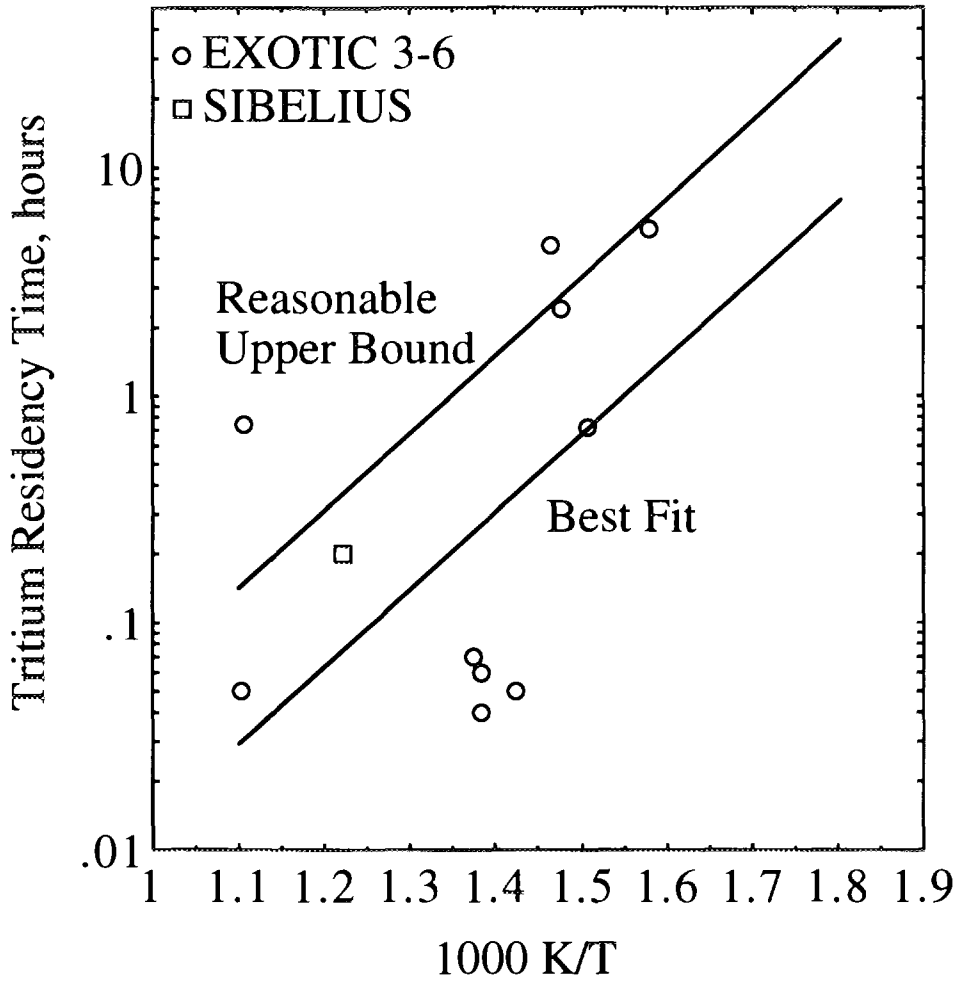

Fig. 7. Best-fit and reasonable upper bound correlations for Li_2ZrO_3 pellet residency time based on the EXOTIC-3,4,5,6 and SIBELIUS inventory measured directly (after irradiation) divided by the generation rate during the last reactor cycle. The activation energy is pre-determined from the EXOTIC-5,6 transient data. The pre-exponential for the best fit correlation is based on an average of 10 of the data points (EXOTIC-3 residency time of 0.75 hours at an average breeder temperature of 630°C excluded). The pre-exponential for the "reasonable" upper bound is based on matching the highest inventory data within a given temperature range. Pellet density and grain diameter ranges are 73-86% and 0.7-2.5 μm, respectively. The SIBELIUS data point has been normalized from 100 to 300 Pa of purge H_2 by dividing by $(3)^{0.5}$. Purge flow rate is the standard 100 ml/min.

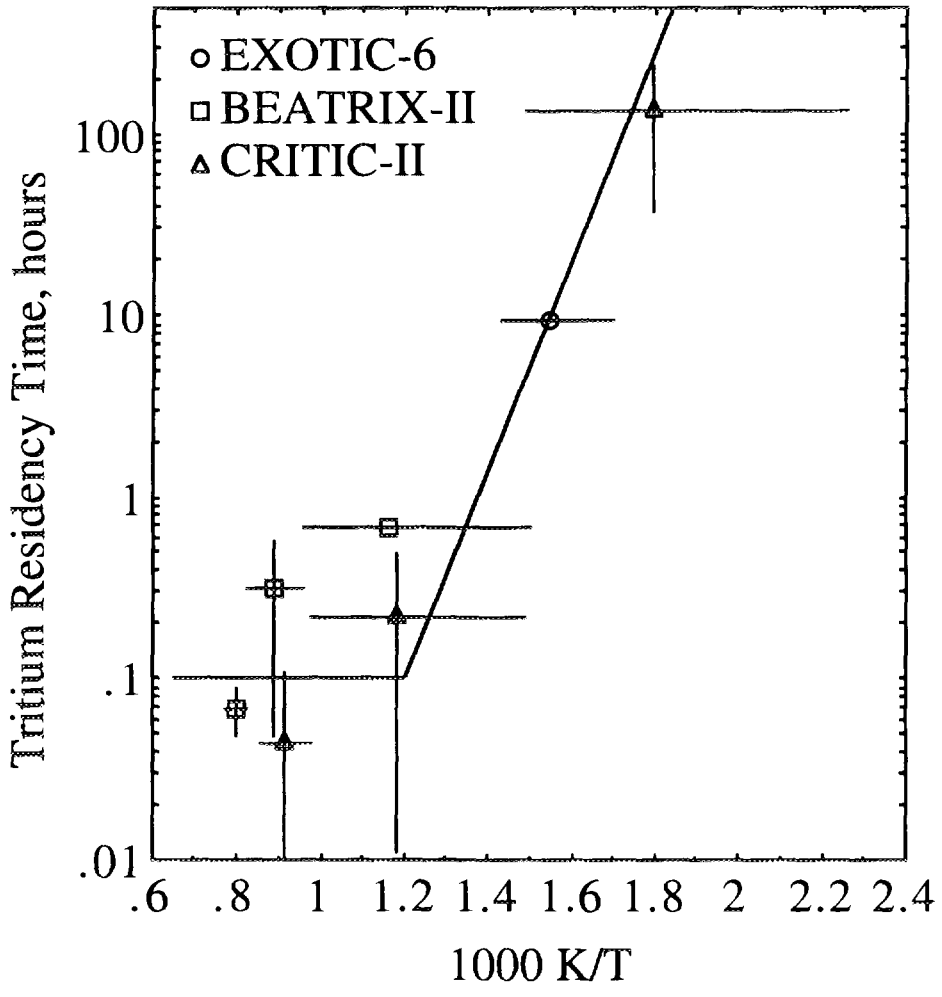

Fig. 8. Comparison of recommended upper bound correlation for pebble-bed Li_2ZrO_3 tritium residency time with pebble-bed data from EXOTIC-6, BEATRIX-II and CRITIC-II experiments. Experimental residency time is derived from the ratio of the measured tritium inventory after the irradiation divided by the generation rate during the last test cycle. All results have been normalized to the EXOTIC-II protium pressure (300 Pa) by assuming that the inventory is inversely proportional to the square root of the protium pressure. The data set includes pebble densities of 80-94%, grain diameters of 5-40 μm, pebble diameters of 0.5-2 mm and smear densities ≈ 53%. The purge flow rate is 100 ml/minute for all test data.

AB-INITIO HARTREE-FOCK STUDY OF TRITIUM DESORPTION FROM Li_2O

Masaki Taniguchi and Satoru Tanaka
Department of Quantum Engineering and Systems Science,
The University of Tokyo
7-3-1 Hongo, Bunkyo-ku, Tokyo 113, Japan

Abstract

Dissociative adsorption of hydrogen on Li_2O (110) surface has been investigated with ab-initio Hartree-Fock quantum chemical calculation technique. Heat of adsorption and potential energy surface for H_2 dissociative adsorption was evaluated by calculating the total energy of the system. Calculation results on adsorption heat indicated that H_2 adsorption is endothermic. However, when oxygen vacancy exists adjacent to the adsorption sites, heat of adsorption energy became less endothermic and the activation energy required to dissociate the H−H bonding was smaller than that for the terrace site. This is considered to be caused by the excess charge localized near the defect.

1. INTRODUCTION

Lithium oxide is one of the candidate materials for the fusion reactor blanket because of its high tritium breeding performance. Producted tritium by neutron irradiation is released into the sweep gas through diffusion in grain, diffusion along grain boundaries and desorption from the surface. Among these, recent experimental results have strongly suggested the importance of surface processes. In numerous in-pile tritium release experiments, enhancement of tritium release by adding H_2 into the sweep gas has been reported[1-3]. Therefore it is strongly required to understand the interaction of H_2 with Li_2O surface.

In the group of presenting authors, adsorption and desorption behavior of H_2 have been investigated using the infrared absorption spectroscopy[4,5]. The results indicated that hydrogen is dissociatively adsorbed on Li_2O surface to produce surface -OH and that the nature of -OH is affected by the oxygen potential in the system. In the present paper, we performed the quantum chemical calculation in order to study the dissociative adsorption of H_2 on the surface of Li_2O. On the surface of oxide materials such as MgO and Ti_2O, H_2 is known to dissociates only on the defective sites[6,7]. Therefore we focused on the effects of surface defect, specially, oxygen vacancy on dissociation of H_2.

2. CALCULATION METHOD

For calculation, we used the CRYSTAL 92 program[8] which can be used for ab-initio

quantum chemical calculations in the periodic systems. This computational program enables us to conduct the ab-initio Hartree-Fock calculations for 2 or 3-dimensional periodic systems such as the bulk or surface of the crystal. In this calculation code, the crystalline orbital is expressed by the linear combination of the atomic orbital. The basis set used in this work was the optimized one by Dovesi and co-workers for bulk Li_2O[9]. This basis set is triple zeta quality for the oxygen and includes the polarization function for the lithium atom. It is reported that lattice constant, elastic constant and some other properties for Li_2O crystal could be calculated accurately by using this basis set. For hydrogen atom of the adsorbed H_2, the STO-3G (Slater-type orbital expressed by three Gaussian-type orbital) basis set was adopted.

In order to study the surface phenomena by this kind of calculations, we need to approximate the surface because it is impossible to treat all the atoms included in the system. In the previous work to investigate the H_2 and H_2O adsorption on the terrace site of Li_2O surface, we used a slab model, which corresponds to the finite atomic layers parallel to the selected plane of the crystal. However, this approach may not be adequate for the system which contains the defective structure such as the oxygen vacancy because of the low symmetry configurations. Therefore in this work, we mainly used the cluster model to approximate the surface. In the CRYSTAL92 code, cluster could be easily created from the crystalline structure and we can conduct ab-initio calculations for this system.

3. RESULTS AND DISCUSSIONS

3.1 DISSOCIATIVE ADSORPTION OF H_2 ON Li_2O

Figure.1 shows the cluster for Li_2O (110) surface used in this work. This cluster contains 14 lithium ions and 7 oxygen ions in the system and ions below third layer of the crystal was neglected. In the case of surface adsorption and desorption phenomena, bonding orbital which causes the chemisorption is localized near the adsorbate. Therefore it is sufficient to treat the electronic state near the adsorbate. The structure of the cluster was optimized including the effect of surface rumpling and relaxation which plays an important role in adsorption and desorption behavior[10]. The (110) surface was selected because it contains two lithium atoms and one oxygen atom and the each layer is neutral. This means that the (110) surface is stable compared to the (100) surface.

Using the cluster described above, we evaluated the possible sites for H_2 dissociative adsorption. Three types of configurations shown in figs.2(a)~(c) was examined as an adsorption site. In site A, hydrogen atom of H_2 is adsorbed on surface oxygen ion to produce hydroxyl group and extra hydrogen is attracted to the neighboring lithium ion. In site B, extra hydrogen is adsorbed between the two nearest lithium ions on the top layer. In site C, two hydroxyl groups are created by H_2 dissociation. In each case, we assumed that surface hydroxyl group (O−H bonding) or lithium hydride (Li−H) is created by the dissociative adsorption of H_2 molecule. Because in the author's previous experiments using the infrared absorption spectroscopy, surface hydroxyl groups was observed on the surface of Li_2O under the H_2 atmosphere[4,5]. J.P.Kopasz and co-workers also observed

the Li_2O surface by the same method and they reports the formation of Li−H bonding under H_2 atmosphere especially at high temperature[11].

To find the suitable position of the adsorbed hydrogen atom on the surface at the given configuration, we have optimized the distance between hydrogen atom and the surface by minimizing the total energy of the system. For simplification, we assumed that O−H or Li−H bonding is always perpendicular to the surface. Using the total energy of the optimized system, we can estimate the heat of H_2 dissociative adsorption by the following equation:

$$E_{ad} = E(Li_2O + H_2) - [E(Li_2O) + E(H_2)].$$

In this equation, $E(Li_2O + H_2)$ represents the energy of the H_2 adsorbed surface, $E(Li_2O)$ denotes the energy of the cluster used in this calculation, and $E(H_2)$ denotes the energy of free H_2 in the gas phase. Energy of free H_2 was evaluated by optimizing the H−H distance of H_2. Basis set for hydrogen atom to calculate H_2 energy was the same one as used for calculation of hydroxyl group in this work. Estimated heat of adsorption for each site are summarized in table.1. A' and B' denotes the adsorption energy for site A and B with oxygen vacancy respectively.

In the case of site A and B, calculation was also conducted for the oxygen removed cluster (removed oxygen is shown in fig.2) in order to investigate the effect of oxygen vacancy on H_2 adsorption. Such a structure might not be the realistic model, but is helpful to understand the H_2 adsorption behavior on defective Li_2O surface. The adsorption was endothermic for all the sites considered in this work. However, in the case of site B', the difference in energy between the initial state (before H_2 adsorption) and the final state (H_2 adsorbed surface) is enough small to exist as a stable adsorption site on the surface. It was found that the heat of adsorption was larger for vacancy introduced cluster than that for the perfect cluster. This fact suggests that the surface with oxygen vacancy is more reactive than the ideal surface. This tendency is explained as follows: When oxygen vacancy is created on the surface, the flow of electron from lithium ion to oxygen ion adjacent to the defect is considered to increase. This may cause the strong O−H bonding leading to the large adsorption energy.

3.2 ACTIVATION ENERGY FOR HYDROGEN DISSOCIATION

In order to evaluate the activation energy for H_2 dissociative adsorption on Li_2O, we calculated the potential energy surface for this reaction by the ab-initio calculation. As the first step of our investigations, we studied the adsorption site B and B' of the previous section, which had the largest adsorption energy considered in this work. Potential energy surface could be obtained by plotting the total energy of the system as a function of the position of the atom which concerns the reaction. However, such a calculation is inconsistent with reality because of the large computational time. Therefore, to reduce the parameter which can be varied independently, we made the following assumptions.

1) The angle of H_2 molecular axis against the surface is maintained the same angle as the H−H axis of the final state (H_2 adsorbed surface) during the reaction.

2) The axis of O−H bonding for hydroxyl group is always perpendicular to the surface.

Under these conditions, we can identify the reaction path by two parameters "d"(the distance between the hydrogen atoms) and "h" (the distance between H_2 and the surface) as shown in fig.3. Total energy of the system was calculated as a function of parameters h and d. Parameter h was changed from 0.94 Å to 2.20 Å and parameters d was from 0.65 Å to 1.75 Å. Calculated potential energy surfaces are shown in fig.4(a)~(b). In this figure, the darker point represents the lower energy and the more stable structure. The point A corresponds to the initial state (Li_2O surface + free H_2 molecule) and point F corresponds to the final state (H_2 adsorbed surface) of the reaction. Therefore, H_2 dissociative adsorption is considered to proceed from point A to F along the reaction path shown with the dashed line in fig.4. Activation energy for H_2 adsorption reaction on Li_2O could be evaluated as the difference between E_D and E_A. Where, E_A represents the energy of the initial state and E_D represents the energy of the activation state of this reaction. In our calculation, it was 250kJ/mol for the terrace(perfect surface) site and 192kJ/mol for the defective site.

Activation energy for H_2 adsorption was larger on the terrace site than that for the oxygen vacancy site. Addition to this, in the case of the defective site, dissociation of H−H bonding seems to start at a longer distance point from the surface compared with the terrace site as shown in figs.4(a) and 4(b). This fact indicates that oxygen vacancy promotes the dissociation of H_2 molecule on the surface of Li_2O. This is considered to be due to the rearrangement of electronic structure of the surface by introducing the oxygen vacancy. To clarify this, we conducted the mulliken population analysis for the cluster used in this work. Table.2 summarizes the net charge of the oxygen ion, which formates the O−H bonding when H_2 is adsorbed on the surface. It is shown that oxygen ion with neighboring oxygen vacancy has larger electron charge than that without vacancy sites. It is well known that H−H bonding is stabilized by occupying the bonding orbital with 1s electrons of hydrogen atoms. In order to overcome the strong H−H bonding, it is effective to introduce the electron to the anti-bonding orbital of H_2 molecular orbital. The excess charge which exists on oxygen ion for the defective site might accelerate the dissociation of H−H bonding by this mechanism.

In this work, adsorption of H_2 on defective sites was investigated using the simple model of the oxygen vacancy. The structure of the actual surface must be more complicated especially at high temperature under H_2 or H_2O atmosphere. Moreover, we should be noted that local relaxation of the surface due to the creation of oxygen vacancy or adsorption of H_2 was neglected. In the actual case, surface ions (Oxygen and Lithium ion) are considered to move when oxygen vacancy is created. There might exist a reaction path for H_2 dissociation with a smaller potential barrier by considering these surface defects or relaxation. Calculation of the activation energy including these effects will be the next step of our investigations.

4.CONCLUSIONS

Dissociative adsorption of H_2 on the surface of Li_2O was studied by ab-initio quantum chemical calculation technique using the CRYSTAL92 code. Adsorption of H_2 on Li_2O was endothermic for the sites examined in this work. The presence of the oxygen

vacancy caused the strong bonding between hydrogen and the surface oxygen ion to form surface -OH and the adsorption became less endothermic.

The potential energy surface for the dissociative adsorption of H_2 on Li_2O was obtained by calculating the total energy of the system. Activation energy for dissociation of H_2 became larger when oxygen vacancy exists adjacent to the adsorption sites. This might be caused by the excess charge which is localized near the defect structure.

References

[1] J.P.Kopasz, C.A.Seils and C.E.Johnson, J.Nucl.Mater., **191-194,** (1992) 231.

[2] W.Breitung and H.Werle, J.Nucl.Mater., **179-181** (1991) 847. 847 (1991).

[3] H.Kwast, A.Kout, R.P.Muis, M.P.Stjikel, A.J.Flipot and J.D.Elen, Fusion Engineering and Design, **8** (1989) 359.

[4] M.Taniguchi and S.Tanaka, Fusion Technol., **30** (1996) 874.

[5] M.Taniguchi, S.Tanaka and V.Grishmanov, Fusion Technol., **28** (1995) 1284 .

[6] E.A.Colbourn, J.Kendrick and W.C.Mackrodt, Surf.Sci., **126** (1983) 550 .

[7] G.Rocker, J.A.Schaefer and W.Gopel, Phys.Rev.B, **30** (1984) 3704 .

[8] C.Pisani, R.Dovesi and C.Roetti, Hartree-Fock Ab Initio Treatment of Crystalline Systems, Lecture Notes in Chemistry (Springer, Heidelberg, 1988).

[9] R.Dovesi, Solid State Communications, **54** (1985) 183.

[10] M.Taniguchi and S.Tanaka, Fusion Technol., **30** (1996) 874.

[11] J.P.Kopasz, J.Ortiz-Villafuerte, and C.E.Johnson, Proceedings of the Third International Workshop on Ceramic Breeder Blanket Interactions, (1994) 116.

Table 1 Energy for the H2 dissociative adsorption

	Adsorption Energy
A	**+0.502 eV**
A'	**+0.330 eV**
B	**+0.220 eV**
B'	**+0.05 eV**
C	**+1.80 eV**

Table 2 Net charge for oxygen ion of the cluster estimated by Mulliken population analysis.

	Net Charge for Oxygen ion
Defective site	- 9.985
terrace site	- 9.690

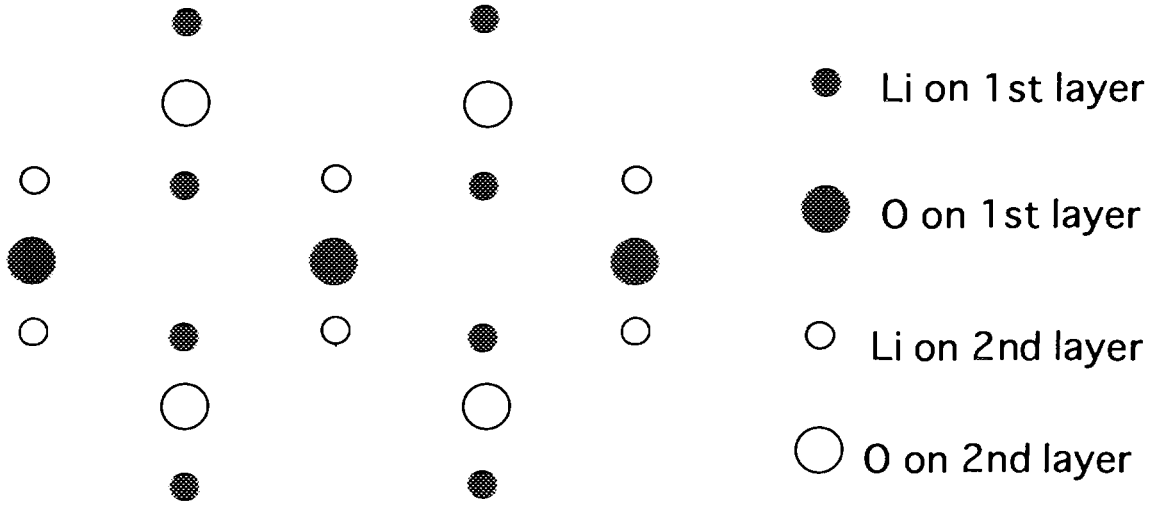

Fig.1 $Li_{14}O_{17}$ cluster used in this work. Closed and open circle represents the top and second layer relatively.

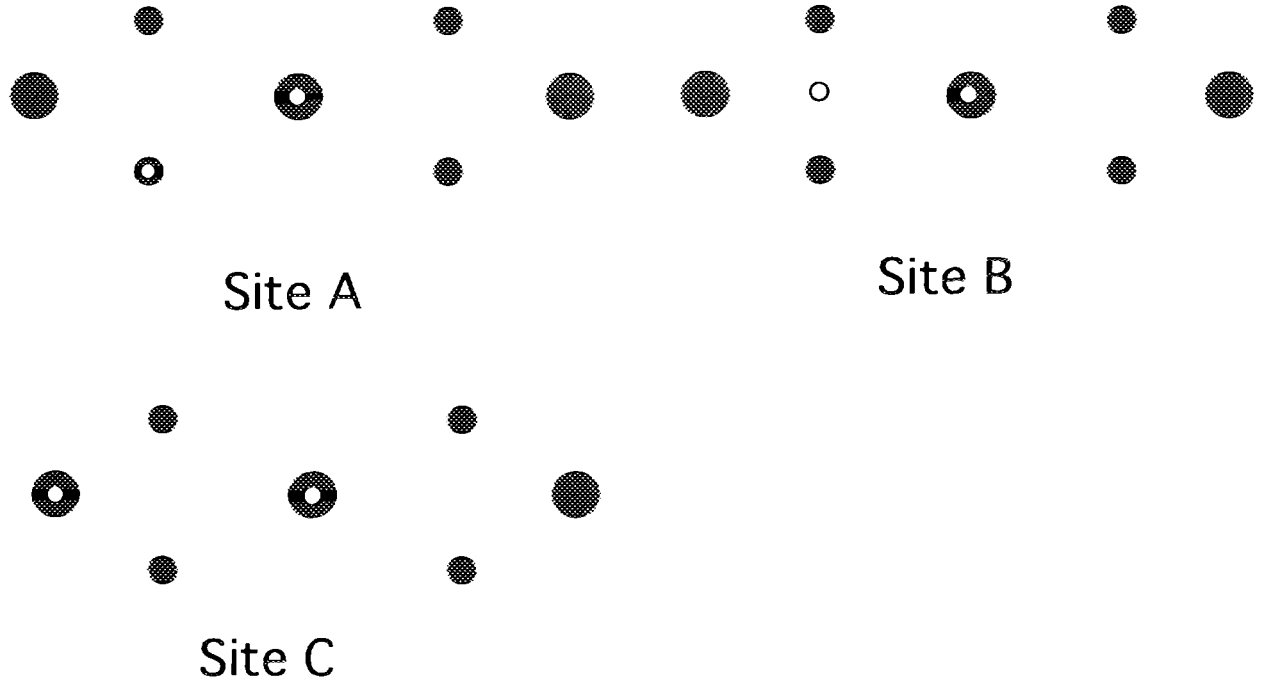

Fig.2 Model of the H_2 adsorbed Li_2O (110) cluster. Hydroxyl group or lithium hydride was supposed to be produced by the adsorption of H_2

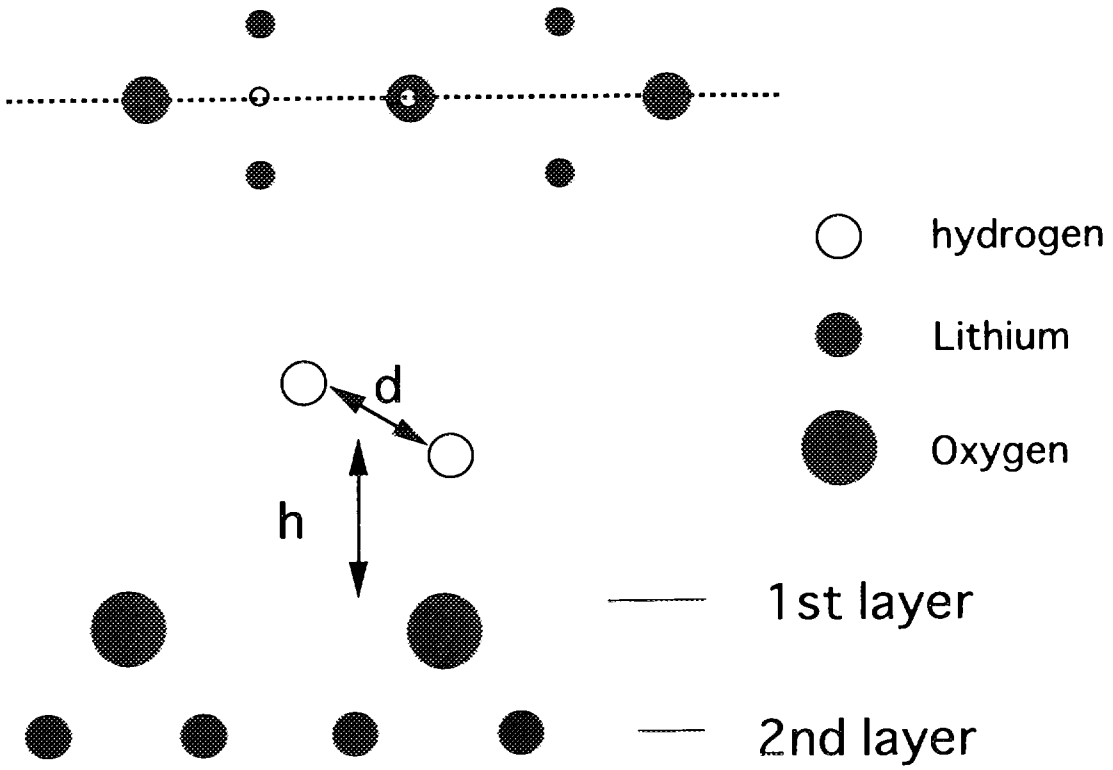

Fig.3 Cross section of Li2O cluster during the H2 adsorption.

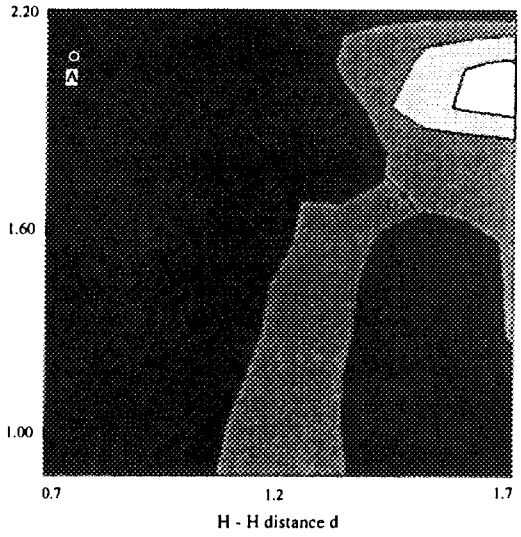

Fig.4 (a) Potential energy surface for H_2 dissociative adsorption. Oxygen vacancy was introduced adjacent to the adsorption site.

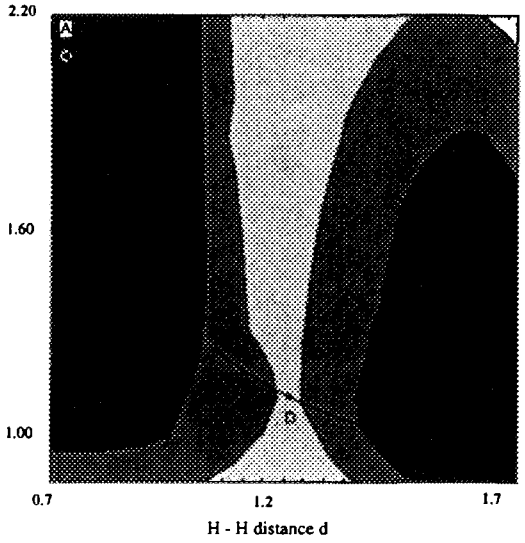

Fig.4 (b) Potential energy surface for H_2 dissociative adsorption on terrace site.

SESSION 3

Irradiation Effects on Tritium Release Behavior

Tritium release kinetics of Li_2O with radiation defects

Victor Grishmanov and Satoru Tanaka

Department of Quantum Engineering and Systems Science,
Faculty of Engineering, The University of Tokyo
7-3-1 Hongo, Bunkyo-ku, Tokyo 113, Japan

The study of an influence of radiation defects on tritium release behavior from polycrystalline Li_2O was performed by the in-pile and out-of-pile tritium release experiments. The samples were pre-irradiated by accelerated electrons to various absorbed doses up to 140 MGy and then exposed to the fluence of 10^{17} thermal neutrons/m^2. The radiation defects introduced by electron irradiation in Li_2O cause the retention of tritium. The linear temperature increase of the electron-irradiated samples disclosed two tritium release peaks: first starts at ~600 K with the maximum at ~800 K and second appears at ~950 K with the maximum at ~1200 K. It is thought that the tritium release at high temperatures (> 950 K) is due to the thermal decomposition of LiT.

In order to further investigated the formation of lithium hydrides, the diffuse-reflectance Fourier transform infrared (FTIR) absorption spectroscopy was applied. The Li_2O powder was irradiated by electron accelerator under D_2 containing atmosphere (N_2 + 10% D_2). An absorption band specific to the Li_2O was observed at 668 cm^{-1} and attributed to the Li–D stretching vibration.

1. INTRODUCTION

Lithium oxide has been suggested as a suitable breeding blanket material for a fusion reactor. In an operating fusion reactor, the tritium breeding blanket should reach a condition whereby the tritium release rate equals the production rate. The tritium release must be fast enough that the tritium inventory in the blanket does not become excessive. Slow tritium release will result in a large tritium inventory, which is unacceptable from the both economic and safety viewpoints.

The irradiation damage in Li_2O single crystals exposed to high fluence of fast neutrons ($3.9 \cdot 10^{26}$ neutrons/m^2) at about 650 K has been investigated by methods of electron spin resonance and optical absorption in the BEATRIX-II program [1]. The electron spin resonance data have been interpreted to indicate the presence of the colloidal Li in Li_2O single crystals with 1.8 and 0.07% ^6Li concentration. In most of the blanket designs using the Li_2O, the ^6Li enrichment of Li_2O is high (about 50–60%) and the neutron fluence at the lifetime is expected to be greater than that reached in the experiments performed by *Noda et al.* [1], and hence a high concentration of metal Li colloids could be created in the blanket. The operating temperature for a typical blanket design using Li_2O is in the range of 720 to 920 K [2]. The colloidal Li will remain in Li_2O in a lower temperature part of the blanket, since the colloidal Li are not completely recovered up to 870 K [3]. At the blanket temperature, the Li metal colloids will exist in the liquid state wherein the solubility of tritium is very large [4], and this can cause a large tritium inventory in irradiated Li_2O.

In addition, the tritium may react with colloidal Li to form LiT. The formation of Li–T bond, which is tolerant to high temperatures (for instance, the thermal decomposition of Li–H bond is estimated at 1223 K [5]), may significantly affect the tritium recovery from Li_2O. The intensive studies on an interaction of tritium with radiation defects were performed for lithium silicates ceramics [6–8]. It was reported [8] that the tritium retention can be increased up to 25–35% due to the formation of thermostable Li–T and Si–T bonds. Thus, the present work deals with the study on an influence of irradiation dose on tritium release behavior from polycrystalline Li_2O.

To evaluate an efficient temperature for the formation of lithium hydrides, the following experiment was carried out. The Li_2O powder was irradiated by electron accelerator under D_2 containing atmosphere (N_2 + 10% D_2) at various temperatures, and the formation of LiD was investigated by using the diffuse-reflectance FTIR absorption spectroscopy.

2. EXPERIMENTAL

The polycrystalline Li_2O pellets (80% of TD) were used for the in-pile tritium release experiments. The dimensions of specimens were following: 10.0 mm in height and 12.3 mm in diameter. The specimens were pre-irradiated by electrons (energy - 5 MeV; dose rate - 10 kGy/s; temperature - 440 K) to absorbed doses up to 140 MGy. Afterwards, these specimens were exposed to the fluence of 10^{17} thermal neutrons/m^2 at 300 K followed by the temperature increase up to 900 K. The recovered tritium was removed by a sweep

gas of N_2 + 1% H_2 and detected by an ionization chamber. Analogously, the experiments using an annealed polycrystalline pellets of Li_2O were performed.

The out-of-pile tritium release experiments were carried out using a polycrystalline Li_2O of the particle size of 2–4 *mm*. The sample was 95% pure. The specimens were sealed in quartz containers filled with air and irradiated by accelerated electrons (energy - 2.2 MeV, dose rate - 8 kGy/s, temperature - around 370 K) to absorbed doses up to 100 MGy. Afterwards, these specimens were exposed to the fluence of 10^{17} thermal neutrons/m^2 at about 300 K. The samples without pre-irradiation by electrons were exposed to the same fluence of thermal neutrons and used as reference samples. The out-of-pile tritium release experiments were carried out during the temperature transient from 293 to 1273 K. The temperature ramp was 10 K per minute. The released tritium was removed by the sweep gas of N_2 and detected by the ionization chamber.

The formation of LiD under the electron irradiation was investigated by using the diffuse-reflectance FTIR absorption spectroscopy. The Li_2O powder (48–65 mesh) was irradiated by electron accelerator under D_2 containing atmosphere (N_2 + 10% D_2) at around 373, 673 and 893 K. As a reference sample we used an annealed Li_2O powder, which was examined by the diffuse-reflectance FTIR absorption spectroscopy under Ar and Ar + D_2 atmospheres.

3. RESULTS AND DISCUSSION

3.1. In-pile tritium release

The radiation defects in Li_2O were created by electron irradiation. This method gives a possibility to vary an absorbed dose for Li_2O specimens. Afterwards, the tritium was generated by reactor irradiation at 300 K and in-pile tritium recovery from Li_2O was performed. The release curves of total tritium from the polycrystalline pellets of Li_2O are shown in Fig.1. The tritium release curve of the sample pre-irradiated by electrons (curve **A**) is compared with the tritium release curve of the same sample after annealing (curve **B**). The neutron exposure for annealed specimen with the fluence of 10^{17} thermal neutrons/m^2 at 300 K and followed increase of the temperature up to 900 K resulted in the appearance of the sharp tritium recovery peak. As we see subsequently, the rate of tritium release quickly reached a steady state. Alternatively, the tritium release from the pre-irradiated sample, measured in the same experimental conditions, is characterized by a slower release rate during the temperature transient than that from the annealed sample. After the shutdown of reactor, the tritium release rate of the annealed sample reached the background level quicker then that of the sample pre-irradiated by electrons. The above observations imply the influence of the radiation defects on tritium release processes.

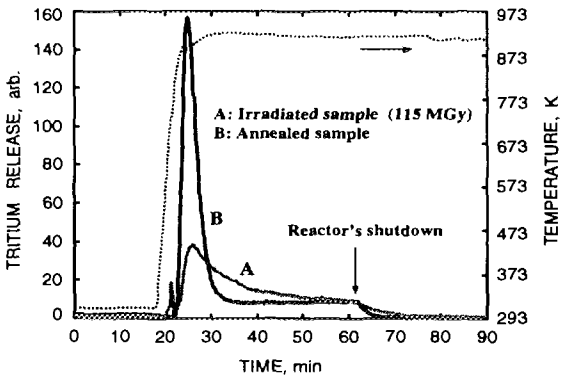

Figure 1: In-pile tritium release from polycrystalline Li_2O pellets irradiated by the fluence of 10^{17} thermal neutrons/m^2 at 300 K in the sweep gas of N_2 + 1% H_2.

The total amount of tritium released during the operation of reactor and during the one hour after the shutdown of reactor was calculated. The quantity of tritium recovered from the samples pre-irradiated by electrons was smaller than that from the annealed samples by 10–40% in dependence on irradiation dose. It is proposed that the interaction of tritium with radiation defects, in particular case with colloidal Li, leads to the formation of Li-T bond, which is stable at high temperatures. As a result, the tritium retardation in Li_2O specimens pre-irradiated by electrons was observed.

The greater was the absorbed dose of the sample, the less was the amount of retarded tritium. At first glance, it would seem a very puzzling pattern. However, the speculation can be done reasoning from the model of reaction schemes worked out by *Moriyama and Kurasawa* [9] which includes the examples of the mutual transformation of LiOT and LiT under irradiation condition:

$$LiOT + F^o \rightarrow LiT + Li_2O \qquad (1)$$

$$2LiT + O_2 \rightarrow 2LiOT \qquad (2)$$

Let's assume that the reaction (1) is valid at low irradiation dose wherein the formation of simple F-centers proceeds and their clustering is not yet started. On the other hand, the reaction (2) is valid at high irradiation dose wherein the radiolysis of the Li_2O matrix occurs resulting in the formation of colloidal Li as well as molecular O_2.

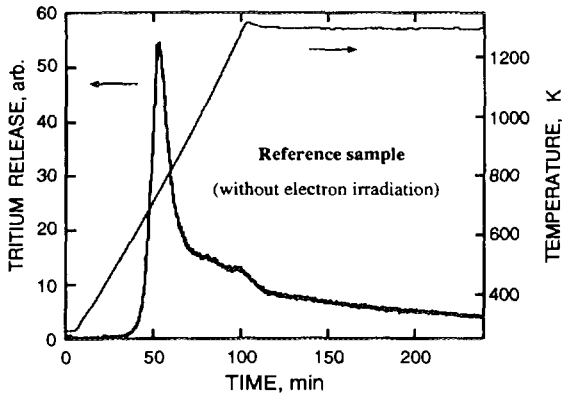

Figure 2: Ouf-of-pile tritium release from the polycrystalline Li_2O specimen irradiated by the fluence of 10^{17} thermal neutrons/m^2.

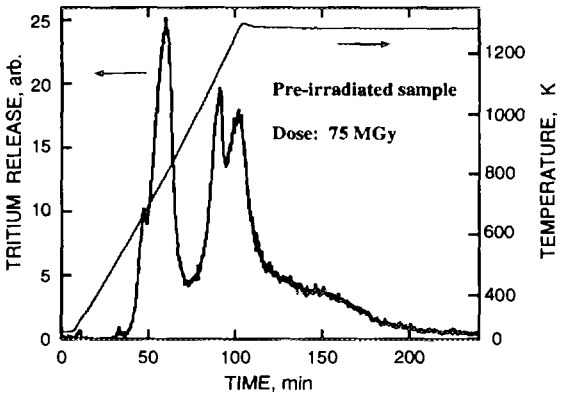

Figure 3: Ouf-of-pile tritium release from the Li_2O specimen pre-irradiated by electrons to absorbed dose of 75 MGy and by the fluence of 10^{17} thermal neutrons/m^2.

If so, the decrease of the amount of retarded tritium with increasing irradiation dose is caused by the formation of LiOT which is less tolerant to high temperatures that LiT.

Conceivably this mechanism might work, however the decrease of the amount of retarded tritium with increasing irradiation dose can also be caused by other reason. This is an oxidation of the colloidal Li by molecular O_2. If so, the formation of LiT should be suppressed and hence the amount of retarded tritium will be small. The problem is only one of experimental data about the formation of molecular O_2 in irradiated Li_2O are not available to make sure that oxidation of the colloidal Li by molecular O_2 proceeds at high irradiation dose. The interaction of tritium with such defects as colloidal Li, O_2, O_2^- and O^-, and synergism with tritium migration behavior require further experimental and modeling studies.

3.2. Out-of pile tritium release

Fig.2 shows the tritium release curve of the polycrystalline Li_2O specimen exposed to the fluence of 10^{17} thermal neutrons/m^2 at 300 K. The sharp peak of released tritium can be seen at around 750 K. There is not a grain of evidence to suggest an influence of radiation defects on tritium release. The absorbed dose for this specimen is estimated at around 10 kGy wherein the formation of simple F-centers occurs in Li_2O [10, 11]. It seems likely that the interaction of F-centers with tritium under low irradiation dose is negligible.

The irradiation of Li_2O specimens by 2.2 MeV electrons followed with the fluence of 10^{17} thermal neutrons/m^2 causes the change of the tritium release kinetics. The tritium recovery curve of the sample pre-irradiated by electrons to absorbed dose of 75 MGy is shown on Fig.3. Two broad peaks can be recognized at the tritium release curve: first starts at 600 K with the maximum at 800 K and second appears at 950 K with two maxima peaked at 1150 and 1270 K. The first broad peak at 800 K is associated with (1) desorption of physically and chemically adsorbed tritium at the sample surface, (2) decomposition of LiOT, and (3) migration of tritium dissolved in the bulk. The second broad peak is thought to be due to the tritium binded in Li–T bond, which was formed by the reaction of colloidal Li with tritium. According to a handbook of the thermo-dynamical data [5], the decomposition of LiH undergoes by spontaneous chain reaction. The process of the thermal decomposition of Li–T bond is dependent on tritium partial pressure and hence this is probable a reason of the presence of two maxima peaked at 1150 and 1270 K in the second complex peak of tritium release (Fig.3).

The experimental results indicate the possibility of the formation of Li–T bond, which is thermally stable at high temperatures up to 950–1200 K. This effect is undesirable from the tritium inventory standpoint. However, the generation of tritium by thermal neutron irradiation was conducted at about 300 K, what is inconsistent with operating temperature of the blanket of fusion reactor. Thus, the investigation of an influence of the colloidal Li on tritium release kinetics from Li_2O under the conditions approaching that expected in the thermonuclear reactor is desirable.

3.3 Observation of Li–D stretching vibration by FTIR absorption spectroscopy

In order to simulate the formation of Li–T bond under irradiation condition, the following approach was applied. The Li_2O powder was exposed to accelerated electrons under N_2 + 10% D_2 atmosphere at various temperatures: 373, 673 and

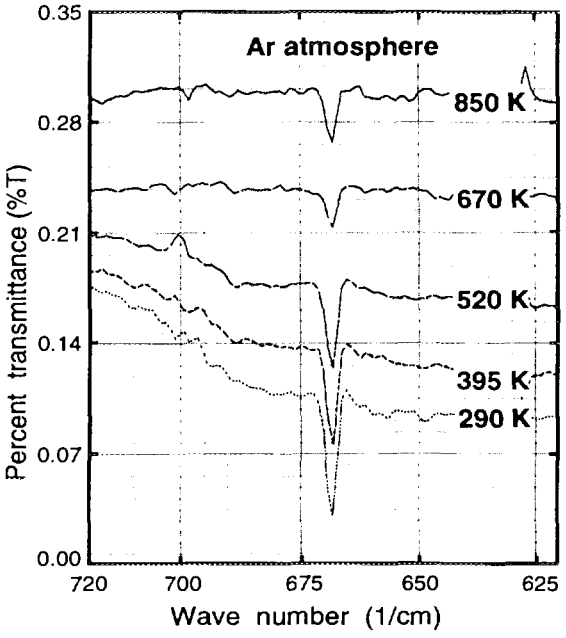

Figure 4: Temperature dependence of absorption spectra of the Li_2O specimen irradiated by electrons to absorbed dose of 100 MGy under N_2 + 10% D_2 atmosphere at 373 K.

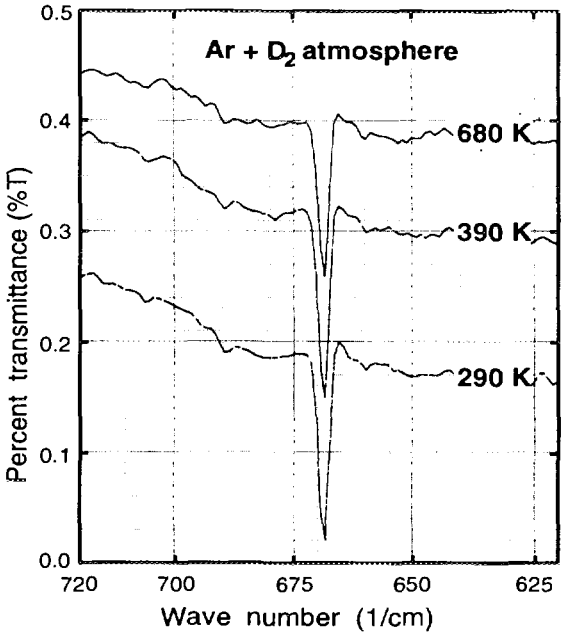

Figure 5: Temperature dependence of the diffuse-reflectance FTIR absorption spectra of the Li_2O specimen under Ar + D_2 atmosphere.

893 K. The absorbed dose was close to the range wherein the formation of colloidal Li can take place [12]. In that research, we found that the formation of colloidal Li in polycrystalline Li_2O under electron irradiation at 380 K occurs at absorbed dose of about 100 MGy. It was presumed that the formed colloidal Li during electron irradiation will react with D_2 absorbed in Li_2O powder to form the Li–D bond.

The samples prepared in the way described above were examined by using diffuse reflectance method of FTIR absorption spectroscopy. This method was successfully applied for the research on Li_2O surface nature [13, 14]. Two absorption peaks of surface –OH groups were observed at 3677 and 3565 cm^{-1}, and three stretching vibration peaks of surface –OD groups were detected at 2748, 2717 and 2696 cm^{-1} [13]. The stretching vibration at 1218 cm^{-1} was attributed to Li–H bond [14].

Fig. 4 shows the absorption spectra of Li_2O irradiated by electrons to adsorbed dose of 100 MGy under N_2 + 10% D_2 atmosphere at ~373 K. The stretching vibration peak can be seen at around 668 cm^{-1}. This peak is detected at the first time and attributed to the Li–D bond. The intensity of the 668 cm^{-1} peak decreases with temperature up to 850 K (Fig.4), however thereupon it reduces to almost the same value while the temperature was decreased. This fact indicates the thermal stability of the 668 cm^{-1} absorption peak. The irradiation of Li_2O powder by electrons at 673 and 893 K under N_2 + 10% D_2 atmosphere also resulted in the appearance of the stretching vibration peak at 668 cm^{-1}. However, the intensities of these absorption peaks were lower than that detected for the sample irradiated at 373 K. In such a manner, this testifies that the formation of Li–D bond is less efficient at high temperatures. The observational data suggest that the formation of Li–D bond can occur up to 893 K. However, a possibility of the production of Li–D bond at more higher temperature than 893 K is a subject to be studied.

The research on the FTIR absorption spectra of annealed Li_2O under Ar and Ar + D_2 atmospheres disclosed that the formation of Li–D bond occurs at the sample surface in the latter case. The absorption peak at 668 cm^{-1} observed for annealed Li_2O sample (Fig.5) is coincident with that detected for irradiated by electrons specimen under N_2 + 10% D_2 atmosphere (Fig.4). This fact does not allow us to conclude with confidence how the formation of Li–D bond proceeds in Li_2O during electron irradiation under D_2 containing atmosphere: (1) due to the interaction with colloidal Li or (2) by reaction at the Li_2O surface. The one is clear that the formation of Li–D bond at the Li_2O surface easily takes place under D_2 containing atmosphere.

4. CONCLUSIONS

It has been shown that the radiation defects significantly influence the tritium recovery from

Li_2O. The tritium retention was observed from the samples pre-irradiated by electrons. It is proposed that the retention of tritium is caused by the formation of Li–T bond, which is stable at high temperatures. For absorbed dose range from 50 to 140 MGy, the tritium retardation decreases with increasing absorbed dose. It is thought that, at high irradiation doses, the prevalence formation of LiOT proceeds which is less tolerant to high temperatures than LiT.

It has been shown that the radiation defects introduced by electron irradiation cause the retention of tritium due to its binding in the thermally stable state. The interaction of tritium with colloidal Li produced by electron irradiation is thought to result in the formation of Li–T bond. The tritium release at high temperatures (> 900 K) indicates the decomposition of Li–T bond.

Specific absorption band for the Li_2O sample was observed by the diffuse-reflectance FTIR absorption spectroscopy at 668 cm^{-1} and attributed to the Li–D stretching vibration. However, a prevalence mechanism of the production of Li–D bond during the electron irradiation under D_2 containing atmosphere is unclear: the binding of D_2 into LiD can proceed by a reaction at the Li_2O surface as well as by an interaction of D_2 with colloidal Li produced by irradiation.

REFERENCES

[1] N.M.Masaki, K.Noda, H.Watanabe, R.G.Clemmer and G.W.Hollenberg, *J. Nucl. Mater.* **212–215** (1994) 908.

[2] H.Takatsu, S.Mori, H.Yoshida, T.Hashimoto, T.Kurasawa, K.Koizumi, M.Enoeda, S.Satoh, T.Kuroda, T.Suzuki, K.Ioki and T.Kanazawa, *Proc. SOFT-17, Roma, Italy* (1992) 1504.

[3] K.Noda, K.Uchida, T.Tanifuji and Sh.Nasu, *J. Nucl. Mater.* **91** (1980) 234.

[4] D.K.Sze, P.A.Finn, J.Bartlit, S.Tanaka, T.Terai and M.Yamawaki, *Fusion Eng. Des.*, **8** (1989) 339.

[5] I.Barin, *Thermodynamical Data for Pure Substances* (VCH, New York,1989).

[6] A.A.Abramenkovs, J.E.Tiliks and V.G.Vasiljev, *Fusion Eng. Des.* **17** (1991) 61.

[7] A.Abramenkovs, J.Tiliks and H.Werle, *Proc. SOFT-17, Roma, Italy* (1992) 1261.

[8] A.Abramenkovs, J.Tiliks, G.Kizane, H.Werle and S.Tanaka, *Proc. SOFT-19, Lisbon, Portugal* (1996) 1463.

[9] H.Moriyama and T.Kurasawa, *J. Nucl. Mater.* **212–215** (1994) 932.

[10] V.Grishmanov, S.Tanaka, J.Tiliks, G.Kizane, A.Supe and T.Yoneoka, *Fusion Eng. Des.*, in press.

[11] V.Grishmanov, S.Tanaka and J.Tiliks, *Proc. SOFT-19, Lisbon, Portugal* (1996) 1451.

[12] V.Grishmanov, S.Tanaka, J.Tiliks, G.Kizane, A.Supe and L.Grigorjeva, *Nucl. Instr. and Meth. in Phys. Res. B,* in press (NIMB 40398).

[13] S.Tanaka, M.Taniguchi, M.Nakatani, D.Yamaki and M.Yamawaki, *J.Nucl. Mater.* **218** (1995) 335.

[14] J.P.Kopazs, J.Ortiz-Villafuerte and C.E.Johnson, *Proc. 4th Symposium on the Fabrication and Properties of Fusion Ceramics* (1995) 116.

STATUS OF THE EXOTIC-8 PROGRAMME and FIRST IN-PILE RESULTS FOR Li_2TiO_3 PEBBLES*)

J.G. van der Laan[1], M.P. Stijkel[1], R. Conrad[2]

1) ECN Nuclear Research, P.O. Box 1, NL 1755 ZG, Petten, The Netherlands
2) European Commission, JRC-IAM, Petten, The Netherlands

1. Introduction

In the European Blanket Project (EBP) two DEMO-blanket lines are considered of which the Helium-Cooled Pebble Bed blanket (HCPB) is based on ceramic breeder. The main aim of the EBP is the design and construction of the ITER Test Modules (ITM) [1]. Key areas, with respect to neutron irradiation testing, to be addressed in the present phase of the EBP R&D programme are besides design optimisation: tritium control, development of tritium permeation barrier techniques, tritium extraction systems, development of beryllium and ceramic breeder materials and testing of blanket subassemblies with reference tritium breeding materials. The necessary data base needs to be completed about 3 years prior to the envisaged start of ITER operation (≥ 2005).
Preliminary designs of a tritium breeding blanket for the ITER Extended Performance Phase have relatively low operating temperatures for the ceramic breeder material. Li_2ZrO_3, Li_2TiO_3, either shaped as pebbles or pellets, highly enriched in ^6Li are candidates. These characteristics urge to obtain data on the irradiation behaviour of these materials, in particular in the range of 200-400°C for Li_2ZrO_3 and 200-600°C for Li_2TiO_3 material, for which up to now no results of in-pile experiments are available [2].
This paper describes the status of the ongoing irradiation programme, on lithium ceramics in the HFR Petten, known as 'EXOTIC'. Within the EXOTIC-programme (acronym for EXtraction Of Tritium In Ceramics) candidate ceramic breeders are tested by in-pile experiments. Such reactor irradiations are needed to quantify tritium release behaviour as a function of temperature, purge gas and lithium burnup, and to determine mechanical stability of pebbles and pebble-beds for lithium burnups up to projected end-of-life values. The series known as EXOTIC-1 to -7 comprised a number of 56 indivual experiments with lithium burnups in a range of 5 up to 20 % in EXOTIC-7. Results have been reported elsewhere, including previous CBBI's, see e.g. [3-7].

2. The EXOTIC-8 programme

2.1 Design and Test Objectives for EXOTIC-8

The present series, EXOTIC-8, is focussed on Li_4SiO_4, Li_2ZrO_3 and Li_2TiO_3 as candidates for ceramic breeder pebbles for ITER EPP, DEMO and EBP Test Blankets. The set-up of the experiments denoted as EXOTIC-8 is deviating from the previous 7 EXOTIC's. A basic difference is that, instead of being a full-batch type experiment, EXOTIC-8 provides a higher flexibility of breeder irradiation testing, with 4 legs being operated independently, i.e. enabling different in-pile durations for the separate experiments. This structure allows to perform experiments with dedicated objectives, like tritium-release behaviour, high bur-

*) Presented at CBBI-6 by N. Roux, CEA Saclay

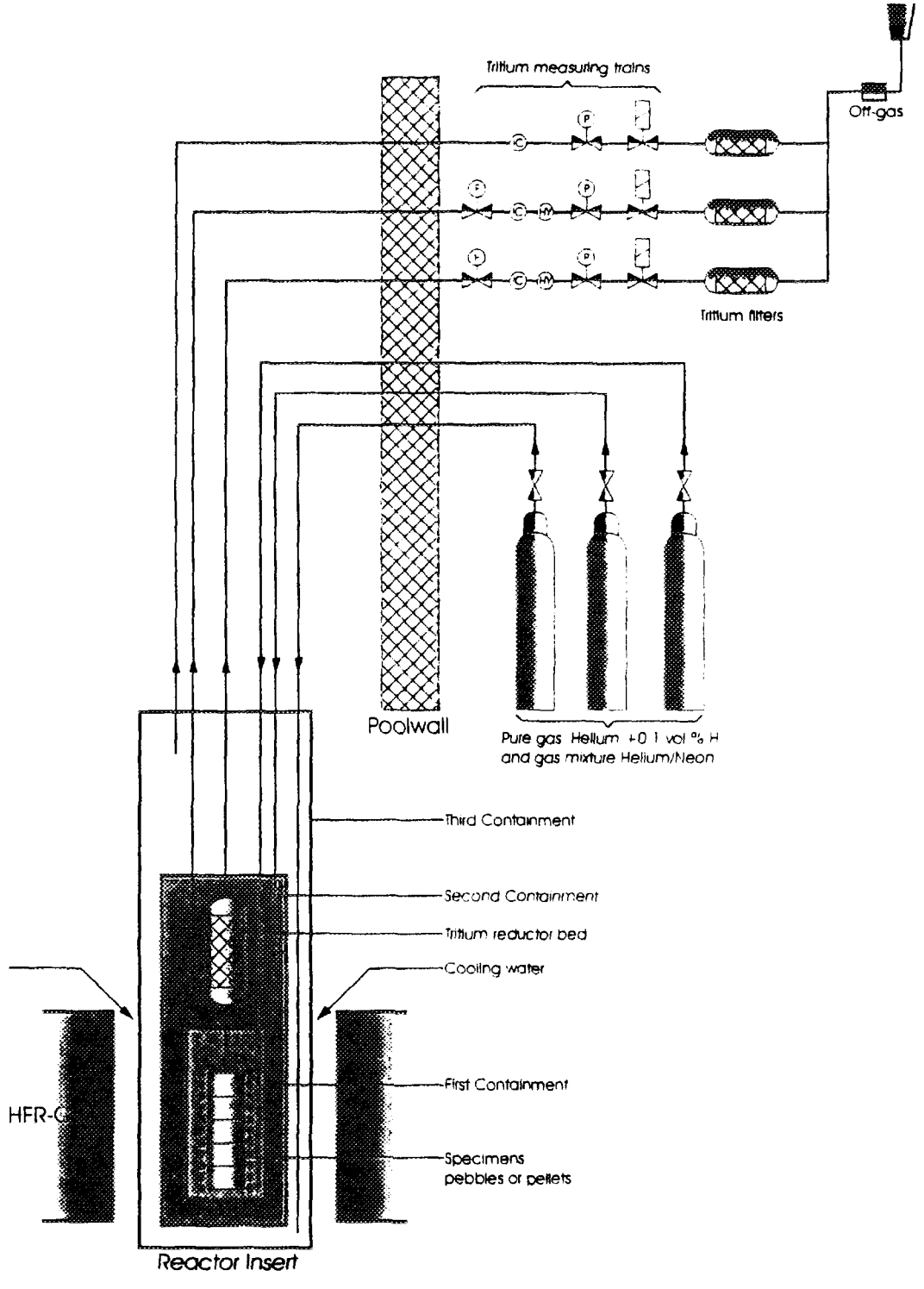

Figure 1: *Schematic lay out of a typical in-pile experiment for EXOTIC-8*

nup, permeation studies and purge gas chemistry. Figure 1 shows the principle scheme for the gas handling system for an EXOTIC-8 leg consisting of three containments with an in-built reductor bed. There is a separate containment for the rig head that connects the in-pile and out-of-pile sections. For the first experiments two particular designs have been developed so far. Designs and characteristics of the facilities are given below [8].

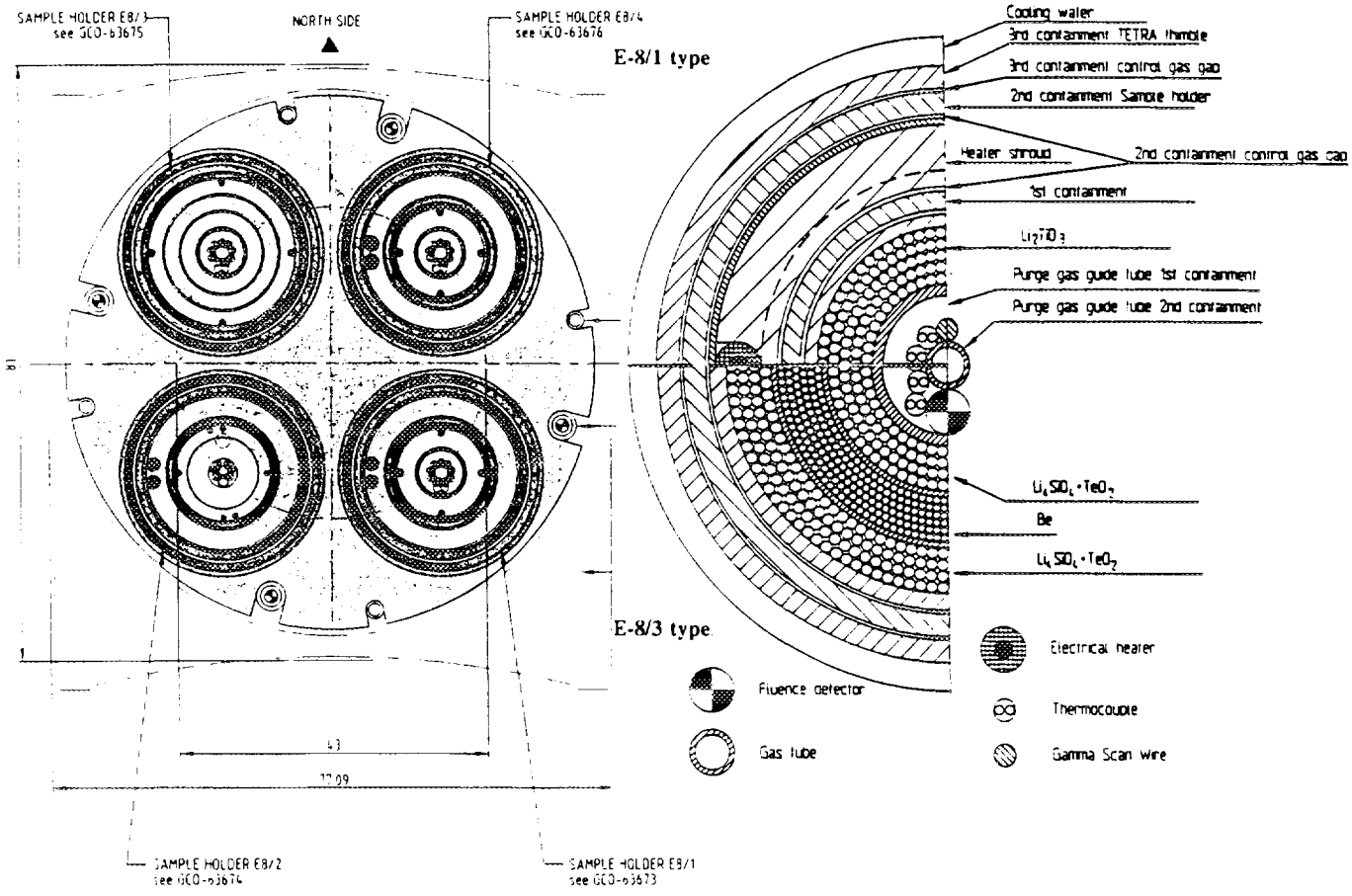

Figure 2: *Horizontal cross-sections for a) TETRA rig, b) E-8/1 type and c) E-8/3 type experiments.*

2.1.1 Tritium release characteristics (E-8/1 type)

The basic design developed for *tritium release characteristics* aims at the irradiation of pebbles contained in the annular space between two concentric tubes, see figure 2 for a cross-section. The inner space is used for instrumentation and purge gas feed line. The outer diameter is limited by the presence of ohmic heaters around the capsule, which are needed for temperature control and for the performance of stepwise temperature transients. The inner and outer diameter of the pebble-bed are 7 and 12 mm respectively. With a stack length of 120 mm the available volume amounts to 9 cm^3. This configuration enables to achieve moderate radial temperature gradients for a bed of ceramic pebbles with natural ^{6}Li-abundance. A relatively homogeneous temperature field is advantageous when in-pile temperature transients are performed so that residence times can be derived from the transients. The irradiation temperature is controlled by gas-mixture technique and the heating elements.

In order to obtain on a short notice in-pile release data on Li_2TiO_3 a second, only slightly modified, design concerns the irradiation of pellet-shaped specimens (diameter in/out = 5.2/9.5 mm , which are available from earlier development work at CEA [2]. This capsule, E-8/2, accommodates a pellet stack of about 55 mm in height.

2.1.2 E-8/3 type: High lithium burnups

A specific design was made for *irradiation to high lithium burnups*. Up to now in most experiments only limited material quantities have been irradiated. For qualification of candidate breeder materials extensive out-of-pile thermal cycling is performed on unirradiated material. For post-irradiation thermal cycling experiments quantities in the order of several tens of grams will be necessary. The design can basically be considered as a subsized integral test and comprises three concentric annular volumes: two for the breeder material pebbles and a central one for beryllium pebbles as the neutron multiplier, see figure 2 for a cross-section. The inner/outer diameters are successively 7/11, 11.5/15.5 and 16/20 mm, providing space for about 37 cm^3 of breeder material. The irradiation temperature can be controlled by gas-mixture technique. The purge gas flows parallel in the three sections with pebble-beds.

2.1.3 The HFR Tritium Measuring Station

The modified philosophy for EXOTIC-8, i.e. increased flexibility by having 4 independent legs, required extensive modification of the out-of-pile equipment of the Tritium Measuring Station (TMS). These modifications were conducted in the period 1995-1997 [8,9]. The new TMS has tritium measuring trains for four independent experiments, each composed of three containments allowing in-situ tritium release and permeation monitoring, and temperature control by gas mixture technique and/or electrical heaters (figure 1). New sets of glove boxes were manufactured that contain the gas handling equipment, measuring

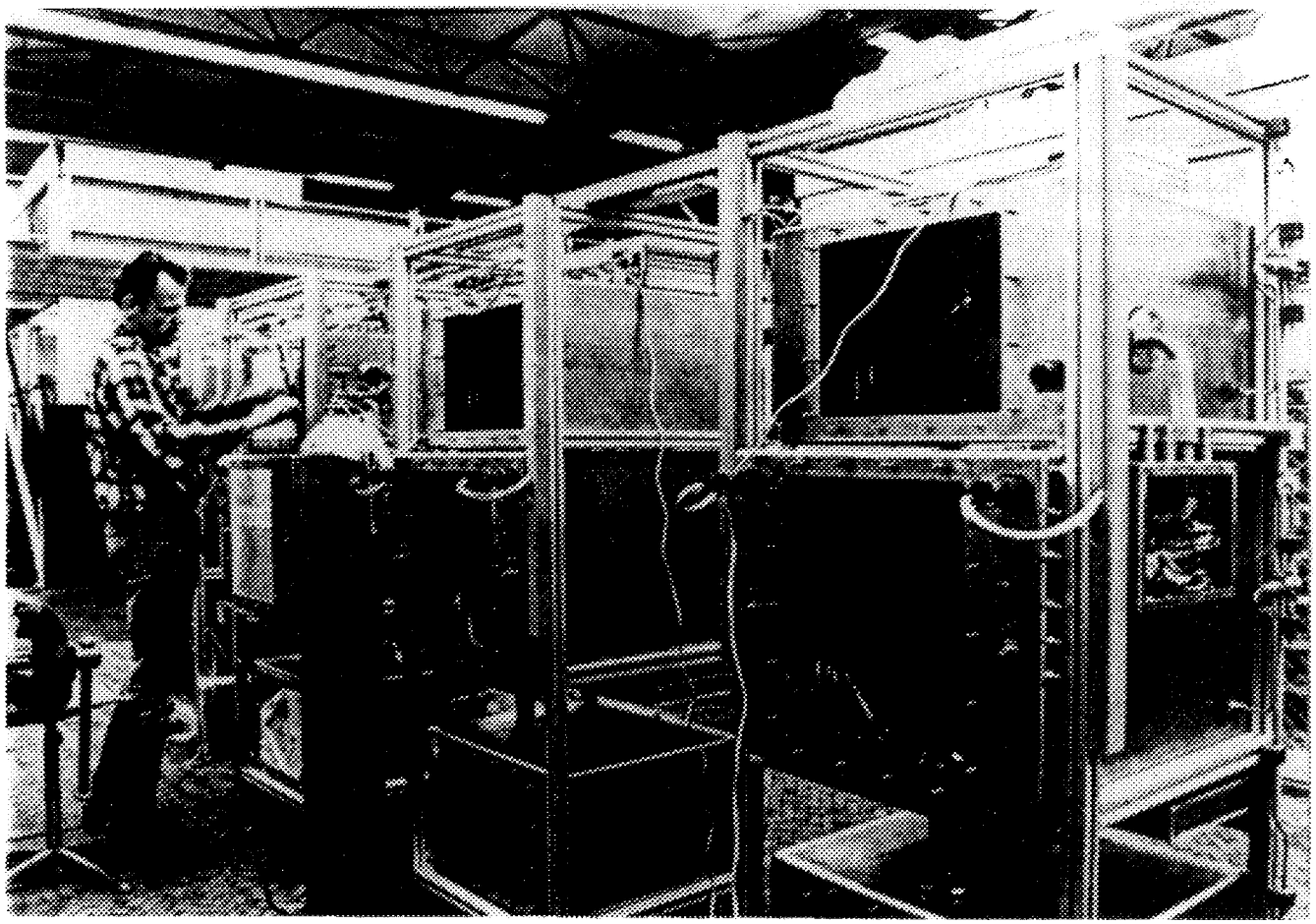

Figure 3: *View of TMS glove boxes during assembly phase.*

instruments and filter beds for the first and second containment. A separate box contains an expansion volume, and tritium filters for the 3rd containment and rig head. Composite tritium getter beds were manufactured with molecular sieves and SAES St.707 Material.

2.2. Loading plan for EXOTIC-8

The loading plan and test matrix of EXOTIC-8 is given in table 1. The first 3 experiments started on June 12, 1997 with HFR cycle number 97-06 along with an aluminum dummy in the 4th position. Operation of the three experiments and the new TMS is according to previous experiences: the experimental parameters obtained are close to the design calculations. First results for Li_2TiO_3 pebbles irradiated in E-8/1 are highlighted below. The experiments E-8/3 and E-8/4 concern Li_4SiO_4 pebbles with a 2 wt% TeO_2 addition. This material appeared to be sensitive to depletion of tellurium in a reducing environment already at temperatures around 900 K [10]. This has been confirmed by separate laboratory experiments. It has been decided to continue these irradiations at lower temperatures to diminish the contamination of the TMS by condensated tellurium and to substitute them by appropriate alternatives as soon as possible.

Table 1: ***Testmatrix of Presently Ongoing E-8 Irradiation Experiments****

Capsule ID :	E-8/1	E-8/3	E-8/4
Material	Li_2TiO_3	2 x Li_4SiO_4(+Te) + Be-bed	Li_4SiO_4(+Te)
Supplier	CEA	FZK	FZK
Objective	T-release	High Li burnup	T-release
^{6}Li-abundance	7.5	50	7.5
Central Temp. (°C)	250-600	350-600	350-700
Total Li-burnup (%)	1-3	7-10**	1-3**
HFR-cycles (plan)	4-6	11-12**	4-6**
Specimens:	pebbles	pebbles	pebbles
- Pebble density (% T.D.)	90	98	98
- Size range (mm)	0.7-0.85	0.25-0.63 Be: 0.1-0.2	0.25-0.63
- Bed dia (In/Out, mm)	7/12	7/11 ; 16/20 Be: 11.5/15.5	7/12
- Stack length (mm)	116	211	118
- Weight (g)	13.6	52.9 ; Be: 20.3	12.4
- Bed density (g/cm^3)	1.66	1.42 ; Be:1.10 ; 1.48	1.48

* 4th position filled with Al-dummy

** To be withdrawn/substituted because of Te-depletion/contamination

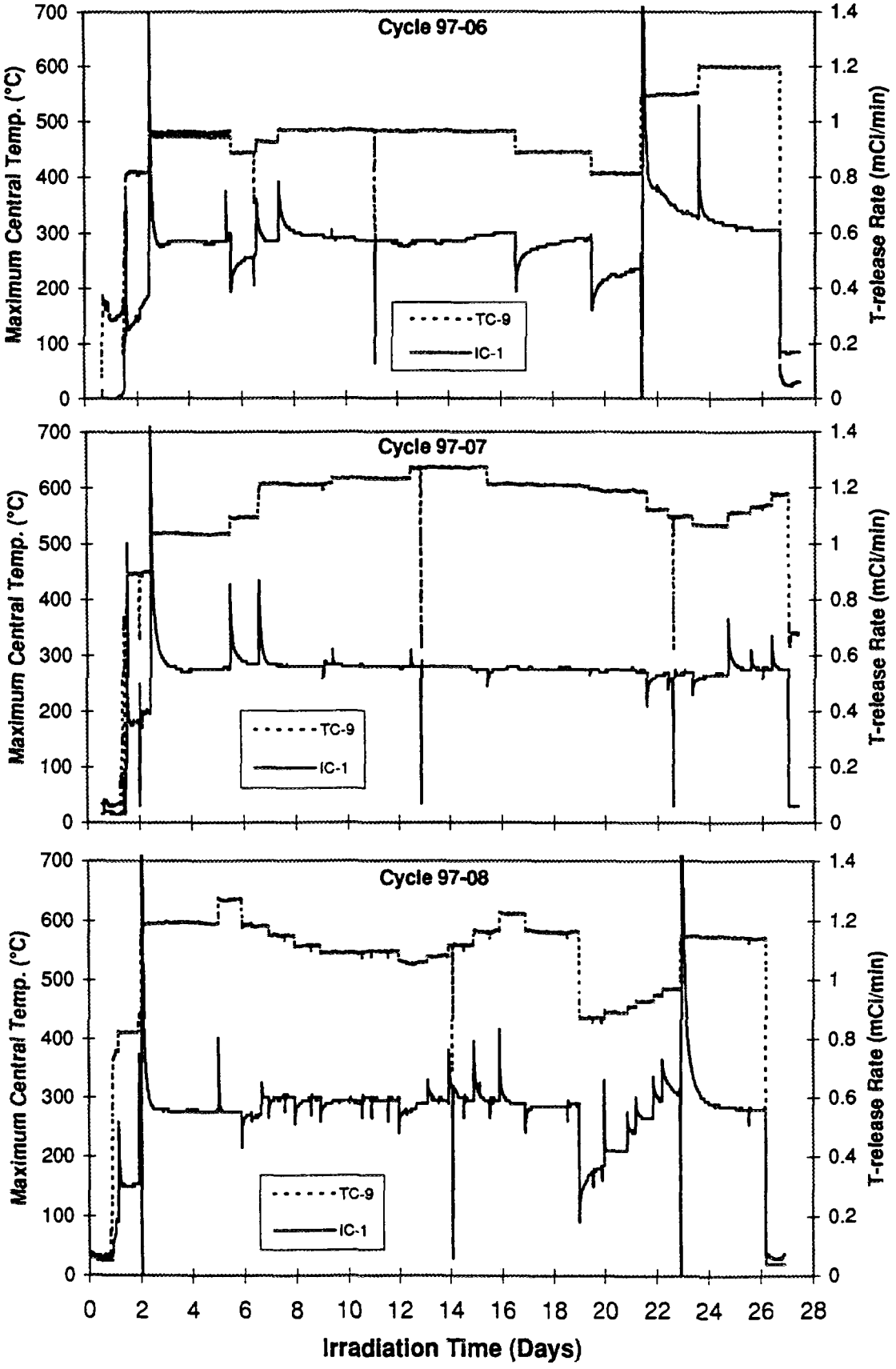

Figure 4: *Irradiation histories of experiment E-8/1 showing tritium release and leading central thermocouple for HFR Cycle numbers 97-06 (top), 97-07 (middle) and 97-08 (bottom).*

3. First In-pile Results for Li_2TiO_3 pebbles in EXOTIC-8/1

The first in-pile experimental results for Li_2TiO_3-pebbles supplied by CEA [11] are highlighted. The loading of E-8/1 is shown in table 1. Figures 4 show the irradiation history for the first two irradiation cycles of E-8/1: the temperature value is the highest reading of the six central thermocouples and the tritium release is from the first containment. It shows a fairly constant steady state signal in particular for the second cycle. A total of about 35 temperature transients have been performed and in general a fast recovery of the IC-signal from transients is observed. Main experimental parameters are summarized in table 2. Although no analysis has been made yet to quantify this behaviour in terms of tritium residence times, the trend of these results confirm expectations on the behaviour of this new material. The irradiation of E-8/1 will be continued up to about 2% burnup. It is foreseen to perform some dedicated tests to address purge gas chemistry effects.

Table 2: *Irradiation history capsule E-8/1 in first 3 HFR Cycles*

HFR-Cycle Number	Full Power Days (Cum.)	Lithium Burnup	T-prod.rate mCi/min	Central Temp. range (°C)	Transients performed
97-06	25.2	~0.27	~0.6	400-600	7
97-07	50.8	~0.57	~0.55	440-635	13
97-08	76.1	~0.87	~0.6	420-640	17

4. Planning for EXOTIC-8

The present pannning for EXOTIC-8 is depicted in table 2. Five further experiments have been defined which implies that in the present planning EXOTIC-8 is filled completely up to Fall'98 and 2 of 4 positions are occupied up to Spring'99. Post irradiation examinations will include inspections, scanning-electron microscopy and out-of-pile tritiuum release. High lithium burn-ups will also be checked experimentally.

Table 3: *Planning of presently defined EXOTIC-8 experiments*

Capsule	Material	Objective	Schedule
E-8/1	Li_2TiO_3-pebbles, CEA	T-release	Jun'97-Feb'98
E-8/3	Li_4SiO_4(+Te)-pebbles, FZK	High burnup	Jun'97-Feb'98
E-8/4	Li_4SiO_4(+Te)-pebbles, FZK	T-release	Jun'97-Feb'98
E-8/2	Li_2TiO_3-pellets, CEA	T-release	Dec'97-May'98
E-8/5	Li_2ZrO_3-pebbles, CEA	T-release	Feb'98-Sep'98
E-8/6	Li_2TiO_3-pebbles, ENEA	T-release	May'98-Dec'98
E-8/7	Li_2TiO_3-pebbles, CEA	High burnup	Feb'98-May'99
E-8/8	Li_4SiO_4-pebbles, FZK	High burnup	Feb'98-Mar'99*

* Replacement for E-8/3.

5. Conclusions

- After renewal of the Tritium Measuring Station the HFR is again fully operational for in-pile breeder irradiations. The EXOTIC-8 series has started with first three experiments on June 12, 1997.
- First in-pile results have been obtained for Li_2TiO_3-pebbles supplied by CEA: preliminary analyses indicate satisfactory in-pile behaviour with fast recovery from transient conditions.
- Five further experiments have been defined which implies that in the present planning EXOTIC-8 is filled completely up to Fall'98 and 2 of 4 positions are occupied up to Spring'99.
- P.I.E. results will be obtained from Spring'98 onwards.

Acknowledgements

The authors acknowledge N. Roux for presentation of the paper at the workshop. They further acknowledge the inputs by the HCPB Working Group on Ceramic and Beryllium Pebbles: M. Dalle Donne, W. Dänner, S. Casadio, N. Roux and H. Werle.
This work is performed mostly within the European Blanket Project and is financially supported by the European Commission and the Netherlands Ministry of Economic Affairs.

References

[1] L. Giancarli, M. Dalle Donne and W. Dietz: "Status of the European Breeding Blanket Technolgy", Fusion Engineering and Design 36 (1997) 57-74.
[2] N. Roux et al.: "Low-temperature Tritium Releasing Ceramics as Potential Materials for the ITER Breeding Blanket", Proc. ICFRM-7, Obninsk, J. Nucl. Mater. 233-237 (1996) 1431-35.
[3] H. Kwast: "Tritium recovery from Ceramic Breeder Materials", Proceedings CBBI-1, Tokyo, 1992.
[4] H. Kwast, M.P. Stijkel, R.P. Muis and R. Conrad: "EXOTIC: Development of Ceramic Tritium Breeding Materials for Fusion Reactor Blankets", ECN Report, ECN-C--95-123, December 1995.
[5] J.G. van der Laan, H. Kwast, M. Stijkel, R. Conrad et al.: "EXOTIC-7: Irradiation of ceramic breeder materials to high Li burnup", Proc. ICFRM-7, Obninsk, J. Nucl. Mater. 233-237 (1996) 1446-51, see also proceedings CBBI-4, Tokyo, 1995.
[6] J.G. van der Laan et al., Proceedings 19th SOFT, Lisbon, September 1996, pp. 1511-14.
[7] J.G. van der Laan and R. Conrad, paper presented at ISFNT-4, Tokyo, April 1996, submitted for publication in Fusion Engineering and Design.
[8] R. Conrad and J.G. van der Laan, Proceedings 19th SOFT, Lisbon, 1996, pp. 1611-1614.
[9] J.G. van der Laan (Ed.): "Progress Report 1996 on Fusion Technology Tasks", ECN-C--97-014, August 1997.
[10] M. Dalle Donne, private communication.
[11] N. Roux, CEA-Saclay, IEA-Workshop CBBI-6, Mito, October 1997.

SESSION 4

Hydrogen Behavior in Materials

Counter-diffusion and -permeation of deuterium and hydrogen through metals

Kaname KIZU* and Tetsuo TANABE**

*Department of Nuclear Engineering, Graduate School of Engineering, Nagoya University, Furo-cho, Chikusa-ku, Nagoya 464, Japan

**Center for Integrated Research in Science and Engineering Nagoya University, Furo-cho, Chikusa-ku, Nagoya 464, Japan

Abstract

The first experiments for counter-diffusion and -permeation of deuterium and hydrogen through palladium were performed. Deuterium permeation rates against D_2 pressure were measured under the condition where hydrogen permeated to opposite direction by supplying H_2 gas at the permeated side of D_2. It was found that not a small amount of deuterium was clearly permeated even if the deuterium pressure was much smaller than the hydrogen pressure. Deuterium permeation rate was gradually reduced by increasing the counter H permeation.

The deuterium permeation rate under the counter H permeation is well represented by a simple model in which the ratio of the deuterium permeation rates with and without the counter H permeation was proportional to the fractional concentration of deuterium in the bulk. As increasing the hydrogen counter flow, however, the deuterium permeation rate deviates from the model. This means that adsorption (absorption) of D_2 from gas phase is inhibited and surface recombination of deuterium is blocked by hydrogen.

1. Introduction

Tritium permeation through the first wall and blanket system is one of the most important safety issues. Various efforts have been paid on the estimation of permeation rate[1], reduction of inventory[2], effect of surface barrier[3,4] and so on. In most cases, only the permeation from plasma or blanket side to the cooling side is considered. At the cooling side, however, hydrogen uptake which is accompanied by water corrosion of the wall is not so small[3] that the dissolved hydrogen from the cooling side permeates to the plasma side.

Accordingly tritium and hydrogen permeate to the opposite direction with each other. Until now such counter-diffusion and -permeation have not been examined.

Before discussing the details of the counter-diffusion and -permeation mechanism of three hydrogen isotopes (hydrogen deuterium and tritium), we need a reliable data for understanding the two component (H, D) counter-permeation mechanism. In the present work we have conducted the first (within the author's knowledge) counter-diffusion and -permeation experiment with using a new experimental system in which deuterium and hydrogen permeate to the opposite directions.

2. Experimental

Figure 1 shows the permeation apparatus. The system was separated into two vacuum chambers by a sample palladium (Pd) membrane. Both chambers were evacuated by rotary pumps and turbo-molecular pumps. The base pressure of the system was maintained below 1×10^{-6} Pa measured by an ionization vacuum gauge. For convenience each chambers were refereed as the "D side" and the "H side" corresponding to the side which deuterium gas was injected and the side which hydrogen gas was injected, respectively. The injected deuterium and hydrogen gas pressure of the each side was monitored by an ionization vacuum gauge and quadrupole (QMS) mass spectrometer. The relative sensitivity factor of the ionization vacuum gauge for hydrogen was calibrated to be 0.4 and the pumping speed of the system was 1.0×10^{-1} $m^3 s^{-1}$.

Two types of counter-permeation experiments were carried out. The first experiment was following. After H_2 gas introduced into the H side at a fixed pressure to obtain a steady state permeation of hydrogen to the D side (deuterium pressure was equal to zero), D_2 gas was introduced into the D side, and permeated D_2 flux to the H side was measured by QMS. Increasing the D_2 pressure step wise, sequential changes of the permeated D_2 flux to the H side were measured under the fixed H_2 pressure. In another experiments H_2 gas was introduced into both sides at a fixed pressure to obtain the steady state permeation.

The deuterium permeation rate(Q(t)) through the membrane was determined from partial pressure increment at the H side ($\Delta PD_2(t)$) multiplied by the effective pumping speed of the system (*Seff*) as,

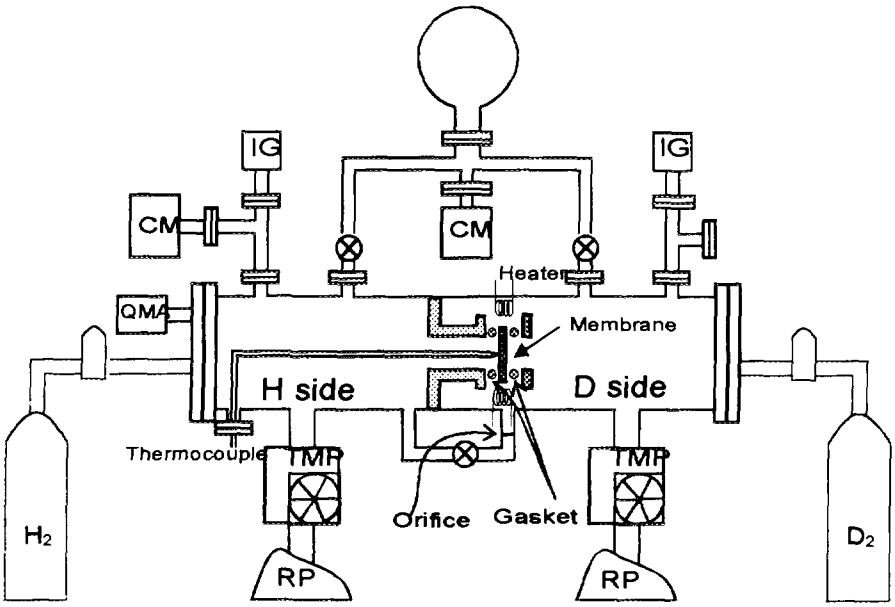

Figure 1. Schematic diagram for apparatus of counter-permeation measurement.

$$Q(t) = \frac{\Delta PD_2(t) \times Seff}{RT}, \qquad (1)$$

where R and T are the gas constant and the membrane temperature, respectively. The steady state permeation rate was given by,

$$J(\infty) = \frac{Q(\infty)}{A}, \qquad (2)$$

where A is the surface area of the membrane.

In the present work we could not determine deuterium partial pressure in the H side directly. The permeated deuterium atoms are released as D_2 (m/e=4) and DH(m/e=3). However the H_2 pressure in the H side was high enough to produce H_3 molecule(m/e=3) in the ionization source of QMS which was several orders of magnitude larger than observed DH. Therefore we estimated partial pressure of deuterium in the H side from D_2 signal(m/e=4) in QMS which was calibrated using gas mixture of D_2 + H_2 in equilibrium in a separate system assuming that released D_2, DH and H_2 molecules were in equilibrium in the H side. This procedure would give rise the maximum uncertainty of about ±25% when deuterium pressure was the minimum.

Pd membrane was supplied by Nilaco Co. Ltd. Japan with a purity of 99.95 %. The thickness of the membrane was 0.025 mm with a surface area of 1.8×10^{-4} m^2. The membrane was fixed on a stainless steel sample holder using metal gaskets without any vacuum leak, and

heated up to 1000 K by a molybdenum heater. The sample temperature was measured by a thermocouple. Measurements were performed at the temperature of 840 K under a D_2 pressure ranging from 7×10^{-4} to 3 Pa in the D side and a fixed H_2 pressure either 1.3×10^{-1}, 6.7×10^{-2} or 2.7×10^{-2} Pa .

3. Results and discussion

At first, a normal deuterium gas driven permeation (GDP) experiment was conducted without H_2 gas in the H side. For the first permeation experiment, hydrogen permeation rate showed the initial increase followed by a quasi-steady state. The quasi-steady state permeation rate, however, continued to increase very slowly and several hours were needed to attain the true steady state[5] where the permeation rate showed no further change. All values of $J_D(\infty)$ in the present work were thus determined after the true steady state was attained. The dependence

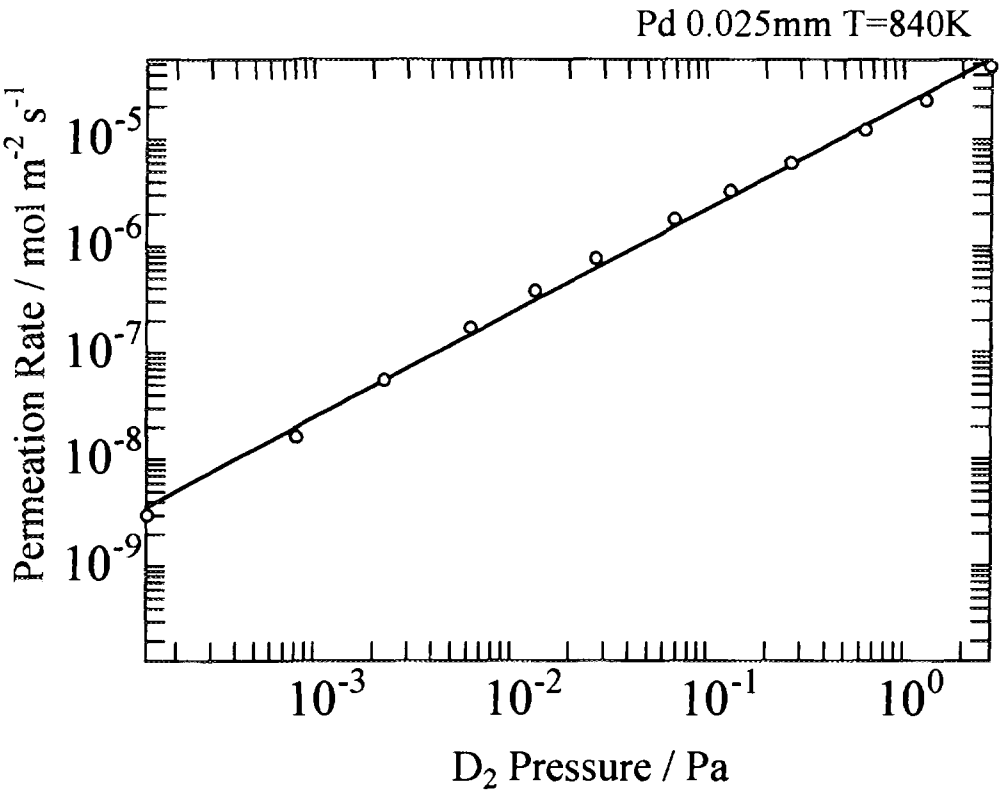

Figure 2. Deuterium pressure dependence of the steady state deuterium permeation rate.

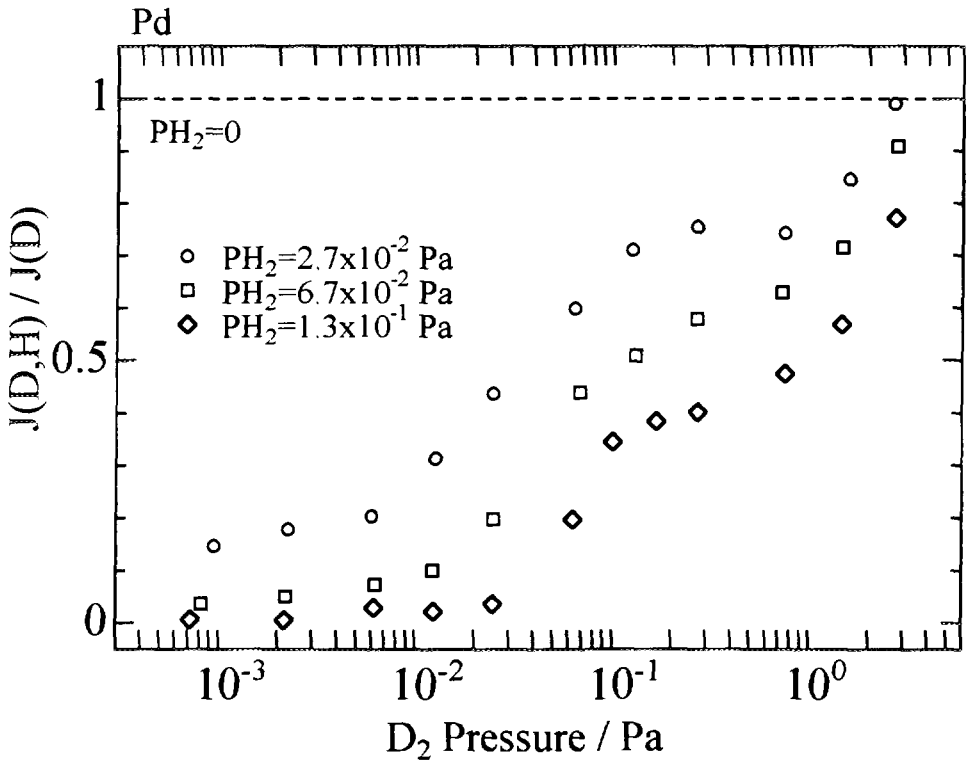

Figure 3. Normalized deuterium permeation rates against D_2 pressure with counter hydrogen permeation.

of the steady state permeation rate on deuterium pressure of the D side at 840 K is shown in fig. 2. The solid line in the figure shows the linear dependence of the pressure. This means that deuterium permeation in Pd in the present pressure range is the surface rate limited process but not the diffusion limited process.

Figure 3 shows sequential change of deuterium permeation rates against D_2 pressure with a fixed H_2 pressure in the H side. The rates were normalized by the values obtained without H_2 gas in the H side. The deuterium permeation was clearly suppressed by the existence of H_2. However it is significant that not a small amount of deuterium permeated even if H_2 pressure is higher than D_2 pressure ($PD_2<PH_2$).

Figure 4 shows results of another type of experiments where H_2 gas was introduced into both sides at a fixed pressure. In the figure part of the previous data were superposed as open symbols. Closed circles were obtained under the same H_2 pressure in both side, whereas closed squares represent the data obtained under H_2 pressure in the D side was higher, i.e. D

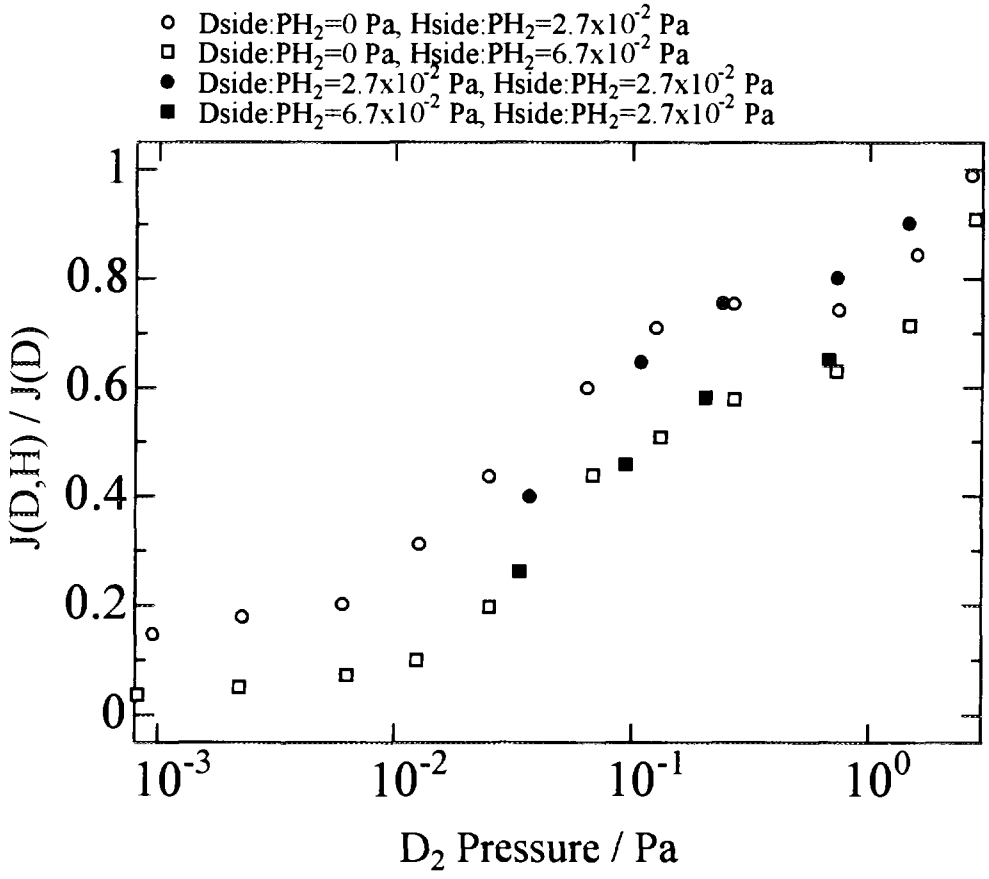

Figure 4. Normalized deuterium permeation rates with co-permeation (closed symbols) of H and counter-permeation (open symbols) of H.

and H permeate to the same direction. It is rather surprising to find that open and closed symbols are completely overlapped. One should note that co-diffusuion (closed squares) where H_2 pressure in the D side (6.7×10^{-2} Pa) was higher than that of the H side (2.7×10^{-2} Pa) give the same deuterium permeation that obtained with 6.7×10^{-2} Pa H_2 in the H side only. This means that deuterium permeation is not influenced by counter diffusing H nor existence of H on the surface, which is another indication that the permeation is not controlled by diffusion but the surface limited.

All these results are well explained by a simple model, assuming the surface rate limited process[6] and no concentration gradient throughout the bulk. The concentration of hydrogen can be expressed as

$C_H=S_H PH_2^{1/2}$ and $C_D=S_D PD_2^{1/2}$, (3)

with S solubility and PH_2 hydrogen pressure. Suppose the surface condition is the same for both side the surface areas available to H_2 and D_2 release are blocked by respective fraction $C_D/(C_D+C_H)$ and $C_H/(C_D+C_H)$, respectively. Then the permeated D flux under the existence of H would be suppressed as,

$J(D,H)/J(D) \propto C_D/(C_D-C_H)$. (4)

As the same reason hydrogen permeation to the opposite direction should be reduced as,

$J(H,D) \propto C_H/(C_D-C_H) \times J(H)$, (5)

but not measured in the present work. According Lacher[7], solubility rate of hydrogen to deuterium in Pd is given by,

$$\log\frac{S_H}{S_D}=\frac{161.5}{\mathrm{T}}-0.094. \qquad (6)$$

Substituting eq.(3) for T=840K into eq. (4),

$$\frac{J(D,H)}{J(D)}=\left(\frac{C_D}{C_D+C_H}\right)\approx\frac{\sqrt{PD_{2Dside}}}{\sqrt{PD_{2Dside}}+1.25\sqrt{PH_{2Hside}}}. \qquad (7)$$

Experimental values were compared with the simple model (eq. (7)) as shown in fig. 5. One can clearly see that eq.(7) represents the experimental value quite well when H_2 pressure in the H side is 2.7×10^{-2} Pa, With increasing hydrogen pressure the experimental data tend to deviate to down side. This can be attributed either or both of the suppression of deuterium concentration in Pd bulk by hydrogen solution, or surface blocking by H atom. Of course if hydrogen pressure is significantly large the assumption of the surface limited permeation breaks and one can attributed these deviation to H-D interaction in the bulk and/or in the diffusion process.

To investigate the surface blocking effect, Argon (Ar) gas with pressure of 7.7×10^{-3} Pa was injected instead of H_2 gas in the H side and deuterium permeation from the D side was measured. Results were the reduction of the permeation rate by a factor of 0.25 compared to that of pure D_2 permeation irrespective of the D_2 pressure. Thus Ar blocked the surface recombination site but did not change the permeation mechanism. Considering much larger reduction by H_2 introduction than Ar, however, it is very likely that hydrogen not only blocks the surface recombination site but also inhibit adsorption (absorption) of D_2 from gas phase. This might be the reason for the down side deviation in the Fig. 5.

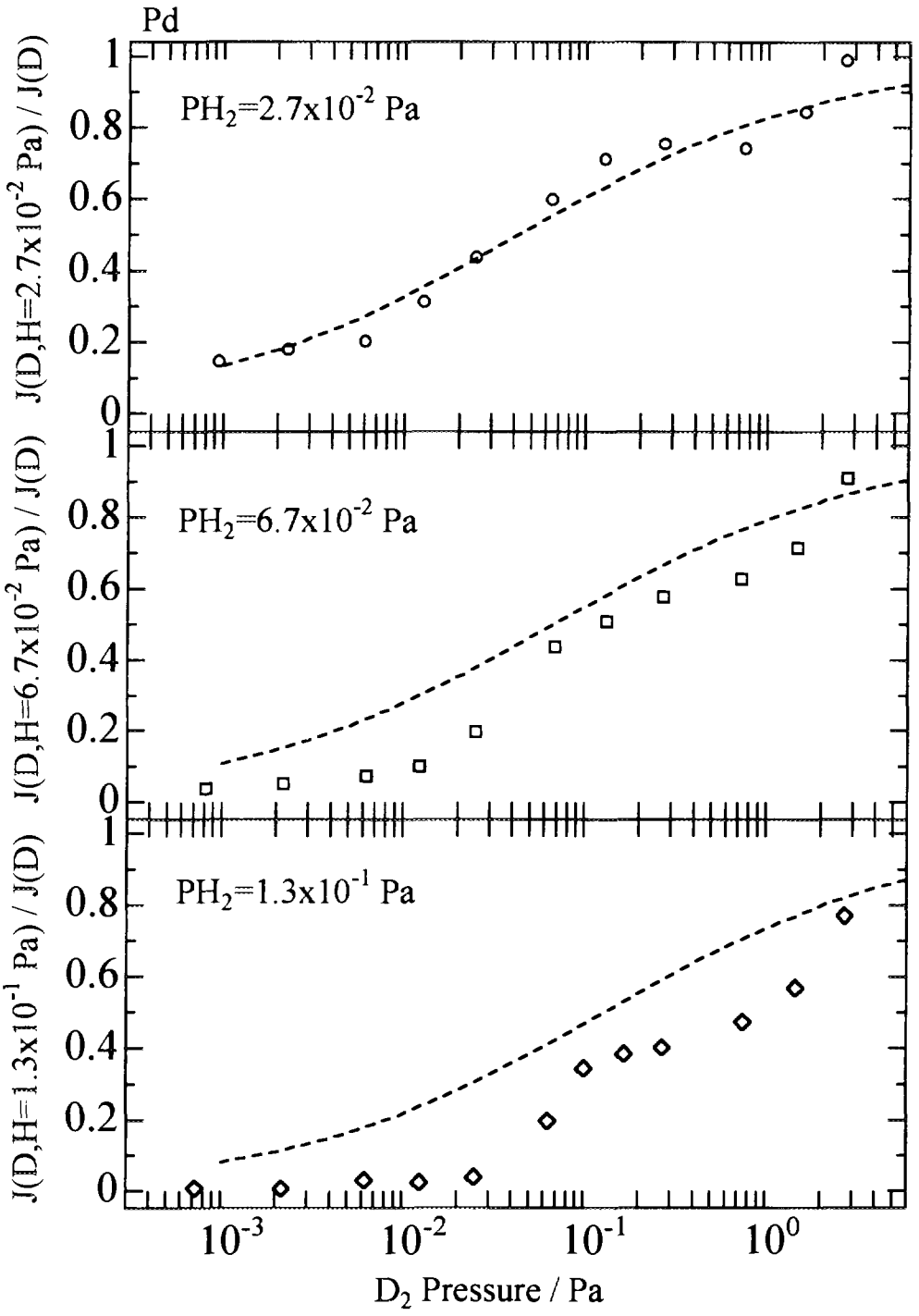

Figure 5 The comparison of experimental values with simple model (see text).

4. Conclusion

The first counter-diffusion and -permeation experiment through palladium membrane was conducted using a new experimental system in which deuterium (D_2) and hydrogen (H_2) permeate to the opposite directions. In the present experimental conditions, deuterium permeation through Pd was found to be surface rate limited process but not controlled by the diffusion process.

Deuterium permeation rate decreased with increasing hydrogen counter flow (increase of H_2 pressure at the H side). However the counter deuterium permeation was retained, even if deuterium pressure in the D side was much smaller than hydrogen pressure in the H side. The dependence of the deuterium permeation rate on the H_2 pressure as well as D_2 pressure were well reproduced by a simple model where the ratio of the deuterium permeation rates with and without the counter H permeation is proportional to the fractional concentration of deuterium ($C_D/(C_H+C_D)$) in the bulk. As increasing hydrogen counter flow, however, observed permeation rate deviates from the model probably because the surface recombination of deuterium is blocked and adsorption (absorption) of D_2 from gas phase is inhibited by hydrogen.

References

[1] T. J. Dolan and R. A. Anderl, EGG-FSP-11348 September (1994)

[2] B. L. Doyle, J. Nucl. Mater. **111&112**, 628 (1982)

[3] T. Tanabe, Fusion Technol. **28**, 1278 (1995)

[4] M. Yamawaki, T. Namba, T. Kiyoshi, T. Yoneoka and M Kanno, J. Nucl. Mater. **133&134**, 292 (1985)

[5] J. Park, T. Bennett, J. Schwarzmann, S. A. Cohen, J. Nucl. Mater. **220-222**, 827 (1995)

[6] R. A. Kerst and A. Swansiger, J. Nucl. Mater. **122/123**, 1499 (1983)

[7] J. R. Lacher, Proc. Roy. Soc. (London), Ser. A, **161**, 525 (1937)

Dynamic Behavior of Protium and Deuterium Implanted into an Oxide Ceramic Studied by Means of ERD Techniques

Emi Iizuka, Tomoaki Horikawa, Bun Tsuchiya, Kazuo Soda,
Kenji Morita and Hiroyasu Iwahara*

Department of Crystalline Materials Science, School of Engineering, Nagoya University, Nagoya 464-01
**Center for Integrated Research in Science and Engineering, Nagoya University, Nagoya 464-01*

We have investigated exchange of deuterium (or protium) implanted into an oxide ceramic, $SrCe_{0.95}Yb_{0.05}O_{3-\delta}$, for protium (or deuterium) due to exposure to H_2O (or D_2O) vapor at room temperature by means of the elastic recoil detection (ERD) technique. It is found that D is completely exchanged for H by expose to H_2O vapor, while H is hardly exchanged for D by expose to D_2O vapor, namely there exists a great isotope difference between the exchange of D for H and that of H for D. This result suggests that the exchanges do not take place on a conventional model of following subsequent reactions; dissociative absorption at the surface, diffusion (H), replacement of D by H, diffusion (D), and release due to surface recombination, but on a new model of following reactions; dissociative absorption at the surface, diffusion and release through bulk recombination due to mixed molecule formation.

In order to clarify the reaction leading to the great isotope difference, the experiments on the retention of H and D by simultaneous H^+, D^+ implantation and the release of 5 keV D_2^+ implants by 0.5 keV H_2^+ irradiation and 5 keV H_2^+ implants by 0.5 keV D_2^+ irradiation have been done. The retention experiment shows that the D/H ratio of the saturation implantation concentration is 1.3. Competition among H-H, H-D and D-D bulk recombination prefers to enrich D, which is opposite to the isotope difference observed. The release experiment shows that the slow and continuous decay of 5 keV D_2^+ implants is induced by 0.5 keV H_2^+ irradiation for long term, while that of 5 keV H_2^+ implants is hardly induced by 0.5 keV D_2^+ irradiation for long term. The latter result suggests that the diffusion may play a major rule in the great isotope difference.

1. Introduction

Dynamic behaviors of hydrogen atoms in oxide ceramics has received intensive attention in applied point of views such as high temperature protonic conductors in electrochemical devices and tritium breeding materials in fusion devices. $SrCe_{0.95}Yb_{0.05}O_{3-\delta}$ is a typical proton conducting oxide ceramic which is perovskite-type and exhibits high protonic conductivity under hydrogen-containing atmosphere at elevated temperatures [1] Processes of up-take and release of hydrogen isotopes in the ceramics have been studied by many authors, using various experimental techniques such as the conductivity measurement [2], and ion beam analysis [3]. However, detailed properties of hydrogen atoms in the ceramics have not been well understood yet. The fundamental understanding is important for further applications.

For tritium breeding ceramic materials, important key issues concerning hydrogen behaviors are recovery of tritium produced during reactor operation and reduction of tritium inventory for maintenance. These are closely related to release of tritium and replacement of tritium by other isotopes. In the present study, for more common purpose, retention and re-emission of H and D implanted into an oxide ceramic, $SrCe_{0.95}Yb_{0.05}O_{3-\delta}$, up to saturation has been studied by means of the elastic recoil detection (ERD) technique. It has been eventually found that deuterium implanted into the ceramic is almost completely replaced by protium in normal air-vapor when the as-implanted ceramic is exposed to normal air introduced in the vacuum chamber.

In this paper, we report the experimental results on the anomalous exchange of deuterium in $SrCe_{0.95}Yb_{0.05}O_{3-\delta}$ for protium in H_2O-vapor and the limited exchange in vice versa case at room temperature, on the retention of H and D in the ceramic irradiated simultaneously with 4 keV H_2^+ and 3 keV D_2^+ ions and on the replacement of 5 keV D_2^+ implants by 0.5 keV H_2^+ irradiation and of 5 keV H_2^+ implants by 0.5 keV D_2^+ irradiation, and moreover discuss the reaction processes for the replacement between hydrogen isotopes.

2.Experimental

The specimen used was a disc of $SrCe_{0.95}Yb_{0.05}O_{3-\delta}$ of 15 mm in diameter and 1 mm in thickness, which was prepared by a solid state reaction and sintering process [4]. The specimen was placed on a manipulator in contact with a ceramic heater in a conventional UHV chamber, which was evacuated to the base pressure of 4.0×10^{-7} Torr. Prior to hydrogen ion implantation, the specimen was heated at 973 K for 15 minutes in order to remove out residual hydrogen (protium). The temperature was measured with a thermocouple of almel-chromel. The specimen was implanted with 5 keV D_2^+ ions or 5 keV H_2^+ ions at a flux of 4.0×10^{13} /cm^2•s up to saturation at room temperature.

The specimens implanted up to saturation were soaked in H_2O water (distilled water), or D_2O water (pure water). They were also exposed to H_2O-vapor or D_2O-vapor, which were carried by dry-air through solution of H_2O or D_2O. Before and after these treatments, the depth profiles of H and D in each specimen were measured by the ERD technique [5], where the recoil H^+ and D^+ ions were detected through thin foil filter at a forward recoil angle of 20° to the incident direction of 1.7 MeV He^+ ion beam which is inclined at 80° to the surface normal. The Rutherford backscatteing (RBS) spectrum was measured simultaneously at an angle of 150° to the incident direction in order to monitor the fluent of 1.7 MeV He^+ ion beam.

Furthermore, in order to investigate the release process of H and D, the retention of H and D in the ceramic irradiated simultaneously with 4 keV H_2^+ and 3 keV D_2^+ ions was measured. In the experiment, the peak depths of H and D implants were coincided with each other.

Finally, in order to investigate the effect of diffusion on the isotope difference in the hydrogen

replacement, the specimen, into which has already implanted with 5 keV H_2^+ ions up to saturation, was irradiated with 0.5 keV D_2^+ ions and vice versa.

All irradiations and procedures were done at room temperature.

3. Experimental Result and Discussion

Typical ERD spectra of 1.7 MeV He^+ ion beam from the specimen measured at each stage of the standard procedures in the present study are shown in Fig. 1, where ERD spectra obtained for the specimen as-received (a), heated at 973 K for 15 minutes (b), exposed to D_2 gas at 10^{-4} Torr (c), implanted up to saturation with 5 keV D_2^+ ions (d), and heated at 343 K for 3 minutes (e) are shown, and the horizontal axis of channel number corresponds to the kinetic energy of recoiled species. One can estimate the depth of hydrogen retained in the specimen from the kinetic energy of the recoiled species using the standard method, as shown in Fig. 1(a) and (b). It is clearly found from Fig. 1 that protium is retained in the as-received specimen and it is removed out after heated at 973 K for 15 minutes. It is also found from a small peak in (c) that deuterium is retained at the top surface for the specimen exposed to D_2 gas at 10^{-4} Torr, which gives the surface position in the depth scale and moreover that deuterium retained in the specimen by 5 keV D_2^+ ion implantation is mostly distributed at a depth of 25 nm. This depth corresponds to the projected range of 2.5 keV D^+ ion in the specimen. Fig. 1(e) shows that deuterium is almost re-emitted after heated 70 °C for 3 minutes.

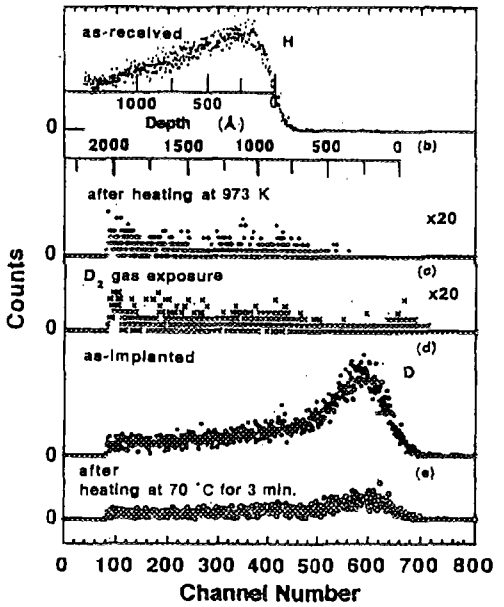

Fig. 1. The ERD spectra of 1.7 MeV He^+ ion beam from the specimen as-received (a), heated at 973 K for 10 minutes (b), exposed to D_2 gas at 10^{-4} Torr (c), implanted up to saturation with 5 keV D_2^+ ions (d), and heated at 343 K for 3 minutes (e).

From the standard analysis of ERD spectrum for the specimen as-implanted, it was found that the ratio of the saturation concentration of D implants to the molar concentration of $SrCe_{0.95}Yb_{0.05}O_{3-\delta}$ is 1.1 ± 0.1. It was also found that the saturation concentration of H implants is almost the same as that of D implants. The isochronal annealing experiments indicated that the H and D implants were almost re-emitted at the temperature of around 90 °C

During the previous experiment, the specimen loaded by saturation implantation with 5 keV D_2^+ ion beam was again analyzed by means of the ERD measurement after once exposed to normal air in the chamber. Fig. 2 shows the ERD spectra for the specimen exposed to normal air for 7 hours at the room temperature. Fig. 2 indicates that most of D atoms implanted into the specimen were exchanged for H atoms only by exposure to the normal air at room temperature.

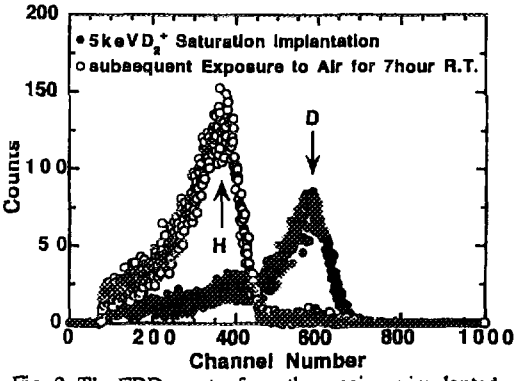

Fig. 2. The ERD spectra from the specimen implanted with 5keV D_2^+ ions up to saturation and subsequently exposed to normal air for 7 hours in the chamber at room temperature.

Firstly, in order to investigate the key parameter for the anomalous hydrogen exchange, the specimen was soaked in water after saturation implantation. Fig. 3

shows the ERD spectra for the specimen soaked in H_2O (distilled water) after implanted 5 keV D_2^+ ions up to saturation (a) and soaked in D_2O (pure water) after implanted with 5 keV H_2^+ ions up to saturation (b). The result in Fig. 3(a) and(b) indicate that D implants are completely replaced by H atoms, while H implants are not replaced at all. Although comparison between these results is not quantitatively because the nature of distilled water and pure water are different indeed, it indicates a great difference in the exchange between hydrogen isotopes.

Secondly, the specimens were exposed to H_2O-vapor (or D_2O-vapor) at 20 °C after 5 keV D_2^+(or H_2^+) saturation implantation. Fig. 4 shows the time variation of the concentrations of D and H which were estimated from the peak area of D or H in the ERD spectra. Fig. 4 indicates that more than 20% of D implants (marked by ○) are replaced by exposure to H_2O-vapor for 30 minutes and H implants (marked by ▲) are not replaced by exposure to D_2O-vapor at all, even if it stands 7 hours later. Judging from the initial slope, it is found that the exchange coefficient of D for H (4.6×10^{12} /cm^2•s) is about a hundred times as great as that of H for D (4.6×10^{10} /cm^2•s). This result indicates that the process of exchange of D for H is not explained by model-1 in Fig. 5; dissociative absorption of H_2O molecule at the surface, diffusion of H into the bulk, exchange of D for H, diffusion of D to the surface, recombination of HDO molecule at the surface. In Fig. 5, model-2 is proposed to explain this great difference in exchange of hydrogen isotopes; dissociative absorption of H_2O molecule, diffusion of H, bulk recombination due to HD molecule formation and trapping of H. According to this model, it is expected that diffusion or dissociation contribute to the great difference in isotopes exchange.

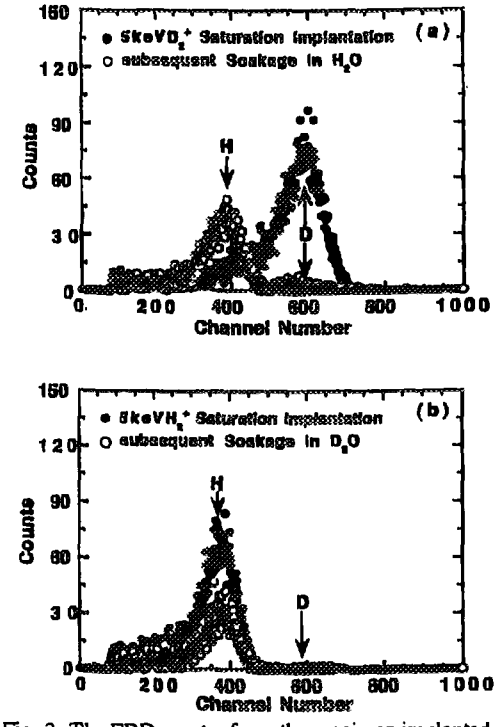

Fig. 3. The ERD spectra from the specimen implanted with 5 keV D_2^+ ions up to saturation and subsequently soaked in solution of H_2O (a) and implanted with 5 keV H_2^+ ions up to saturation and subsequently soaked in solution of D_2O (b).

Thirdly, in order to investigate the replacement process of model-2 in detail, the retention of H^+ and D^+ ions simultaneously implanted into the specimen was measured. The retention curves are shown in Fig. 6, which indicates that the retained number of H and D increase in a same way in the beginning, and hereafter that of H saturates faster than that of D. And also, the D/H concentration ratio of hydrogen isotopes retained in the oxide ceramics is about 1.3. This fact indicates that D retained in the specimen is released harder than H. It is ascribed to competition among recombination reactions of H-D, H-H and D-D in the H and D simultaneous implanted region [6]. From the above result, it has been concluded that the bulk recombination brings opposite effect to the anomalous difference in hydrogen isotopes exchange observed experimentally.

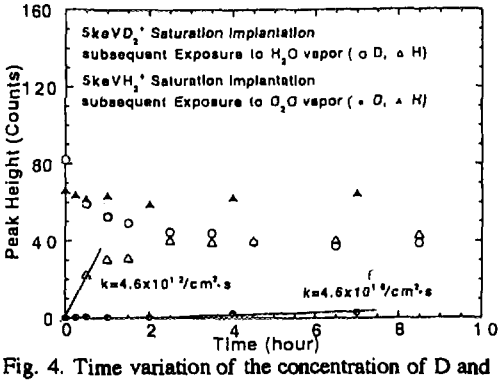

Fig. 4. Time variation of the concentration of D and H retained in $SrCe_{0.95}Yb_{0.05}O_{3-\delta}$ by saturation implantation; when exposed to vapor of H_2O and D_2O at room temperature, respectively.

Finally, in order to investigate the effect of diffusion

on the anomalous hydrogen isotopes exchange, 0.5 keV D_2^+ ions were bombarded on the specimen which had been already implanted with 5 keV H_2^+ ions up to saturation and vice versa. The time variation of the retained number of H and D are shown in Fig. 7(a) and (b), respectively, Fig. 8(a) and (b) show the ERD spectra in the beginning and at the end of irradiation. Fig. 7(a) indicates that the retained number of H rapidly decreases in the beginning of D_2^+ irradiation and hereafter gradually decreases. The retained number of D gradually increases with increasing the $H2^+$ irradiation. After 800 minutes irradiation, the retained number of H and D attain at equilibrium. Fig. 7(b) is different from Fig. 7(a) after 800 minutes, where the retained number of D continues to decrease and H continues to increase. Both initial rapid decays of the H implants in Fig. 7(a) and D implants in Fig. 7(b) are not caused by the diffusion effect, but by the direct effect of ion irradiation on replacement in the region which corresponds the depth distribution of 0.5 keV D_2^+ and 0.5 keV H_2^+ ions. From the graphite data [7], the decay amount of the H implants in the region by D_2^+ ion irradiation is expected to larger than that of the D implants by $H2^+$ ion irradiation due to the larger mass ratio of the ion implants. Therefore, the diffusion effect should be obtained from the difference between the decay curves in Fig. 7(a) and Fig. 7(b) and those induced by the direct effect of irradiation. Furthermore, Fig. 8(a) indicates that H decrease takes place only near the surface as seem from the difference the ERD spectra in the beginning and at the end of irradiation. On the other hand, it is seen from Fig. 8(b) that D decrease takes place over the whole depth. The equilibrium in the decay curve of H implants in Fig. 7(a) and the decay curve H implants limited only to the near surface in Fig. 7(b) can be regarded to indicate that the decay curve of H implants in Fig. 7(a) is caused by the direct effect of D_2^+ irradiation and hardly include the diffusion effect.Since the decay of H implants due to the direct effect of irradiation is larger than that of D implants, this interpretation means that the continuous and gradual decay of D implants during prolong irradiation is ascribed to the diffusion of H from the 0.5 keV H_2^+ implanted region, which is very consistent with the result in Fig. 4. The quantitative difference in the isotopes replacement will be estimated in future. And also the contribution of the dissociative absorption on the isotopes replacement will be quantitatively investigated with exposure of the specimen to H_2O and D_2O vapor under low pressure conditions.

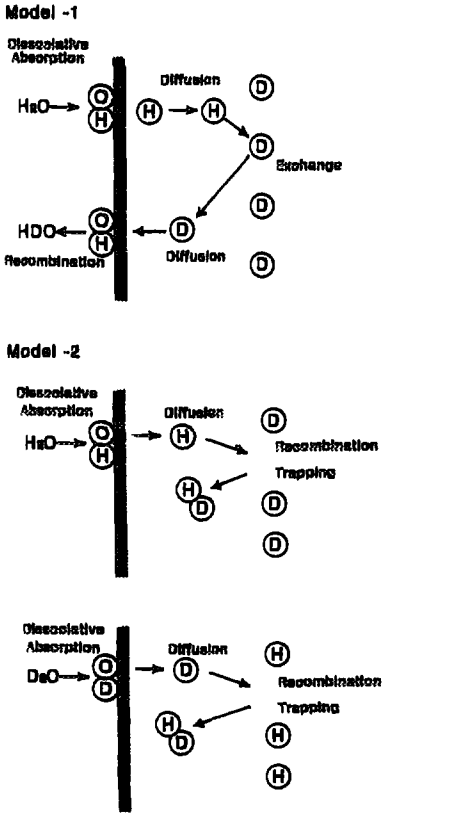

Fig. 5. Schematical models for exchange of hydrogen isotopes in $SrCe_{0.95}Yb_{0.05}O_{3-\delta}$; model-1 represents a conventional process and model-2 a new one proposed in this work.

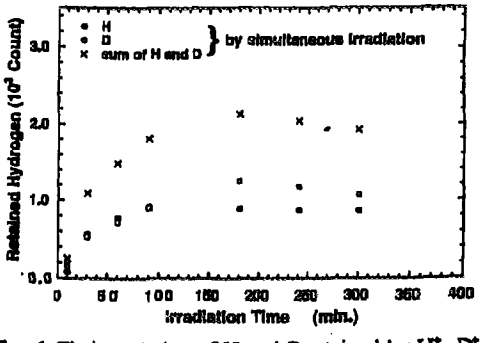

Fig. 6. Time variation of H and D retained by H^+, D^+ simultaneous irradiation.

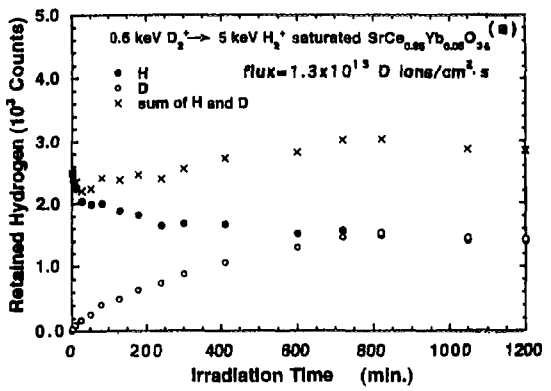

Fig. 7. Time variation of hydrogen isotopes exchange; exchange of 5 keV H_2^+ implants by 0.5 keV D_2^+ irradiation (a) and exchange of 5 keV D_2^+ implants by 0.5 keV H_2^+ irradiation (b).

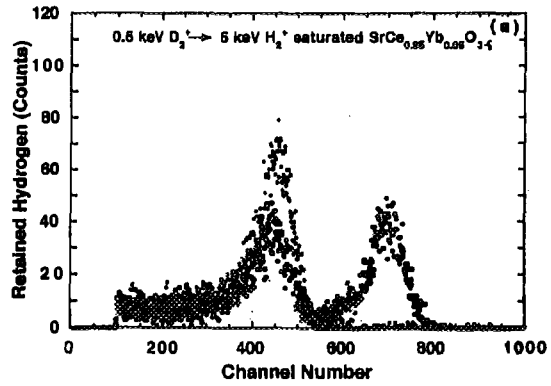

Fig. 8. The ERD spectra for 5 keV H_2^+ implants before and after irradiation with 0.5 keV D_2^+ ions (a) and 5 keV D_2^+ implants before and after irradiation with 0.5 keV H_2^+ ions (b).

Summary

The concentration change of D and H implanted into the specimen, $SrCe_{0.95}Yb_{0.05}O_{3-\delta}$ by soakage in water (H_2O, D_2O) and exposure to water vapor (H_2O, D_2O) irradiation with H_2^+, D_2^+ ions was measured by the ERD technique, in order to investigate exchange of D for H and of H for D was observed.

1. When the specimen was soaked in water after the saturation implantation, H implants were not replaced at all for D although D implants were completely replaced by H atoms.
2. When the specimen was exposed to water vapor after the saturation implantation, the coefficient of exchange of D for H was about a hundred times as large as that of H for D. This great difference of the hydrogen exchange in oxide ceramics was observed for the first time in the present study. The isotope exchange is reasonably explained on a model of subsequent reaction; dissociative absorption of water molecule at the surface, hydrogen diffusion and bulk recombination due to molecule formation. It suggests that diffusion or dissociative absorption contribute to the isotope difference of hydrogen exchange.
3. The concentration measurement of H and D retained in the specimen by H^+, D^+ simultaneous irradiation indicates that the D/H centration ratio in the steady state was about 1.3. The result indicates that the bulk recombination brings an opposite effect of isotope difference to the in hydrogen exchange observed experimentally.

4. The concentration measurement of 5 keV H_2^+ implants in the specimen by 0.5 keV D_2^+ irradiation indicates that the retained number of H decreases rapidly in the beginning and there after attain at equilibrium and the retained number of D implanted increases and also attain at equilibrium. on the other hand, the concentration measurement in vice versa case indicates that the retained number of D decreases rapidly in the beginning and hereafter continues to decrease gradually and the retained number of H implanted also continues to increase. These results indicate that the diffusion process does not appear in the exchange of H for D, but in the exchange of D for H, namely, the diffusion may play an important role in the great isotope difference in hydrogen exchange.

References

1) H. Iwahara : Solid States Ionics 77, (1995) 289 and 86-88, (1996) 9.
2) S. Shin, H. Huang, M. Ishigame and H. Iwahara : Solid States Ionics 40/41, (1990) 910.
3) N. Matsunami, T. Yajima and H. Iwahara : Nucl. Insts. Meth. B65, (1992) 278.
4) H. Uchida, H. Yoshihara, T. Esaka, S. Ohisu and H. Iwahara : Solid States Ionics 36, (1992) 278.
5) B. Tsuchiya and K. Morita : J. Nucl. Mater. 227, (1996) 195.
6) B. Tsuchiya and K. Morita : J. Nucl. Mater. 241-243, (1997) 1065-1070.
7) B. Tsuchiya and K. Morita : J. Nucl. Mater. 226, (1995) 293.

Experimental loop at ENEA for compatibility and hydrogen permeation studies relevant to fusion reactors

Marie Françoise Maday, L. Bimbi, A.Iasonna, A.Mariani, V.Pietrelli, B Tranchina and G.Zummo

ENEA-CRE-Casaccia, Dip. Innovazione, Div. Nuovi Materiali
C.P. 2400- 00100 Rome- Italy

POTENTIAL FIELDS OF ACTIVITY

- To study the performances of various helium cooled pebble bed blanket options for DEMO, by varying one or more factors of the combination: structural material/ breeder/ cooling and extracting gas chemistry.
- To evaluate the viability of the He+H_2O coolant/alloy 800 combination proposed for tritium permeation reduction through DEMO steam generator.
- To compare the efficiencies of candidate tritium permeation barriers on structural materials (required in ITER)

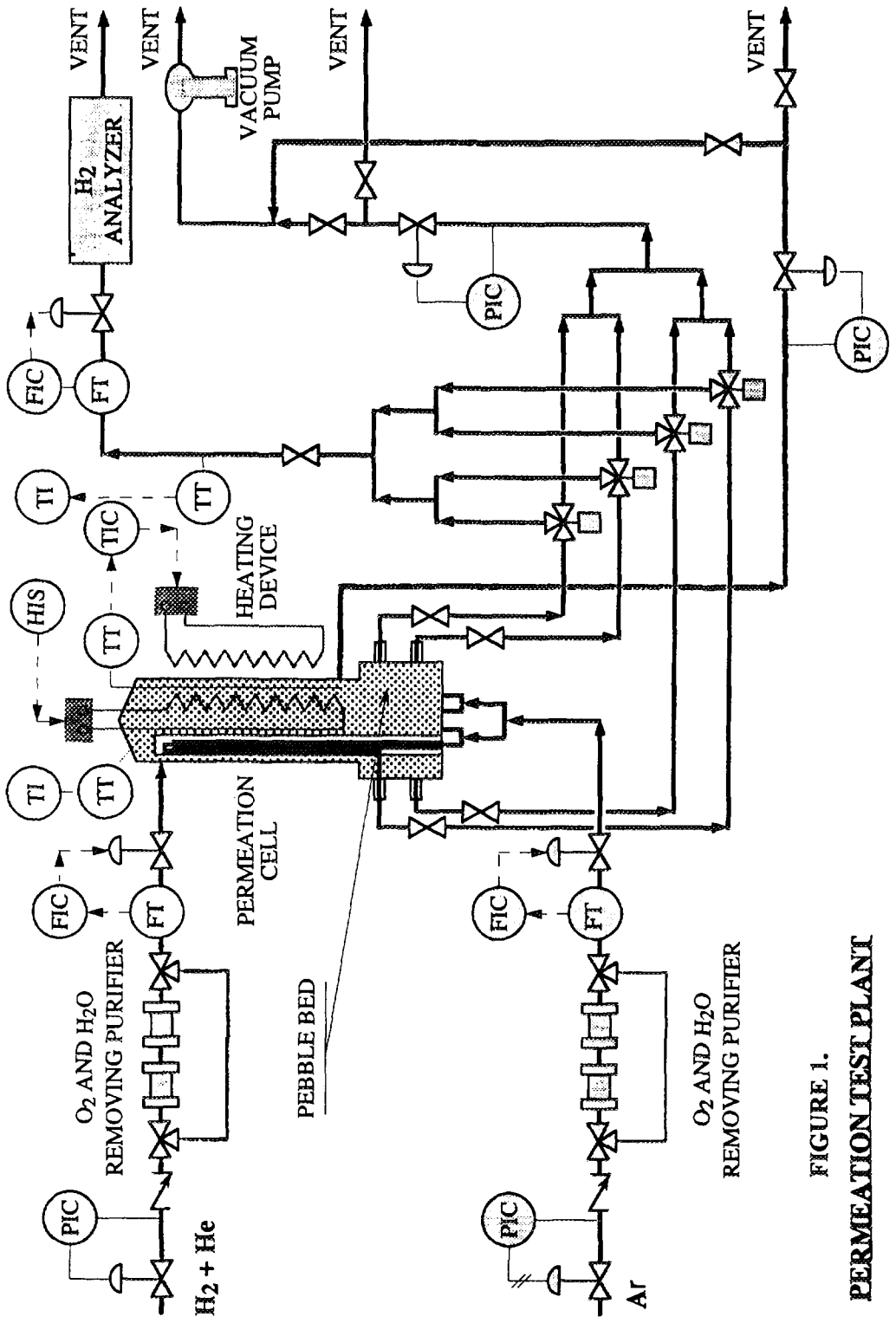

FIGURE 1.
PERMEATION TEST PLANT

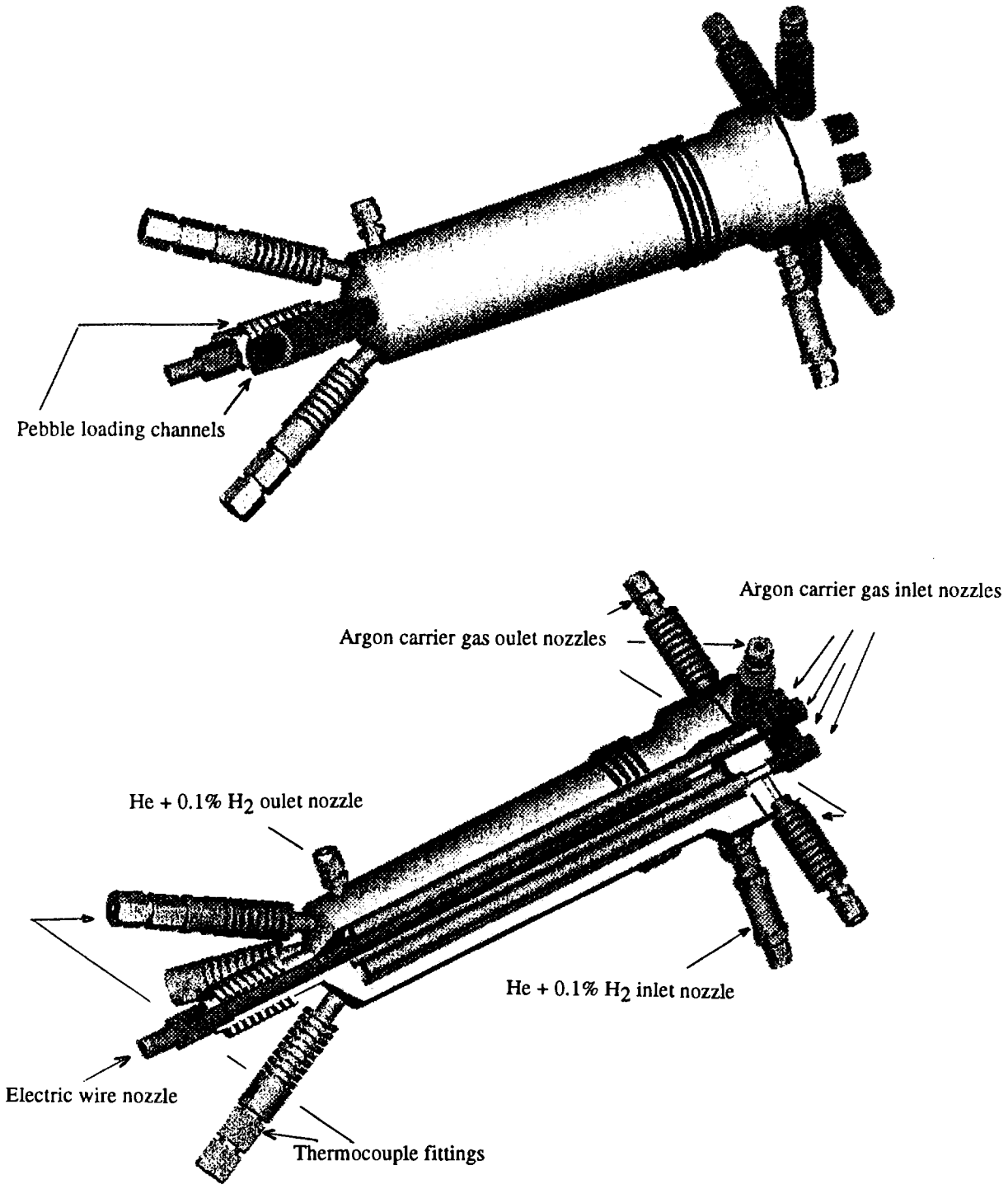

Figure 2: a) Overview of the permeation cell. b) Permeation cell cross section showing the tubes as testing specimens.

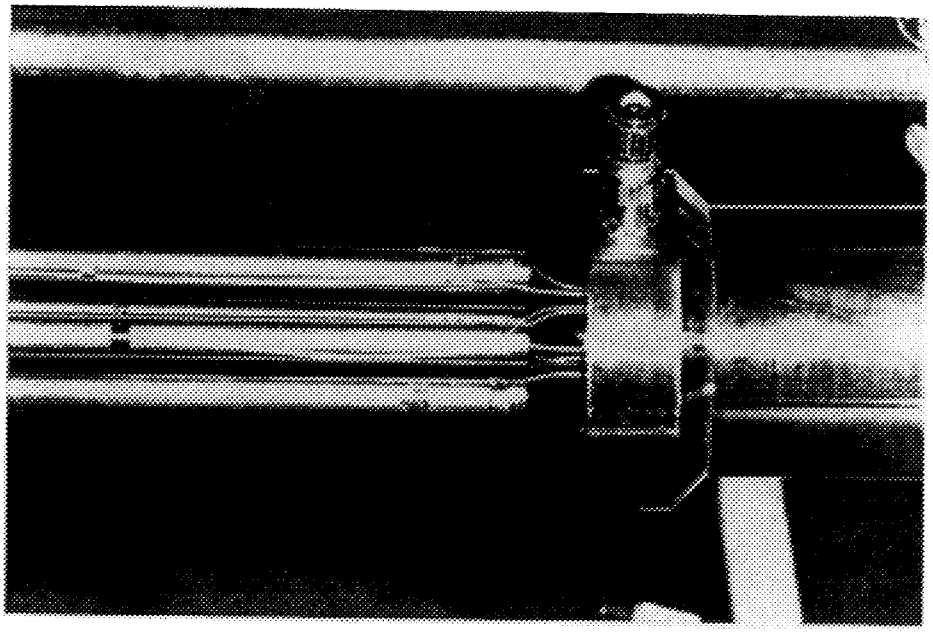

b

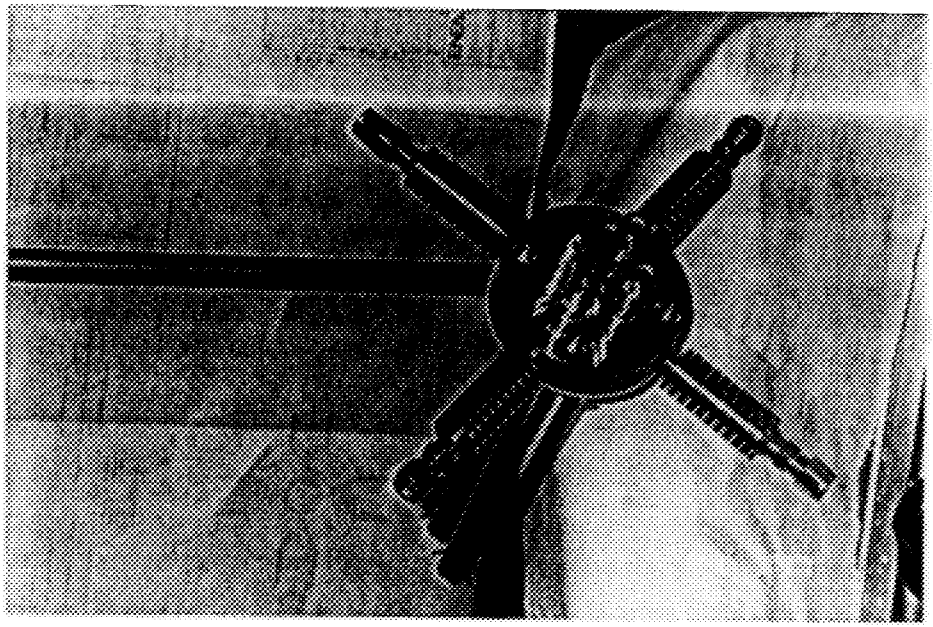

a

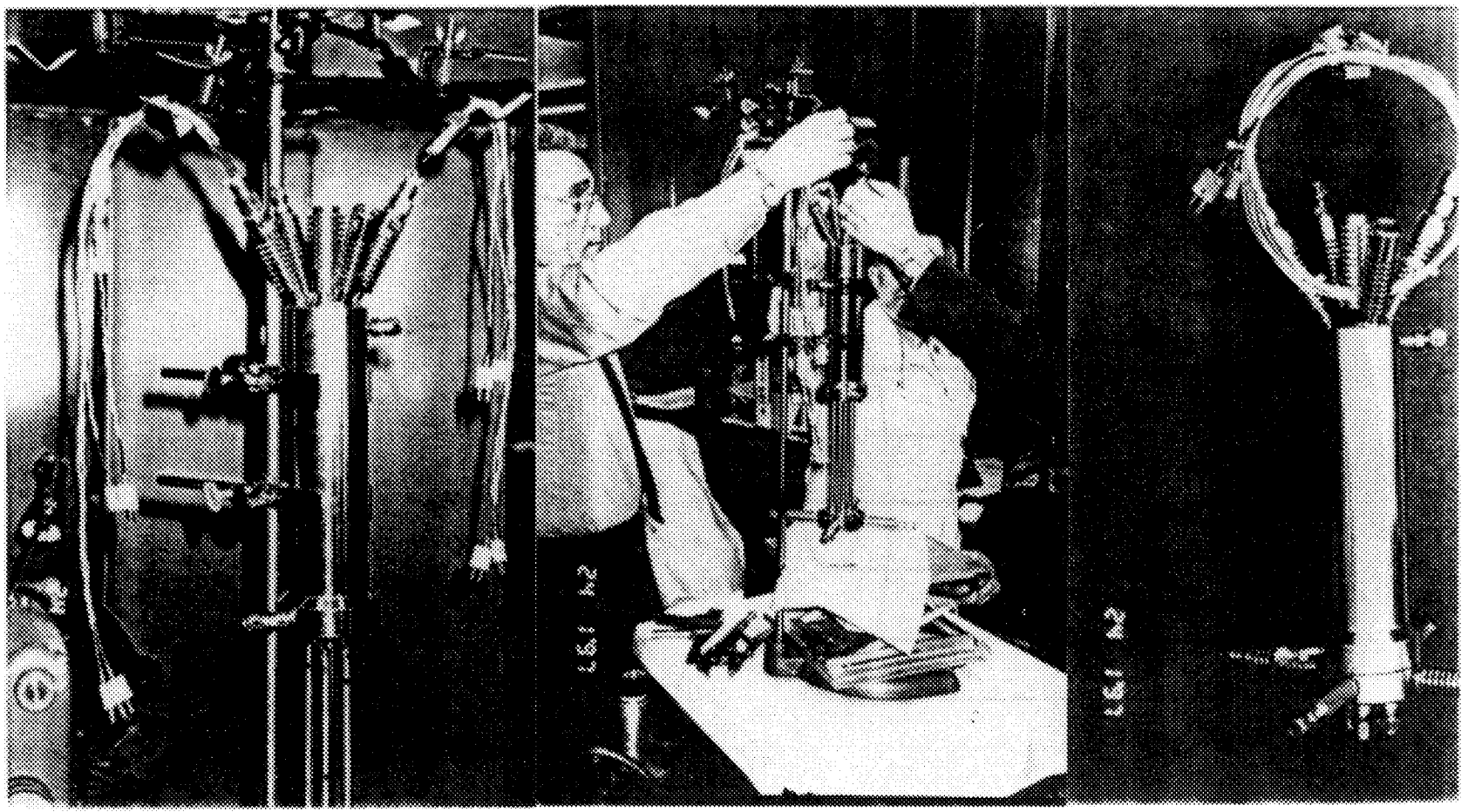

Figure 11: Photographs of a) the tube holding flange, b) the thermocouple arrangement c) thermocouple external wires, d) tube installation phase inside the cell body e) the completed cell

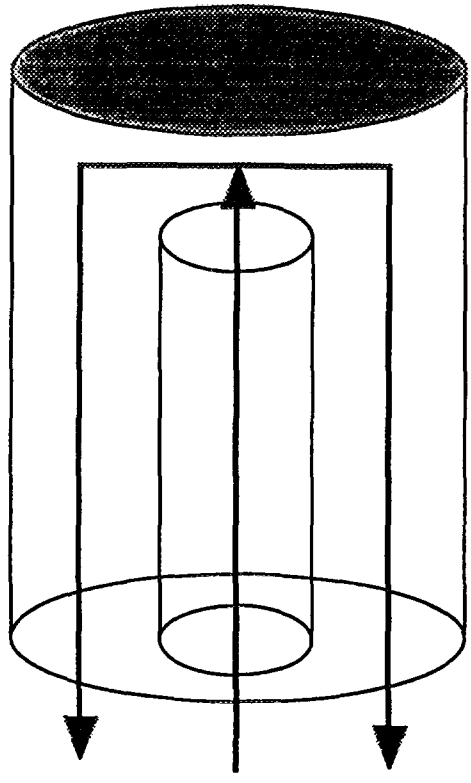

Figure 4: Schematic drawing of a tube specimen with inner Ar carrier gas flow

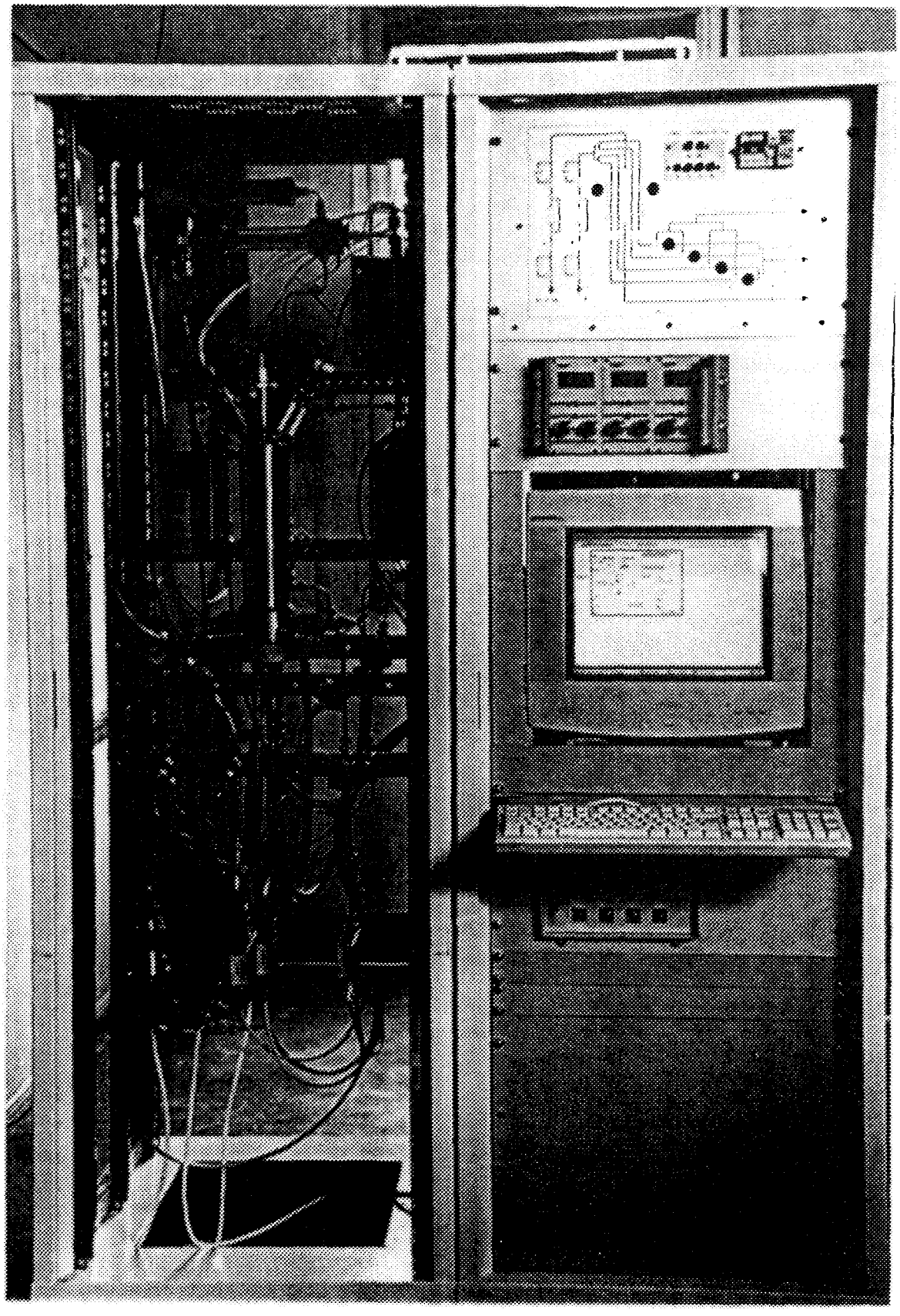

SESSION 5

Blanket Design

CBBI-6
Mito, Japan
Oct. 22 - 24, 1997

Breeding Blanket Design for ITER and Prototype (DEMO) Fusion Reactors and Breeding Materials Issues

H. Takatsu and M. Enoeda
Blanket Engineering Laboratory
Naka Fusion Research Establishment
Japan Atomic Energy Research Institute

0. Preface

Current status of the designs of the ITER breeding blanket and DEMO blankets is introduced placing emphasis on the breeding materials selection and related issues. The former design is based on the up-to-date design activities, as of October 1997, being performed jointly by Joint Central Team (JCT) and Home Teams (HT's), while the latter is based on the DEMO blanket test module designs being proposed by each Party at the TBWG (Test Blanket Working Group) meetings.

The following executive summary is supplemented by the OHP copies of the handout attached.

1. ITER Breeding Blanket

The design of the ITER breeding blanket, to be installed at the second phase (Extended Performance Phase) of the ITER operation to breed tritium needed for its operation, is being designed to provide both of high tritium breeding capability (TBR > 0.8) and enough shielding performances under the conditions that it has the same external geometry, the same structural material (type 316 LN-IG stainless steel) and the same cooling water conditions (4 MPa and 150/190°C for pressure and inlet/outlet temperature, respectively) as the shielding blanket to be installed at the first phase (Basic Performance Phase) of the ITER operation. The design shown in the ITER/DDR (Detailed Design Report) has a layered configuration (in the radial direction) with the breeder pebble bed layers (Breeder : Li_2ZrO_3 with an alternative of Li_2TiO_3) sandwiched by porous beryllium block layers. Li_2ZrO_3 has been selected as a reference breeder material because of its better tritium release characteristics at lower temperatures below 400°C, though the data is very limited, and estimated tritium inventory is well below 100 g.

Recently this design has been changed in a fashion that the beryllium form is replaced from "block" to "binary pebble bed" and the internal configuration of the breeding region from "radial layer" to "toroidal layer". These design modifications can be justified by larger R&D basis in the HT's and DEMO relevancy (for the form of beryllium) and by better accommodation against a large inner pressure rise (4 MPa) anticipated in the case of in-module LOCA event (for the internal configuration). In this design breeder pebbles are housed in a number of pins (BIP), sorrounded by binary beryllium pebble beds. Preliminary evaluation of the net TBR performed by EUHT (TBR~0.9) shows this design satisfies well the TBR requirement.

R&D issues have been already addressed by JCT. The proposed R&D list are categorized into a) Ceramic breeder material development, b) Beryllium material development, c) Mockup neutronics experiments, d) Small scaled engineering experiments, d) Fabrication and testing of medium scaled modules, e) Fabrication and testing of full scaled module and f) Fabrication and testing of small blanket mockup in fission reactor. Among them, high priority has been laid on evaluation of tritium release properties on Li_2ZrO_3 at lower temperature (200 - 400°C), which is unique to the ITER breeding blanket, and those of Li_2TiO_3 at wider temperature ranges concerned. Some of the above R&D's are common to DEMO blanket and are expected to be covered by

domestic R&D efforts by each Party. Some of the ITER specific R&D's have already been launched by some HT's, including tritium release experiments from Li2TiO3 at lower temperatures.

2. DEMO Blanket

Module testing of the DEMO blanket in ITER is recognized as a very important near-term milestone in the course of DEMO blanket development in each Party, and from such a sense, extensive discussions have been made within the TBWG activities. TBWG has reviewed the DEMO blanket designs proposed by each Party, elaborated module testing plan in ITER, and developed test module designs including ancillary systems. The testing plan and the test module designs are consistent with the current ITER operation schedule and the ITER machine/plant designs. TBWG has also reviewed the R&D plans of each Party to promote it and to enhance international collaboration where needed and possible.

Each Party has proposed two types of the DEMO blanket concepts, based on their own national program, and they are summarized below by the combination of structural materials/breeding material/coolant. All of the four Parties have an intention to develop solid breeder blanket concepts, most of which utilize the breeder and beryllium in the form of pebble bed, and the differences among them are the breeder material selection, see below, and the internal configuration either radial, toroidal or poloidal layer.

Party	DEMO blanket concepts	Solid Breeder
EU	Ferritic Steel/Solid breeder/He	Li_4SiO_4
	Ferritic steel/LiPb/Water	
JA	F82H/Solid Breeder/Water	Li_2O
	F82H/Solid Breeder/He	Li_2O
RF	Ferritic Steel/Solid Breeder/He	Li_4SiO_4
	V-alloy/Li/Li	-
US	Ferritic Steel/Solid Breeder/He	Li_2TiO_3
	V-alloy/Li/Li	-

Current ITER design has three ports, among twenty, fully devoted to the DEMO blanket module testing, and TBWG and JCT have elaborated a tentative port assignment plan based on the cooling system, namely, one for He-cooled concepts, one for water-cooled concepts and the other for a combination of Li- and He-cooled concepts. Each party is encouraged to develop their own concept by their own domestic R&D's or international collaboration so that they can provide the test modules in time of the ITER operation with enough R&D data base.

Current status of the solid breeder DEMO blanket development is the following, more or less common to all of the four concepts proposed by four Parties. Fabrication technologies of the solid breeder pebble have been well developed so far, including sol-gel method and melt spray method, and characterization and irradiation tests are now under way. BEATRIX-II Program has confirmed good tritium release characteristics and soundness of Li_2O and Li_2ZrO_3 under the neutron irradiation up to 5% Li-burnup, and EXOTIC Program has produced promising data for Li_4SiO_4 and other candidate breeders. Higher irradiation plan over 10% Li-burnup is under discussion. Thermal cycle durability, mass transfer properties and compatibility tests have been performed in the course of breeder materials evaluation.

One of the key issues in the solid breeder DEMO blanket development is the temperature controllability of the breeder pebble bed, and from this viewpoint, evaluations of the thermal and mechanical properties of the pebble bed both for breeder and beryllium are essential, and extensive R&D's have been performed in each Party on equivalent thermal conductivity measurement and mechanical performance evaluation for the packed

bed. And further collaborative and comparative experiments are being planned within the framework of IEA Collaboration on Fusion Reactor Nuclear Technology.

Breeding Blanket Design for ITER and Prototype (DEMO) Fusion Reactors and Breeding Materials Issues

H. Takatsu, M. Enoeda (JAERI-Naka)

6th Internat. Workshop on
Ceramic Breeder Blanket Interactions
Sangyo-kaikan, Mito, Japan
Oct. 22 - 24, 1997

Contents

Introduction & Background

1. ITER Breeding Blanket

- Design changed three weeks ago
  (JCT Internal Meeting @San Diego, Oct. 4, '97)
- Be-form from "block" to "binary-pebble-bed"
- Internal config. from "raidal" to "toroidal" layer
- R&D issues addressed by JCT

2. DEMO Blanket

- ITER "Test Modules" as a near-term target
- Four solid breeder concepts from four Parties
- "Test Module" design in ITER FDR (Final Des. Report)
- R&D's by each Party with possible collaboration
  by IEA-IA-FM and NT (under discussion)

ITER Breeding Blanket Design

1. Conditions/Requirements
   - SS316LN-IG/Water (150/190°C)
   - Same geometry as Shielding Blanket (BPP)
   - Enough shielding capability and TBR > 0.8

2. Design change
   - Be : (porous) block → Binary pebble bed
     - Larger R&D basis in HT's
     - DEMO blanket relevancy
   - Configuration : radial layer → toroidal layer
     - Higher stiffness @ in-module LOCA event
   - TBR ～ 0.9

ITER Breeding Blanket Design (Cont'd)

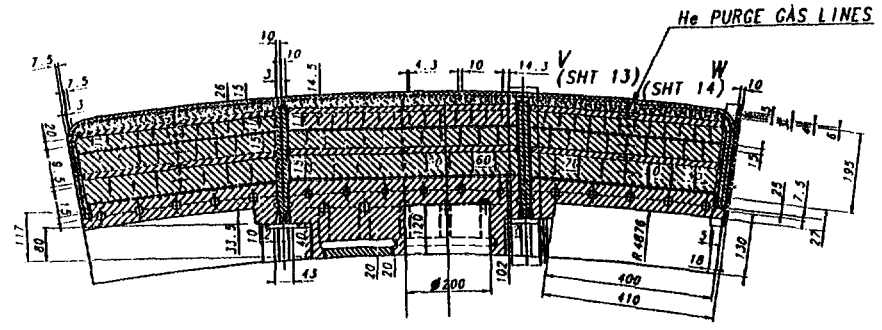

(a) DDR Design

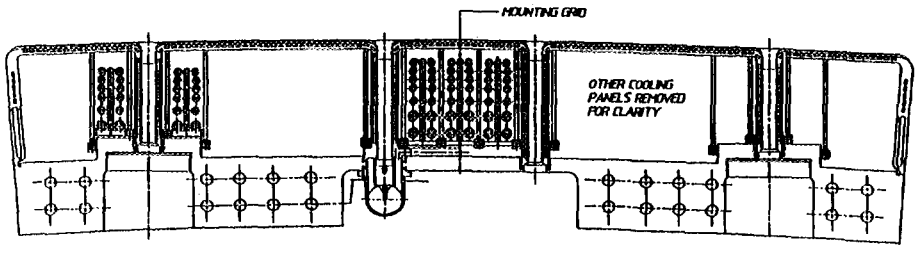

(b) FDR Design

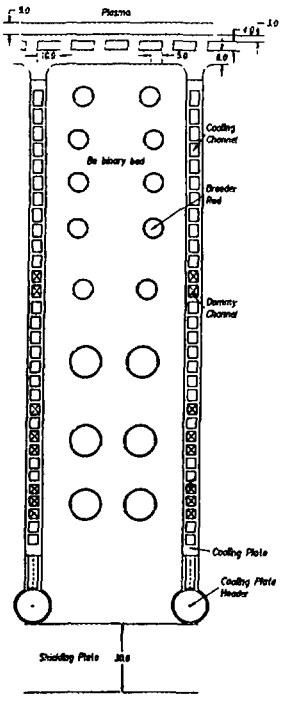

Detail (b)

Breeder Material Selection - ITER Breeding Blanket

- Material selection
  - Reference : Li2ZrO3
  - Alternative : Li2TiO3
- Form
  - Pebble
  - 90% 6Li enrichment
- Rationale
  - Lower T-inventory at lower temp. range
  - Needs further qualification

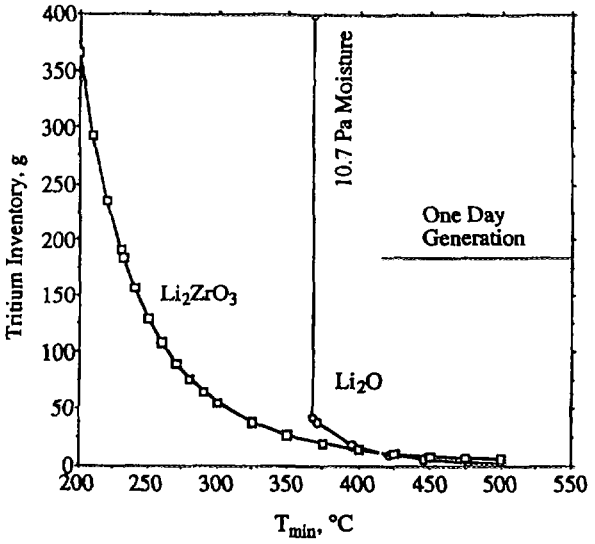

M. Billone et al., CBBI-Kyoto (1995) ets.
N. Roux et al., CBBI-Kyoto (1995).

ITER

R&D Requirements for The ITER Breeding Blanket

A - Ceramic Breeder Material Development

Reference material: lithium metazirconate (Li_2ZrO_3)
Alternative material: lithium metatitanate (Li_2TiO_3)
Material form: pebbles and pellets

1 Tritium Release Properties
- In-pile tritium release tests at low temperature (200-400°C) for Li_2ZrO_3 and the full temperature range for Li_2TiO_3
- Model development for tritium release including the low temperature range
- Experiments to provide information on hydrogen isotope adsorption, solubility, diffusion/desorption, and precipitation as a function of temperature and hydrogen partial pressure.

2 Fabrication
- Development of low cost industrial fabrication method for the Li_2ZrO_3 pebbles and both forms of Li_2TiO_3

3 Fabricated Material Characterization
- Impurity content, porosity, and grain size for both forms
- Sphericity and size distribution for pebble form

4 Thermal and Mechanical Properties of the Fabricated Material
- Temperature and porosity effects
- Thermal stability, specific heat, thermal conductivity, thermal expansion , Young's modulus, Poisson ratio, ultimate compressive strength, ultimate tensile/bending strength, thermal creep, thermal shock resistance, compatibility with 316LN SS, chemical reactivity with water

YG/Garching October, 1997

ITER

A - Ceramic Breeder Material Development (continued)

5 Irradiation Behavior Confirmation of the Fabricated Material
- Temperature and porosity effects
- Tritium release properties (capsules and in-situ experiments), swelling, integrity, and irradiation impact on thermal and mechanical properties

YG/Garching October. 1997

DEMO Blanket Testing in ITER - Tentative Planning

(1) Background
- Based on discussion in TBWG (Test Blanket Working Gr.)
- Documented in ITER DDR (Detailed Design Report) issued in Dec. '96

(2) Tentative Planning
- Started from the early stage of BPP and continued till End/EPP
- Three ports devoted to DEMO Blanket testing

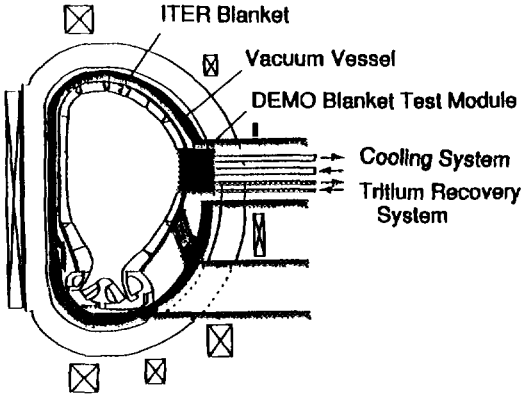

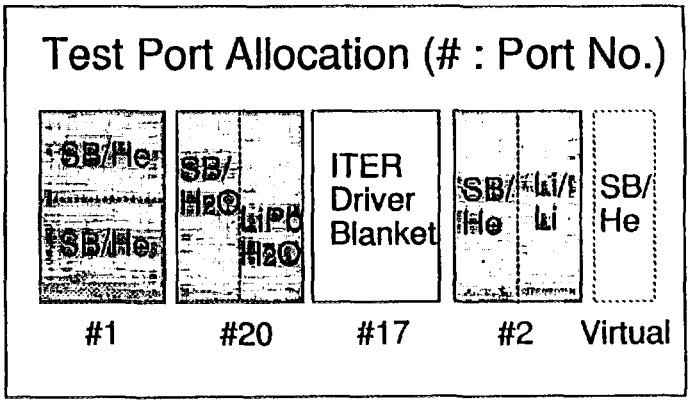

DEMO Blanket Testing in ITER - Proposal from Parties

Party	Breeder	Structural Material	Coolant
EU	Solid Breeder	Ferritic-Martensitic Steel	He gas
	Liquid Pb-17Li		High-T Water
JA	Solid Breeder	Reduced Activation Ferritic Steel F82H*	High-T Water
			He gas
RF	Solid Breeder	Ferritic Steel	He gas
	Liquid Li	V-alloy	Liquid Li
US	Solid Breeder	Ferritic Steel	He gas
	Liquid Li	V-alloy	Liquid Li

* Ti-Al intermetallic Compound and SiC/SiC Composite are advanced Alternatives for He-Cooled Concept

DEMO Blanket Concept for ITER Module Testing - JA Proposal with Water Cooling

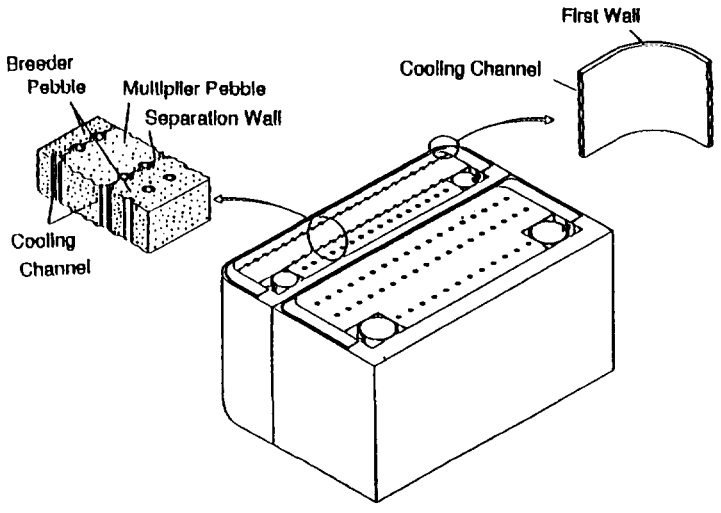

DEMO Blanket Concept

Reference DEMO Reactor Design
- SSTR-1

Main Parameters
- Coolant : Pressurized water (285/325°C, 15 MPa)
- Structure : F82H
- Breeder : Li_2O Pebble
- Multiplier : Be Pebble
- T-recovery : He purge gas

Main Features
- Higher integrity (pebble form)
- Larger TBR (layered configuration of breeder/multiplier)
- Higher safety (less reactive)
- Less R&D needs (PWR technol.)

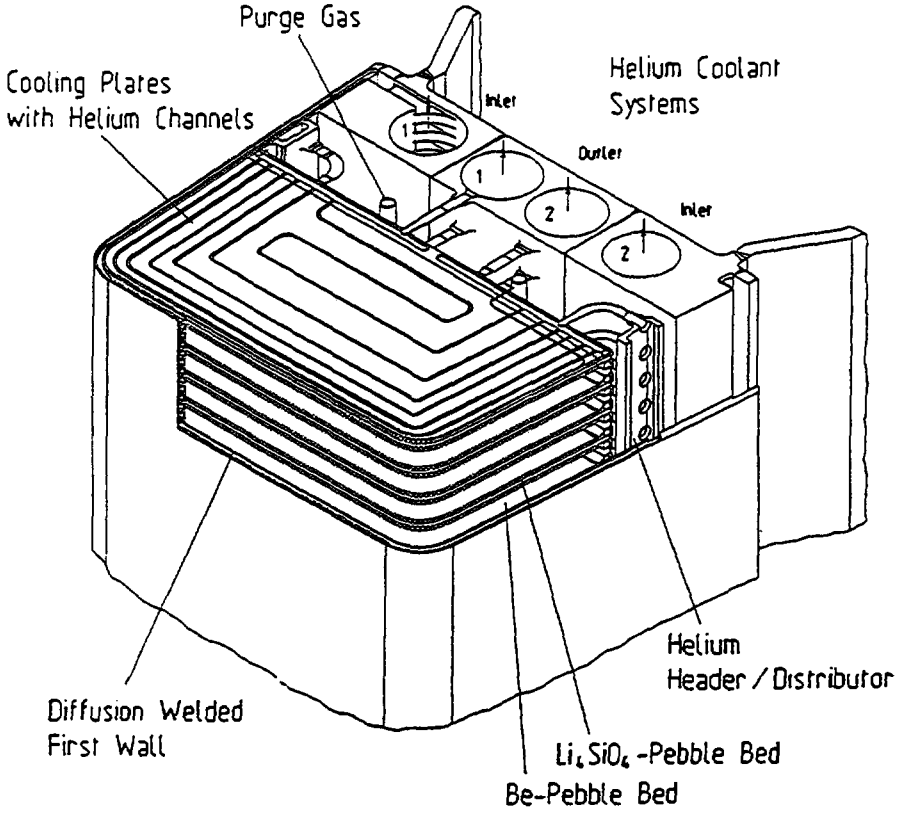

Figure 2.0.2-1 Isometric view of a poloidal portion of the DEMO outboard blanket segment around the torus equatorial plane

Fig. 2.0.2-1 shows an isometric view of the poloidal portion of the DEMO HCPB outboard blanket segment around the torus equatorial plane, where the highest power deposition, highest stresses and temperatures are expected. This portion of the HCPB blanket shall be tested in ITER. The HCPB DEMO blanket exhibits the following basic design features:

1. The ceramic breeder pebbles and the neutron multiplier are contained in a tightly closed box called blanket box.
2. The plasma facing wall of the blanket box is the first wall (FW). The back side of the blanket box is formed by a plate which contains the poloidal helium feeding and collecting manifolds.
3. The blanket box and the blanket structure are cooled by helium at 8 MPa. The coolant flows in series through the blanket box and the blanket structure.

Ceramic Breeder and Beryllium Development - Status

- Development of Pebble Fabrication Methods and Characterization Almost Completed for both Breeder and Beryllium
- IEA/BEATRIX-II Program confirmed (@Li2O/Li2ZrO3, <5% Li-Burn-up)
  - Sound Tritium Release Characteristics
  - Integrity of Ceramic Breeder
- Further Irradiation Tests of Ceramic Breeders up to 12% Li-Burn-up being planned (IEA, Phenix)
- Thermal Cycle Durability Tests Confirmed Integrity of Li2O up to 10^4 cycles

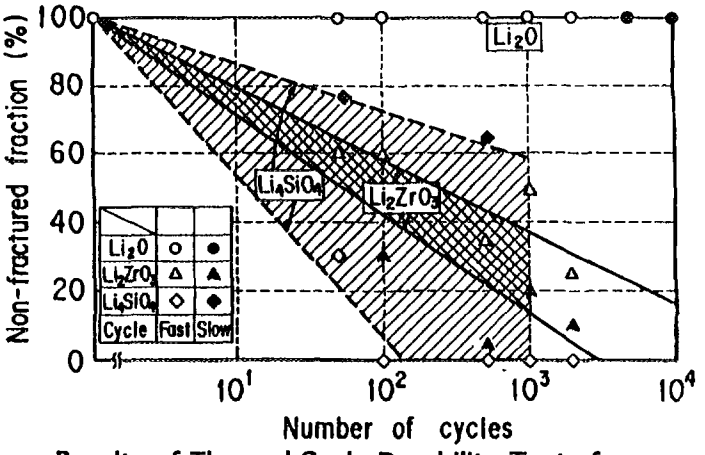

Results of Thermal Cycle Durability Tests for Three Kinds of Ceramic Breeder Pebbles

Fabrication Development of Ceramic Tritium Breeder

	Melting Granulation Method	Rotating Granulation Method	Sol-Gel Method
Summary of Fabrication	LiOH Li_2CO_3 Melting → air Dropping → Alcohol	Rolling, Li_2O Powder	PVA, $LiNO_3$ Mixing → Dropping → Alcohol
Tritium Breeding Materials	Li_2O	Li_2O γ-$LiAlO_2$ Li_2ZrO_3 Li_2TiO_3	Li_2O Li_2TiO_3
Development Period	'92	'92～'97	'94～'98
Sphericity	Excellent	Good	Good
Impurity	Excellent	Good	Good
Mass Production	Good	Good	Excellent
Cost	Good	Good	Excellent
Reprocessing	Bad	Bad	Excellent

Possible Areas of Cooperation between Parties on Breeding Blanket R&D
- based on TBWG discussion -
(1) Ceramic Breeder Pebble Bed

No.	Sub-area	What	C*	Who	Where	When	Comments
1	Pebble Fabrication Technology						
2	Basic Reserach on Tritium Release Mechanism						
3	Characterisation of Pebbles						
4	Engineering-oriented Material Tests of Pebbles						
5	Irradiation Tests in Fission Reactors ("BEATRIX") and PIE						
6	Out-of-pile Eng. Tests of Pebble Bed						

* C : Category of Scope (I : Information Exchange, M : Mutual Exp., J : Joint Exp.)

Summary

1. ITER Breeding Blanket

- Design changed to use Be in a binary pebble bed
- R&D issues addressed with a high priority on T-release from breeder materials at lower temp.

2. DEMO Blanket

- Test module design progressed, to appear in FDR
- R&D issues listed and on going by each Party on
  - Develop. of pebble bed fabrication technol.
  - Characterization of pebble bed
  - Irradiation of pebble bed
- Collaboration (@IEA-FM and NT) under discussion

SESSION 6

Ceramic Breeder Properties (2)

COMPILATION OF PROPERTIES DATA FOR Li_2TiO_3

Nicole ROUX

COMMISSARIAT A L'ENERGIE ATOMIQUE - Centre de SACLAY
DTA/CEREM/CE2M/LECMA
91191 - GIF/SUR/YVETTE Cédex - France

ABSTRACT

Properties data obtained at CEA for Li_2TiO_3 are reported. The compilation includes : stability of Li_2TiO_3 β phase, specific heat, thermal diffusivity, thermal conductivity, linear thermal expansion, thermal creep, interaction with water and acid.

1 - INTRODUCTION

Lithium titanate (Li_2TiO_3) recently emerged as being an attractive tritium breeding ceramic for fusion reactor blankets. Significant advantages are low activation under neutron irradiation, and good tritium release behaviour to low temperatures. However, the data base still limited needs to be completed in order to ascertain that this ceramic fulfills major requirements of current blanket concepts.

Li_2TiO_3 is being investigated at CEA. Current focus is placed on the development of pebbles as ceramic breeder for the European helium-cooled pebble bed DEMO blanket concept.

Part of the R and D work was reported in [1,2]. Several properties data yet unpublished are compiled in this paper.The compilation includes :

- Stability of the monoclinic phase
- Thermal properties, i.e., specific heat, thermal diffusivity, thermal conductivity, linear thermal expansion
- Thermal creep
- Interaction of Li_2TiO_3 with water and acid medium.

The composition of all Li_2TiO_3 specimens referred to in this work is 0.95 Li_2TiO_3 + 0.05 TiO_2.

2 - PHASE STABILITY OF β MONOCLINIC Li_2TiO_3

According to literature [3] three crystal phases, i.e., α, β and γ are identified for Li_2TiO_3. The α cubic phase transforms irreversibly into the β monoclinic phase at 300°C. The β phase transforms reversibly into the γ cubic phase at 1150°C. The densities of the α, β and γ phases are 2 $g.cm^{-3}$, 3.43 $g.cm^{-3}$, and 2.57 $g.cm^{-3}$ respectively; the lithium densities are 0.25 $g.cm^{-3}$, 0.43 $g.cm^{-3}$, and 0.32 $g.cm^{-3}$ respectively. Thus, the β phase which is the most attractive because of its highest lithium density is the stable phase at anticipated blanket operating temperatures. The temperature value of 1150°C reported in literature can be in the range of sintering temperature of Li_2TiO_3 materials fabricated by powder technology processes, depending on the material microstructural characteristics aimed at. It is preferable that the sintering temperature be lower than the phase transformation temperature so as to avoid any density change. Therefore, the β/γ phase transformation temperature was verified.

To this end, high-temperature X-ray diffraction analysis and differential thermal analysis were used.

2.1 - High-temperature X-ray diffraction analysis (HTXRD)

The study was performed with the collaboration of the Laboratoire de Cristallochimie et de Physico-Chimie du Solide at ENSCL.

X-ray diffraction patterns of Li2TiO3 powder were examined in the 27°C - 1250°C range : 27°C (start), 550°C, 950°C, 1250°C, and 27°C (end) see Fig.1.

- The X-ray diffraction pattern at 27°C indicates the presence of β Li_2TiO_3 (peaks at 2 θ = 18°, 36°, 43°6, 47°8, 57°5, 63°8, 66°8), and of TiO_2 which was expected because there is an excess of TiO_2 in the composition. Peaks at 2 θ = 39°6, 46°08 and 67°3 are Pt peaks due to the interference of the sample holder.
- The X-ray diffraction pattern at 550°C indicates the appearance of γ Li_2TiO_3 (peaks at 2 θ = 43°7 and 63°2)
- The X-ray diffraction pattern at 950°C more clearly shows the appearance of γ Li_2TiO_3
- The X-ray diffraction pattern at 1250°C shows the absence of the peaks of β Li_2TiO_3 and the presence of those of γ Li_2TiO_3.

Next, the 1100°C-1200°C range was spanned with temperature steps of 10°C. From the X-ray diffraction patterns displayed in Fig.2 the transformation is found to be complete at 1140°C. It is reversible since the X-ray diffraction patterns at 27°C (end) and 27°C (start) are identical.

2.2 - Differential Thermal Analysis (D.T.A.)

The analysis was made using the NETZSCH STA 409 thermoanalyzer. Li_2TiO_3 specimens were heated in air from room temperature to 1300°C and cooled down from 1300°C to room temperature at the rate of 6°C/minute. The D.T.A. curve in Fig.3 displays the peak of the β → γ transformation at 1170°C on heating up and of the γ → β transformation at 1150°C on cooling down indicating the reversibility of the transformation.

Both techniques confirm the reversible phase transformation of β Li_2TiO_3 around 1150°C. HTXRD indicates the onset of the transformation as low as ~ 550°C.

3 - THERMAL CONDUCTIVITY OF Li_2TiO_3

Thermal conductivity was calculated from specific heat and thermal diffusivity values. Specific heat was measured in an argon atmosphere using the DSC 111 SETARAM differential scanning calorimeter. Thermal diffusivity was measured in a helium atmosphere using the laser pulse technique. Measurements were made from room temperature to 800°C using Li_2TiO_3 pellets

12 mm in diameter and 2 mm thick [4]. Pellet density is 87% T.D which is close to the density of pebbles of current C.E.A fabrication (~ 90% T.D).

In both measurements the specimens were heated three times successively, in order to identify any difference such as that one previously observed with hygroscopic, fine-grained ceramics and which was explained by the removal of adsorbed water on the 1st heating. Results of specific heat, thermal diffusivity, and thermal conductivity as a function of temperature are displayed in Fig.4. The value of 3.45 was taken as the density of the composition 0.95 Li_2TiO_3, 0.05 TiO_2 in the calculation of thermal conductivity. Below 500°C, results are higher than those reported by Davis and Haasz [5] for a material of the same density. Thermal conductivity of candidate ceramics rank $Li_4SiO_4 < Li_2ZrO_3 < Li_2TiO_3 < LiAlO_2 < Li_2O$.

4 - LINEAR THERMAL EXPANSION OF Li_2TiO_3

Linear thermal expansion of Li_2TiO_3 was measured using the NETZSCH dilatometer type 402 E [4]. Cylindrical specimens 5 mm in diameter, 15 mm long, density 81.5% T.D were heated in air from room temperature to 800°C at the rate of 5°C/minute. Values of linear thermal expansion coefficients are :

Temperature range	Thermal expansion coefficient
300°C - 400°C	$20.3 \times 10^{-6} K^{-1}$
400°C - 500°C	$20.6 \times 10^{-6} K^{-1}$
500°C - 600°C	$21.2 \times 10^{-6} K^{-1}$
600°C - 700°C	$21.8 \times 10^{-6} K^{-1}$

The Li_2TiO_3 thermal expansion coefficient is larger than that of $LiAlO_2$ and Li_2ZrO_3 and lower than that of Li_4SiO_4 and Li_2O.

5 - THERMAL CREEP OF Li_2TiO_3

Creep characteristics of Li_2TiO_3 were investigated and compared with creep characteristics of Li_2ZrO_3.

To this end, the same test conditions were adopted, i.e., compressive stress of 50 MPa, at 600°C, in air atmosphere. Specimens characteristics are : diameter 10 mm, height 15 mm, grain size 1-2 μm, and density 84.2% T.D and 80% T.D for Li_2TiO_3 and Li_2ZrO_3 respectively.

Results of creep strain as a function of time are displayed in Fig.5. Creep strain rate of Li_2TiO_3 is larger than that of Li_2ZrO_3, namely 12.5 10^{-6} h^{-1} as compared to 1.6 10^{-6} h^{-1} for Li_2ZrO_3. This is in agreement with the higher sinterability observed for Li_2TiO_3.

6 - INTERACTION OF Li_2TiO_3 WITH LIQUID WATER AND ACID

6.1 - Interaction of Li_2TiO_3 with liquid water

This issue is of interest from a safety viewpoint under the accidental condition of ceramic breeder and coolant contact in water-cooled ceramic blankets such as ITER for example.

To investigate any interaction, specimens of Li_2TiO_3 (Li_2TiO_3 blocks, and Li_2TiO_3 particles of various sizes) were immersed in water at room temperature during a five month period [4]. Li_2TiO_3 concentration was 5 $g.l^{-1}$. The suspension was stirred at intervals. Samples of the solution were removed at intervals, and dissolved lithium was titrated using flame photometry analysis. Results of this test indicate that 4% only of the lithium contained in Li_2TiO_3 is dissolved in water after a five month period, showing almost no interaction of Li_2TiO_3 with water at room temperature. Another test was made with boiling water. In this case, Li_2TiO_3 specimens were immersed in water heated to boiling point in a flask topped by a reflux column. Results indicate ~ 20% dissolution of the lithium contained in Li_2TiO_3 after 3 months. TiO_2 was identified as the solid residue by X-ray diffraction analysis.

Therefore accidental contact of Li_2TiO_3 and water coolant is not of concern.

6.2 - Interaction of Li_2TiO_3 with hydrochloric acid

This study is part of a larger focus on the reprocessing of ceramic breeders. Indeed, there will be a significant amount of unburnt lithium-6 in ceramic breeders after service in a fusion reactor. Because of its high cost lithium-6 will have to be recovered and recycled. Dissolution of lithium contained in Li_2TiO_3 was attempted by material immersion in HCl (M) and HCl (12M) [4]. The suspension was stirred at intervals and the solution was sampled for lithium titration like in the tests in water described above. Results in Fig.6 show the dissolved fraction of lithium as a function of time for a concentration of 5 $g.l^{-1}$ of Li_2TiO_3 in HCl (M) and for several sizes of Li_2TiO_3 particles. The lithium contained in Li_2TiO_3 is totally dissolved after 15 days.

Although further work is necessary to finalize a dissolution process of lithium for the reprocessing of Li_2TiO_3 these results show the feasibility of dissolution in acid medium.

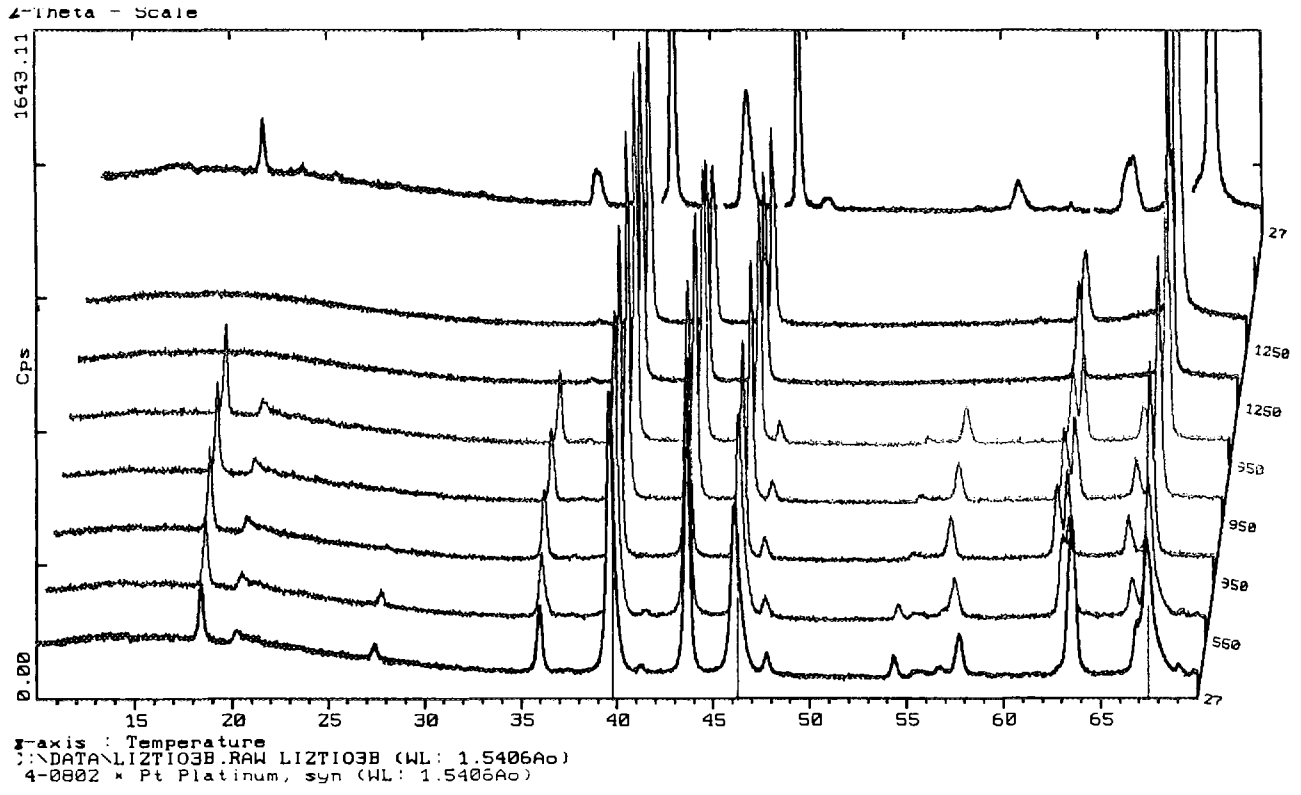

Figure 1

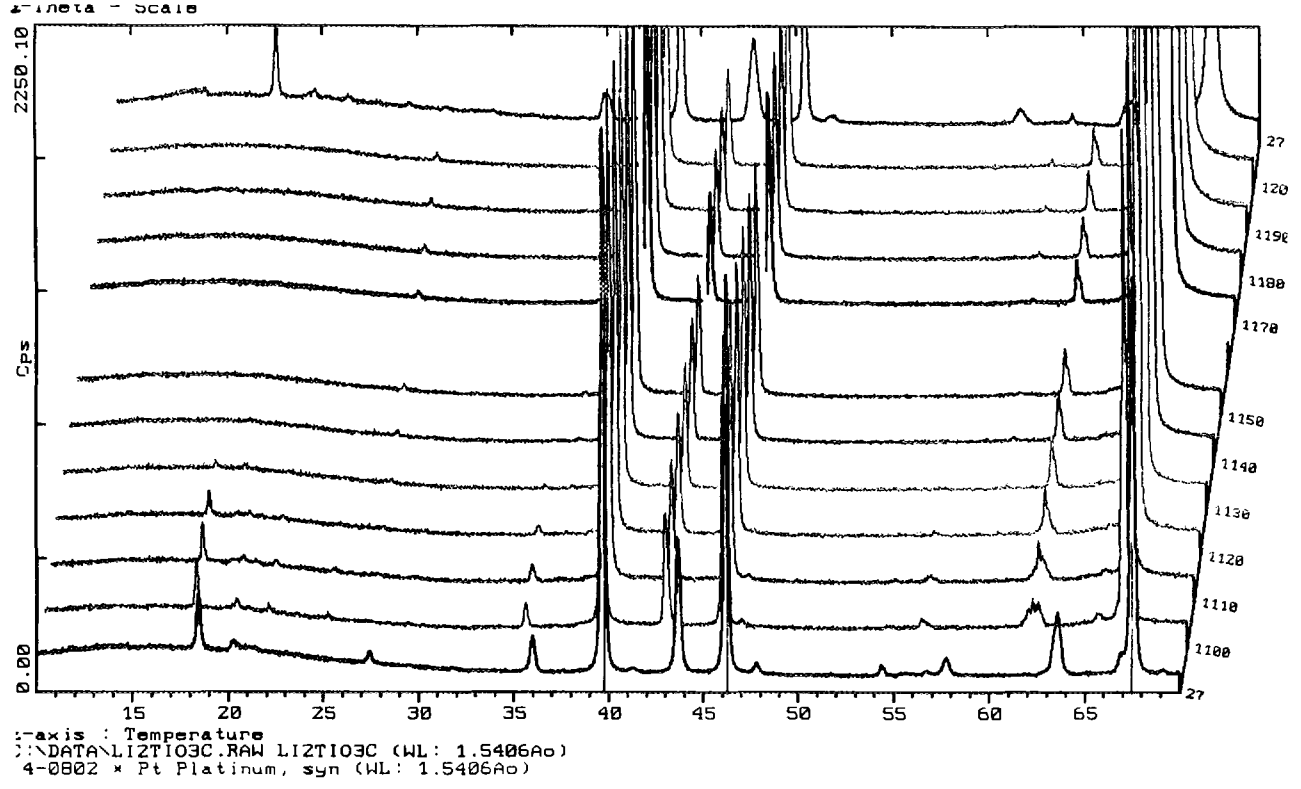

Figure 2

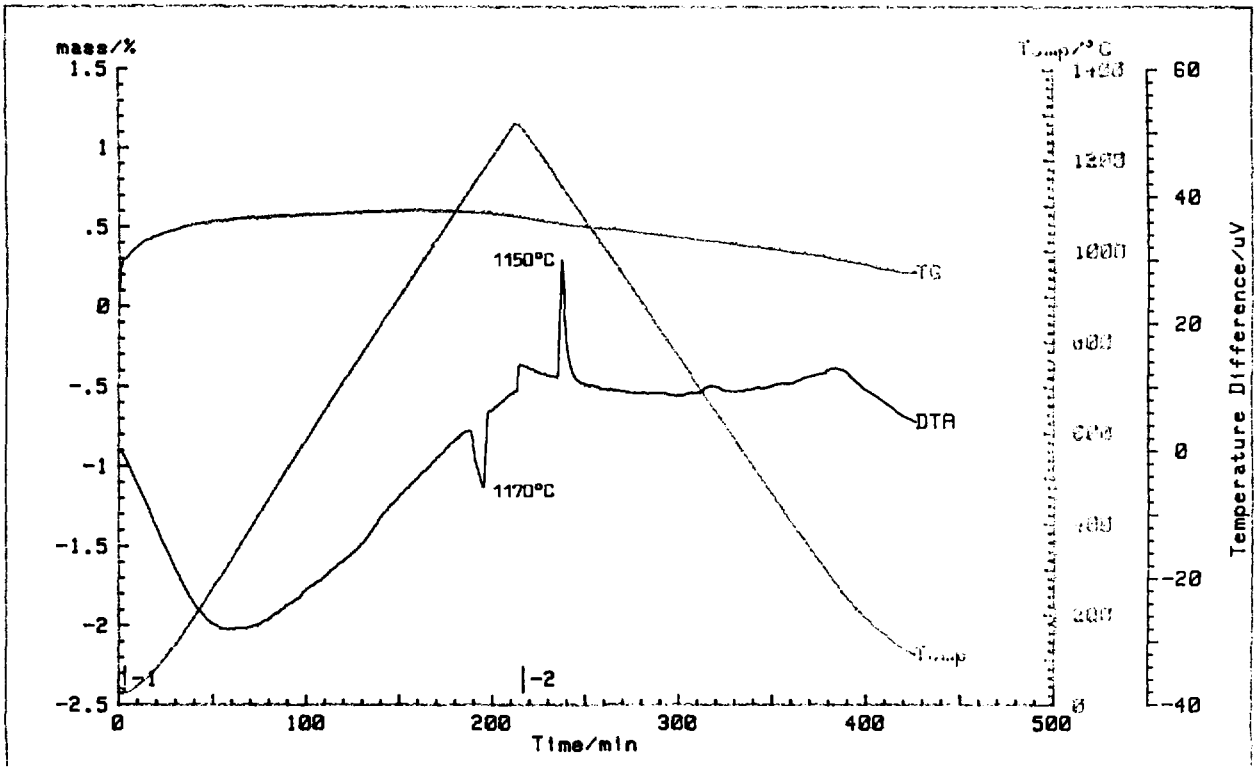

Figure 3

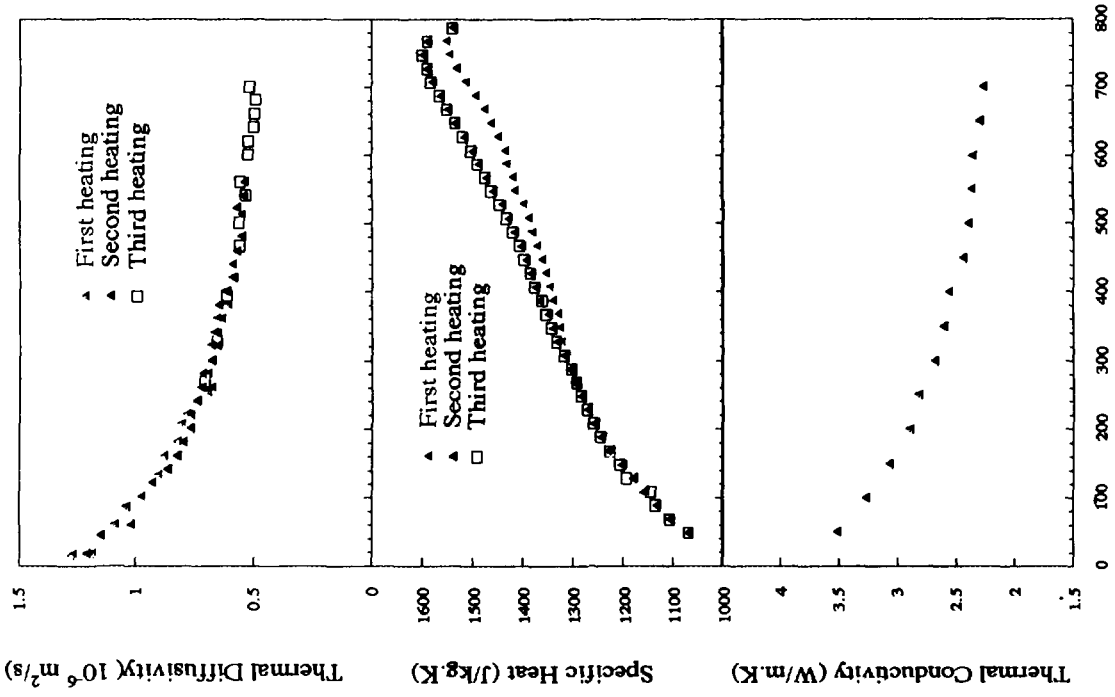

Figure 4

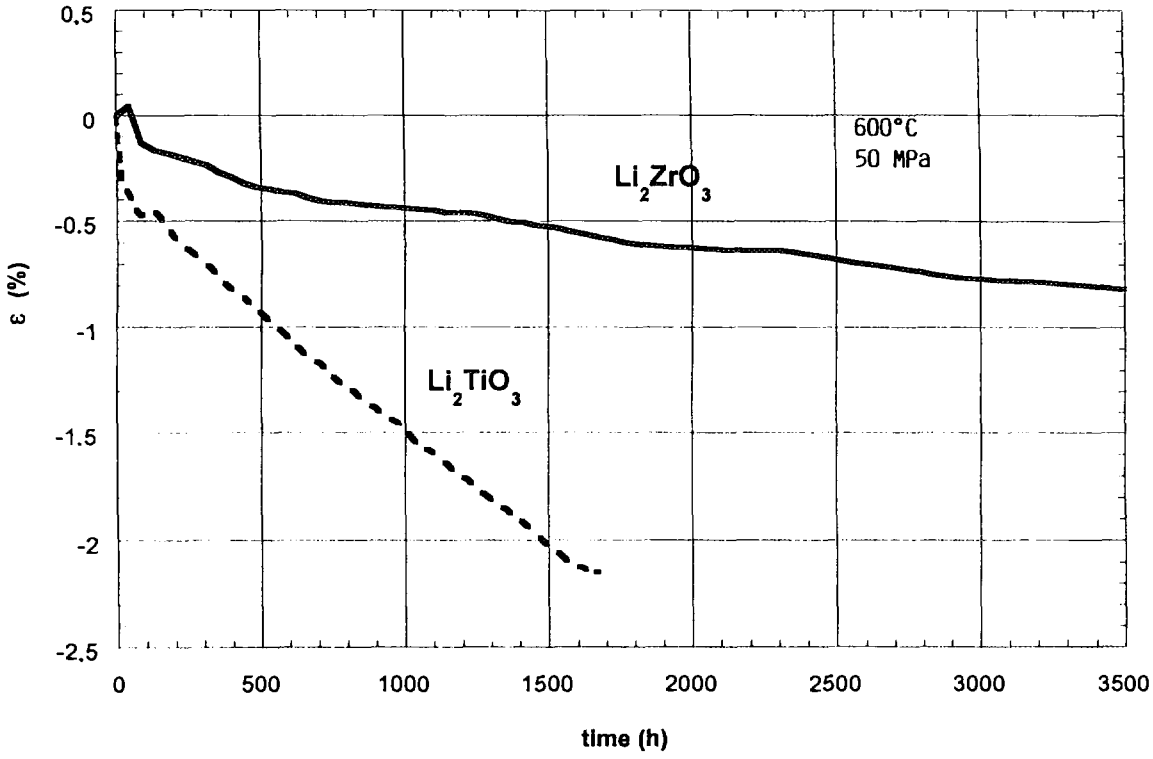

Figure 5

Creep strain as a function of time for Li_2ZrO_3 and Li_2TiO_3

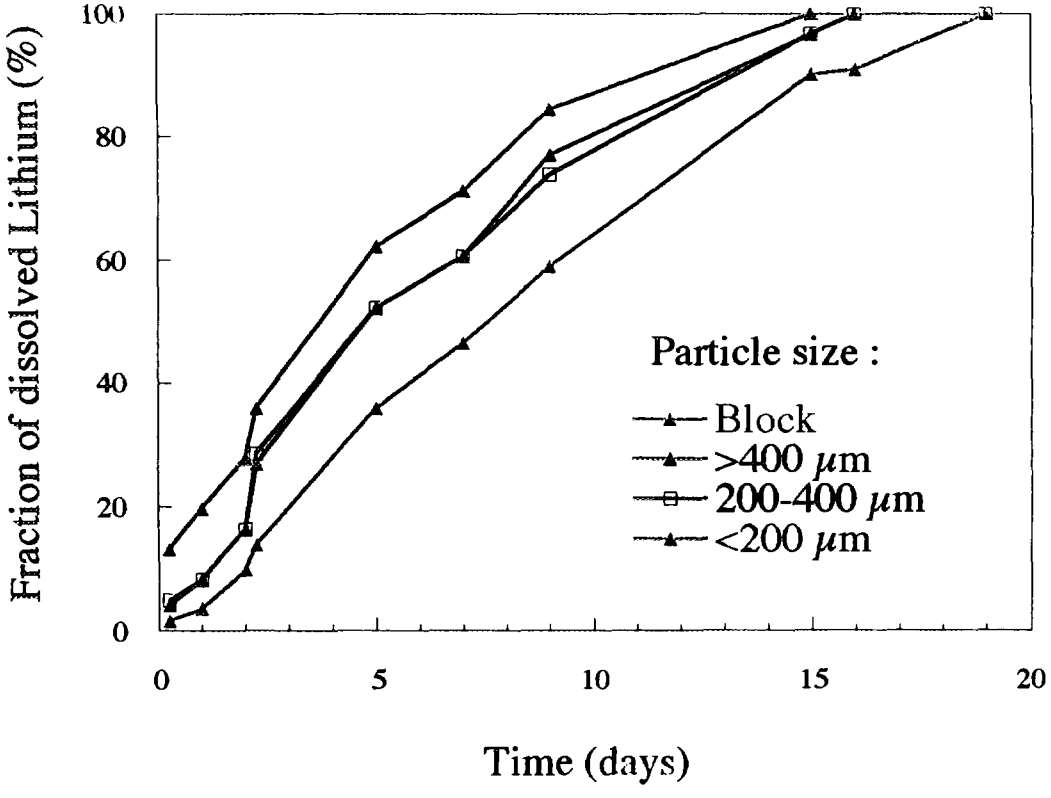

Figure 6

7 - CONCLUDING SUMMARY

Experimental data for Li_2TiO_3 properties are reported. They are relevant to blanket design analysis, safety, and reprocessing of the ceramic. The data affirm the attractiveness of Li_2TiO_3 as ceramic breeder material for fusion reactor blankets.

Acknowledgements

Several persons took part in this work. The contribution of B.Rasneur, J.P.Desmoulin, C.Robert, D.Gosset, B.Girard, from CEA, and J.C.Boivin from ENSC Lille is especially acknowledged.

REFERENCES

[1] N.Roux, J.Avon, A.Floreancig, J.Mougin, B.Rasneur, S.Ravel, Low-temperature tritium releasing ceramics as potential materials for the ITER breeding blanket, J.Nucl.Mater. 233-237 (1996) 1431.

[2] J.D.Lulewicz, N.Roux, First results on the investigation of Li_2ZrO_3 and Li_2TiO_3 pebbles. ISFNT 4, to be published in Fusion Engineering and Design.

[3] D.J.Suiter, Lithium based oxide ceramics for tritium breeding applications. Report MDC E2677 UC 20 (1983).

[4] B.Rasneur, Fabrication and properties of Li_2TiO_3, internal report (1995)

[5] J.W.Davis and A.A.Haasz, Thermal diffusivity/conductivity of AECL Li_2TiO_3 ceramic, J.Nucl.Mater. 232 (1996) 65

Effect of deuterium addition the vaporization of Li_2ZrO_3

Masahisa Tonegawa[1], Atsushi Suzuki[1], Masaru Yasumoto[2], Kenji Yamaguchi[1], Michio Yamawaki[1], Nicole Roux[3]

1 Graduate School of Quantum Engineering and Systems Science, Faculty of Engineering, The Univ. of Tokyo.

2 Research Center for Nuclear Science and Technology, The Univ. of Tokyo.

3 CE/Saclay, France

Abstract

It has been proposed to add a small amount of H_2 to inert purge gas for the purpose of enhancing the release of tritium from ceramic breeder materials. However, it is pointed out that the total pressure of the lithium-containing species becomes very large by addition of H_2. In this study, the partial pressures of vapor spices under D_2 addition were measured by means of high temperature mass spectrometry. When D_2 was introduced the formation of LiOD(g) was observed and the total pressure of lithium-containing species was higher than the case without D_2 admission. From the measured partial pressures, the enthalpy of LiOD forming reaction; $Li_2ZrO_3(s) + D_2O(g) = LiOD(g) + ZrO_2(s)$ was calculated. Moreover, the change of the total pressure of lithium-containing species under the condition that the He + 0.1 using the pressure of D_2 and D_2O as parameters.

Effect of deuterium addition on the vaporization of Li_2ZrO_3

○ Masahisa TONEGAWA[1], Atsushi SUZUKI[1],
Masaru YASUMOTO[2], Kenji YAMAGUCHI[1],
Michio YAMAWAKI[1], Nicole ROUX[3]

1 Graduate School of Quantum Engineering and System Science, Faculty of Engineering, The Univ. of Tokyo.
2 Research Center for Nuclear Science and Technology, The Univ. of Tokyo.
3 CE/Saclay, France

Sixth International Workshop on
CERAMIC BREEDER BLANKET INTERACTIONS
October 22-24, 1997
Sangyo-kaikan, Mito, Ibaraki, Japan

Background

It has been proposed to add a small amount of H_2 to inert purge gas for the purpose of enhancing the release of tritium from ceramic breeder materials.

↓

However, it is pointed out that the total pressure of the lithium-containing species becomes very large by addition of H_2.

JAERI–Conf 98–006

Study of this field

- Various Li-containing materials such as $Li_2O(s)$, $LiAlO_2(s)$, $Li_8PbO_6(s)$, $Li_4SiO_4(s)$, $Li_2SnO_3(s)$, $Li_2TiO_3(s)$, $Li_2ZrO_3(s)$, $Li_6Zr_2O_6(s)$ and $Li_8ZrO_6(s)$ were measured by use of high temperature mass spectrometer.
- Partial pressures of materials such as $Li_4SiO_4(s)$, $LiAlO_2(s)$ and $Li_2TiO_3(s)$ were measured in hydrogen atmosphere by means of atmosphere-controllable high temperature mass spectrometer.
- $Li_2ZrO_3(s)$ is a promising candidate, because zirconium is a neutron multiplier to enhance the tritium breeding.
- In addition to $Li_4SiO_4(s)$[1,2], the presence of non-stoichiometry of $Li_2ZrO_3(s)$[3] in the hydrogen atmosphere has been pointed out.

1 H. R. Ihle et al., SOFT Conf., Rome, Italy, September(1992).

2 M. Yamawaki et al., J.Nucl. Mater. 223(1995)80.

3 Y. Kawamura et al., J. Nucl. Mater. 230(1996)287.

Purpose of This Study

- Detecting the vapor species in equilibrium with $Li_2ZrO_3(s)$ and evaluating the partial pressure of each vapor species by means of "atmosphere-controllable high temperature mass spectrometer".
- Evaluating the thermodynamic data of the gas / solid equilibria in the $Li_2ZrO_3 - D_2$ system.
- Evaluating the influence of addition of hydrogen on vaporization behavior.

Experimental

- Sample

  Li_2ZrO_3(s) supplied from Commissariat *à* l'Energie Atomique, France (monoclinic Li_2ZrO_3 ; 95% + monoclinic ZrO_2 ; 5%) was ground into powder and was heated in vacuum at 773 K for 5 hours before measurement.

- Conditions

  Experiments were performed under 4 conditions.

  run1 ; No gases were introduced.

  run2 ; D_2 gas was introduced.

  run3 ; No gases were introduced.

  run4 ; D_2 gas was introduced.

  Temperature of the system ; 1413K-1673K

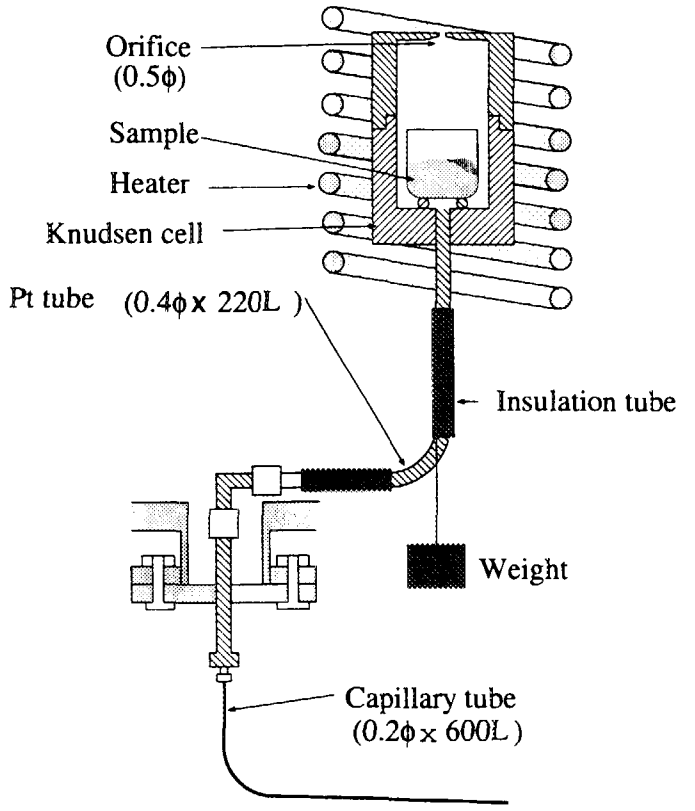

Figure : Knudsen cell and gas inlet system of atmosphere-cotrollable high temperature mass spectrometer

Device Constant

Partial pressure of vapor species i : P_i

$$P_i = K \cdot I_i \cdot T \qquad (K = \frac{k}{\sigma_i \cdot \gamma_i \cdot n_i})$$

K : constant, I : ion intensity, T : temperature,

k : device constant, σ_i : ionization cross section,

n_i : isotope abundance γ_i : gain of the electron multiplier

Device constant, k , was evaluated by mesuring the intensity of the $^{107}Ag^+$ ion.

Results and Discussion

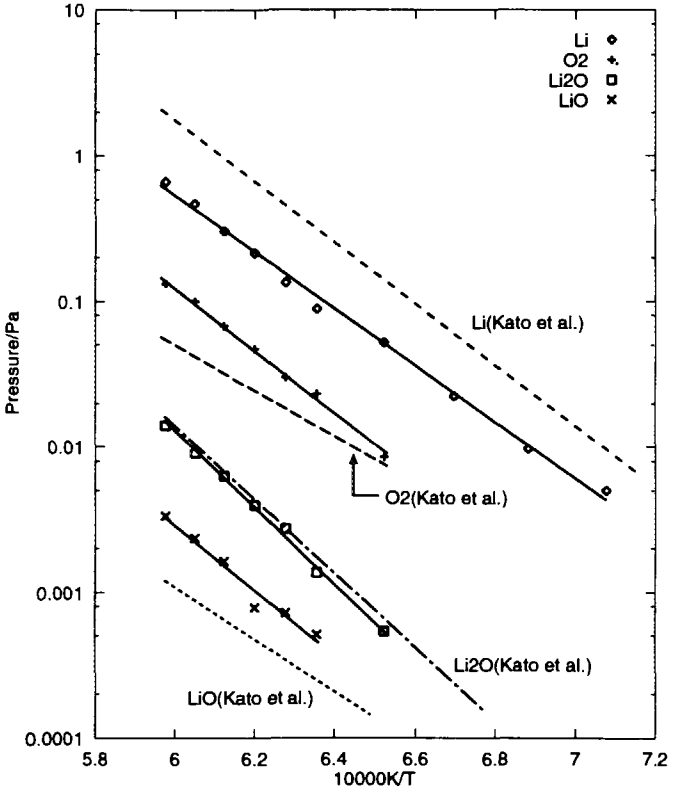

Figure : Partial pressure of vapor species over Li_2ZrO_3. (run1)

Dashed line is the partial pressure of Y.Kato et al. (Y.Kato et al., J. Nucl. Mater. 203(1993)27.)

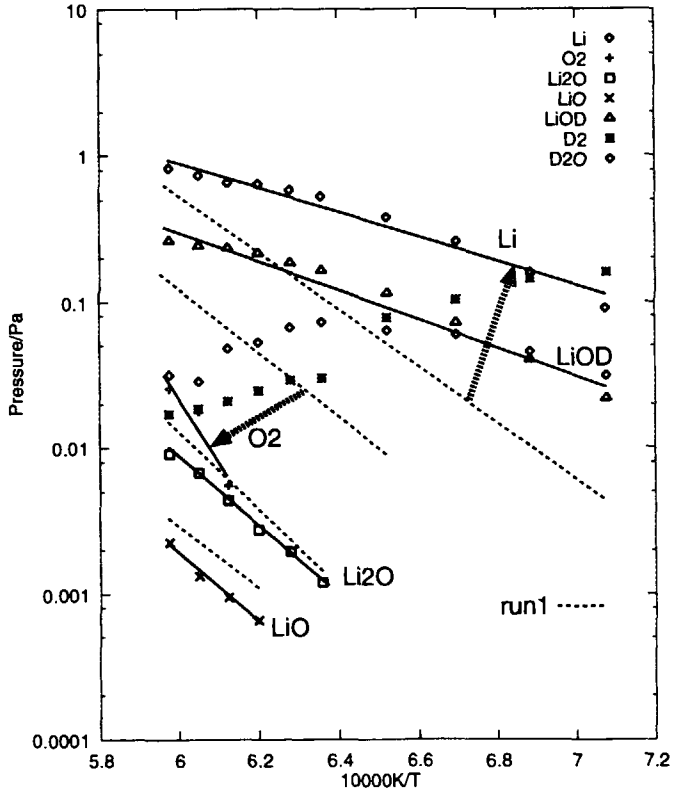

Figure : Partial pressure of vapor species over Li_2ZrO_3-D_2 system. (run2)

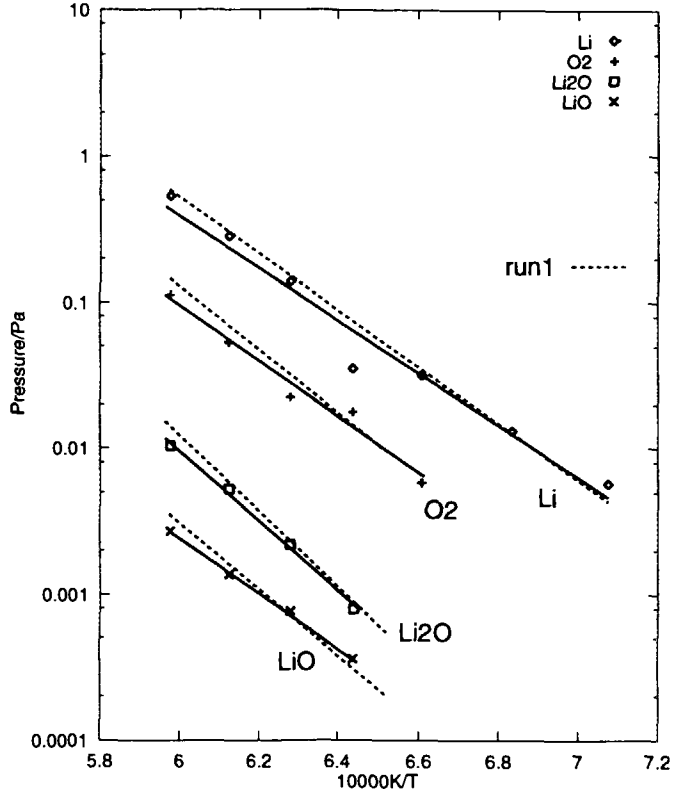

Figure : Partial pressure of vapor species over Li_2ZrO_3 (run3).

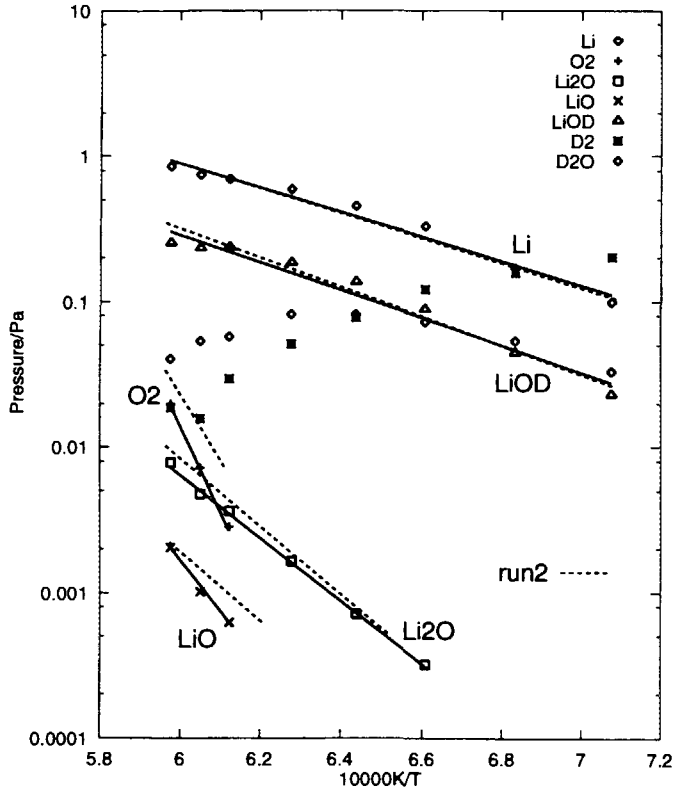

Figure : Partial pressure of vapor species over Li_2ZrO_3-D_2 system (run4).

Thermodynamic Data

Reactions considered ;

$$Li_2ZrO_3(s) \rightleftharpoons Li_2O(g) + ZrO_2(s) \qquad (a)$$

$$2Li(g) + \tfrac{1}{2}O_2(g) \rightleftharpoons Li_2O(g) \qquad (b)$$

$$Li_2ZrO_3(s) \rightleftharpoons 2Li(g) + \tfrac{1}{2}O_2(g) + ZrO_2(s) \qquad (c)$$

$$Li_2ZrO_3(s) + D_2O(g) \rightleftharpoons 2LiOD(g) + ZrO_2(s) \qquad (d)$$

$$D_2 + \tfrac{1}{2}O_2(g) \rightleftharpoons D_2O(g) \qquad (e)$$

Table : 3rd law standard reaction enthalpy ; $\Delta_r H^\circ_{298}$ [kJ/mol]

	reac. (a)	reac. (b)	reac. (c)	reac. (d)
run1	510.1 ± 0.9	-465.1 ± 2.8	975.0 ± 2.8	— —
run2	514.3 ± 0.8	**-458.2 ± 2.1**	973.6 ± 3.2	439.7 ± 1.3
run3	512.5 ± 1.0	-470.0 ± 6.2	981.6 ± 5.8	— —
run4	516.6 ± 1.9	**-458.1 ± 1.1**	976.6 ± 2.1	444.3 ± 2.0
Kato et al.#	507.4 ± 2.8	-439.9 ± 1.5	947.4 ± 3.6	——
JANAF##	495.8	-485.5 ± 2.5	981.3	——

M.W.Chase et al., JANAF Thermochemical Tables, 3rd ed.

By addition of $D_2(g)$ (run2,run4) , the equilibria of (b) lean to left-hand side and right-hand side.

— The equilibria favors the formation of $O_2(g)$.

— Oxygen deficient layer may be formed at the near-surface layer of $Li_2ZrO_3(s)$.

Li-loss (1)

In the blanket designs, the sum of the partial pressures of Li-containing species is recommended to be less than 0.01 Pa.

$$P_{\mathrm{Li}}^{\mathrm{total}} = P_{\mathrm{Li}} + P_{\mathrm{LiOD}} + P_{\mathrm{Li_2O}} + P_{\mathrm{LiO}}$$

T_{max}, a temperature at which $P_{\mathrm{Li}}^{\mathrm{total}}$ reaches 0.01 Pa, was evaluated under the condition $P_{\mathrm{D_2}}$ and $P_{\mathrm{D_2O}}$ were fixed and by using equilibrium constant.

$$P_{\mathrm{Li}}^{\mathrm{total}}(\mathrm{T_{max}}) = 0.01\ \mathrm{Pa}$$

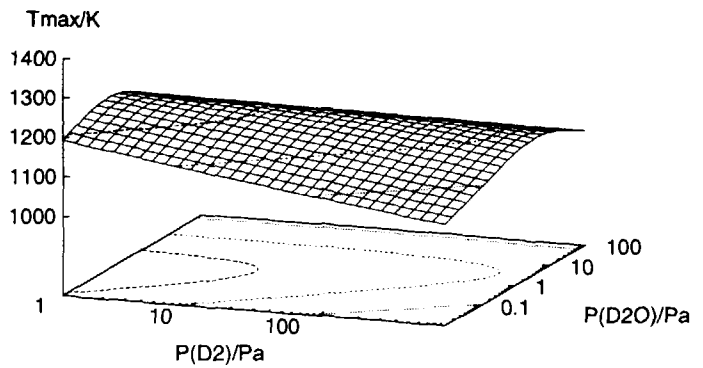

Figure : Temperature at which the total pressure of Li-containing species in Li_2ZrO_3-D_2 system reaches 0.01 Pa.

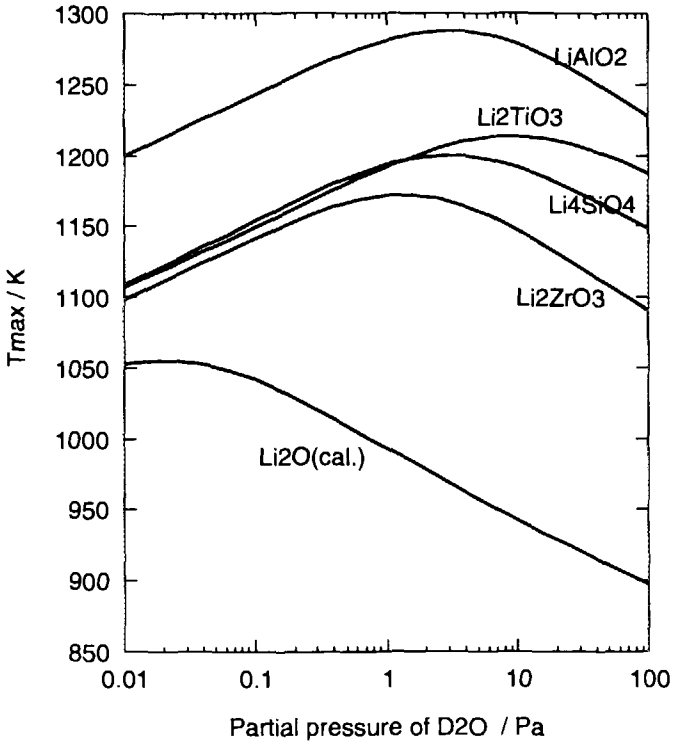

Figure : Temperature at which the total pressure of Li-containing species of Li_2O, Li_4SiO_4, $LiAlO_2$, Li_2TiO_3 reaches 0.01 Pa at $P_{\mathrm{D_2}} = 100\mathrm{Pa}$

Li-loss (2)

When a pressure of hydrogen (deuterium) which is added to purge gas is 100 Pa, the following equation holds ;

$$P_{D_2} + P_{D_2O} + \frac{1}{2}P_{LiOD} = 100\text{Pa}$$

The formation of ZrO_2 is confirmed by an X-Ray Diffraction Analysis for powdered sample.
So, the ratio of Li and O in the gas phase is assumed 2 : 1.

$$\frac{P_{Li} + P_{LiOD} + 2P_{Li_2O} + P_{LiO}}{2P_{O_2} + P_{D_2O} + P_{LiOD} + P_{Li_2O} + P_{LiO}} = 2$$

From these two assumptions and equilibrium constant, P_{Li}^{total} is written as a function of temperature.

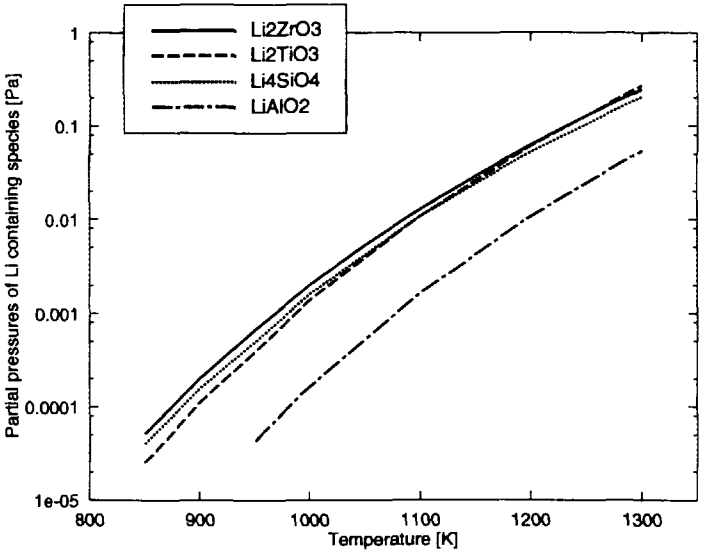

Figure : Comparison of ceramic breeding materials in terms of a total pressure of Li-containing species.

Summary

- By addition of $D_2(g)$ to vacuum the enhancement of vaporization of Li(g) and formation of LiOD(g) were confirmed.
- Standard reaction enthalpy of

  $Li_2ZrO_3(s) + D_2O(g) \rightarrow 2LiOD(g) + ZrO_2(s)$

  was evaluated to be 442.0±2.39 kJ/mol for the first time by means of high temperature mass spectrometry.
- From the standpoint of Li-loss caused from vaporization, breeder materials were ranked as follows :

  $LiAlO_2(s) > Li_2TiO_3(s)$

  $\simeq Li_4SiO_4(s) \simeq Li_2ZrO_3(s)$

SESSION 7

Tritium Release from Solid Breeder Materials

Tritium Release from EXOTIC-7 Orthosilicate Pebbles: Effect of Burnup and Contact with Beryllium During Irradiation

F. Scaffidi-Argentina, H. Werle

Forschungszentrum Karlsruhe, Institut für Neutronenphysik und Reaktortechnik
Postfach 3640, D-76021 Karlsruhe, F.R.G.

ABSTRACT

EXOTIC-7 was the first in-pile test with ^{6}Li-enriched (50 %) lithium orthosilicate (Li_4SiO_4) pebbles and with DEMO representative Li-burnup. Post irradition examinations of the Li_4SiO_4 have been performed at the Forschungszentrum Karlsruhe (FZK), mainly to investigate the tritium release kinetics as well as the effect of Li-burnup and/or contact with beryllium during irradiation. The release rate of Li_4SiO_4 from pure Li_4SiO_4 bed of capsule 28.1-1 is characterized by a broad main peak at about 400 ^oC and by a smaller peak at about 800 ^oC. The broad main peak was observed in all previous studies with low Li-burnup ($\leq$ 3%). The release rate of the Li_4SiO_4 from the mixed beds of capsule 28.2 and 26.2-1 shows again these two peaks, but most of the tritium is now released from the 800 ^oC peak. This shift of release from low to high temperature may be due to the higher Li-burnup (capsule 28.1-1 Li-burnup 10%; capsule 28.2 Li-burnup 18%; capsule 26.2-1 Li-burnup 13%) and/or due to contact with Be during irradiation. Due to the very difficult interpretation of the in-situ tritium release data, residence times have been estimated on the basis of the out-of-pile tests. The residence time for Li_4SiO_4 from caps. 28.1-1 irradiated at 10% Li-burnup agrees quite well with that of the same material irradiated at Li-burnup lower than 3% in the EXOTIC-6 experiment. In spite of the observed shift in the release peaks from low to high temperature, also the residence time for Li_4SiO_4 from caps. 26.2-1 irradiated at 13% Li-burnup agrees quite well with the data from EXOTIC-6 experiment. On the other hand, the residence time for Li_4SiO_4 from caps. 28.2 (Li-burnup 18%) is about a factor 1.7-3.8 higher than that for caps. 26.2-1. Based on these data on can conclude that up to 13% Li-burnup neither the contact with beryllium nor the Li-burnup have a detrimental effect on the tritium release of Li_4SiO_4 pebbles, but at 18% Li-burnup the residence time is increased by about a factor three.

1 INTRODUCTION

In the period 1989-94 two DEMO blanket concepts were studied within the European Fusion Technology Programme: the Breeder Inside Tube (BIT) concept

based on $LiAlO_2$ or Li_2ZrO_3 in form of pellets mainly by CEA and ENEA and the Breeder Outside Tube (BOT) concept based on lithium-orthosilicate (Li_4SiO_4) and beryllium pebbles by FZK. Irradiation behaviour of the various breeder materials up to medium lithium burnup (≤ 3 %) have been studied in previous EXOTIC tests. The goal of EXOTIC-7 was to study the irradiation behaviour (mainly mechanical integrity and tritium release) up to and beyond DEMO relevant lithium burnup (~ 7 % for BOT). EXOTIC-7 was therefore the first in-pile test with ^{6}Li-enriched (50%) Li_4SiO_4 pebbles and with DEMO representative Li-burnup [1,2]
At planning of EXOTIC-7 (1993) mixtures of Li_4SiO_4 and beryllium pebbles were considered as blanket material for the BOT concept. Therefore, in EXOTIC-7, pure Li_4SiO_4 and mixed Li_4SiO_4/beryllium beds were irradiated. One irradiation capsule containing a mixed bed was made of DEMO relevant steel (MANET) in order to study chemical interactions and determine irradiation induced swelling by changes in the measured radial temperature gradient of the bed.
Post irradition examinations of the Li_4SiO_4 delivered by FZK have been performed at both ECN Petten [3] and FZK. In this report results of FZK out-of-pile tritium release studies of Li_4SiO_4 pebbles are summarized.

2 SAMPLES AND IRRADIATION CONDITIONS

Type, mass and drying procedure of the Li_4SiO_4 pebbles delivered to ECN for irradiation in EXOTIC-7 are given in Table 1.
The pebbles were sent to ECN/JRC Petten, November 2, 1993 in glass ampoules under inert gas atmosphere. Three irradiation capsules (26.2, 28.1 and 28.2) contained FZK material. Capsule 28.1 contained Li_4SiO_4 pebbles of 0.1-0.2 mm diameter. The pebble bed height was separated into three parts of each 20 mm length in order to enable three temperature levels. The pebble bed diameter for the upper part was only 6.3 mm, in order to achieve the required 400 °C. The middle and lower part had a diameter of 8 mm. Capsule 28.2 contained Li_4SiO_4 pebbles of 0.1-0.2 mm diameter and Be pebbles of 2 mm and 0.1-0.2 mm diameter. The pebble bed diameter was 11.35 mm and the pebble bed height 8 cm. The pebble bed of this capsule was enclosed by a MANET tube (DEMO relevant steel) of 1.75 mm thickness. The objective was to determine during irradiation indirectly beryllium swelling by measuring the radial temperature gradient of the pebble bed. Capsule 26.2 contained Li_4SiO_4 pebbles of 0.1-0.2 mm diameter and beryllium pebbles of 2 and 0.1-0.2 mm diameter. Also here the pebble height was separated into three parts of each 20 mm length, in order to enable three temperature levels. The pebble bed diameter of the lower and middle part was 7.2 mm and that of the upper part 8 mm. Loading characteristics of the three capsules are given in Table 2.
The capsules were filled at ECN/JRC November 1993 under air. The mixed beds were prepared by filling first the 2 mm diameter Be pebbles and afterwards into the residual space a mixture of about equal volume fractions of 0.1-0.2 mm Li_4SiO_4 and

0.1-0.2 mm Be pebbles. The ^{6}Li content of the Li_4SiO_4 pebbles was measured at ECN Petten prior to irradiation and it was 51.8% [3].
The irradiation started February 1994 and has been completed in February 1995 (11 reactor cycles, 261 full power days). The peak neutron fluences near the capsule walls were: fast fluence (^{54}Mn) 1-2x10^{21} n/cm^2, thermal fluence (^{60}Co) 1-1.6x10^{21} n/cm^2. The depression of the thermal fluence at the capsule centers was a factor 2 to 4 [3]. Other irradiation conditions are given in Table 3.

3 FACILITIES AND PROCEDURES

One of the main characteristics of the tritium release facilities is that the sample chamber is connected by a short, heated line (≈300 °C) to a Zn-reductor (≈390 °C). The reductor transforms any tritium water to tritium gas. This avoids problems with tritium water absorption and allows quantitative tritium measurements. The tritium activity of the purge gas is measured with an ionization chamber and/or a proportional counter. The released tritium inventory is determined by integrating the measured release rate over the time. Release kinetics and total amount of released tritium were determined by annealing the pebbles by temperature ramps of 5 °C/min up to 850 °C, keeping constant this temperature for several hours and purging them with 50 SCCM He+0.1 vol% H_2.

4 RESULTS AND DISCUSSION

The annealing tests are summarized in Table 4. The release rate of Li_4SiO_4 from pure Li_4SiO_4 bed of capsule 28.1-1 (Fig. 1) is characterized by a broad main peak at about 400 °C and a smaller peak at about 800 °C. Totally, about 4•10^9 Bq/g were released. Broad peaks in the region 250 to 600 °C were generally observed in all previous studies with low Li-burnup (≤ 3%) [4]. The release rate of the Li_4SiO_4 from the mixed beds of capsule 28.2 (Fig. 2) and 26.2-1 (Fig. 3) shows again these two peaks, but most of the tritium is now released from the 800 °C peak. This shift of release from low to high temperature may be due to the higher Li-burnup (capsule 28.1-1 Li-burnup 10%; capsule 28.2 Li-burnup 18%; capsule 26.2-1 Li-burnup 13%) and/or due to contact with Be during irradiation.
Previous studies [5] indeed have shown, that chemical interactions in the Be/Li_4SiO_4 system occur during annealing tests for 1000 hours at 650 °C. Usually, along the Be/Li_4SiO_4 contact surfaces, a reaction zone (i.e. BeO + Li_2Si + $Li_2Be_2O_3$) has been observed, the growth rate of which can be described by a parabolic rate law. According to this law, the Li_4SiO_4 pebbles from caps. 28.1-1 and caps. 28.2 should show a reaction zone of about 10 μm at the Be/Li_4SiO_4 contact points.
However, qualitative and quantitative chemical analyses in μm areas were recently performed on EXOTIC-7 metallographic sections using a shielded X-ray

microanalyser Jeol JRXA-50 in the Hot Cells of the FZK [6]. The analyses showed that in case of direct contact of Be and Li_4SiO_4 during the irradiation period, a two-phase reaction layer of about 30 μm in thickness has formed. The layer consists of BeO and probably of a Li-Be oxide of the composition $Li_2Be_2O_3$ on the Be rich side and of Li_2BeSiO_4 on the Li_4SiO_4 side. Furthermore, the Si intensity in the Li_4SiO_4 pebbles was higher than in the Li_4SiO_4 standard indicating a reasonable fraction of a Si richer phase, e.g. Li_2SiO_3, in these pebbles. The presence of the above cited reaction layer could cause the experimentally observed shift of tritium release from low to high temperature. The total release from both capsules 26.2-1 and 28.2 ($\approx 4 \bullet 10^9$ Bq/g) is about a factor ten higher than that from capsule 28.1-1.

At ECN [2] under the same conditions (He + 0.1% H_2, 5 °C/min up to 860 °C) essentially the same release kinetics as in the FZK tests has been observed for Li_4SiO_4 samples from capsule 28.1-1, 28.2 and 26.2-1. In addition, the total release determined at ECN for Li_4SiO_4 from all capsules (caps. 28.1-1: $1.92 \bullet 10^9$ Bq/g; caps. 28.2: $4.28 \bullet 10^{10}$ Bq/g; caps. 26.2-1: $1.49 \bullet 10^{10}$ Bq/g) agrees, within the experimental scatter, with the FZK results.

Due to the very difficult interpretation of the in-pile tritium release data, residence times τ (inventory/production rate) have been estimated on the basis of the out-of-pile tests performed at both ECN and FZK. The Arrhenius plot of the residence time for the capsules 26.2-1, 28.1-1 and 28.2 as a function of the volume averaged temperature (average in radial direction assuming constant power density) is shown, together with in-pile data from EXOTIC-6 [7,8], in Fig. 4. The residence time for Li_4SiO_4 from caps. 28.1-1 irradiated at 10% Li-burnup agrees quite well with the EXOTIC-6 data (Li-burnup lower than 3%) [8]. In spite of the observed shift in the release peaks from low to high temperature, also the residence time for Li_4SiO_4 from caps. 26.2-1 irradiated up to 13% Li-burnup agrees quite well with the EXOTIC-6 data. On the other hand, the residence time for Li_4SiO_4 from caps. 28.2 (Li-burnup 18.%) lies slightly above the EXOTIC-6 line and is about a factor 1.7-3.8 higher than that for caps. 26.2-1. Based on these data on can conclude that the tritium release from Li_4SiO_4 pebbles is not influenced by Li-burnup up to 13%. On the contrary, the presence of Be in contact with ceramics during irradiations seems to influence tritium release at higher Li-burnup by increasing the residence time of about a factor 3. A summary of the residence times for all capsules, according to both ECN and FZK out-of-pile tests is shown in Table 5.

5 CONCLUSIONS

Post irradiation examinations of Li_4SiO_4 pebbles irradiated in the HFR reactor during the EXOTIC-7 experiment have been performed at ECN Petten and at FZK. In agreement with previous studies it was found that, from Li_4SiO_4 (Li-burnup 10%) which was not in contact with Be during irradiation, tritium is mainly released at about 400 °C. On the contrary, Li_4SiO_4 pebbles (Li-burnup 13% and 18%) which were in

contact with Be, release tritium mainly at about 800 °C. It is not yet completely clear if this shift of the release peaks from low to high temperature is due to contact with Be during irradiation or to due to the higher Li-burnup.
The total release determined at ECN for Li_4SiO_4 from all capsules agrees, within the experimental scatter, with the FZK results. Based on the experimental data, it results that the tritium release from Li_4SiO_4 pebbles is not influenced by Li-burnup up to 13%. For Li-burnups of 10% and 13% the tritium residence times agree quite well with the EXOTIC-6 in-pile data (Li-burnup ≤ 3%). On the contrary, the tritium residence time for Li_4SiO_4 pebbles irradiated at 18% Li-burnup is slightly larger than that for EXOTIC-6. This increase might be caused by Li-burnup or a combiantion of Li-burnup and interaction with beryllium during irradiation.

REFERENCES

[1] J.G. Van der Laan et al. "Irradiation Behaviour of Ceramic Breeder Materials at High Litium burnup", Proceedings of the ICFRM-7 Conference, Obninsk, October 1995.

[2] R. Conrad, R. May, "EXOTIC-7, Irradiation Progress Report No. 11", Technical Memorandum HFR/95/4196, JRC Petten, April 1995.

[3] J.G. van der Laan, ECN Petten, Private Communication.

[4] H. Werle, "EXOTIC-6 PIE and Tritium Release", to be published.

[5] P. Hofmann, W. Dienst, "Chemical Interactions of Beryllium with Lithium-Based Oxides and Stainless Steel", J. Nucl. Mater. 171 (1990) 203-214.

[6] H. Kleykamp, H.D. Gottschalg, "Post Irradiation Studies on the EXOTIC-7 experiment", Interner IMF I-Bericht 035, Forschungszentrum Karlsruhe, Juli 1997.

[7] H. Kwast et al., "The Behaviour of Ceramic Breeder Materials with Respect to Tritium Release and Pellet/Pebble Mechanical Integrity", J. Nucl. Mater. 212-215 (1994) 1010-1014.

[8] R. May, H. Werle, "EXOTIC-6, Inpile Tritium Residence Times of Li_4SiO_4 and Li_2ZrO_3 Pebbles, to be published.

Table 1 Li_4SiO_4 pebbles delivered to ECN

Material type	Mass (g)	Drying	%TD	Grain size (μm)
Li_4SiO_4 + 1.4 wt% SiO_2 ; 50 % ^6Li pebble diameter 0.1-0.2 mm type Schott B-4153, 42/93	~ 20	300 °C, 3 h stagnant air	97	20 - 40

Table 2 Loading characteristics of FZK capsules

Capsule number	V (cm^3)	Material	M (g)	$\rho_b = M/V$ (g/cm^3)	ρ_b/ρ_{th} (%)
28.1	3.38	Li_4SiO_4	4.99	1.476	61.8
26.2	3.43	Li_4SiO_4 Be 0.1 - 0.2 mm Be 2 mm	1.40 0.94 3.53 2.59	0.408 — 1.029 —	17.1 — 55.9 —
28.2	8.06	Li_4SiO_4 Be 0.1 - 0.2 mm Be 2 mm	1.88 144 9.81 8.37	0.233 — 1.217 —	9.8 — 66.2 —

Table 3 EXOTIC-7 irradiation conditions

		28.1	26.2	28.2
Central temperature (°C)		465 - 730	410 - 545	410 - 480
Total lithium burn-up (%)	calculated	7 ± 2	14 ± 2	19 ± 2
	experimental	10 ± 2	13 ± 2	18 ± 2

Table 4 FZK annealing tests

Capsule number	Material	Irradiation temperature [°C]	Li-burnup [%]	Sample mass [g]	Total tritium release [MBq]	Specific tritium release [MBq/g]
28.1-1	Li_4SiO_4 (pure bed)	465-565	10	0.0239	100.7	4213.4
				0.0250	107.2	4288
26.2-1	Li_4SiO_4 (in contact with Be)	410-500	13	0.0252	550	21825.4
				0.0265	1295	48867.9
28.2	Li_4SiO_4 (in contact with Be)	410-480	18	0.0245	774.6	31616.3
				0.0229	1278	55807.9

Table 5 Comparison between FZK and ECN Petten tritium residence times

Capsule number	mass [g]	Mean irradiation temperature [°C]	Tritium generation rate [MBq/g s]	FZK Tritium inventory [MBq/g]	ECN Tritium inventory [MBq/g]	FZK Residence time [h]	ECN Residence time [h]
28.1-1	4.99	495	0.1730	4250	1924	6.82	3.09
26.2-1	1.40	411	0.3084	35400	14950	31.89	13.47
28.2	1.88	407	0.2296	43700	42850	52.86	51.84

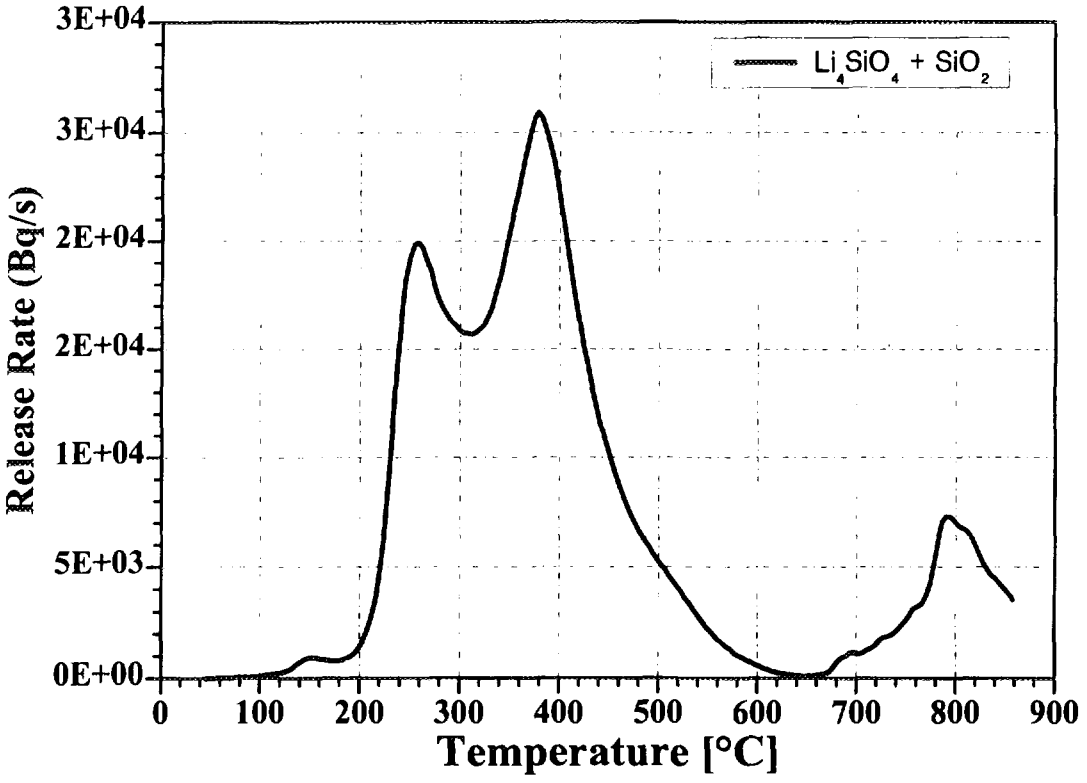

Fig. 1 Tritium release rate as a function of the annealing temperature for Li_4SiO_4 pebbles from the capsule 28.1-1.

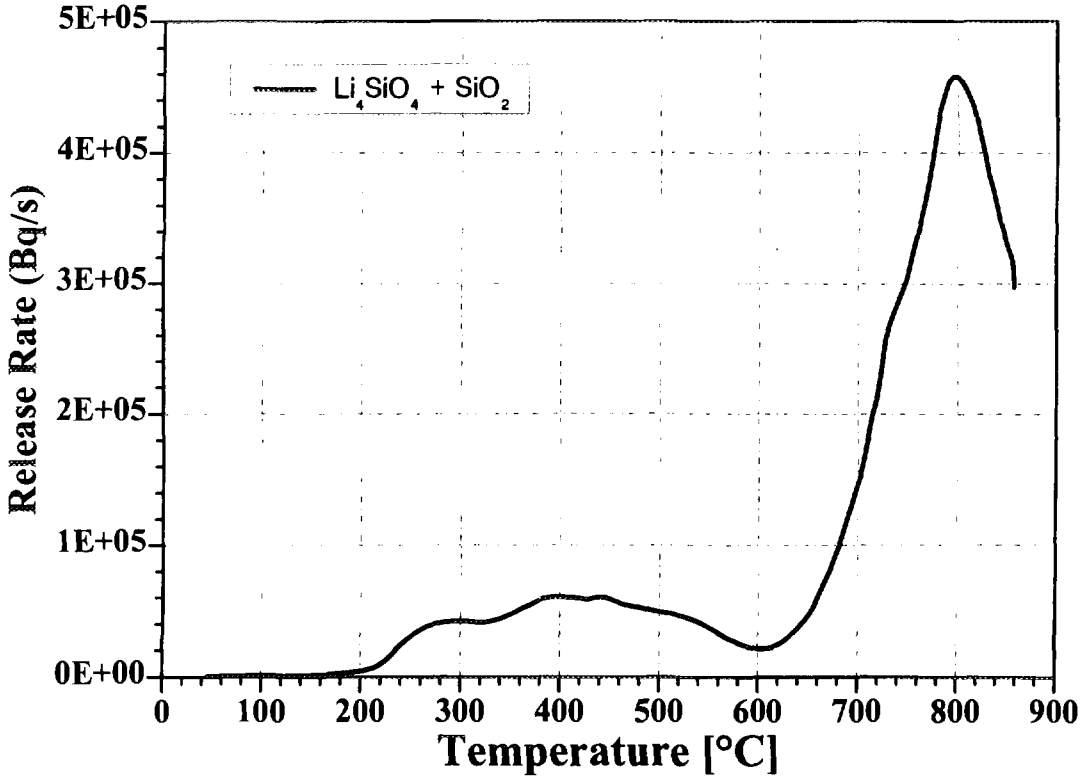

Fig. 2 Tritium release rate as a function of the annealing temperature for Li_4SiO_4 pebbles from the capsule 28.2.

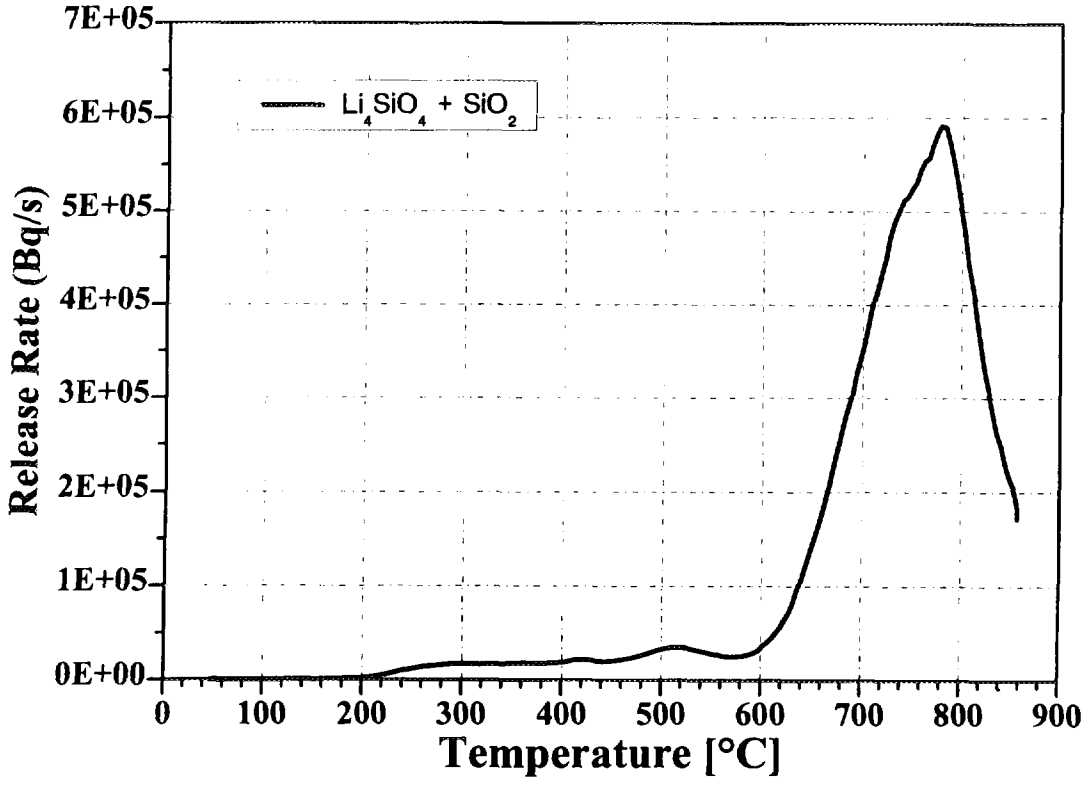

Fig. 3 Tritium release rate as a function of the annealing temperature for Li_4SiO_4 pebbles from the capsule 26.2-1.

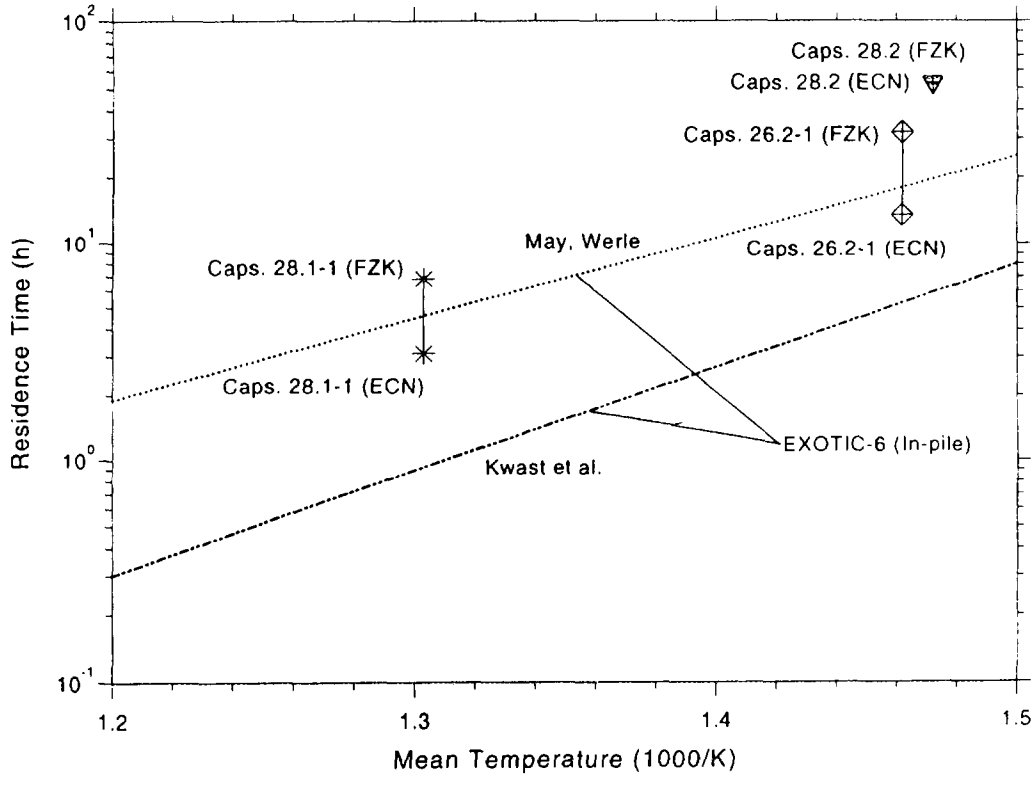

Fig. 4 Tritium residence time for Li_4SiO_4 pebbles as a function of the volume averaged capsule temperature.

Isotope exchange reactions on ceramic breeder materials and their effect on tritium inventory

M. Nishikawa, A. Baba, Y. Kawamura *) and M. Nishi *)

Department of Nuclear Engineering, Faculty of Engineering, Kyushu University
Hakozaki 6-10-1, Higashi-ku, Fukuoka 812-81, Japan
*) *Tritium Engineering Laboratory, Japan Atomic Energy Research Institute*
Shirakata Shirane 2-4, Tokai-mura, Naka-gun, Ibaraki-ken 319-11, Japan

Abstract

Though lithium ceramic materials such as Li_2O, $LiAlO_2$, Li_2ZrO_3, Li_2TiO_3 and Li_4SiO_4 are considered as breeding materials in the blanket of a D-T fusion reactor, the release behavior of the bred tritium in these solid breeder materials has not been fully understood. The isotope exchange reaction rate between hydrogen isotopes in the purge gas and tritium on the surface of breeding materials have not been quantified yet, although helium gas with hydrogen or deuterium is planned to be used as the blanket purge gas in the recent blanket designs. The mass transfer coefficient representing the isotope exchange reaction between H_2 and D_2O or that between D_2 and H_2O in the ceramic breeding materials bed is experimentally obtained in this study.

Effects of isotope exchange reactions on the tritium inventory in the bleeding blanket is discussed based on data obtained in this study where effects of diffusion of tritium in the grain, absorption of water in the bulk of grain, and adsorption of water on the surface of grain, together with two types of isotope exchange reactions are considered. The way to estimate the tritium inventory in a Li_2ZrO_3 blanket used in this study shows a good agreement with data obtained in such in-situ experiments as MOZART, EXOTIC-5, 6 and TRINE experiments.

1. Introduction

Lithium ceramic materials such as Li_2O, $LiAlO_2$, Li_2ZrO_3, Li_2TiO_3 and Li_4SiO_4 are considered as the candidates of tritium breeding materials in a D-T fusion reactor. In early blanket designs, He was used as the purge gas. In this method, however, the time to obtain the steady state conditions in recovery of bred tritium becomes long, because the desorption rate of tritiated water is slow. Therefore, it has been proposed to make use of the isotope exchange reaction for enhancement of the tritium release rate from solid breeder materials. In this purpose, hydrogen or deuterium is added to the He purge gas in various in-situ or annealing after irradiation experiments [1, 2].

In order to estimate the release behavior of the bred tritium in a blanket system, it is necessary to know the contribution of such tritium transfer steps as

(1) tritium formation reaction in crystal grain, (2) diffusion of tritium in crystal grain, (3) interaction of tritium with irradiation defects in crystal grain, (4) adsorption of tritium on grain surface, (5) absorption of tritium into crystal grain, (6) isotope exchange reaction between gaseous hydrogen, H_2, in the gas stream and tritium on grain surface (isotope exchange reaction 1), (7) isotope exchange reaction between water vapor, H_2O, in the gas stream and tritium on grain surface (isotope exchange reaction 2), (8) water formation reaction at addition of H_2 to the blanket purge gas, (9) transfer of hydrogen isotopes and water through pores of the sintered pellet and (10) transfer of hydrogen isotopes and water through boundary layer formed on the surface of a sintered pellet to the gas stream,

together with the system effect of tritium, which consists of

(11) adsorption of tritium on piping surface, (12) isotope exchange reaction between gaseous tritium,

HT or T_2, in the gas stream and water or -OH bases on piping surface, (13) isotope exchange reaction between tritiated water in the gas stream and water or -OH bases on piping surface, (14) permeation of tritium through piping materials, (15) absorption of tritium in piping materials and (16) flow condition of purge gas in each sub-unit constituting the blanket piping system,
and the tritium behaviors in the monitor system such as
(17) memory effect and (18) Jesse effect.

Adsorption or desorption and two types of isotope exchange reactions contribute as the surface reactions. Most results of the in-situ experiments so far have been analyzed assuming that the overall release process of bred tritium is mainly controlled by diffusion in the crystal grain. However, it has been pointed out recently that the contribution of surface reactions can not be ignored [2-5]. The present authors have quantified the amount of water captured in Li_2O, $LiAlO_2$, Li_2ZrO_3 and Li_4SiO_4 in the previous papers [6-9].

However, a quantitative consideration of the isotope exchange reactions has not been done yet except for Li_2O reported by the present authors [10]. In the present work, the isotope exchange reaction between hydrogen isotopes in the purge gas and water adsorbed on ceramic breeding materials surface is studied.

Recently, we have presented the way to estimate the tritium inventory in a uniform solid blanket under the steady-state condition considering diffusion, absorption, adsorption and isotope exchange reactions [6]. The estimated tritium inventory for a $LiAlO_2$ blanket using our model agrees well with data observed in various in-situ experiments such as LILA-3 [12], TEQUILA-1 [13], CORELLI-2 [14], MOZART [15], and EXOTIC-6 [16] experiments. It is also reported in our previous reports that the better agreements are observed when the effectiveness correction factor representing the relative values in reaction rate of two isotope exchange reactions is introduced, and when existence of some water vapor is assumed in the purge gas. The same method as that used in calculation of the tritium inventory in a $LiAlO_2$ blanket is applied to estimate the tritium inventory in a Li_2ZrO_3 blanket in this study, and comparisons of the estimated tritium inventory with data from several in-situ experiments are also performed.

2. Experimental

The schematic diagram of the experimental apparatus is shown in Fig. 1. $LiAlO_2$ and Li_2ZrO_3 made by Mitsubishi Atomic Power Industries were packed in the reaction tube made of quartz, and its specifications are shown in Table 1. Changes of H_2, HD and D_2 concentrations at the outlet of sample bed after introduction of the He gas containing D_2O and H_2 or He gas containing H_2O and D_2 were measured using a gas chromatography. The water concentration in the outlet gas of the sample bed was measured with a hygrometer. The gas flow rate was 0.1 to 1.0 *l*/min and it was controlled by a mass flow meter. Each process gas was passed through a cold trap filled with molecular sieve 5A and cooled with ice water to remove the residual water vapor in the process gas. The water concentration in the process gas is controlled by the hydrogen oxidizing method with a CuO bed at 623K. As was reported by the present authors [17], water was formed in the lithium ceramics bed when hydrogen isotopes were added into the He purge gas. To lower the effect of this water formation reaction on estimation of the isotope exchange reaction, the sample bed was step wisely heated up to the experimental temperature by a electric heater in 50 K step confirming that the vapor concentration from water formation reaction become below a few ppm. The experimental conditions are shown in Table 2. The experiments were performed under the steady state conditions.

3. Theory

3. 1. Theoretical consideration for experimental

The isotope exchange reactions would occur on the grain surface of solid breeder materials. In the

present work, H_2 and D_2 are used for the experiment, and therefore exchange reactions concerning hydrogen isotopes (H_2, HD and D_2) and water vapor (H_2O, HDO and D_2O) in the gas phase and adsorbed water (H_2O, HDO and D_2O) on grain surface should be taken into account. If all the exchange reactions are taken into account, the analysis becomes too complex. In addition, it is technically difficult to separate H_2O, HDO and D_2O in the measurement, although H_2, HD and D_2 can be easily separated by a chromatographic method. Therefore, simplified isotope exchange reaction model is used for the present work. In this model, isotope exchange reaction concerning hydrogen isotopes (H_2 and D_2) and water vapor (H_2O and D_2O) in the gas phase and adsorbed water (H_2O and D_2O) on grain surface are only taken into account assuming

$$C_{H_2} = C'_{H_2} + \frac{1}{2} C'_{HD}, \tag{1}$$

$$C_{D_2} = C'_{D_2} + \frac{1}{2} C'_{HD}, \tag{2}$$

$$C_{H_2O} = C'_{H_2O} + \frac{1}{2} C'_{HDO}, \tag{3}$$

$$C_{D_2O} = C'_{D_2O} + \frac{1}{2} C'_{HDO}, \tag{4}$$

where C is the nominal concentration in the gas phase [mol/m^3] and C' is the real concentration [mol/m^3]. The exchange reactions on basis of the simplified model are expressed as

$$H_2(g) + D_2O(s) \leftrightarrow D_2(g) + H_2O(s), \tag{5}$$

$$H_2O(g) + D_2O(s) \leftrightarrow D_2O(g) + H_2O(s). \tag{6}$$

Under the steady state conditions, the mass balance in the sample bed is expressed in the same way for Pt-Alumina catalyst, Pt-M.S.-5A catalyst and other catalysts bed which was obtained by the present authors [18,19] referring Perry's "Chemical Engineering's Handbook"[20],

$$u \frac{\partial C_{H_2}}{\partial z} = -K_{F,ex1} a_v X_1, \tag{7}$$

$$u \frac{\partial C_{D_2}}{\partial z} = K_{F,ex1} a_v X_1, \tag{8}$$

$$u \frac{\partial C_{H_2O}}{\partial z} = -K_{F,ex2} a_v X_2, \tag{9}$$

$$u \frac{\partial C_{D_2O}}{\partial z} = K_{F,ex2} a_v X_2, \tag{10}$$

$$X_1 = C_{D_2} - \frac{(C_{H_2}/K + C_{D_2}) q_{D_2O}}{q_{H_2O} + q_{D_2O}}, \qquad X_2 = C_{D_2O} - \frac{(C_{H_2O} + C_{D_2O}) q_{D_2O}}{q_{H_2O} + q_{D_2O}},$$

where u is the superficial gas velocity [m/s], z is the length in the axial direction of sample bed, $K_{F,ex1}$ is overall mass transfer coefficient of isotope exchange reaction between H_2 in the gas phase and D_2O adsorbed on grain surface [m/s], $K_{F,ex2}$ is overall mass transfer coefficient of isotope exchange reaction between H_2 in the gas phase and D_2O adsorbed on grain surface [m/s], K is equilibrium constant of isotope exchange reaction between H_2 in the gas phase and D_2O adsorbed on grain surface [-], q is concentration of water adsorbed on grain surface [mol/mol].

The boundary conditions at the bed inlet are given as follows in the experimental conditions of

this work.

$$C_{H_2} = C_{H_2,in} \quad (\text{at } z = 0), \tag{11}$$

$$C_{D_2} = 0 \quad (\text{at } z = 0), \tag{12}$$

$$C_{H_2O} = 0 \quad (\text{at } z = 0), \tag{13}$$

$$C_{D_2O} = C_{D_2O,in} \quad (\text{at } z = 0), \tag{14}$$

where $C_{H_2,in}$ and $C_{D_2O,in}$ are H_2 concentration in the process gas at inlet and D_2O concentration at inlet [mol/m^3], respectively. The mass balance in the sample bed gives

$$C_{H_2} + C_{D_2} = C_{H_2,in}, \tag{15}$$

$$C_{H_2O} + C_{D_2O} = C_{D_2O,in}, \tag{16}$$

$$q_{H_2O} + q_{D_2O} = q_{D_2O,in}, \tag{17}$$

and the mass balance about H-atoms and D-atoms gives

$$C_{H_2} = C_{H_2,in} - C_{H_2O}, \tag{19}$$

$$C_{D_2} = C_{D_2O,in} - C_{D_2O}. \tag{20}$$

The experimental condition of this work makes the following approximation possible

$$C_{H_2} \approx C_{H_2,in}, \tag{21}$$

because $C_{H_2,in}$ is much larger than $C_{D_2O,in}$ in this work. It is presumed that the isotope exchange reaction between water vapor and tritium on the surface is much larger than the isotope exchange reaction between gaseous hydrogen and tritium on the surface ($K_{F,ex1} << K_{F,ex2}$).

$$\frac{q_{D_2O}}{q_{D_2O,in}} \approx \frac{C_{D_2O}}{C_{D_2O,in}}. \tag{22}$$

Substitution of Eqs. (20), (21) and (22) into Eq. (8) gives the change of D_2 concentration in the gas phase as

$$u\frac{\partial C_{D_2}}{\partial z} = K_{F,ex1}a_v\left(C_{H_2,in}/K\right)\left\{1-\left(\frac{K}{C_{H_2,in}}+\frac{1}{C_{D_2,in}}\right)\cdot C_{D_2}-1\right\} \tag{23}$$

Then, the following equation is obtained by integration of Eq. (23).

$$K_{F,ex1}a_v = \frac{1}{\tau}\cdot\frac{-K}{M_{in}+K}\cdot\ln\left[1-\frac{M_{in}+K}{M_{in}}\cdot X\right], \tag{24}$$

$$M_{in} = C_{H_2,in}/C_{D_2O,in}, \qquad X = C_{D_2}/C_{D_2O,in},$$

where τ is the average residence time in the sample bed [s] which is given by the bed height divided by superficial gas velocity z_b/u, and M_{in} is the molar ratio of H_2/D_2O at inlet [-] and X is the conversion ratio of D_2O to D_2 [-].

The value of a_v is the specific surface area of the sample grain in packed bed [m^2/m^3], and is given as

$$a_v = (1-\varepsilon_b)(1-\varepsilon_p)\rho A_{BET} \quad [m^2/m^3], \qquad (25)$$

where ε_b is void fraction of packed bed [-], ε_p is void fraction of pellet [-], ρ is theoretical density of grain [g/m^3], and A_{BET} ($= 6/\rho d_p$) is BET surface area [m^2/g].

3. 2. Inventory estimation method

Contributions of diffusion inventory in crystal grains I_D, absorption inventory in bulk of lithium ceramic I_{ab}, adsorption inventory on the grain surface I_{ad} and inventory due to the isotope exchange capacity on the grain surface I_{ex} are discussed in our previous papers [21], and the total tritium inventory in the blanket packed with solid breeder particles made of spherical grains I_{Total} is given as

$$\begin{aligned} I_{Total} &= I_D + I_{ab} + I_{ad} + I_{ex} \\ &= G_T d_p^{\,2}/60D_T + Q_{ab} M P_{T_2O}/(P_{T_2O} + P_{H_2O} + P_{H_2O'}) \\ &\quad + Q_{ad} M P_{T_2O}/\{(P_{H_2}/\alpha_{ex}) + (P_{T_2O} + P_{H_2O} + P_{H_2O'})/\alpha'_{ex}\} \\ &\quad + Q_{ex} M P_{T_2O}/\{(P_{H_2}/\alpha_{ex}) + (P_{T_2O} + P_{H_2O} + P_{H_2O'})/\alpha'_{ex}\} \end{aligned} \qquad (26)$$

where G_T is tritium generation rate in the whole blanket [mol/s], d_p is grain diameter [m], D_T is the effective diffusivity of tritium in grain [m^2/s], M is amount of Li ceramics in blanket [mol], α_{ex} and α'_{ex} is the effectiveness correction factor [-], Q_{ab} is the amount of water absorption [mol/mol], Q_{ad} is the amount of water adsorption [mol/mol] and P_{H_2}, P_{H_2O} and $P_{H_2O'}$ [Pa] are partial pressure of H_2 in the purge gas, H_2O swamped to the purge gas and residual H_2O in the purge gas, respectively.

The partial pressure of tritium in the purge gas, P_{T_2O}, is given as

$$P_{T_2O} = P_{He} G_T / G_{He} \quad [Pa], \qquad (27)$$

where all tritium bred in the grain is considered to be released in the chemical form of water, and P_{He} [Pa] and G_{He} [mol/s] are total pressure of helium purge gas and flow rate, respectively.

It is assumed in the uniform blanket model of this study that the isotope exchange reaction 1 and the isotope exchange reaction 2 competes each other if both H_2 and H_2O exist in the purge gas. In such a case, the effectiveness correction factor shown in Eq. (26) is given by

$$\left.\begin{aligned} \alpha_{ex} &= K_{F,ex2}/K_{F,ex1} \\ \alpha'_{ex} &= 1 \end{aligned}\right\} \quad \text{when} \quad K_{F,ex2} \geq K_{F,ex1},$$

or (28)

$$\left.\begin{aligned} \alpha_{ex} &= 1 \\ \alpha'_{ex} &= K_{F,ex1}/K_{F,ex2} \end{aligned}\right\} \quad \text{when} \quad K_{F,ex2} \leq K_{F,ex1},$$

where $K_{F,ex1}$ and $K_{F,ex2}$ mean the rate constant of the isotope exchange reaction 1 and that of isotope exchange reaction 2, respectively. Accordingly, the effectiveness correction factor means the relative strength of two isotope exchange reactions.

The total partial pressure of water in various forms is given as

$$P = P_{T_2O} + P_{H_2O} + P_{H_2O'} \quad [Pa]. \qquad (29)$$

The mass transfer resistance at transfer of tritium through pores of sintered pellets and that through boundary layer are considered to be negligibly small in this study.

The average residence time of tritium at each transfer step is given by division of inventory by the tritium generation rate. Then, the total average residence time in a solid breeder blanket is given as

$$\theta_{Total} = (I_D + I_{ad} + I_{ab} + I_{ex})/G_T$$
$$= \theta_D + \theta_{ad} + \theta_{ab} + \theta_{ex} \quad [s]. \quad (30)$$

As can be seen from above equations, the effects of tritium generation rate, temperature, grain size, partial pressure of H_2, partial pressure of water vapor or flow rate of purge gas on each tritium inventory are different. Accordingly, it is necessary to understand the all mass transfer steps dominating the tritium migration behavior before estimation of the tritium inventory in the blanket operated under a certain condition. Other than the tritium inventory in the blanket material, the tritium inventory in the piping system, I_{System} arisen from the system effect of tritium should be also taken into account when small amount of tritium with high T/H ratio is handled in a piping system with large surface area.

4. Results and Discussions

4. 1. Isotope exchange reaction rate

The observed values for the overall mass transfer capacity coefficients representing the isotope exchange reaction on $LiAlO_2$ and Li_2ZrO_3 are shown in Fig. 2 where evaluation using Eq. (24) is performed assuming K is unity. Agreement of data under various experimental conditions implies that equations for the isotope exchange reaction on $LiAlO_2$ and Li_2ZrO_3 would be propre. The squares and circles are obtained experimental values for $LiAlO_2$ and Li_2ZrO_3 respectively. The open squares and circles in Fig. 2 indicating the isotope exchange reaction between H_2 in gas phase and D_2O on grain surface, shows the same tendency as the solid squares and circles indicating the isotope exchange reaction between D_2 in gas phase and H_2O on grain surface. Therefore, the value of K in Eq. (24) decided to be 1. This observation implies that there is no isotope effect in the isotope exchange reaction between gaseous hydrogen isotopes in the purge gas and water adsorbed on grain surface. Accordingly, it can be said that the following correlative equation can be applied to the tritium-hydrogen or tritium-deuterium system. The following equation is obtained from Fig. 2 as the mass transfer capacity coefficient representing the isotope exchange reaction on the $LiAlO_2$ and Li_2ZrO_3 surface of this work.

$$K_{F,exl}a_v = 6.26 \times 10^8 \exp(-134[\text{kJ/mol}]/RT) \quad (\text{for } LiAlO_2) \quad [s^{-1}], \quad (31)$$
$$K_{F,exl}a_v = 3.40 \times 10^7 \exp(-121[\text{kJ/mol}]/RT) \quad (\text{for } Li_2ZrO_3) \quad [s^{-1}]. \quad (32)$$

The value of a_v is 3.40×10^5 m^{-1} and 2.12×10^5 m^{-1} for $LiAlO_2$ and Li_2ZrO_3 bed in this work. Therefore, the overall mass transfer coefficient representing the isotope exchange reaction $K_{F,exl}$ is obtained as

$$K_{F,exl} = 1.84 \times 10^3 \exp(-134[\text{kJ/mol}]/RT) \quad (\text{for } LiAlO_2) \quad [\text{m/s}], \quad (33)$$
$$K_{F,exl} = 1.60 \times 10^2 \exp(-121[\text{kJ/mol}]/RT) \quad (\text{for } Li_2ZrO_3) \quad [\text{m/s}]. \quad (34)$$

Figure 3 shows the comparison of $K_{F,exl}$ obtained for $LiAlO_2$ and Li_2ZrO_3 in this work with $K_{F,exl}$ for Li_2O which is evaluated in the same way for this work using data reported in the previous paper [10]. The value of $K_{F,exl}$ for Li_2O is obtained as

$$K_{F,exl} = 8.55 \times 10^3 \exp(-143[\text{kJ/mol}]/RT) \quad (\text{for } Li_2O) \quad [\text{m/s}], \quad (35)$$

and it is about the same value that for $LiAlO_2$ and Li_2ZrO_3 in the temperature range shown in Fig. 3.

4. 2. Tritium inventory estimation

4. 2. 1. Surface inventory

The present authors have observed the amount of water adsorbed onto the surface of Li_2ZrO_3 is given as

$$Q_{ad} = 6.3 \times 10^{-6} A_{BET} P^{1/2} \exp(10.7[\text{kJ/mol}]/RT) \quad [\text{mol/mol}]. \quad (36)$$

It is also observed in the recent study that Li_2ZrO_3 has no isotope exchange capacity which is attributed to the -OH bases strongly bounded to the grain surface, though $LiAlO_2$, Li_4SiO_4 and Li_2O have a fair amount of the isotope exchange capacity in addition to the adsorption capacity [21]. No absorption capacity of H_2 or H_2O into bulk of Li_2ZrO_3 particles has been observed in our study [9]. Accordingly, the surface inventory of tritium in a Li_2ZrO_3 blanket depends only on the adsorption inventory.

The present authors also have presented the following equation for the rate constant of the isotope exchange reaction between H_2O in the purge gas and tritium on the surface of 304SS and Aluminum [22].

$$K_{F,ex2} = 2.20 \times 10^{-4} \quad \text{[m/s]}, \qquad (37)$$

and $K_{F,ex1}$ is obtained in this study as Eq. (34).

The effectiveness correction factors defined in eq. (28), α_{ex} and α'_{ex} are evaluated using above equations in this study as shown in Fig. 4, assuming that $K_{F,ex2}$ on Li_2ZrO_3 is similar to $K_{F,ex2}$ on 304SS. Then, the surface inventory of tritium in a Li_2ZrO_3 blanket can be evaluated for various conditions using Eqs. (27), (28) and (29).

The total residence time of tritium in the Li_2ZrO_3 bed measured in the EXOTIC-6 experiment by Kwast et al. [16] are compared by the average residence times due to surface inventory on Fig. 5-a which are estimated following the way presented in this study. It is known from this figure that the surface inventory controls the total tritium inventory in the Li_2ZrO_3 bed of the EXOTIC-6 experiment when the bed temperature is higher than 650K, because the surface inventory estimated for various conditions agree with data observed by Kwast et al. It is also concluded from this comparison that some amount of water vapor exists in the blanket purge gas because assumption of existence of water vapor gives better agreement. In the latest paper, Kwast et al. reported that the bed temperature in their EXOTIC experiments could have been lower than the observed temperature by about thirty degrees [23]. In that case, the good agreement of our estimation with their data is obtained when existence of water vapor of 10 ~ 20 pascals (35 ~ 70 ppm) is assumed in their purge gas. However, the higher observed temperature is used in the further discussion of their study because no observed evidence is presented in their discussion about the temperature gradient in Li_2ZrO_3 bed.

4. 2. 2. Diffusion inventory

The total residence time observed in the EXOTIC-6 experiment rapidly increases with decrease of temperature in the lower temperature range than 600 K as shown in Fig. 5-a. Two causes can be presented to explain this tendency. One is to explain by increase of the effective diffusivity of tritium in grain and the other is to explain by sorption phenomena of tritium to the piping surface of the experimental apparatus. It is reasonably assumed that interaction of tritium with irradiation defects makes the tritium transfer rate in grain so slow. Accordingly, it is taken in this study for the time being that the diffusion process of tritium in Li_2ZrO_3 grains gives the main effect on the total residence time in the lower temperature range as shown in Fig. 5-b, though the residence time due to diffusion is only one-thousandth of the total residence time observed in the EXOTIC-6 experiment when the diffusivity of tritium by Kudo and Okuno [24] is used in estimation.

Then, the effective diffusivity of tritium in Li_2ZrO_3, which represents the results of in-situ experiment well, is given as

$$D_T = 2.5 \times 10^{-3} \exp(-131[\text{kJ/mol}]/RT) \quad [\text{m}^2/\text{s}]. \qquad (38)$$

The total residence times observed in the EXOTIC-5 and MOZART experiments are compared by the estimated total average residence time in Fig. 6 and 7. The estimated values of this study show good agreement with those data when existence of water vapor in the purge gas is assumed.

4. 2. 3. Inventory in piping system

The total residence times measured in the TRINE experiment by Alvani et al. [25] are shown in Fig. 8-a for both cases where He with 20 Pa H_2 and He with 200 Pa H_2 are used as Li_2ZrO_3 bed purge gas, and the tendency of these data is not well explained by Eq. (26) of this study. It can be assumed that the system effect is remarkable in the TRINE experiment because the tritium generation rate is only one-seventeenth of the EXOTIC-6 experiment. The packed bed of Zn particles placed to convert HTO to HT in the TRINE experiment also contributes to increase the system effect, because it has been experienced by the present authors that the Zn bed traps some amount of tritium. If the overall residence time due to the system effect of the TRINE experiment is assumed to be 20 hours for the case where 20 Pa H_2 is used and 2 hours for the case where 200 Pa H_2 is used, the observed residence time in the TRINE experiment can be well represented by the estimated curves as shown in Fig. 8-b. Because the system effect arisen from the sorption behavior of tritium to the piping surfaces can change the shape of the response curve of tritium especially when a small amount of tritium is handled in a long piping, the quantitative clarification about the sorption behaviors of tritium on piping surfaces is also required for further discussions on release behaviors of tritium from lithium ceramic materials.

5. Conclusions

The overall mass transfer coefficients of isotope exchange reaction between H_2 and D_2O or that between D_2 and H_2O on $LiAlO_2$ and Li_2ZrO_3 is obtained by the steady state experimental method. And an isotope effect for isotope exchange reaction between H_2 and D_2O or that between D_2 and H_2O on $LiAlO_2$ or Li_2ZrO_3 is not observed in this work.

The tritium inventory in the Li_2ZrO_3 blanket under the uniform and steady state condition is estimated by considering the processes of diffusion in grain, adsorption on the grain surface and two isotope exchange reactions between H_2 or H_2O and tritium on the grain surface.

Estimation using the model of this study gives a good agreement with total residence time reported in various in-situ experiments for Li_2ZrO_3 when the effective diffusivity evaluated in this study using the residence time reported by Kwast et al. (EXOTIC-6) is applied.

It is also observed that system effect arisen from interaction of tritium with piping surfaces of the experimental apparatus can give profound effects on estimate of tritium inventory.

References

[1] H. Kwast et al., *J.* Nucl. Mater. 155-157 (1988) 558.

[2] T. Kurasawa, H. Watanabe and G.W. Hollenberg, *J.* Nucl. Mater. 155-157 (1988) 544.

[3] H. Werle et al., J. Nucl. Mater. 155-157 (1988) 538.

[4] J.P. Kopasz, S. W. Tam and C. E. Johnson, *J.* Nucl. Mater. 155-157 (1988) 500.

[5] G. Federici, A. R. Raffray and M. A. Abdou, *J.* Nucl. Mater. 173 (1990) 185.

[6] K. Munakata, M. Nishikawa and K. Yoneda, Fusion Technol. 15 (1989) 1451.

[7] Y. Kawamura et al., *J.* Nucl. Sci. Technol. 29 (1992) 436.

[8] Y. Kawamura, M. Nishikawa and K. Tanaka, *J.* Nucl. Mater. 208 (1994) 308.

[9] Y. Kawamura, M. Nishikawa, *J.* Nucl. Mater. 218 (1995) 218.

[10] K. Munakata and M. Nishikawa, *J.* Nucl. Mater. 170 (1990) 187.

[11] M. Nishikawa, A. Baba and Y. Kawamura, *J.* Nucl. Mater. 246 (1997) 1-8.

[12] M. Briec et al., *J.* Nucl. Mater. 155-157 (1988) 549.

[13] C. Alvani et al., *J.* Nucl. Mater. 208 (1994) 259.

[14] C. Alvani et al., Proc. Int. Workshop on Ceramic Breeder Blanket Interact., Los Angels, June,

(1994) P.22-24.
[15] M. Briec et al., Proc. 15th SOFT Conf., Utrecht, Sept., (1988) P.19-23.
[16] H. Kwast et al., Private communication, partly reported in Proc. Int. Workshop on Ceramic Breeder Blanket Interact., Tokyo, Oct. (1992) P.22-25.
[17] Y. Kawamura, M. Nishikawa, T. Shiraishi and K. Okuno, *J.* Nucl. Mater. 230 (1996) 287.
[18] M. Nishikawa, T. Takeishi, K. Munakata and S. Izumi, *J.* Nucl. Sci. Technol. 26 (1989) 261.
[19] M. Nishikawa, K. Munakata, S. Izumi and T. Takeishi, *J.* Nucl. Mater. 161 (1989) 182.
[20] R. H. Perry, G. W. Green, Perry's Chemical Engineering Handbook (McGraw-Hill, 1984).
[21] A. Baba, M. Nishikawa, Y. Kawamura and K. Okuno, *J.* Nucl. Mater. Now printing.
[22] M. Nishikawa et al., Fall Meeting of the Atomic Energy Society of Japan, Okinawa, Oct. B52 (1997) [in Japanese].
[23] H. Kwast et al. *J.* Nucl. Mater. 212-215 (1994) 101.
[24] H. Kudo and K. Okuno, *J.* Nucl. Mater. 155-157 (1988) 524.
[25] S. Casadio et al., Proc. 4th Int. Workshop on Ceramic Breeder Blanket Interact., Kyoto, Oct. (1995) P.400-408.

Table 1 Specifications of $LiAlO_2$ and Li_2ZrO_3 pellet used in this work.

Sample		$LiAlO_2$	Li_2ZrO_3
Theoretical density	[g/m^3]	2.60×10^6	4.15×10^6
Density	[g/m^3]	2.21×10^6 (85%T.D.)	3.57×10^6 (86%T.D.)
Grain size	[μm]	20	13
Pellet size		12～16 mesh	1.0 mmϕ
BET surface area	[m^2/g]	0.29	0.09
Specific surface area of bed	[m^{-1}]	3.40×10^5	2.12×10^5
Void fraction of packed bed	[-]	0.47	0.34

Table 2 Experimental conditions.

Sample		$LiAlO_2$	Li_2ZrO_3
Concentration of H_2	[ppm]	4000	2500～10000
Concentration of D_2O	[ppm]	260	100～600
Molar ratio of H_2/ D_2O at inlet	[-]	15	6～23
Concentration of D_2	[ppm]	3200	2100～2900
Concentration of H_2O	[ppm]	290	170～550
Molar ratio of D_2/ H_2O at inlet	[-]	11	8～16
Amount of sample	[g]	7.5	40.0
Temperature range	[K]	648～873	573～873
Gas flow rate	[*l*/min]	0.1 - 1.0	0.1 - 1.0

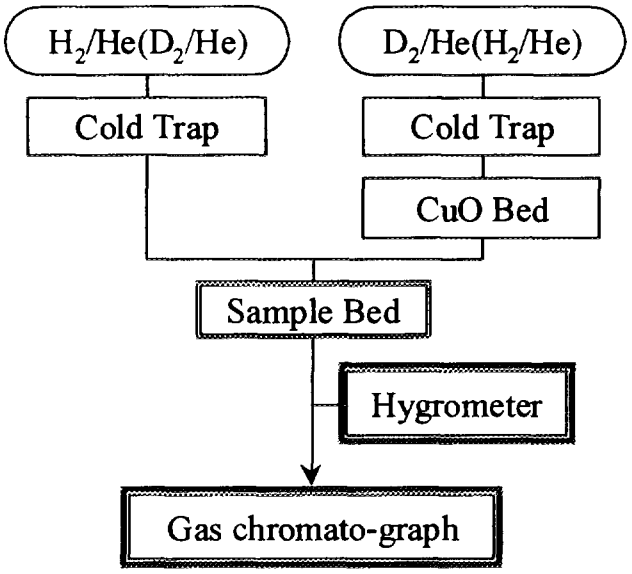

Fig. 1 The schematic diagram of the experimental apparatus.

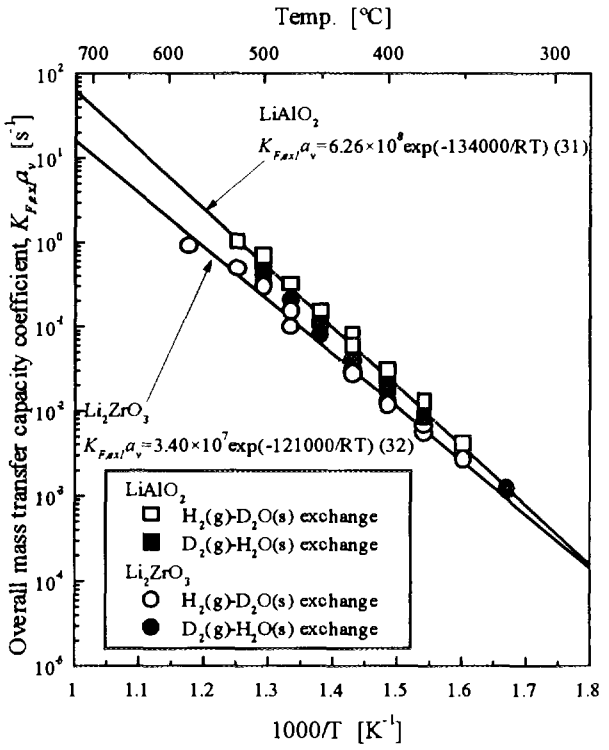

Fig. 2 The overall mass transfer capacity coefficient of representing isotope exchange reaction on $LiAlO_2$ and Li_2ZrO_3.

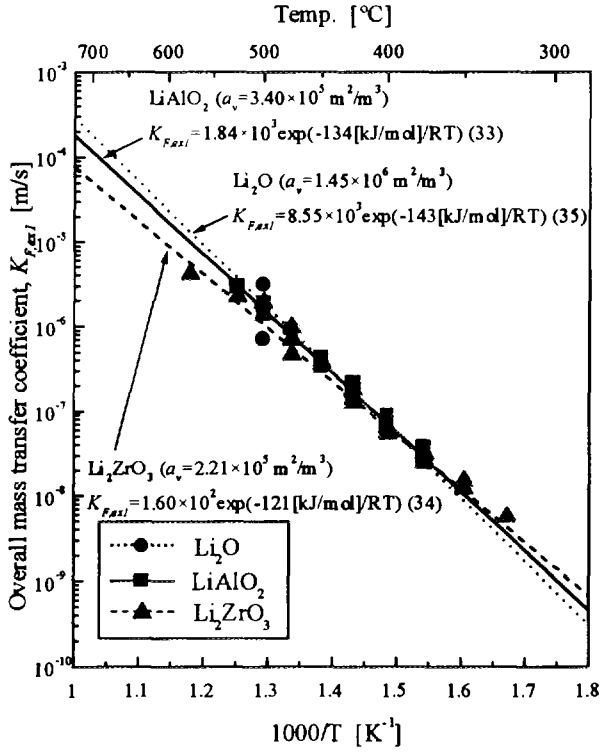

Fig. 3 The comparison of $K_{F,ex1}$ obtained for $LiAlO_2$ and Li_2ZrO_3 in this work with $K_{F,ex1}$ for Li_2O which is evaluated in the same way for $LiAlO_2$ and Li_2ZrO_3 using data reported in the previous paper [10].

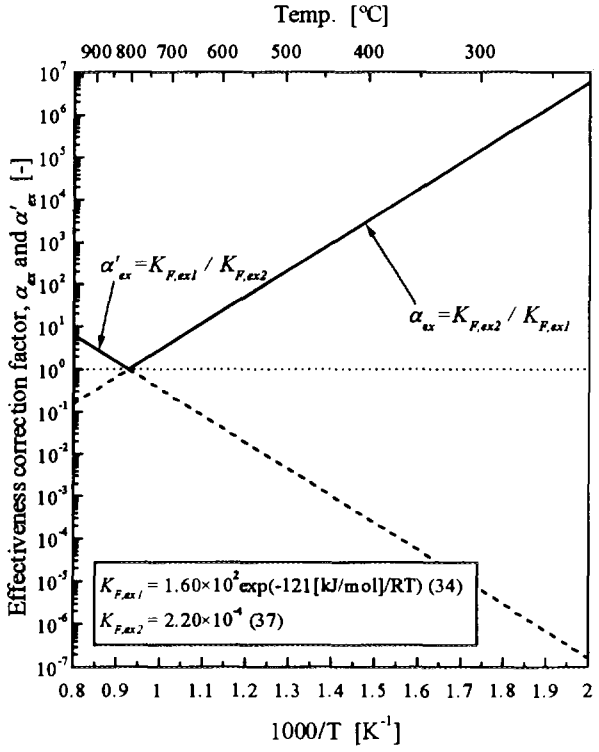

Fig. 4 Temperature dependency of effectiveness correction factor.

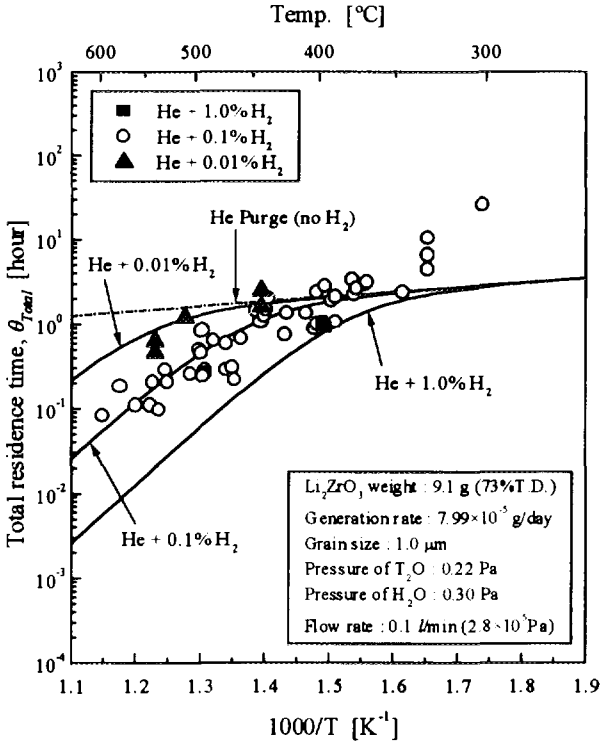

Fig. 5-a Comparison of estimated residence time due to surface inventory with observed total residence time at EXOTIC-6 experiment.

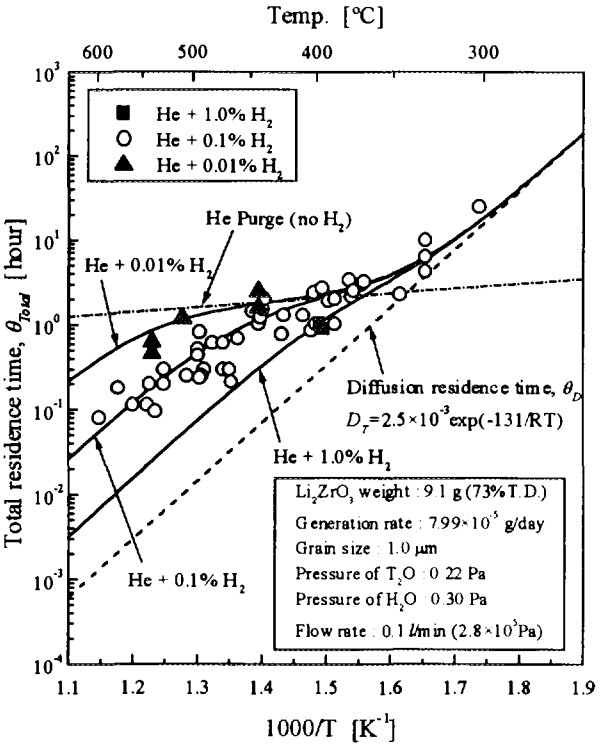

Fig. 5-b Comparison of estimated total residence time with observed total residence time at EXOTIC-6 experiment.

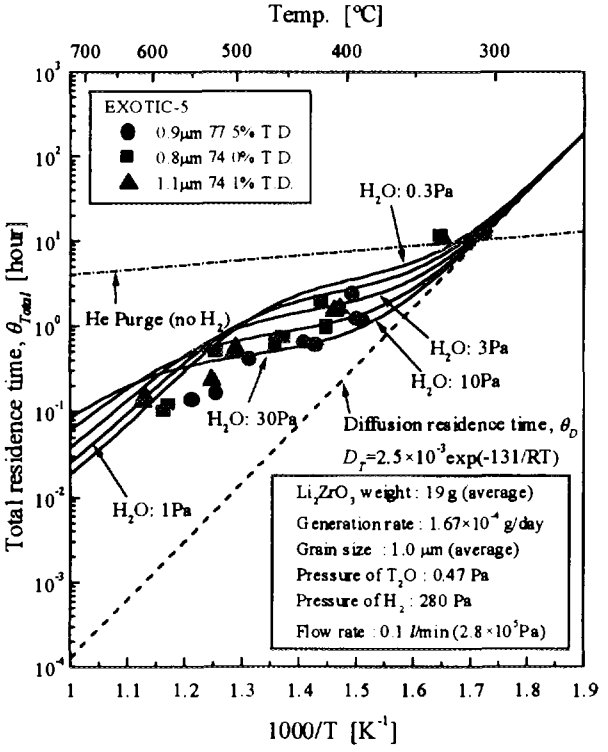

Fig. 6 Comparison of estimated values of total residence time with observed residence time at EXOTIC-5 experiment.

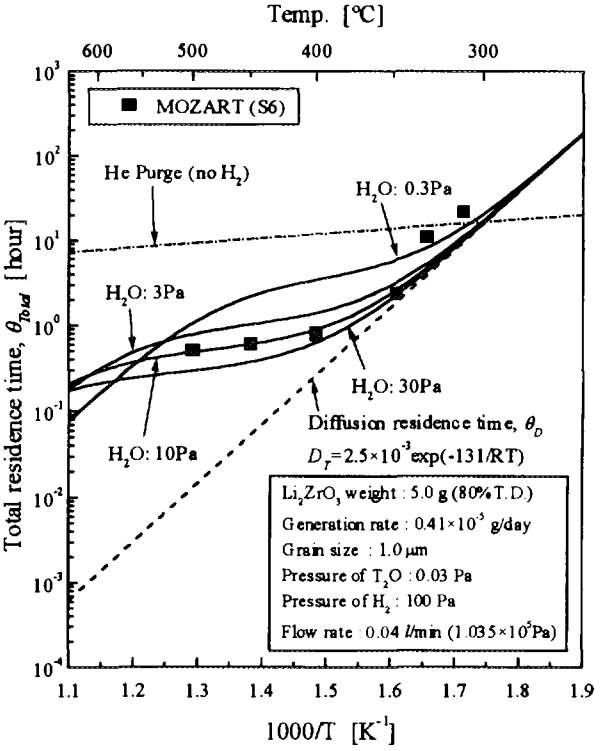

Fig. 7 Comparison of estimated values of total residence time with observed residence time at MOZART experiment.

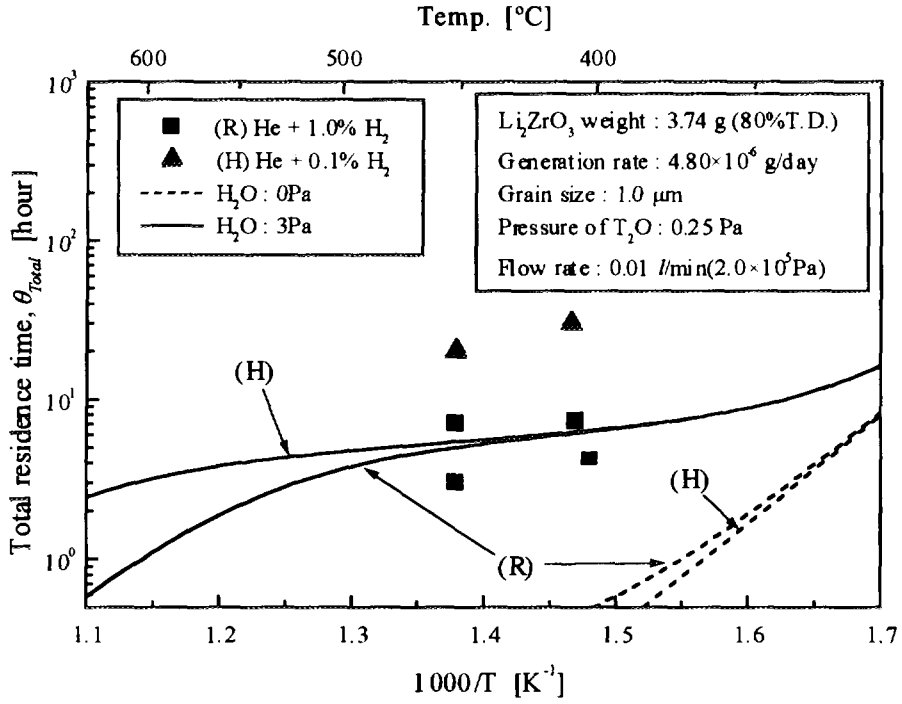

Fig. 8-a Comparison of estimated values of total residence time with observed residence time at TRINE experiment.

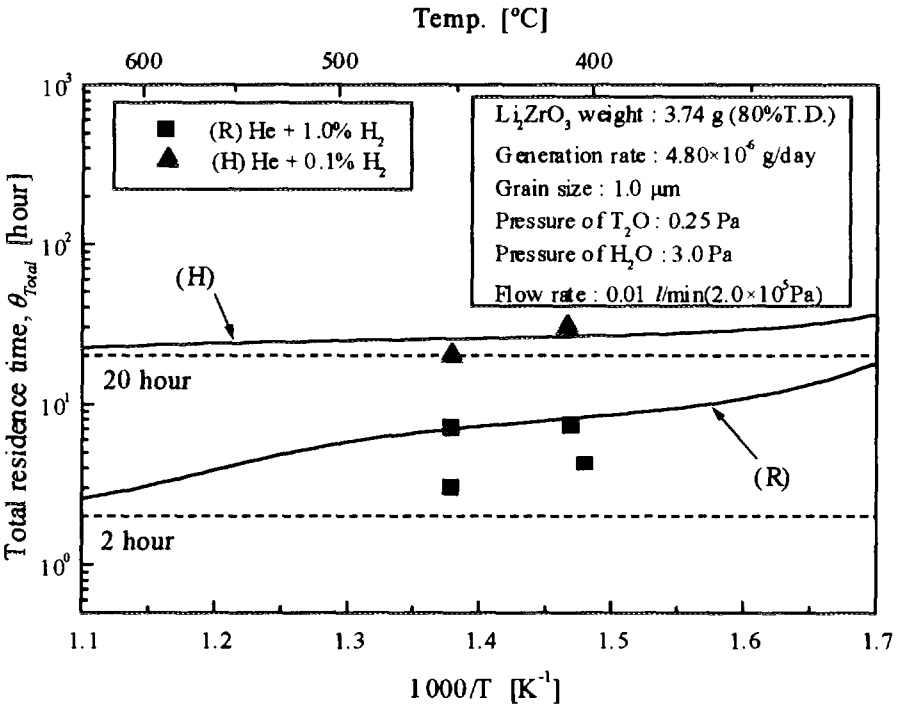

Fig. 8-b Comparison of estimated values of total residence time with observed residence time at TRINE experiment where residence time due to the system effect is taken into account.

Nomenclatures

A_{BET} : BET surface area [m^2/g],
a_v : specific surface area of the grain in packed bed [m^2/m^3],
C : nominal concentration in the gas phase [mol/m^3],
C' : real concentration [mol/m^3],
$C_{H_2,in}$: H_2 concentration in the process gas at inlet [mol/m^3],
$C_{D_2O,in}$: D_2O concentration at inlet [mol/m^3],
D_T : effective diffusivity of tritium in grain [m^2/s]
d_p : grain diameter [m],
G_{He} : flow rate of He purge gas [mol/s],
G_T : tritium generation rate in the whole blanket [mol/s],
I_{ab} : absorption inventory in bulk of lithium ceramic [mol],
I_{ad} : adsorption inventory on the grain surface [mol],
I_D : tritium inventory in crystal grains [mol],
I_{ex} : inventory due to the isotope exchange capacity on the grain surface [mol],
I_{Total} : total tritium inventory in the [mol],
$K_{F,ex1}$: overall mass transfer coefficient of isotope exchange reaction between hydrogen isotopes in the gas phase and water adsorbed on grain surface [m/s],
$K_{F,ex2}$: overall mass transfer coefficient of isotope exchange reaction between water vapor in the gas phase and tritium adsorbed on grain surface [m/s],
K : equilibrium constant of isotope exchange reaction between H_2 in the gas phase and D_2O adsorbed on grain surface [-],
M : amount of Li ceramics in blanket [mol],
M_{in} : molar ratio of H_2/D_2O at inlet [-],
P_{H_2} : partial pressure of H_2 in the purge gas [Pa],
P_{H_2O} : partial pressure of H_2O swamped to the purge gas [Pa],
$P_{H_2O'}$: partial pressure of residual H_2O in the purge gas [Pa],
P_{He} : total pressure of helium purge gas [Pa],
Q_{ab} : amount of water absorption [mol/mol],
Q_{ad} : amount of water adsorption [mol/mol],
q : concentration of water adsorbed on grain surface [mol/mol],
u : superficial gas velocity [m/s],
X : conversion ratio of D_2O to D_2 [-],
z : length in the axial direction of sample bed [m],
α_{ex}, α'_{ex}: effectiveness correction factor [-],
ε_b : void fraction of packed bed [-],
ε_p : void fraction of pellet [-],
ρ : theoretical density of grain [g/m^3],
τ : average residence time in the sample bed [s],
θ_{ab} : average residence time of tritium due to absorption [s],
θ_{ad} : average residence time of tritium due to adsorption [s],
θ_D : average residence time of tritium due to diffusion in crystal grains [s],
θ_{ex} : average residence time of tritium due to inventory due to the isotope exchange capacity [s],
θ_{Total} : total average residence time of tritium in the blanket [s].

Description of Tritium Release From Lithium Titanate at Constant Temperature

L. Peña, S. Lagos, J. Jiménez, E. Saravia.

Comisión Chilena de Energía Nuclear
Centro de Estudios Nucleares La Reina
Casilla 188-D, Santiago - CHILE

Abstract

Lithium Titanate Ceramics have been prepared by the solid-state route, pebbles and pellets were fabricated by extrusion and their microstructure was characterized in our laboratories. The ceramic material was irradiated in the La Reina Reactor, RECH-1. A study of post-irradiation annealing test, was performed measuring Tritium release from the Lithium Titanate at constant temperature. The Bertone's method modified by R. Verrall is used to determine the parameters of Tritium release from Lithium Titanate.

Description of Tritium Release From Lithium Titanate at Constant Temperature

L. Peña, S. Lagos, J. Jiménez, E. Saravia.

Comisión Chilena de Energía Nuclear
Centro de Estudios Nucleares La Reina
Casilla 188-D, Santiago - CHILE

Abstract

Lithium Titanate Ceramics have been prepared by the solid-state route, pebbles and pellets were fabricated by extrusion and their microstructure was characterized in our laboratories. The ceramic material was irradiated in the La Reina Reactor, RECH-1. A study of post-irradiation annealing test, was performed measuring Tritium release from the Lithium Titanate at constant temperature. The Bertone's method modified by R. Verrall is used to determine the parameters of Tritium release from Lithium Titanate.

Introduction

The Comisión Chilena de Energía Nuclear, CCHEN, initiated four years ago several activities to develop the capability to produce high quality Lithium Ceramics of potencial use in breeding blankets for fusion reactors.

Lithium Metatitanate Ceramics conformed as pebbles and pellets were prepared, fabricated and characterized the Laboratories at CCHEN. this was followed by the irradiation in RECH-1 in core.
This study is part of the project named as "Development of Lithium Ceramics to Fusion Reactors", sponsored by the International Atomic Energy Agency, IAEA, by which technical assistance of experts has been received from Argonne National Laboratory and Chalk River Laboratories.

The results of post-irradiation annealing tests, obtained by measuring out-reactor Tritium release from the Lithium Titanates at constant temperature, are examined. The Bertone's method modified by R. Verrall is applied to the release data to help in distinguishing the processes involved, and to determine the diffusion or desorption coefficients of Tritium release from cylindricals pebbles and pellet of Lithium Titanate.

Fabrication and characterization of pebbles and pellets

Lithium Metatitanate Ceramics conformed as pebbles and pellets were prepared, fabricated and characterized at the Laboratories of CCHEN

Scheme of Preparation and Fabrication:

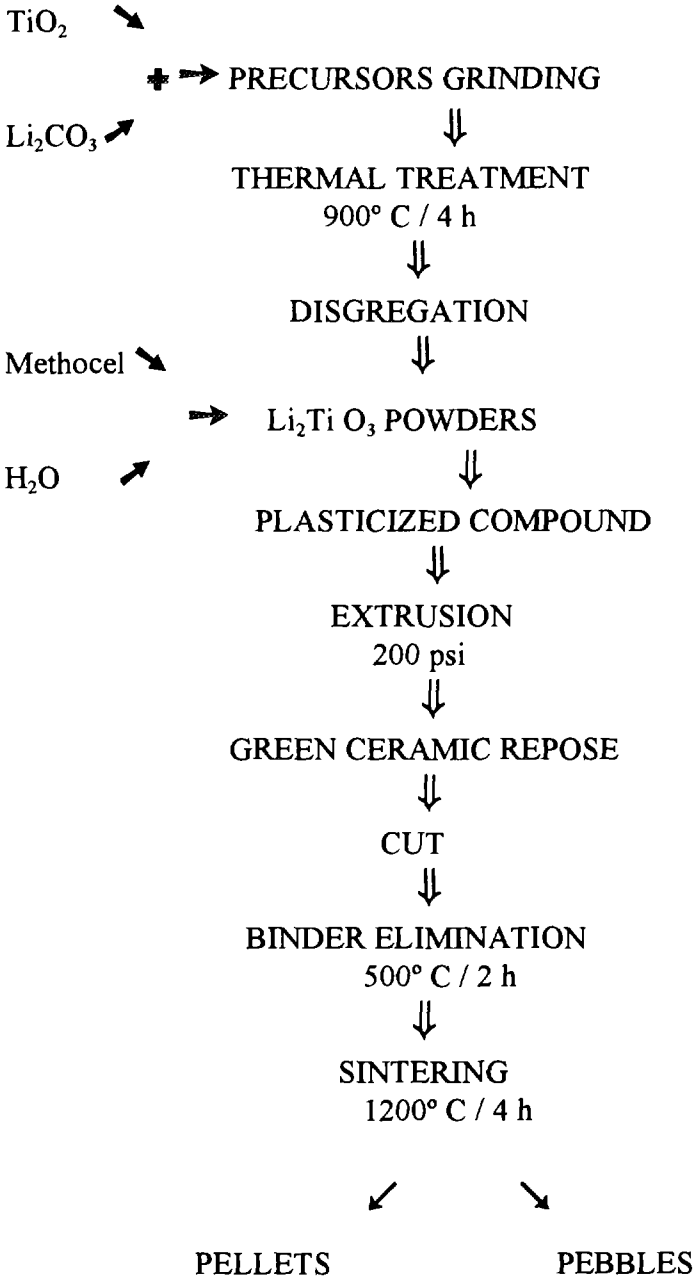

Powder characteristics are as follows:

TABLE # 1

Crystalline Structure : β-phase monoclinic
Grain Size (Master Size) : 20 μm (average)
Density : 3.47 g/cc
Surface Area (BET Method):0.69 m^2/g

Ceramics have the following characteristics:

TABLE # 2 , $Li_2Ti\ O_3$ PEBBLES

Crystalline Structure : β-phase monoclinic
Average weight : 2.546 mg
Average volume : 0.000995 cc
Apparent density : 2.56 g/cc
Density, He picnometry : 3.38 g/cc
Tap density : 1.13 g/cc
Surface area : 0.652 m^2/g
% Total porosity : 25.58 %
% Open porosity : 23.84 %
% Close porosity : 1.74%
Open / Total porosity : 0.93

TABLE # 3 , $Li_2Ti\ O_3$ PELLETS

Crystalline Structure : β-phase monoclinic
Average weight : 0.265 g
Average volume : 0.1002 cc
Apparent density : 2.64 g/cc
Density, He picnometry : 3.32 g/cc
% Porosity, (Hg) :15.43 %
% Total porosity : 23.26 %
% Open porosity : 19.77 %
% Close porosity : 3.49 %
Open / Total porosity : 0.85
Average pores' radius :0.065 μm

R. Verrall's Modifications of Bertone's Formulation

The Bertone's method modificated by Verrall, [2] for distinguishing diffusion- controlled release from desorption-controlled release, is shortly shown.

When this method applied to test sintered Li_2TiO_3 pebbles and pellets; a first order desorption seems to be the control mechanism for the Tritium release for this tests.

From the Fick's first law the following approximation suffices to describe when the Tritium release from a sphere of radius **a** is controlled by diffusion:

$$f = 6 \cdot \left(\frac{Dt}{\pi a^2}\right)^{1/2} - 3 \cdot \frac{Dt}{a^2} \quad , \text{for } f \leq 0.95 , \quad \text{Eq. (2)}$$

where **f** is the fractional Tritium release at time **t**, and
D is the diffusion coeffient (cm^2/s) at temperature **T**.

When the release is controlled by desorption from the surface the following differential equation for **c(t)** applies:

$$\frac{dc(t)}{dt} = -k \cdot c \cdot (t)^n \qquad \text{Eq. (3)}$$

where **c(t)** is the concentration in the sample
k is the desorption coefficient, and
n is the order of desorption

For 1st and 2nd order desorption, eq.(3) has the following solutions:

$$f = 1 - e^{-kt} \quad , \quad \text{1st order} \qquad \text{Eq. (4)}$$

$$f = \frac{kt}{1+kt} \quad , \quad \text{2nd order} \qquad \text{Eq. (5)}$$

The actual quantity to be measured with the ionization chamber is the Tritium recovery rate, r (t), i.e., the amount of Tritium per unit time, which derivatives of equations 2, 4, and 5.

Thus, the recovery rate could be written as follows:

$$r(t) = 6A \cdot \left(\frac{D}{\pi a^2 t}\right)^{1/2} - 3 \cdot \frac{AD}{a^2} \qquad \text{for diffusion, Eq(6)}$$

$$r(t) = A \cdot k \cdot e^{-kt} \qquad \text{for 1st order desorption, Eq. (7)}$$

$$r(t) = \frac{Ak}{(1+k \cdot t)^2} \qquad \text{for 2nd order desorption, Eq. (8)}$$

where **A** is the total Tritium recovered during the release time **t**.

The Equation (6) diverges at **t**=0, so in practice, the recovery rate of Tritium will never follow the diffusion relation, even when the release is controller by diffusion.

Therefore, good fitting could be obtain from Eq. (2) for diffusion and Eq. (7) and Eq.(8) for desorption.

R. Verrall has shown that, althougth for all Tritium release curves the limit:

$$\lim_{t\to 0}\frac{d\ln(f)}{d\ln(t)}=1 \quad ,$$

diffusion and desorption control can still be distinguished by examining the curve:

$$\frac{d\ln(f)}{d\ln(t)}\cdot \text{versus}\cdot t \quad ,$$

for time **t** greater than zero, i.e., many time the **instrument time constat** τ, given by:

$$\tau=\frac{V}{F} \quad ,$$

where **V** is the chamber volumen, and **F** is the gas flow rate.

In our system, the OHT ionization chamber has a volumen of 200cc and a flow rate of about 67 cc/min, giving an instrument time constat of τ=3 min.

Application of the Model to $Li_2Ti\,O_3$

A quantity, close to 300 mg, of Lithium titanate in form of pebbles and pellets were obtained in our laboratories and then were irradiated in RECH-1 reactor, under a thermal neutron flux of 3.3×10^{13} n/cm^{2}s, for a periods of 20 hours for pebbles and 40 hours for pellets.

The samples were vacuum annealed at 5×10^{-6} mBar in quartz glass tubes and then sealed for irradiation without exposure to air. The total Tritium release at 300°C with He/H 0.1%, was measured on line, in an ionization chamber.

The mesurements of the rate of Tritium release from the ionization chamber are obtained with a Keithley 617 electrometer, the results are shown in Fig. 1 for pebbles and in Fig 2 for pellets.

From an electronic sheet, these release **rate data**, r(t), was integrated (trapezoid formula) and multipied by the total tritium recovered to obtain the **fractional Tritium release**, f(t).

The curves Ln(f) versus Ln(t) are got using the software Table Curve 2D, Fig 3 for pebbles and Fig 4 for pellet respectively. Finally differentiated in proper manner to obtain the funtion dLn(f)/dLn(t) versus time which are illustrated on the Fig 5 and 6 for each case.

The shape of the logarithmic derivative curve is smooth from the maximum toward zero, both branches of the curve have a symmetry in relation to the axis. This is typical of the desorption controller release.

The shape for the diffusion controlled is markedly different, with no symmetry, dropping rapidly and with a long cue.

Therefore, the release rate data was fitted, customizing the Eq. 7, Eq. 8 and a linear combination of them with software Table Curve.

The Figure 7 shows a fitting of the recovery rate data to the predictions of first order desorption. Thus the release function for the pebbles at 300° C is of the form:

$$r(t) = B + A \cdot k \cdot e^{-k \cdot t}$$

that is,

$$r(t) = 0.47 + 79.3 \cdot 0.3 \cdot e^{-0.3 \cdot t}$$

where the desorption constant is given by k=0.3 min^{-1}.

Figure 8 shows a best fitting of the recovery rate data with a linear combination of two frst order equations. Thus the funtion release for the pellets at 300° C is of the form:

$$r(t) = B + A_1 \cdot k_1 \cdot e^{-k_1 \cdot t} + A_2 \cdot k_2 \cdot e^{-k_2 \cdot t}$$

that is,

$$r(t) = 19.9 + 138.16 \cdot e^{-0.0155 \cdot t} + 908.04 \cdot e^{-0.1968 \cdot t}$$

For pellets the values of k are therefore 1.55×10^{-2} and 0.1968 min^{-1}.

Conclusions

The Chilean Nuclear Energy Commission has produced high quality Lithium ceramics, by solid state reaction, extrusion and sintering, to contribute to the knowlege of the tritium breeding materials in Fusion Reactor research. The next and natural step is to obtain these ceramics in the form of spheres.

The Verrall's modifications of the Bertone's formulation are reliable, to determinate the parameter of a mechanism of Tritium release.

The information that provides the logarithmic derivative curves, dLnf(t) / dLn(t), as a equation of time is sufficient to distinguish the diffusion and desorption controlling mechanism of Tritium release.

The behavior of the logarithmic derivatives for tests on $Li_2Ti\ O_3$ indicate that the release is controlled by first order desoption at 300° C; one first order desorption for pebbles and a linear combination of two first order desoption for the pellet.

Reliable data on Tritium desorption has been obtained from $Li_2Ti\ O_3$ at 300° C, for pebbles with a desorption constant, k=0.3 min^{-1}. For the pellets the k-values are 0.1968 min^{-1} and 1.55×10^{-2} min^{-1}

With pebbles the time constant value obtained from respective the fitting curve is τ =3.3 min (1/0.3min) The same parameter obtained from the volume chamber and the flow is of 3 min.

The values of the desoption coefficient are within the order of magnitude for those reported in the literature [2]

References

1.- P. C. Bertone , The Kinetics that Govern the Release of Tritium from Neutron Irradiated Lithium Oxide, J. Nucl. Mater. 151(1988) 345-351.

2.- R. A. Verrall and J. M. Miller, Tritium Release from Lithium Ceramics at Constant Temperature: Analysis Methods. Cer Trans. Vol 27, Fab. and Properties of Lithium Ceramics III (1992) 265-280.

3.- C.E. Johnson et al., "Ceramics Breeder Materials", J. Nucl. Materials 155 (1988) 188

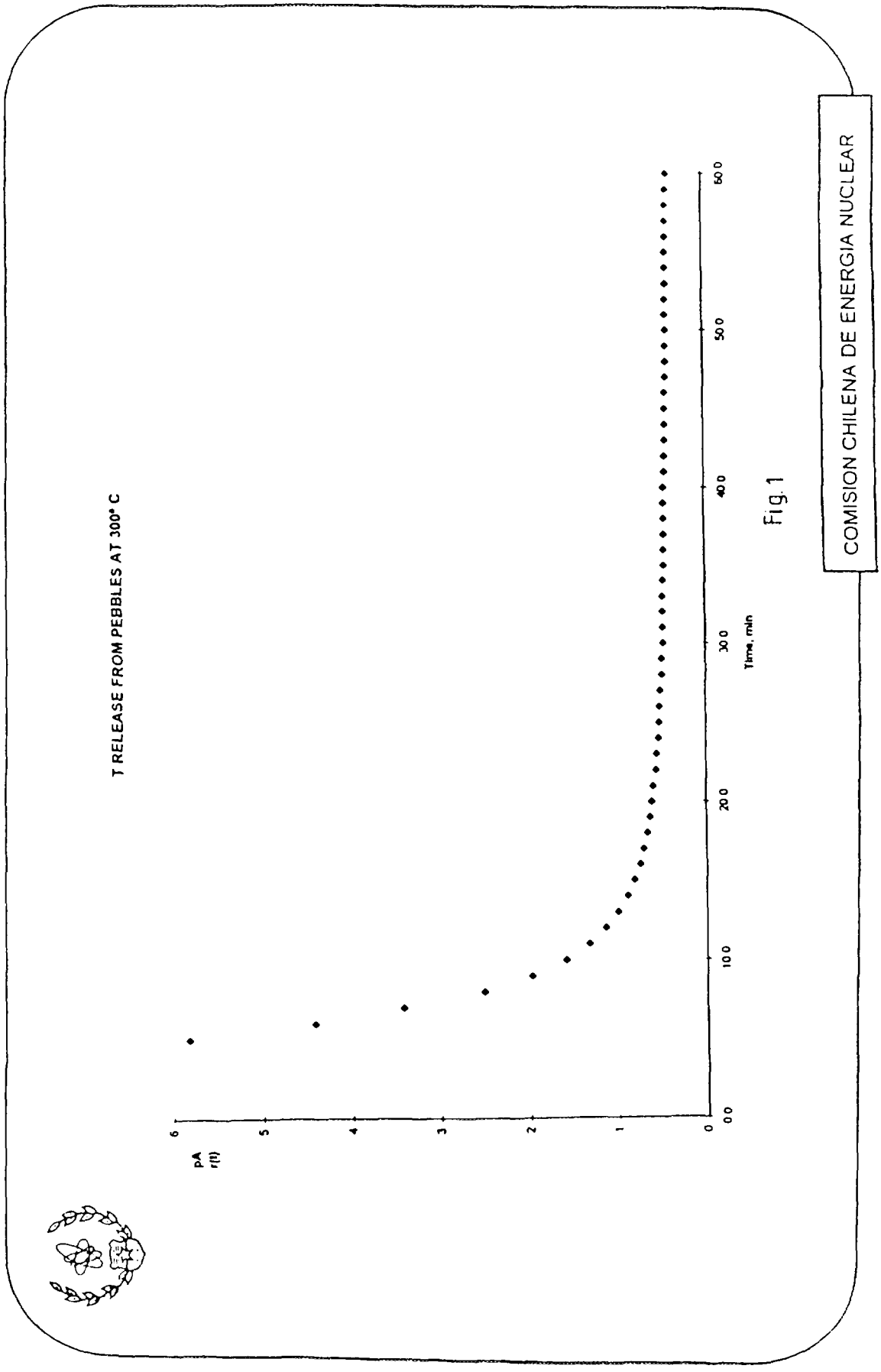
T RELEASE FROM PEBBLES AT 300° C
pA
r(t)
0
1
2
3
4
5
6
0.0
100
200
300
400
500
600
Time, min
COMISION CHILENA DE ENERGIA NUCLEAR

Fig.1

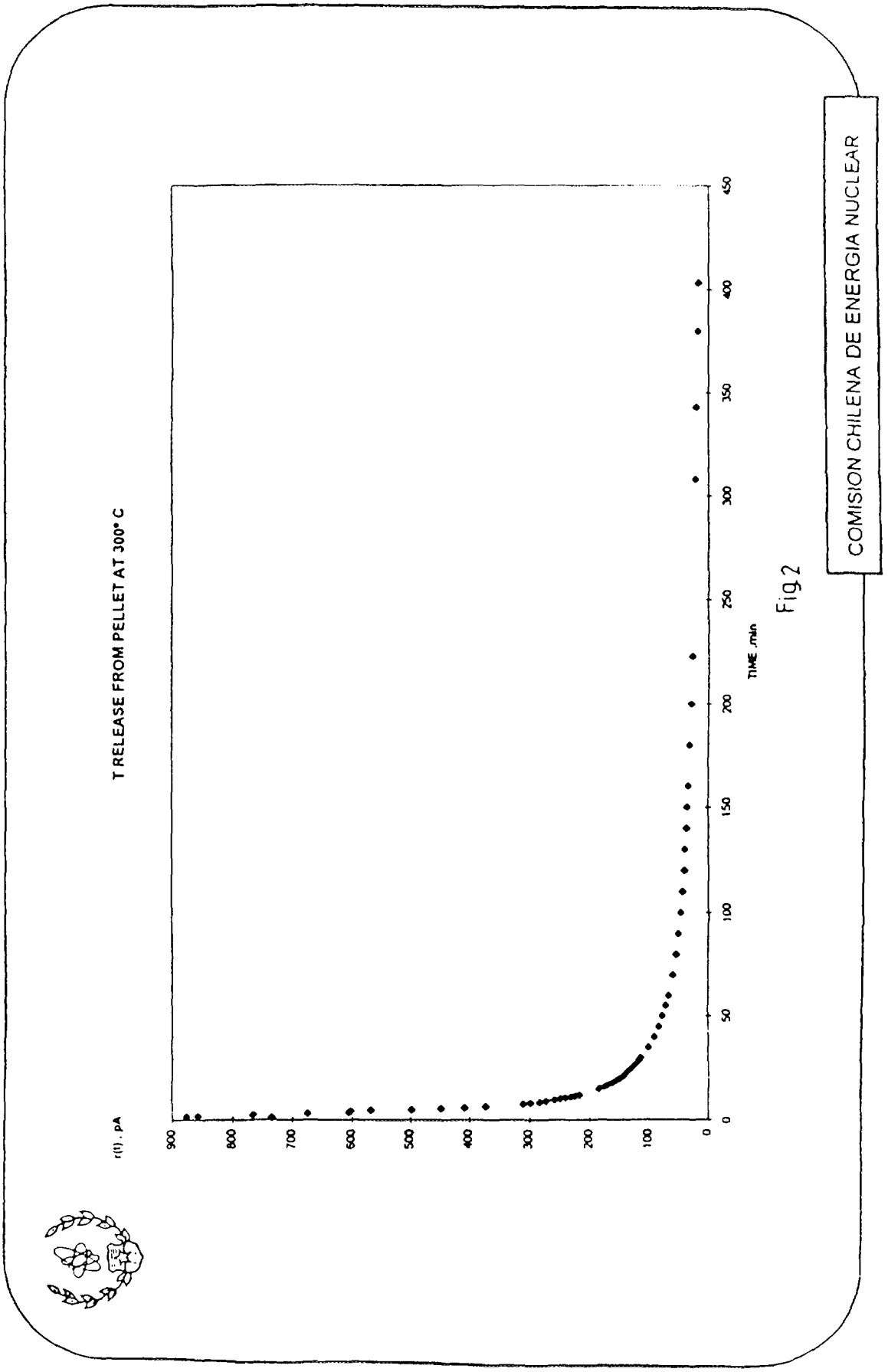
T RELEASE FROM PELLET AT 300° C
r(t) . pA
TIME . min
900
800
700
600
500
400
300
200
100
0
0
50
100
150
200
250
300
350
400
450
COMISION CHILENA DE ENERGIA NUCLEAR

Fig 2

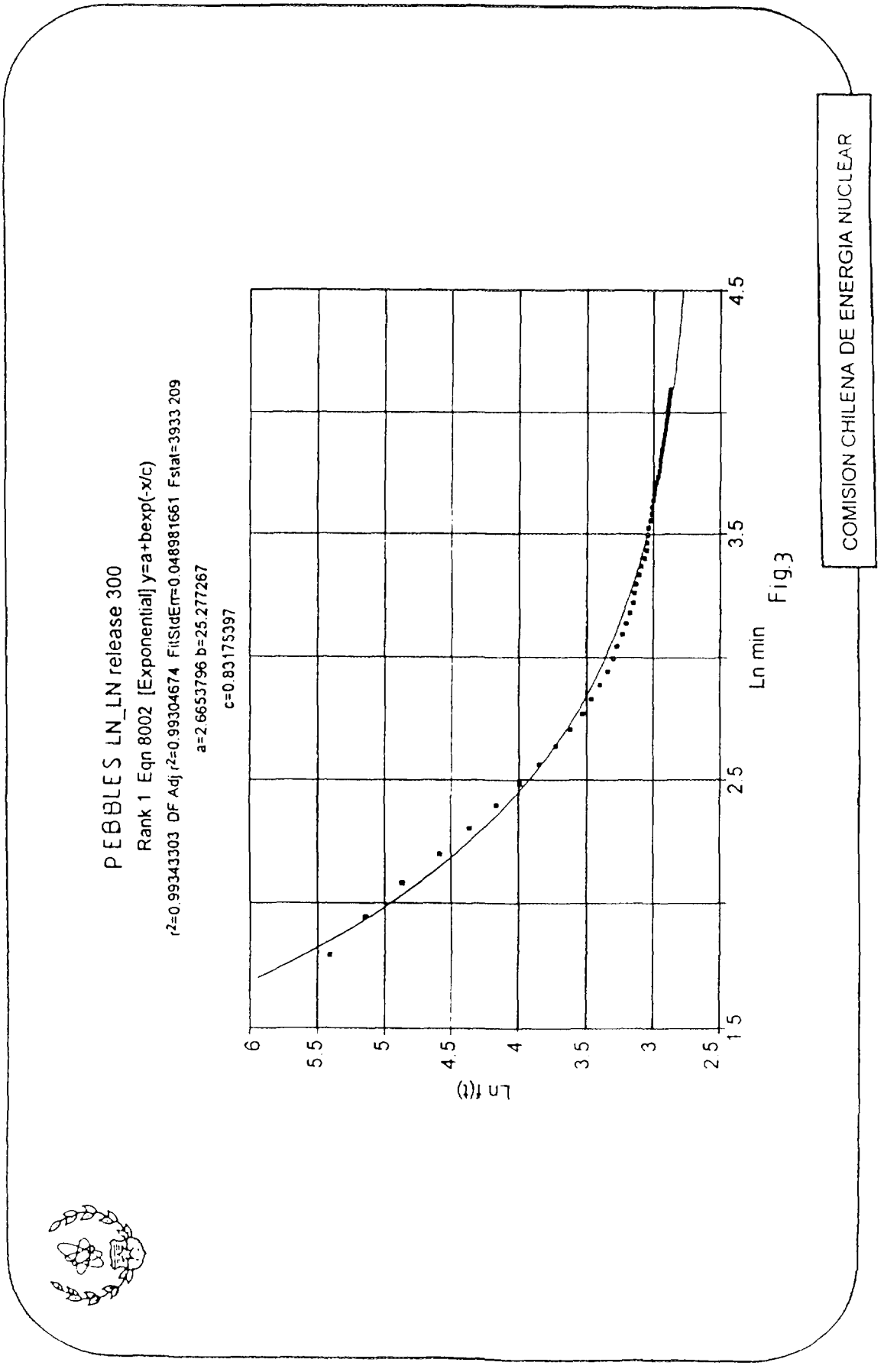
PEBBLES LN_LN release 300
Rank 1 Eqn 8002 [Exponential] y=a+bexp(-x/c)
r²=0.99343303 DF Adj r²=0.99304674 FitStdErr=0.048981661 Fstat=3933.209
a=2.6653796 b=25.277267
c=0.83175397
Ln f(t)
Ln min
6
5.5
5
4.5
4
3.5
3
2.5
1.5
2.5
3.5
4.5
COMISION CHILENA DE ENERGIA NUCLEAR

Fig.3

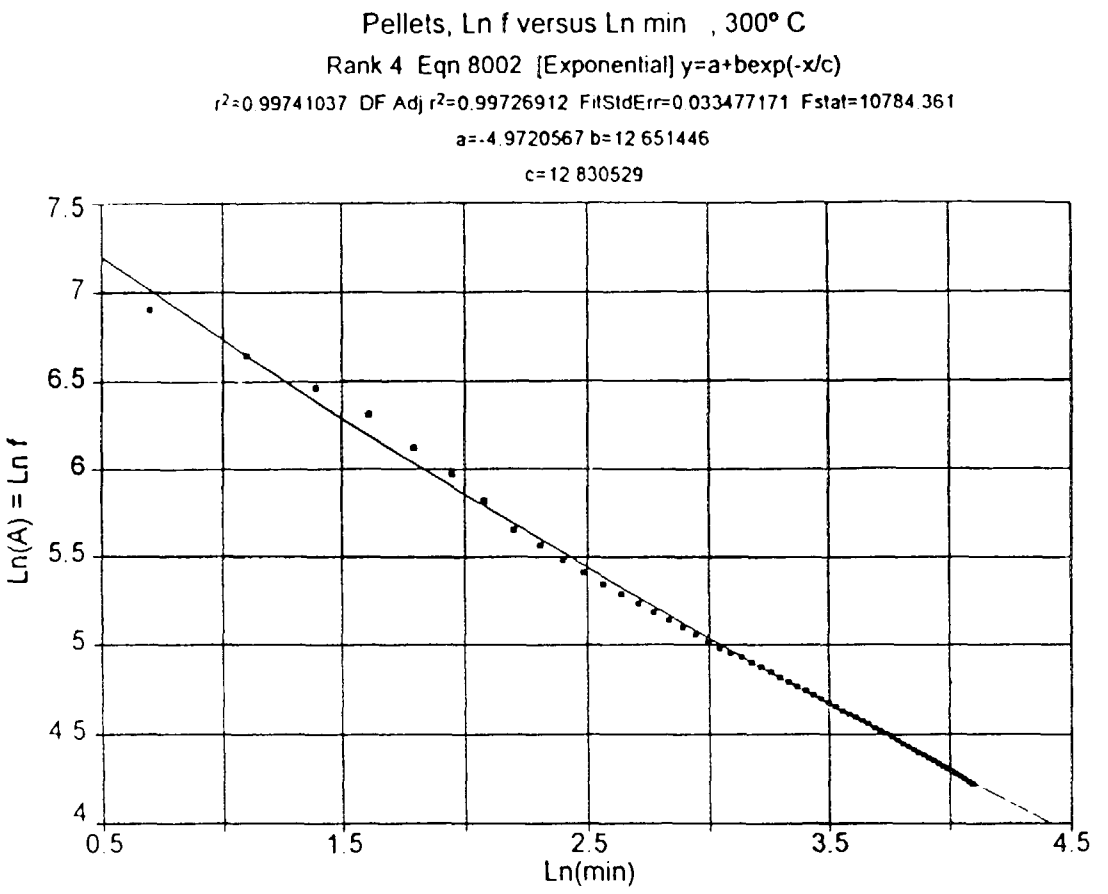

Fig 4

COMISION CHILENA DE ENERGIA NUCLEAR

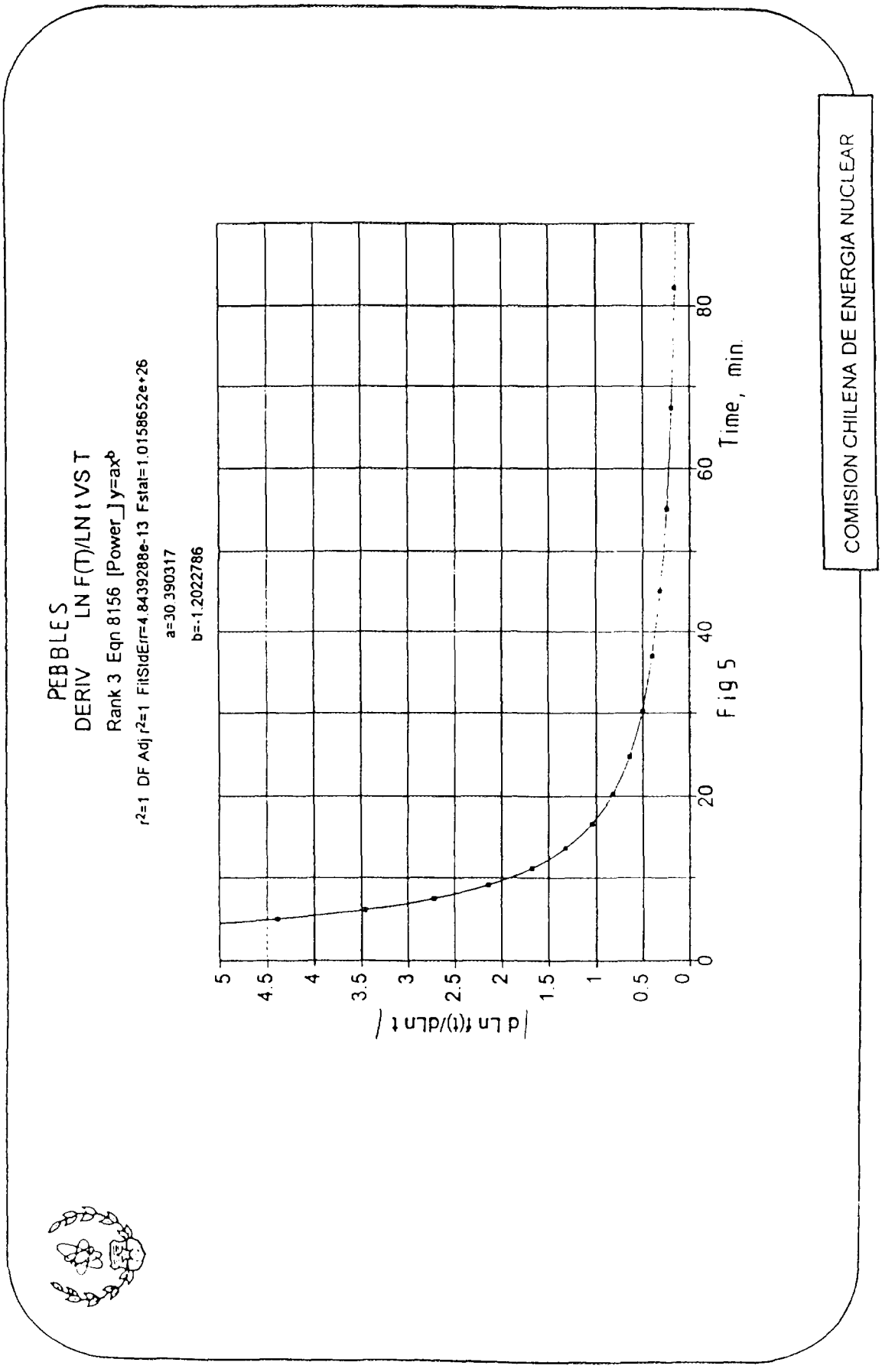
PEBBLES
DERIV LN F(T)/LN t VS T
Rank 3 Eqn 8156 [Power_] y=ax^b
r²=1 DF Adj r²=1 FitStdErr=4.8439288e-13 Fstat=1.0158652e+26
a=30.390317
b=-1.2022786
d Ln f(t)/dLn t
Time, min
0
20
40
60
80
0
0.5
1
1.5
2
2.5
3
3.5
4
4.5
5
COMISION CHILENA DE ENERGIA NUCLEAR

Fig 5

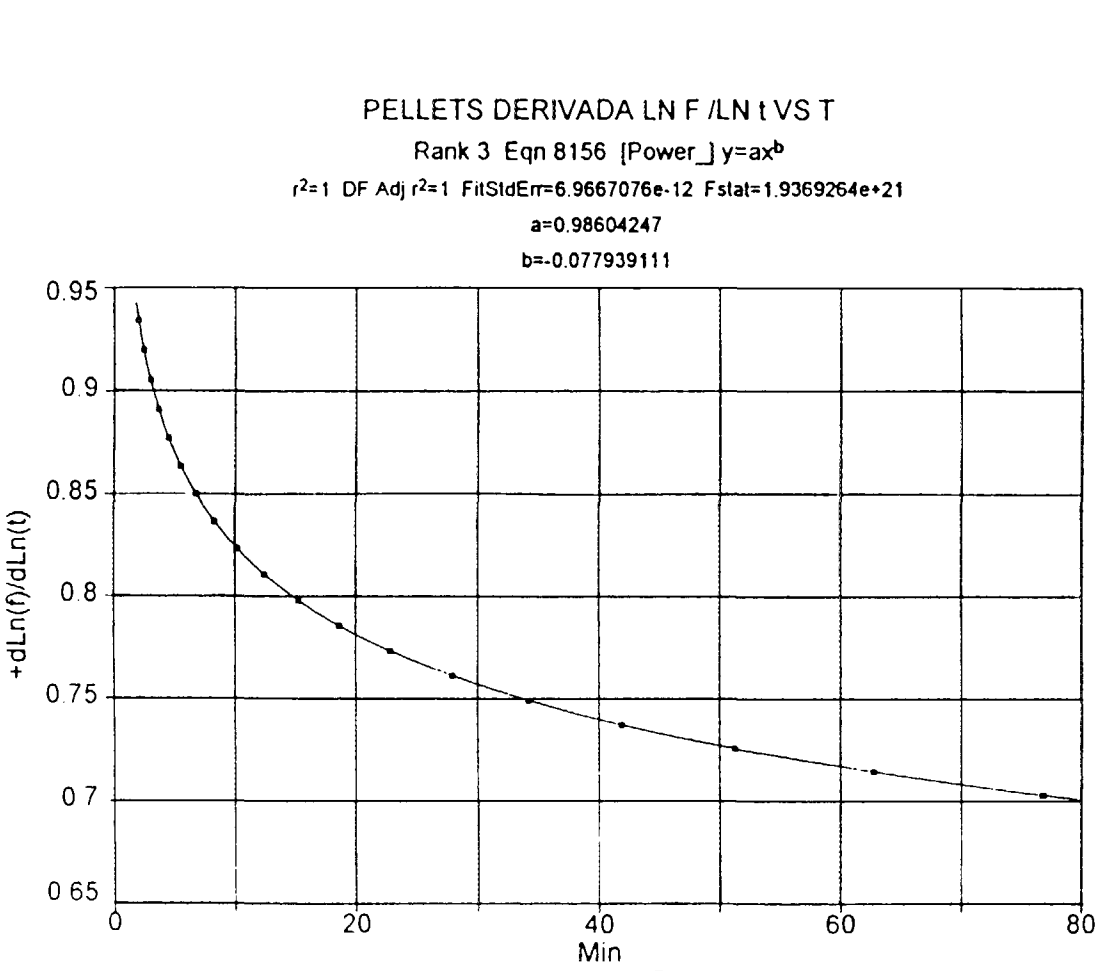

Fig 6

COMISION CHILENA DE ENERGIA NUCLEAR

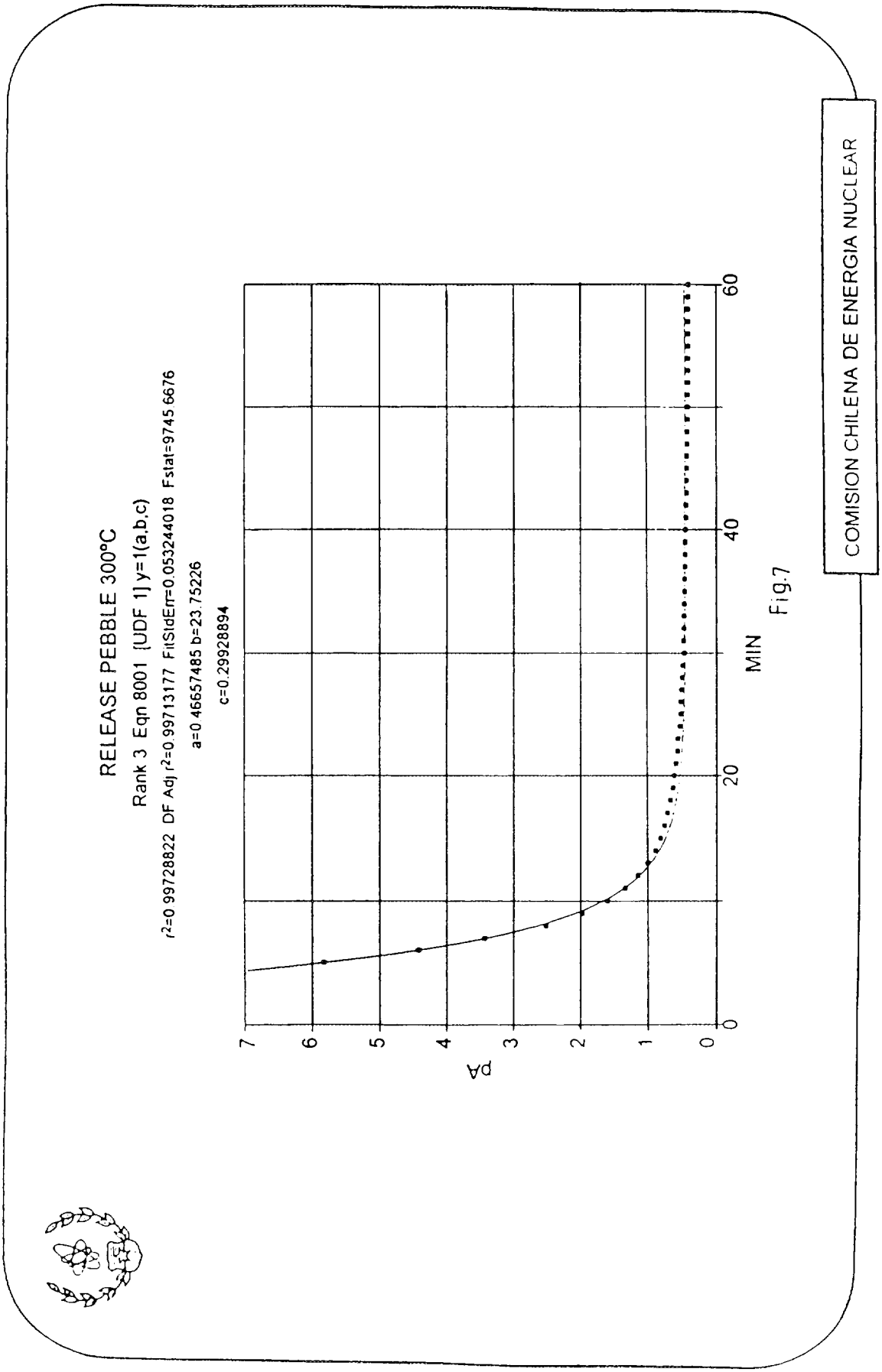
RELEASE PEBBLE 300°C
Rank 3 Eqn 8001 [UDF 1] y=1(a,b,c)
r²=0.99728822 DF Adj r²=0.99713177 FitStdErr=0.053244018 Fstat=9745.6676
a=0.46657485 b=23.75226
c=0.29928894
PA
MIN
0
1
2
3
4
5
6
7
0
20
40
60
COMISION CHILENA DE ENERGIA NUCLEAR

Fig.7

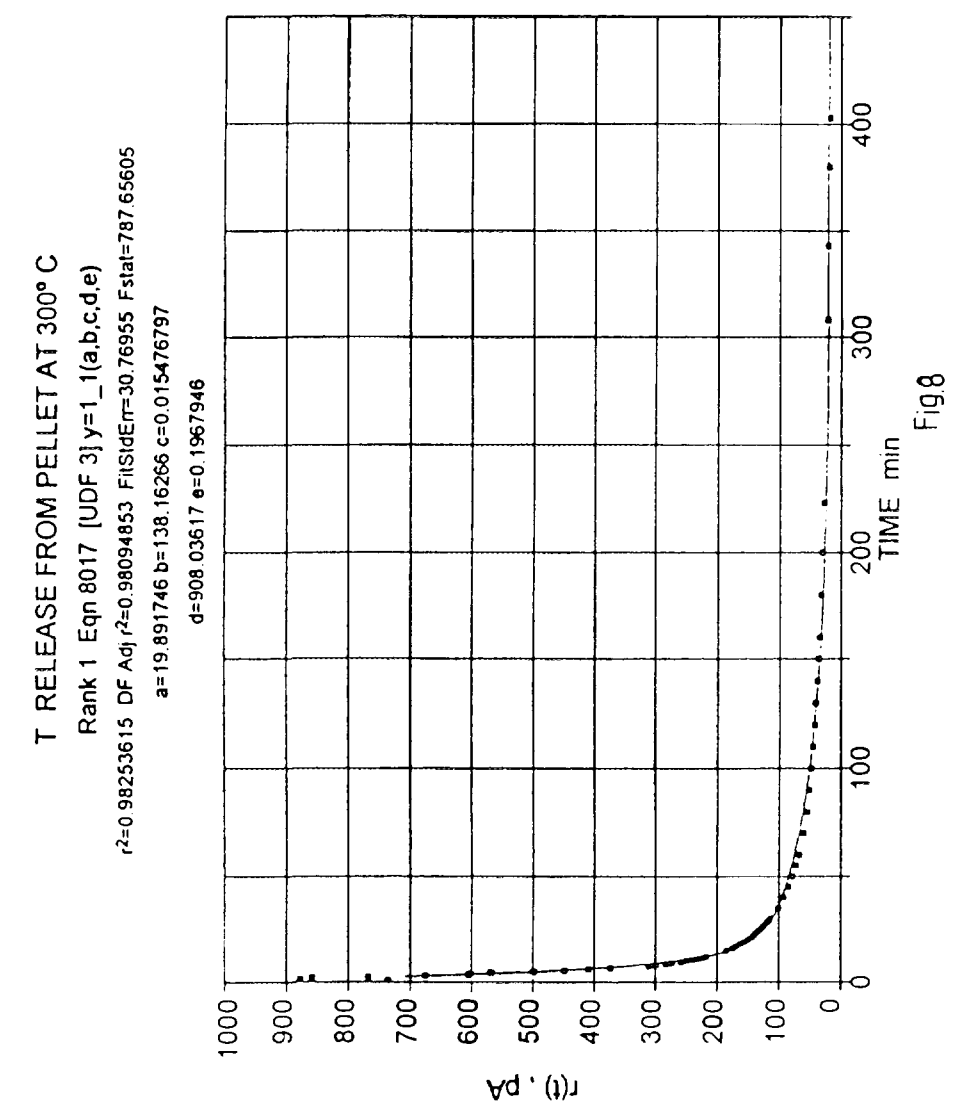

Fig.8

COMISION CHILENA DE ENERGIA NUCLEAR

Tritium Release Behavior from Neutron-Irradiated Li_2TiO_3 Single Crystal

Takaaki Tanifuji*, Daiju Yamaki*, Shoichi Nasu** and Kenji Noda*

*Japan Atomic Energy Research Institute, Tokai-mura, 319-11 Ibaraki, Japan.

**Kanazawa Institute of Technology, Ohgigaoka, Nonoichi, 921-8501 Ishikawa, Japan

Abstract

Li_2TiO_3 single crystals with various size (1-2mm) were used as specimens. After the irradiation up to $4x10^{18}$ n/cm^2 with thermal neutrons in JRR-2, tritium release from the Li_2TiO_3 specimens in isothermal heating tests was continuously measured with a proportional counter. The tritium release in the range from 625K to 1373K seems to be controlled by bulk diffusion . The tritium diffusion coefficient (D_T) in Li_2TiO_3 was evaluated to be D_T[cm2/sec] =0.100exp(-104[kJ/mol]/RT), 625K <T<1373K. In this temperature region, the tritium diffusion coefficients in Li_2TiO_3 is almost equal to those of Li_2O irradiated with thermal neutrons up to $2x10^{19}$ n/cm2. It indicates that the tritium release performance of Li_2TiO_3 is essentially good as Li_2O.

Tritium Release Behavior from Neutron-Irradiated Li_2TiO_3 Single Crystal

Takaaki Tanifuji*, Daiju Yamaki*, Shoichi Nasu** and Kenji Noda*

*Japan Atomic Energy Research Institute, Tokai-mura, 319-11 Ibaraki, Japan.

**Kanazawa Institute of Technology, Ohgigaoka, Nonoichi, 921-8501 Ishikawa, Japan

1. Introduction

Li_2TiO_3 is one of promising candidate for tritium breeding materials because of its low activation, excellent tritium release performance and chemical stability etc.[1,2]. In the early study[3], Li_2TiO_3 sintered pellets were prepared and characterized. It was clarified in the study that compatibility of Li_2TiO_3 with SUS (HT-9, 316SS) is better than that of Li_2O and Li_2ZrO_3, and that tritium release performance of Li_2TiO_3 was better than Li_2ZrO_3 and as well as Li_2O. The tritium release processes in ceramic breeders consist of bulk diffusion, grain boundary diffusion and surface desorption etc. Recently, tritium release behavior from sintered Li_2TiO_3 was investigated[1,2,4-8]. It has been reported that the tritium release behavior from sinterd Li_2TiO_3 is influenced by the bulk density, grain size, surface condition and sweep gas composition, etc., and that the rate determining process of tritium release from Li_2TiO_3 sintered pellets is the surface desorption of adsorbed tritium[4,5]. However, irradiation effects on the diffusion and surface desorption processes should be taken into account to evaluate the tritium release performance of the materials in fusion blanket enviroment, where ceramic breeder are subjected to severe neutron irradiation. From this standpoint, tritium diffusivity in bulk is required as one of baseline properties data. For the investigation on diffusion process, single crystal specimens are recommended to be used since contribution from

surface desorption/adsorption are minimized. Previously, tritium diffusivity in Li_2O was evaluated by measuring tritium release from the single crystals, and furthermore the irradiation effects on tritium diffusion behavior were investigated at various neutron fluence levels[9,10]. In the present paper, Li_2TiO_3 single crystal was prepared, and the tritium release behavior from the Li_2TiO_3 single crystal was investigated to obtain tritium diffusivity in the bulk .

2. Experimental

The starting material is Li_2TiO_3 powder purchased from Cerac/Pure,inc (Purity;98%). Fused Li_2TiO_3 rods with coarse crystal grains were obtained from the sintered rod prepared from the powder by a floating zone (FZ)apparatus using infrared imaging furnace. The fused Li_2TiO_3 rod was heated at 1173K for 1 hour in air, in order to anneal out color centers introduced during fabrication of the fused rod. The x-ray diffraction pattern of the fused rod showed Li_2TiO_3 with monoclinic crystal structure. The microstructure observations by an optical microscope and a scanning electron microscope showed some grains, of which size was about 1 to 2 mm. The Li_2TiO_3 single crystals were obtained from the fused Li_2TiO_3 rod which was subjected to be above-mentioned annealing. The Li_2TiO_3 single crystals were crushed into small pieces of fragments (1-14mg). The preparation and characterization of the Li_2TiO_3 single crystals used as specimens will be described elsewhere in detail [11].

Li_2TiO_3 single crystal specimens obtained were irradiated with thermal neutrons in JRR-2 up to $4x10^{18}$ n/cm^2 at ambient temperature (about 350K). After irradiation , tritium release from the specimen was measured in a flow(180cm^3/min) of ammonia sweep gas(NH_3) at atmospheric pressure during isothermal annealing between 625K and 1373K with a proportional counter. The measuring system is schematically illustrated in figure 1.

In order to heat the specimens up to the desired temperature as quickly as possible, the isothermal annealing was carried out in the manner described below. A platinum crucible containing the specimens was temporarily held in a silicon rubber tube with a clamp. After the desired temperature of furnace was attained, the crucible was dropped into the furnace. After about 1min., the maximum release rate was observed. Behavior of the tritium release was analyzed by assuming that the release started at the time when the maximum release rate was observed. In the measuring system, the counter was kept at about 380K to suppress the contamination of the counter due to adsorption of tritium. The background signal of the counter was 1 to $2x10^2$ cpm before and after every run.

3. Results and Discussion.

3.1. Effects of sweep gas composition

For the purpose of investigating tritium diffusion process in Li_2TiO_3, it is necessary to minimize the tritium inventory on Li_2TiO_3 surface. It is known that the tritium sweep gas composition, such as hydrogen addition to helium, is much effective to minimize the surface tritium inventory of lithium ceramics. Therefore, it is important to select the effective sweep gas composition for minimizing the surface inventory. For selecting the sweep gas used in the tritium release experiments for Li_2TiO_3 single crystals, sweep gas composition effects on tritium release behavior was investigated by using sintered Li_2TiO_3 (81%T.D.) irradiated with thermal neutron up to $1x10^{17}$ n/cm^2. After the irradiation, the tritium release behavior was observed in constant heating rate tests of 10 K/min. by using pure H_2, He-1%H_2, pure He and pure NH_3 sweep gas. As shown in Figure 2, three peaks appeared around 620, 700 and 870K in tritium release curves for all sweep gas. The tritium release from sintered Li_2TiO_3 was shown to be controlled by surface desorption process[6], and therefore

three peaks are considered to be due to the surface process. In the comparison among the four sweep gases, the lowest temperature peak around 630K in pure NH_3 sweep gas is the largest among those for the other three sweep gas. It is considered to indicate that the tritium release rate from the sintered Li_2TiO_3 is the largest in case of the pure NH_3 sweep gas. This means the pure NH_3 sweep gas more effectively sweep the surface tritium than other three sweep gases. It is known NH_3 does not react chemically with Li_2TiO_3 . Therefore, the pure NH_3 sweep gas was used in the Li_2TiO_3 single crystal experiments.

3.2. Tritium release from Li_2TiO_3 single crystals

The isothermal heating tests were performed in the range from 625K to 1373K for Li_2TiO_3 single crystals(weight;1.2-14.2mg) irradiated with thermal neutrons. In the calculation of diffusion coefficient of tritium, it is assumed that the specimens which had irregular shapes were spheres with various radii as a first approximation. When the tritium is controlled by the diffusion process in the specimens, the fraction of released tritium (f) can be expressed by

$$f=1-(6/\pi)\sum(1/n^2)\exp(-n^2\pi^2D't) \quad (1),$$

where t is the time of the isothermal heating, $D'=D_T/a^2$, D_T the diffusion coefficient of tritium and a the radii of the sphere specimens.

The D' value can be obtained by use of a nomograph, as was reported by Guggi et al.[13]. When $\phi(t)$ is defined to be

$$\phi(t)=(6/\pi^{0.5})(D't)^{0.5}, \quad (2),$$

eq.(1) can be substituted by

$$f=1-(6/\pi)\sum(1/n^2)\exp(-n^2\pi^3\phi(t)^2/36] \quad (3),$$

Using eq.(3), $\phi(t)$ can be calculated from the values of f obtained. Figure 4 shows typical log-log

plots of $\phi(t)$ versus heating time. These plots show straight line relationship with gradient of 0.5. This indicates that the tritium release is controlled by the diffusion process of tritium in the crystals, as described by Guggi et al [12]. Figure 5 and table 1 shows the diffusion coefficients of tritium in Li_2TiO_3 single crystals, which were estimated from relationships between $\phi(t)$ and annealing time, as a function of reciprocal temperature. The estimated diffusion coefficient of tritium in Li_2TiO_3 single crystals (D_T) is described as

$D_T[cm^2/sec] = 0.100\exp(-104[kJ/mol]/RT)$, $625K<T<1376K$.

In a previous study tritium release behavior was examined in the range 650 to 1600K for Li_2O single crystals with crystal size from 150 to 3050 μm which were subjected to thermal neutron irradiation at $4X10^{16}$ n/cm^2 and $2X10^{19}$ and fast neutron irradiation at $4X10^{24}$ n/cm^2. It was suggested that by thermal neutron mention above (i.e. gradient $\phi(t)=0.5$) that the rate determining step of tritium release from Li_2O single crystals was bulk diffusion.The tritium diffusion coefficients were evaluated for Li_2O subjected to different level of irradiation. Bertone evaluated the rate-determining step of the tritium release from Li_2O as a function of particle radius and temperature[13]. Most of the experimental conditions examined for Li_2O single crystals in the above-mentioned study were found to belong to "region of diffusional control" defined by Bertone. Thus, experimental result that tritium release in Li_2O crystals examined is controlled by bulk diffusion are supported by Bertone criterion.

In the present experiments, the crystal diameter of Li_2TiO_3 specimens were 880-1990μm; which were calculated using the density value, and the temperature range 625K-1373K. It is known that affinity of tritiated water for Li_2TiO_3 surface is much smaller than that for Li_2O surface. It is therefore, that the threshold crystal size for the region in which the rate-detemining step of tritium

release processes is bulk diffusion is much smaller that for Li_2O. This means that the examined experimental condition for Li_2TiO_3 belongs to "region of diffusion control" which was defined by Bertone.

Figure 5 shows comparison among tritium diffusion coefficient as a function reciprocal temperatures for Li_2TiO_3 and those for Li_2O irradiated with thermal and fast neutrons. The activation energies of the tritium diffusion coefficients in Li_2O single crystal subjected to thermal neutron irradiation at $4x10^{16}$ n/cm^2 of thermal neutron, thermal neutron irradiation at $2x10^{19}$ n/cm^2 and fast neutron irradiation at $4x10^{22}$ n/cm^2 are 82 kJ/mol, 108kJ/mol and 156kJ/mol (<1060K), respectively. The tritium diffusion coefficients in Li_2TiO_3 single crystals irradiated to $4x10^{18}$ n/cm^2 with thermal neutrons is close to that in Li_2O single crystals irradiated to $2x10^{19}$ n/cm^2 with thermal neutrons, and the activation energy of them are also close each other, that is, about 108 kJ/mol.

It is, thus, suggested that the mobility of the tritium in Li_2TiO_3 is close to that in Li_2O. The affinity of H_2O with Li_2TiO_3 is much smaller than that for Li_2O. The use of Li_2TiO_3 at low temperature regime ($<$570K) is expected for blanket design, while the operating temperature of Li_2O in the blanket is designed to be higher than 670K from concern for formation of LiOT. It is seen from the neutron fluence dependence on tritium diffusivity in figure 5 that irradiation damage has a large influence on tritium diffusion process. In general, irradiation damage tends not to recover at low temperature regime. It is, therefore, that data on irradiation effects on tritium diffusivity in Li_2TiO_3 is required for evaluation of tritium release performance in the fusion blanket . Data on neutron fluence dependence of the tritium diffusivity in Li_2TiO_3 will be obtained in near future.

4. Conclusion

Tritium release behavior in post-irradiation heating tests was investigated for Li_2TiO_3 single

crystals which had been irradiated with thermal neutrons in JRR-2 up to $4x10^{18}$ n/cm^2. The tritium release in the range from 625K to 1373K seems to be controlled by diffusion within the crystals. The tritium diffusion coefficient (D_T) in Li_2TiO_3 was evaluated as D_T[cm^2/sec] =0.100exp(-104[kJ/mol] /RT), 625K<T<1373K. In this temperature region, the tritium diffusion coefficients in Li_2TiO_3 is almost equal to those in Li_2O irradiated with thermal neutrons up to $2x10^{19}$ n/cm^2, of which the activation energy was 108kJ/mol . It indicates that the tritium release performance of Li_2TiO_3 is essentially good as well as Li_2O. Li_2TiO_3 is considered to be one of promising candidate of ceramic breeding materials for fusion reactor, although neutron irradiation tests at high burnup high dpa are needed to be performed for Li_2TiO_3 .

References

[1] N.Roux, J.Avon, A.Floreancig, J.Mougin, B.Rasneur and S.Ravel, J.Nucl. Mater. 233-237 (1996) 1431.

[2] P.Gierszewski, H.Hamilton, J.Miller, J.Sullivan, R.Verrall, J.Earnshaw, D.Ruth, R. Macauley-Newcombe and G.Williams, Fusion Engineering and Design 27 (1995) 297.

[3] P.A.Finn, T.Kurasawa, S.Nasu, K.Noda, T.Takahashi, H.Takeshita, T.Tanifuji and H.Watanabe, Proc. 9th Symp. Engineering Problems of Fusion Research (1981) p.1200.

[4] H.Kwast, R.Conrad and J.D.Elen, J. Nucl. Mater.133&134 (1985) 246.

[5] J.M.Miller, H.B.Hamilton and J.D.Sullivan,J. Nucl. Mater. 212-215 (1994) 877.

[6] J.P.Kopasz, J.M.Miller and C.E.Johnson, J. Nucl. Mater. 212-215 (1994) 927.

[7] J. Mougin, B. Rasneur and N.Roux, Proc. of International Workshop on Ceramic Breeder Blanket Interactions (1994) p.227.

[8] K.Pena, S.Lagos, J.Jimenez, L.Chuaqui, E.Saravia and P.Rojas, Proc. of International Workshop on Ceramic Breeder Blanket Interactions (1996) p.221.

[9] T.Tanifuji, K.Noda, T.Takahashi and H.Watanabe, J.Nucl. Mater. 149 (1987)227.

[10] T.Tanifuji, D.Yamaki, K.Noda, O.D.Slagle, F.D.Hobbs and G.W.Hollenberg, Fusion Technology 1996(1997)1455.

[11] S. Nasu and T. Tamura, to be published.

[12] D.Guggi, H.Ihle, D.Bruning, U.Kurz, S.Nasu, K.Noda and T.Tanifuji, J.Nucl. Mater. 118(1983)100.

[13] P.C.Bertone, J.Nucl.Mater. 151 (1988) 281.

Table 1 Diffusion data obtained from Li_2TiO_3 single crystals

Temperature (k)	Weight(mg)	D ' (s^{-1})	D_T (cm^2/s)
625	1.85	$3.0x10^{-8}$	$7.7X10^{-10}$
648	1.78	$2.8X10^{-7}$	$7.0X10^{-10}$
676	1.22	$1.7X10^{-6}$	$3.3X10^{-9}$
725	2.85	$1.0X10^{-6}$	$3.4X10^{-9}$
774	2.29	$2.0X10^{-6}$	$5.9X10^{-9}$
774	1.86	$1.5X10^{-6}$	$3.8X10^{-9}$
835	3.47	$5.5X10^{-6}$	$2.1X10^{-8}$
875	7.32	$1.3X10^{-5}$	$8.3X10^{-8}$
925	1.89	$5.5X10^{-5}$	$1.4X10^{-7}$
978	3.82	$4.0X10^{-5}$	$1.7X10^{-7}$
1032	4.55	$1.7X10^{-4}$	$7.9X10^{-7}$
1075	6.11	$6.0X10^{-4}$	$3.4X10^{-6}$
1176	9.62	$3.6X10^{-4}$	$2.8X10^{-6}$
1276	10.49	$5.5X10^{-4}$	$4.5X10^{-6}$
1373	14.16	$6.0X10^{-4}$	$5.9X10^{-6}$

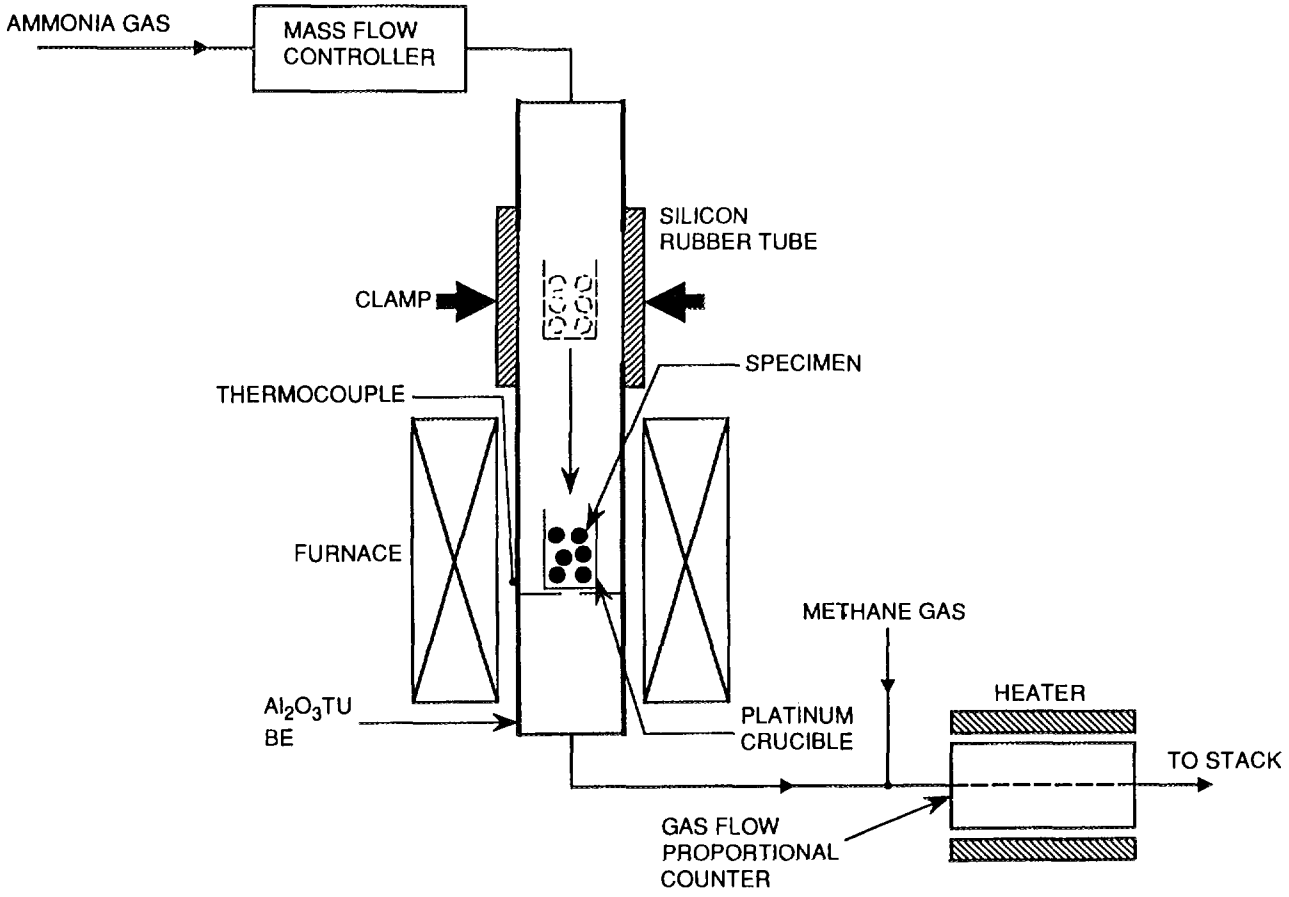

Figure 1 Schematic diagram of tritium extraction and measuring system.

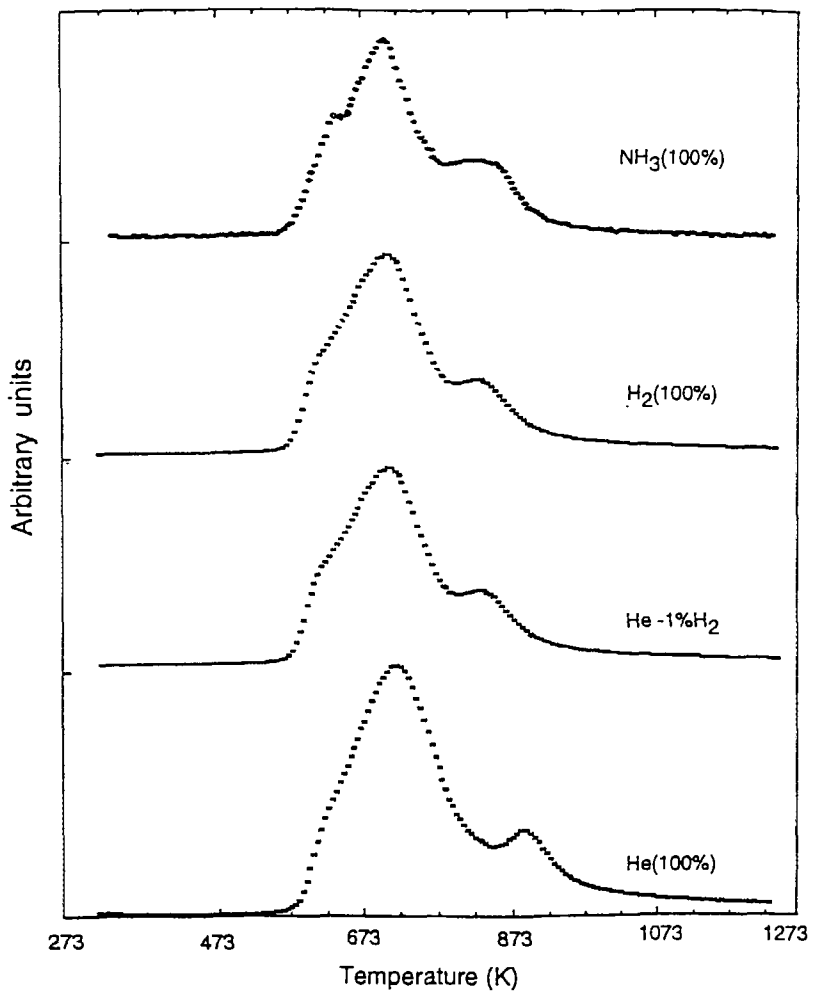

Figure 2 Release behavior from sintrered pellet during constant heating rate of 10K/min in the case of pure NH_3, pureH_2, He-1%$H_2$and pure He

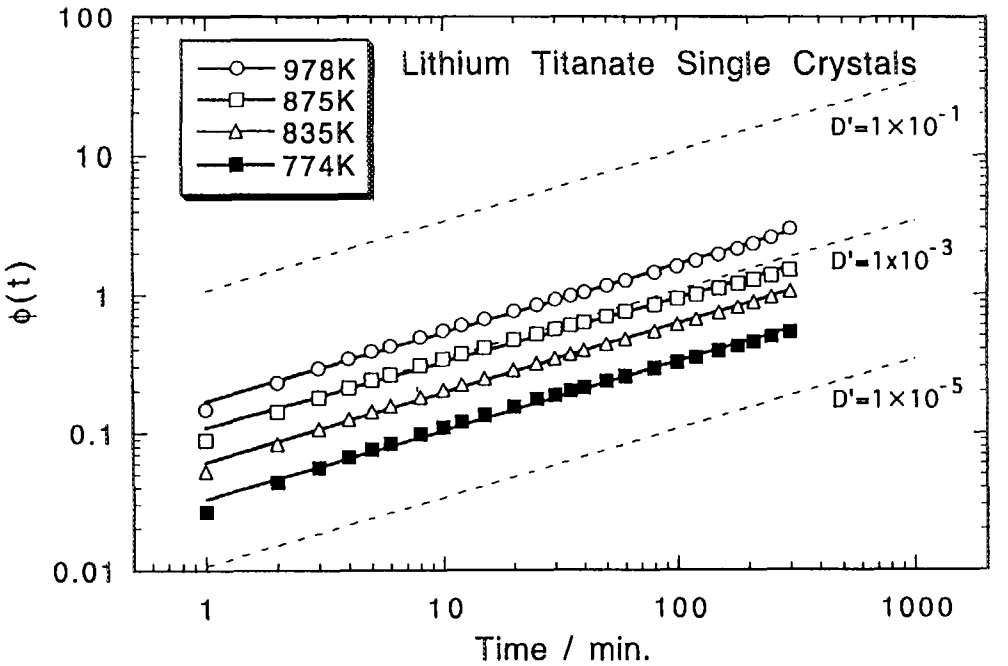

Figure 3 Nomographic presentation of fractional release of tritium from Li_2TiO_3 single crystals irradiated with thermal neutrons.

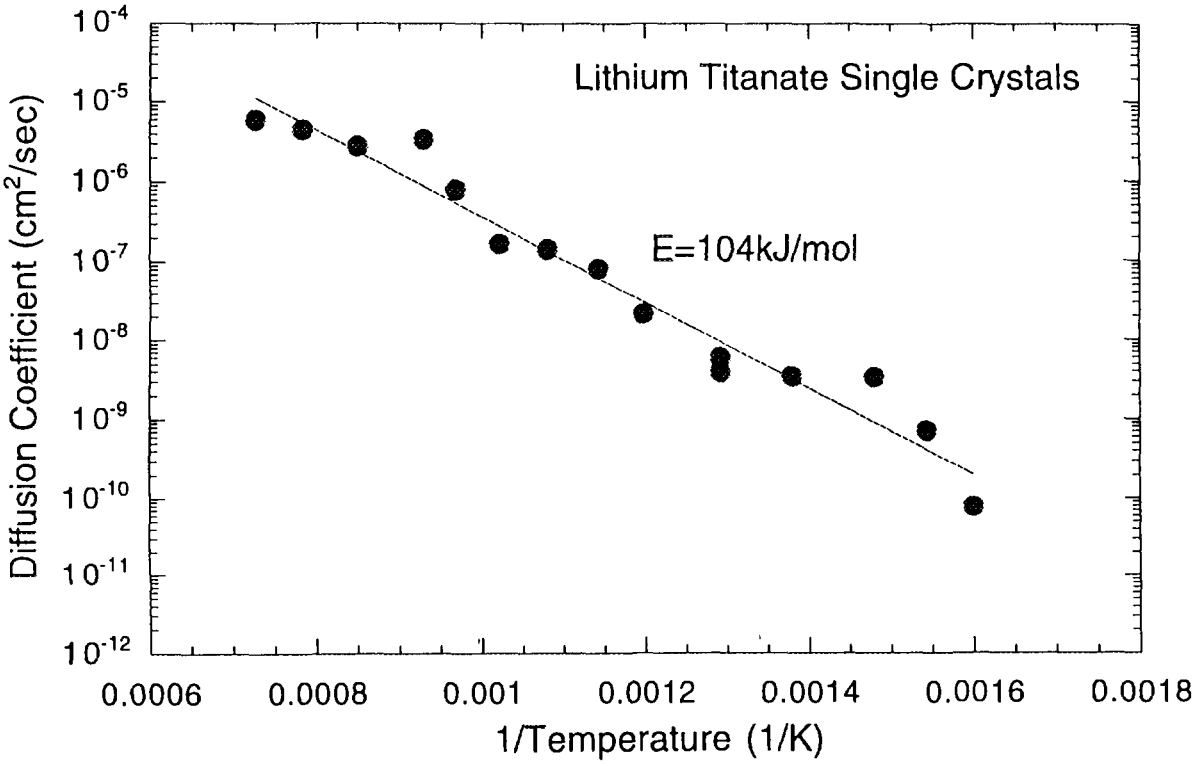

Figure 4 The diffusion coefficients of tritium in Li_2TiO_3 single crystals.

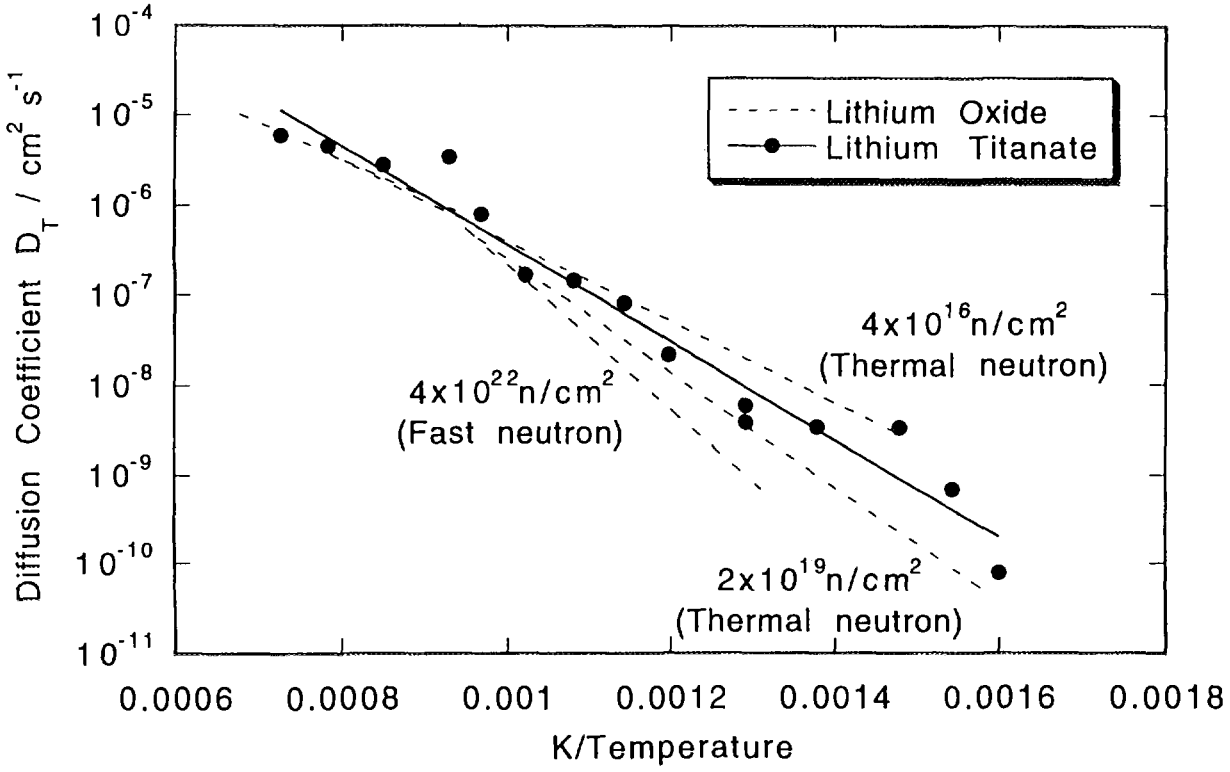

Figure 5 Comparison of tritium diffusion coefficient in Li_2TiO_3 single crystals with tritium diffusion coefficient in Li_2O single crystals.

SESSION 8

Irradiation Behavior of Ceramic Breeders

The radiolysis of lithium oxide ceramics

J.Tiliks[a], A.Supe[a], G.Kizane[a], J.Tiliks Jr.[a], V.Grishmanov[b]and S.Tanaka[b]

[a]Department of Chemistry, The University of Latvia
4, Kr.Valdemara str., Riga, LV-1013, Latvia

[b]Department of Quantum Engineering and Systems Science,
Faculty of Engineering, The University of Tokyo
7-3-1 Hongo, Bunkyo-ku, Tokyo 113, Japan

The radiolysis of Li_2O ceramics exposed to accelerated electrons (5 MeV) at 380 K was studied in the range of high absorbed doses up to 250 MGy. The formation of radiation defects (RD) and radiolysis products (RP) was demonstrated to occur simultaneously in the regions of (1) the regular crystalline lattice and (2) an enhanced content of the intrinsic defects and impurities. The production of the electronic RD and RP is more efficient in the region of the defected lattice than that at the site of the regular crystalline lattice. However, the stability of RD and RP formed in the region of the intrinsic defects is far less than those produced at the crystalline lattice, since most of the first mentioned RD and RP disappears with irradiation dose due to the radiation stimulated recombination. By this means the enhanced quantity of RD and RP is localized in the Li_2O ceramics irradiated to absorbed dose of 40–50 MGy, and hence this can influence the tritium release parameters. As soon as the intrinsic defects have been consumed in the production of RD and RP and the recombination of unstable electronic RD and RP takes place (at dose of ~100 MGy), the radiolysis of Li_2O ceramics occurs only at the crystalline lattice. Furthermore, the concentration of RD and RP increases monotonically and tends to the steady-state level.

1. INTRODUCTION

The Li_2O is a suitable ceramic breeder material for a fusion reactor (high lithium density, good thermal conductivity, suitable temperature of tritium release, etc.) and hence the radiolysis of Li_2O ceramics is one of the urgent problems [1, 2]. The role of RD and RP in the tritium release behavior has been reported elsewhere [3–5]. The tritium retention in Li_2O has been suggested to occur due to the formation of thermally stable Li–T bond [5].

The radiolysis of Li_2O single crystals and polycrystalline samples has been studied previously [6–8]. However, the obtained experimental data are inadequate to predict the radiolysis of Li_2O ceramics under operating conditions of a fusion reactor. The research on the radiolysis of Li_4SiO_4 [9] indicated that the radiolysis of the ceramic material has a different mechanism than that of the crystalline or polycrystalline materials because of the availability of intrinsic defects (vacancies, dislocations, micro-pores, etc) in the Li_4SiO_4 ceramics [10]. Furthermore, the universally accepted method of absorption spectroscopy can not be applied for the research on radiation defects in a ceramics due to its opaqueness. The one of the top methods for the examination of ceramic material is a chemical scavenger method, which allows to perform quantitative and qualitative analysis of RD and RP in the range of high irradiation dose, whereby the saturation of measured signal takes place for the most of experimental methods (for instance, electron spin resonance). The present work is dealing with the investigation of the radiolysis of Li_2O ceramics exposed to accelerated electrons under conditions wherein the formation of colloidal Li can be effective [5, 11].

2. EXPERIMENTAL

Li_2O ceramic pellets (80% of TD) were used for investigations. The dimensions of specimens were following: 10.0 mm in height and 12.3 mm in diameter. The irradiation of specimens by electrons (energy - 5 MeV; dose rate - 14 kGy/s; temperature - 380 K) to absorbed dose up to 250 MGy was performed at the linear accelerator of the University of Latvia. The specimens were placed in the special container filled with air.

The method of chemical scavenger was applied for the analysis of RD and RP in irradiated Li_2O ceramics. This method is based on the distinction in red-ox properties of various electron and hole radiation defects and radiolysis products, revealed at dissolution of irradiated sample in various scavenger solutions [10]. Electron RD and RP were finally transformed into the H_2, which was determined by the method of gas chromatography. Two scavenger solutions were used:

1. 0.4 M H_2SO_4 + 1 M ethanol,
2. 0.4 M H_2SO_4 + 1 M $NaNO_3$.

In the first system, all localized electrons (colloidal

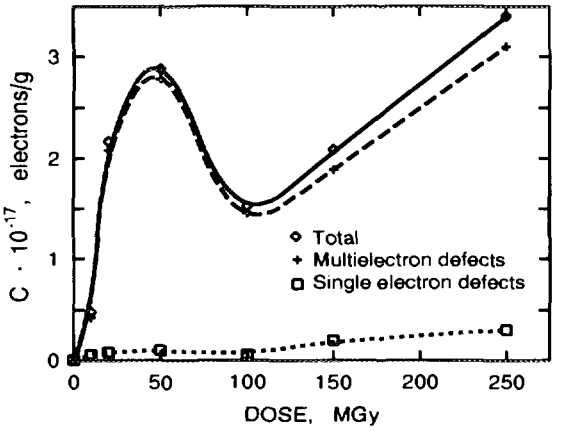

Figure 1: Localization of electrons during irradiation of Li_2O ceramics (dose curve).

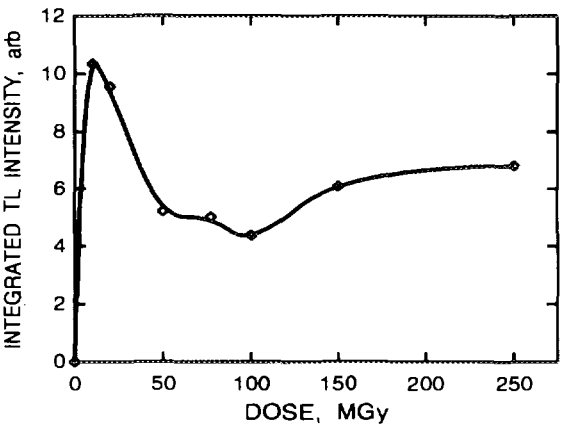

Figure 2: Dose dependence of integrated TL intensity of electron-irradiated Li_2O ceramics.

Li, F^+ , F^0 , F_2 and F_n centers) were scavenged and transformed into the H_2. In the second system, the generation of H_2 occurs only from colloidal Li, F_n and F_2 centers. The difference in the amount of formed H_2 in the first and second systems gives the quantity of localized electrons in the form of F^+ and F^0 centers. The needed quantity of the sample for analysis is equal to 30 50 mg.

The measurements of thermo-luminescence (TL) glow curves from irradiated Li_2O ceramics were carried out in the temperature range from 290 to 670 K. The temperature ramp of a sample (~10 mg) was 1 K/s.

ESR spectra of radiation-induced free radicals were recorded on a RE-1306 x-band radiospectrometer operating at 100 kHz magnetic field modulation. The radical concentration was measured by comparing the area under the absorption curve with $CuSO_4 \cdot 5H_2O$ standard samples.

3. RESULTS AND DISCUSSION

3.1. The chemical scavenger method

The formation of electronic RD such as F^+ , F^0 , F_2 and F_n centers has been demonstrated to occur in Li_2O exposed to irradiation [6, 7, 12]. The colloidal Li was detected as a final product of radiolysis process in Li_2O.

Fig.1. shown the dose dependence of the concentration of localized electrons detected by method of chemical scavenger. One can see that the radiolysis is very effective at the early stage of irradiation. The radiation chemical yield of localized electrons (G_e) in the dose range up to 40 MGy is estimated at $1.6 \cdot 10^{-5}$ electrons/100eV. The complex electronic defects (F_n centers, colloidal Li) are mainly formed (about 96%). The concentration of localized electrons peaks at about 50 MGy, and then decreases passing the minimum and further increases beginning at 100 MGy with G_e equal to $1.6 \cdot 10^{-6}$ electrons/100eV. The contribution to the simple electronic centers to the total amount of localized electrons increases in the dose range of 100 to 250 MGy up to 8%, and their concentration reaches the saturation value estimated at $2.7 \cdot 10^{17}$ electrons/g.

By this means the radiolysis of Li_2O ceramics under present irradiation conditions (380 K, 14 kGy/s) shows the rapid accumulation of electronic radiation defects with absorbed dose up to 35 40 MGy following by their quick disappearance at higher dose. One can recognize (Fig.1, dashed line) that the radiolysis involves two simultaneous processes: (1) the rapid formation of localized electrons and disappearance of electron aggregates and colloids; (2) the monotonic increase of localized electrons in the forms of electron aggregates and colloids, and small amount of simple electron centers. Similar radiolysis process has been observed for several ion-molecular compounds (K_2SO_4, Li_4SiO_4 ceramics, Li_3PO_4, etc.) after their special treatment resulting in the enhancement of the concentration of intrinsic defects [13].

3.2. Thermo-luminescence results

The thermo-luminescence method is based on registration of photons emitted due to the thermally induced recombination of electron and hole types of RD. By the present hypothesis, the electrons are liberated from the traps (F^+ ,F^0, F_2 centers, etc) and recombine with various types of hole RD resulting in the photon emission of various energies. The maximum and the half-width of the TL peak characterize structure of electron centers,

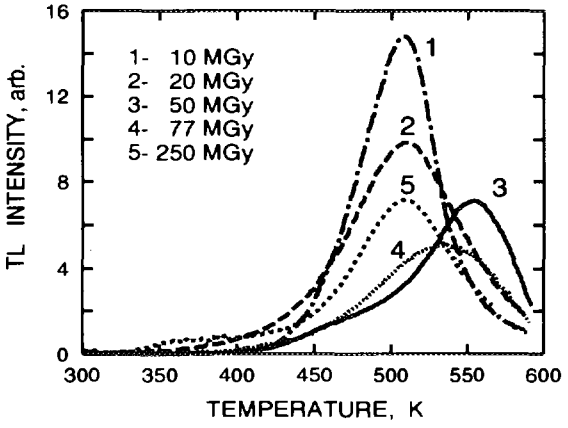

Figure 3: Dose dependence of TL glow curves of electron-irradiated Li_2O ceramics.

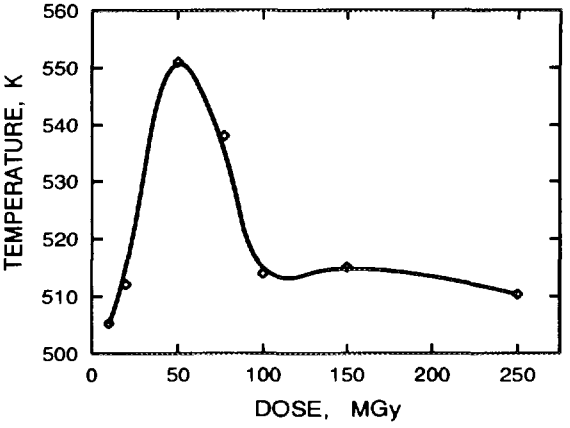

Figure 4: Dose dependence of the maximum position of TL glow curve of electron-irradiated Li_2O ceramics.

and the integral TL intensity indicates their concentration [14]. However, the method allows only to compare the change of the amounts of recombination centers, because the quantum yield of the recombination of a certain electron-hole pair is unknown. It is well recognized that the TL maxima shift to the high temperature range with increasing an aggregation of electron centers since the de-localization energy of electrons from traps increases.

Fig.2 shows the dose dependence of TL integrated intensity and Fig.3. represents the change of the shape and maximum position of TL glow curves with absorbed dose. The TL results indicate that the concentration of RD peaks at about 50 MGy, and then decreases passing the minimum and further increases beginning at 100 MGy with the tendency to reach a saturation value. The dose dependence of maximum position of TL glow curve is depicted on Fig.4. The observed results suggest that the aggregation of localized electrons into F_n centers and colloidal Li effectively takes place at the initial stage of irradiation (the shift of the TL maximum from 500 to 550 K in the dose range up to 50 MGy). However, the maximum of TL glow curve stabilizes at around 505-510 K which is characteristic for electron aggregate centers.

3.3 Stabilization of radicals in ceramics

At least two radical can be seen at the ESR spectrum of irradiated Li_2O ceramics (Fig.5). The singlet with H = 0.5 mT and g = 2.002 (radical "A") is dominant over the all investigated dose range. This signal was attributed by *Beuneu and Vajda* [15, 16] to the metallic Li colloids of a big size > 20 μm. However, this suggestion needs further investigation since the similar signal is characteristic for CO_2^- radical, which can be formed due to the localization of electrons at adsorbed CO_2 molecules. Under certain adsorbed doses (50 MGy), the signal can be determined at g = 2.024 (radical "B"), which is similar to that assigned to O_2^- ion-radical [17].

The curves of the accumulation of radicals are shown in Fig.6. Here again one can observe the rapid increase of the concentration of both (**A** and **B**) radicals with absorbed dose up to 50 MGy. Afterwards, the concentration of radicals decreases with dose in the range from 50 to 100 MGy. The following accumulation is characteristic only for radical "A", but the concentration of radical "B" attains saturation level. It is pertinent to note that in our study, the typical signal for F^+ center has not been observed.

3.4 Radiolysis mechanism of Li_2O ceramics

The radiolysis process of Li_2O is found to be similar to that typical for ion-molecular compounds which contain a high concentration of intrinsic defects before an expose to irradiation. In the case of low possibility for trapping of an electron by an anion forming the compound (sulphates, silicates, phosphates, as well as O^{2-} in lithium oxide), the relaxation of a self-trapped exciton results in the localization of electrons at the intrinsic structural defects (vacancies or vacancy aggregates - dislocations, grain surface, etc). The radiolysis occurs effectively until these "electron traps" exist. In addition, the formation of self-trapped excitons and their decay into the electron-hole pairs effectively takes place in the detected matrix. As a result, the electrons are trapped at a local area wherein the aggregation of simple electron center rapidly proceeds leading to the

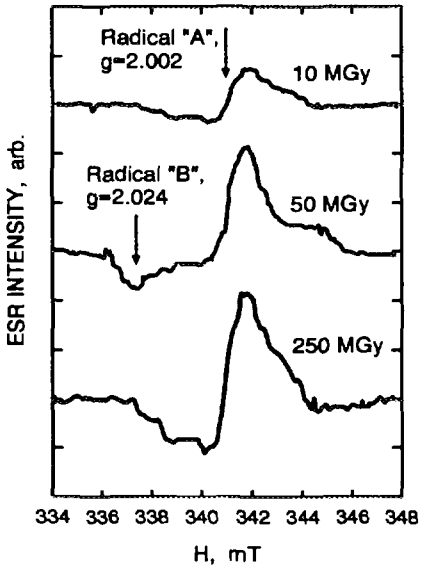

Figure 5: Dose dependence of ESR spectra of electron-irradiated Li_2O ceramics.

formation of F-center aggregates or colloidal Li. Furthermore, the formation of self-trapped excitons and their decay occurs simultaneously at a crystalline lattice, however, the local concentration of non-recombined electrons and holes is low. The effective trapping of electrons by intrinsic defects causes the accumulation of hole RD and their transformation into an mobile compounds. In the case of Li_2O, the O^- can be transformed into O_2 in the area of enhanced concentration of intrinsic defect as well as at the regular crystalline lattice. It is pertinent to note that the formation of voids or oxygen-filled cavities has been already observed [18]. As soon as the intrinsic defects - the traps of electrons - are expended, the radiation stimulated recombination of O_2 and F-center aggregates or colloidal Li begins to proceed. This process leads to a stoichiometry of radiolysis products which corresponds to one of the radiolysis at a crystalline lattice. The observation of O_2^- radical at about 50 MGy supports the suggested mechanism of radiolysis. This radical can be an intermediate between the transformation of hole center O^- into the molecular O_2. In addition, the decreases of a quantity of colloidal Li indicates the validity of the proposed hypothesis.

The suggested mechanism of radiolysis can be described by kinetic equation, which takes into account the localization of electrons at the intrinsic defects as well as at the crystalline lattice:

$$C = \frac{G}{k} \cdot (1 - e^{-kt}) + \frac{bg}{g - k} \cdot (e^{-kt} - e^{-gt}), \quad (1)$$

where C is the concentration of electronic radiation defects, G the radiation chemical yield on

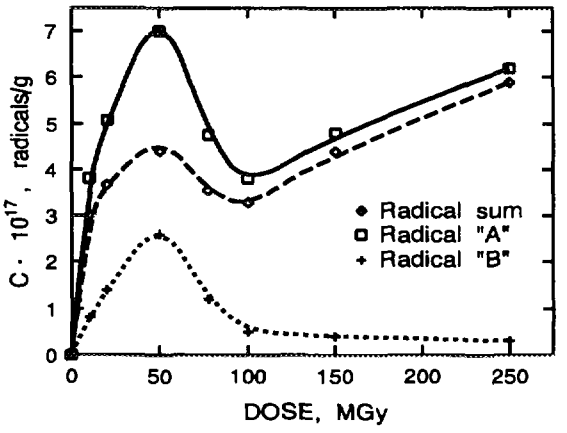

Figure 6: Concentration of free radicals during irradiation of Li_2O ceramics (dose curve).

crystalline lattice, k the rate constant of recombination reaction, t the irradiation time, g the radiation chemical yield on defected lattice, and b the concentration of intrinsic defects.

However, the research on Li_2O radiolysis at low temperature is desirable in order to decrease the radiation and thermo-stimulated recombination of formed RD and RP. This will allow to make a great step toward understanding of radiolysis process of Li_2O ceramics.

4. CONCLUSIONS

(1) The formation of the radiolysis products of electron types (F-center aggregates, colloidal Li) simultaneously occurs at the structural defect sites (vacancies, dislocations, micro-pores, grain surface) and at the crystalline lattice.

(2) The produced radiolysis products at defected lattice recombine during irradiation and hence do not contribute the total yield of radiolysis at doses over the 100 MGy. The radiolysis degree of Li_2O does not exceed 0.01% under irradiation dose of 250 MGy at 380 K.

(3) The formation of radiolysis products of electron types, mainly in the form of colloidal Li, can cause the increase of tritium inventory due to the formation LiT at the initial stage of irradiation.

(4) The observed mechanism of radiolysis can be characteristic for ion-molecular lithium compounds, which have the anions with a low probability for the trapping of electrons (titanates, zirconates, silicates, oxide) and contain a high concentration of structural defects.

REFERENCES

[1] C.E.Johnson, K.R.Kummerer and E.Roth, *J. Nucl. Mater.* **155–157** (1988) 188.

[2] N.Roux, S.Tanaka, C.Johnson and R.Verral, *Fusion Eng. Des.*, in press.
[3] H. Moriyama, A.Okada, Y.Asaoka and Y.Ito, *J. Nucl. Mater.* **179−181** (1991) 839.
[4] A.Abramenkovs, J.Tiliks, G.Kizane, V.Grishmanovs, A. Supe, *J. Nucl. Mater.* **248** (1997) 116.
[5] V.Grishmanov, S.Tanaka, J.Tiliks, G.Kizane, A.Supe and T.Yoneoka, *Fusion Eng. Des.*, in press.
[6] K. Noda, Y. Ishii, M. Matsui and H. Wanatabe, *Radiat. Eff.* **97** (1986) 297.
[7] P.Vajda and F.Beuneu, *Nucl. Instr. and Meth. in Phys. Res.* **B116** (1996) 183.
[8] J.Tiliks, S.Tanaka, G.Kizane, A.Supe, V.Grishmanov, A.Abramenkovs and J.Tiliks Jr., *Proc. CBBI-5; Roma, Italy* (1996) 143.
[9] J.Tiliks, G.Kizane, A.Abramenkovs, A.Supe, J.Tiliks, Jr., V.Vasiljev and H.Werle, *Proc. SOFT-17, Roma, Italy* (1992) 1523.
[10] J.E.Tiliks, G.K.Kizane, A.A.Supe, A.A.Abramenkovs, J.J.Tiliks and V.G.Vasiljev, *Fusion Engrg. Des.* **17** (1991) 17.
[11] V.Grishmanov, S.Tanaka, J.Tiliks, G.Kizane, A.Supe and L.Grigorjeva, *Nucl. Instr. and Meth. in Phys. Res. B*, in press (NIMB 40398).
[12] V.Grishmanov, S.Tanaka and J.Tiliks, *Proc. SOFT-19; Lisbon. Portugal* (1996) 1451.
[13] K.Schwartz and J.Ekmanis, *Dielectric materials: radiation processes and radiation stability* (Zinatne, Riga, 1989), in Russian.
[14] M.Frank und W.Stolz, *Festkorperdosimetrie ionisierender strahlung* (BSB. B.G.Teubner, Verlagsgesellshaft, 1969).
[15] F.Beuneu and P.Vajda, *Physical Review Letters* **76** (1996) 4544.
[16] F.Beuneu, P.Vajda, G.Jaskierowicz and M.Lafleurielle, *Physical Review* **B55** (1997) 11263.
[17] L.L. van Rijen, *Ber. Buns. Ges.* **75** (1971) 1046.
[18] F.Beuneu, P.Vajda and O.J.Zogel, *Nucl. Instr. and Meth. in Phys. Res. B*, in press.

PRODUCTION BEHAVIOR OF IRRADIATION DEFECTS IN SOLID BREEDER MATERIALS

Hirotake Moriyama[1] and Kimikazu Moritani[2]

[1]*Research Reactor Institute, Kyoto University*
[2]*Graduate School of Engineering, Kyoto University*

Abstract:

The irradiation effects in solid breeder materials are important for the performance assessment of fusion reactor blanket systems. For a clearer understanding of such effects, we have studied the production behavior of irradiation defects in some lithium ceramics by an in-situ luminescence measurement technique under ion beam irradiation. The luminescence spectra were measured at different temperatures, and the temperature-transient behaviors of luminescence intensity were also measured. The production mechanisms of irradiation defects were discussed on the basis of the observations.

1. Introduction

In a fusion reactor solid blanket system, tritium breeding lithium ceramics are attacked by high energy neutrons and energetic particles from nuclear reactions, and severe irradiation damage may be expected. The irradiation behavior of lithium ceramics is thus important for the performance assessment of fusion reactor blanket systems. Considering the two functions of blanket systems, which are tritium breeding and energy extraction, the effects of long-term irradiation on tritium release behaviors and microstructural changes of lithium ceramics are of special concern for the design of blanket systems. Then the experimental efforts have been devoted to the irradiation performance testing at higher burn-up levels as seen in the BEATRIX-II experiments[1]. Also, fundamental studies on the irradiation behavior of lithium ceramics have been performed in order to understand and control the phenomena[2].

In the present paper, a fundamental aspect of the irradiation behavior of lithium ceramics is discussed to improve our knowledge on the irradiation effects in lithium ceramics. Some details of their production behaviors, reaction kinetics, and effects on the tritium release performance of lithium ceramics are given.

2. In-situ luminescence measurement of Li_2O

For understanding the kinetic aspects of the production behavior of irradiation-induced defects, the in-situ luminescence measurement technique is very useful and has been applied to some solid breeder materials[3,4]. Knowledge of the irradiation defect production is much improved and is extended to understand the tritium behavior under irradiation.

As shown in Fig. 1[5], the luminescence band of the F^+ centers is predominantly observed in Li_2O at lower temperatures, while the band of the F^0 centers is observed at higher temperatures. This indicates the importance of the F^0 centers in the reactions of tritium at the temperatures of actual blanket conditions. In order to discuss the reaction kinetics, the temperature transient behavior of irradiation defect production has been measured in Li_2O[3].

For a temperature increase, the luminescence intensity of the F^+ centers rapidly decreases as expected from the temperature dependence of the equilibrium luminescence intensity. On the other hand, an abnormal temperature transient behavior has been observed for the F^0 centers; an excess luminescence is observed for the temperature increase, as shown in Fig. 2. Also, the excess luminescence has been found to depend on the irradiation history and to increase with increasing absorbed dose before the temperature change. By considering the observations, the following reaction scheme has been given for the production mechanism of the F^+ and F^0 centers:

$$Li_2O \rightarrow Li_2O^* \quad (1)$$
$$Li_2O^* \rightarrow (F^+ \cdot O^-) + h\nu \quad (2)$$
$$2\,Li_2O^* \rightarrow 2\,F^0 + O_2 + 2\,h\nu' \quad (3)$$
$$(F^+ \cdot O^-) + Li_2O^* \rightarrow 2F^0 + O_2 + 2\,h\nu' \quad (4)$$

Reaction (1) represents the production of an excited Li_2O, Li_2O^*, by ion beam irradiation. The F^+ center is considered to be associated with an O^- interstitial under Coulomb interactions as $(F^+ \cdot O^-)$, and is produced by reaction (2), which dominates at lower temperatures. At higher temperatures, however, reactions (3) and (4) will take place and the F^0 centers and their partners, O_2 molecules, are produced. These second-order reactions for the formation of F^0 centers require some thermal activation, and will take place at higher temperatures. This is the reason why the luminescence of the F^0 centers is observed especially at higher temperatures. Based on this reaction scheme, some calculations have been performed for the luminescence behavior. Agreements between the calculations and observations are satisfactorily good as seen in Fig. 1.

3. In-situ luminescence measurement of ternary lithium ceramics

The same technique has been applied to the ternary lithium ceramics of Li_2TiO_3, Li_2ZrO_3 and Li_2SnO_3[4,6]. Multiple luminescence bands have been observed in the in-situ luminescence measurement of Li_2TiO_3, Li_2ZrO_3 and Li_2SnO_3 under H^+ and He^+ ion beam irradiation. Although the luminescence spectra were decomposed to a number of the luminescence bands, most of these seemed to exhibit similar temperature dependences with one another in each material, and rather similar origins were suggested for these luminescence bands.

Fig. 3 shows a typical result obtained with Li_2TiO_3 in the measurement of thermal transient of luminescence intensity[4]. For a temperature increase, the luminescence intensity immediately increases, thereafter it decreases and settles down to an equilibrium value. The observed phenomena seem to be similar to those for Li_2O[3], but a certain difference is found between both cases. In the case of Li_2O, the excess luminescence was observed to depend on the irradiation history and to increase with increasing irradiation time. It was thus suggested that secondary reactions of irradiation defects are involved in the reaction mechanism. In the case of Li_2TiO_3, on the other hand, such a dependence has hardly been observed. As shown in Fig. 4, the excess luminescence is little dependent on the irradiation time except for the very early stage of irradiation. This means that the observed rise of the luminescence is not dependent on the irradiation history but that the equlibrium condition is attained shortly for the involved reactions. In other words, the observed rise of the luminescence intensity is of the temperature dependence itself of the equilibrium luminescence intensity. Similar conclusions

have also been obtained for Li_2ZrO_3 and Li_2SnO_3.

By the analogy of the reaction scheme for Li_2O[3], a similar production mechanism of irradiation defects in Li_2TiO_3, Li_2ZrO_3 and Li_2SnO_3 has been given as

$$Li_2MO_3 \rightarrow Li_2MO_3^* \quad (5)$$
$$Li_2MO_3^* \rightarrow (F^+ \bullet O^-) + h\nu \quad (6)$$
$$2\,Li_2MO_3^* \rightarrow 2\,F^0 + O_2 + 2\,h\nu' \quad (7)$$
$$(F^+ \bullet O^-) + Li_2MO_3^* \rightarrow 2F^0 + O_2 + 2\,h\nu' \quad (8)$$

In the present measurement, however, it has been shown that the transient behavior of the luminescence is little dependent on the irradiation history and that the equilibrium condition is attained shortly. This may suggest little participation of reaction (8) in Li_2TiO_3, Li_2ZrO_3 and Li_2SnO_3, although the reaction scheme will be similar to that of Li_2O.

It is interesting and important to obtain the rate constants of reactions involved in the production of irradiation defects. Following the reaction scheme, the observed luminescence intensity I is expressed as:

$$I = I_1 + I_2 = k_1[Li_2MO_3^*] + k_2[Li_2MO_3^*]^2 \quad (9)$$

where I_1 and I_2 are the luminescence intensities and k_1 and k_2 the rate constants of reactions (6) and (7), respectively. The life-time of $Li_2MO_3^*$ is assumed to be very short and a steady-state approximation is applied to $Li_2MO_3^*$:

$$d[Li_2MO_3^*]/dt = g' - k_1[Li_2MO_3^*] - k_2[Li_2MO_3^*]^2 - \sum_{i=3}^{n} k_i[Li_2MO_3^*] = 0 \quad (10)$$

where g' is the apparent generation rate of $Li_2MO_3^*$ by reaction (5) and k_i ($i \geq 3$) the rate constants of the back reaction of reaction (5) and of some other reactions of non-radiative transition. In order to calculate the luminescence intensity, the steady-state concentration of $Li_2MO_3^*$ is obtained from equation (10) and substituted into equation (9).

In the present analysis in which the experimental data for the temperature dependence of the luminescence ientensity have been fitted to equations (9) and (10), the rate constants have been assumed to be of the Arrhenius type and the pre-exponential term A_i and activation energy term E_i have been determined[4]. As shown in Figs. 5, 6 and 7, the agreements are satisifatorily good in all the cases examined.

4. Interactions of tritium with irradiation-induced defects

Tritium recovery from solid breeder materials has been investigated extensively, and a number of factors, namely solubility, diffusivity, surface reaction and desorption are recongized to participate in the tritium recovery process[7-9]. In addition to these, several investigations have suggested a definite role of irradiation defects. In fact, apparent effects of irradiation have been observed on the tritium behavior in lithium ceramics[10-20].

For the assessment of tritium release behavior of Li_2O under irradiation, a model reaction scheme has been presented by taking into account the interactions of irradiation defects with tritium[20]. Tritium is produced in Li_2O grains by nuclear reactions and stabilized in the

chemical states of T^+(LiOT) or T^-(LiT). The tritium species interact with the F^0 centers and O_2 molecules which are predominantly produced at higher temperatures, and diffuses to the grain surface where tritium is released in the form of T_2(HT) or T_2O(HTO) to the sweep gas. By taking this reaction scheme, some predictions have been made and compared with the observations in the BEATRIX-II experiment. The observed tritium release behavior has successfully been interpreted.

It is important that irradiation defects participate in the reaction mechanisms even at such high temperatures, because material stability will be affected as well as tritium release kinetics. In the case of H_2-containing sweep gas, F^0 and O_2 are considered to react with H_2 at the grain surface as

$$F^0 + 2\,H_2 \rightarrow LiH \quad (11)$$

$$O_2 + 2\,H_2 \rightarrow 2\,H_2O\uparrow \quad (12)$$

Due to reaction (12), the moisture concentration of H_2O will increase with the increasing H_2 concentration in the sweep gas, as observed in the BEATRIX-II, and then the material degradation will be accelerated in the presence of H_2. Further studies are suggested for its importance.

For the further development of the model, the equilibrium constant and rate constant of each reaction are to be determined. Such data are still lacking at the present time, and are to be determined by further studies. As well as the steady state chemistry, the dynamic behavior of tritium release may be studied for the determination of these constants.

5. Conclusions

(1) The production behavior of the irradiation-induced defects was studied by an in-situ luminescence measurement under ion beam irradiation. Some of the defect species were found to be produced even at higher temperatures of blanket conditions.
(2) Irradiation effects on tritium recovery performance were observed and explained by taking into account the interactions of tritium with the defect species. The equilibrium constants and reaction rate constants are still lacking for a complete evaluation of tritium recovery performance at blanket conditions.
(3) The defect species will participate in the microstructural changes of lithium ceramics and affet the materials performance such as the thermal conductivity. In order to control the phenomena, further experimental efforts are required not only for integrated experiments but also for fundamental aspects of the phenomena.

References

[1] G. W. Hollenberg, H. Watanabe, I. J. Hastings and S. E. Berk, J. Nucl. Mater 191-194 (1992) 23.
[2] K. Noda, J. Nucl. Mater. 179-181 (1991) 37.
[3] Y. Asaoka, H. Moriyama and Y. Ito, Fusion Technol. 21 (1992) 1944.
[4] K. Moritani and H. Moriyama, presented at ICFRM-8, Sendai, Japan, Oct. 26-31, 1997.
[5] Y. Asaoka, H. Moriyama, K. Iwasaki, K. Moritani and Y. Ito, J. Nucl. Mater. 183 (1991) 174.
[6] K. Moritani and H. Moriyama, J. Nucl. Mater., in press (1997).

[7] C. E. Johnson, J. Nucl. Mater. 179-181 (1991) 42.
[8] N. Roux, C. Johnson and K. Noda, J. Nucl. Mater 191-194 (1992) 15.
[9] N. Roux, G. Hollenberg, C. Johnson, K. Noda and R. Verrall, Fusion Engng. Design 27 (1995) 154.
[10] H. Moriyama, S. Tanaka and K. Noda, presented at ICFRM-8, Sendai, Japan, Oct. 26-31, 1997.
[11] H. Kudo, K. Okuno, H. Sugai and Y. Nagame, J. Radioanal. Nucl. Chem., Lett. 93 (1985) 55.
[12] K. Okuno and H. Kudo, J. Nucl. Mater. 138 (1986) 31.
[13] H. Kudo and K. Okuno, J. Nucl. Mater. 101 (1981) 37.
[14] H. Kudo and K. Okuno, J. Nucl. Mater. 133&134 (1985) 192.
[15] H. Kudo, K. Okuno and S. O'hira, J. Nucl. Mater. 155-157 (1988) 524.
[16] K. Noda, Y. Ishii, H. Matsui, H. Ohno and H. Watanabe, Fusion Engng. Design 8 (1989) 329.
[17] H. Moriyama, J. Oishi, T. Terai and K. Kawamura, Fusion Engng. Design 8 (1989) 149.
[18] H. Moriyama, A. Okada, Y. Asaoka and Y. Ito, J. Nucl. Mater. 179-181 (1991) 839.
[19] K. Moritani, T. Magari and H. Moriyama, J. Nucl. Mater., in press.
[20] H. Moriyama and T. Kurasawa, J. Nucl. Mater. 212-215 (1994) 932.

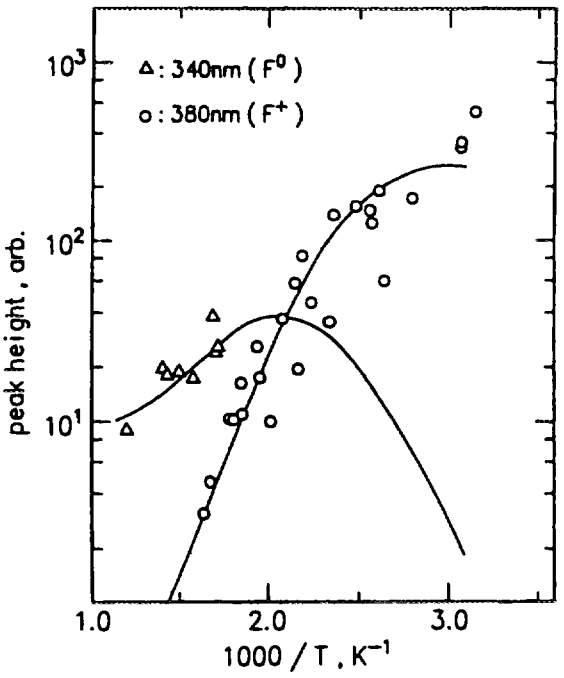

Fig. 1. Arrhenius plots of luminescence intensities at 340nm and 380nm[3]. Marks are experimental and curves are calculated.

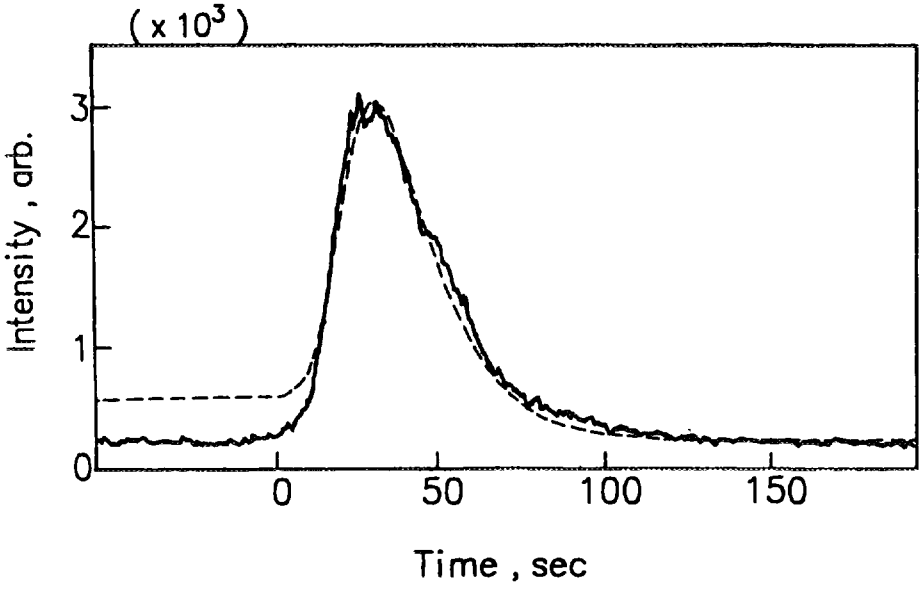

Fig. 2. Temperature-transient behavior of the 340nm luminescence for a change from 528K to 723K[3]. Irradiation time before a temperature increase was 10 min and irradiation current was 40nA. Solid curve is experimental and dashed is calculated.

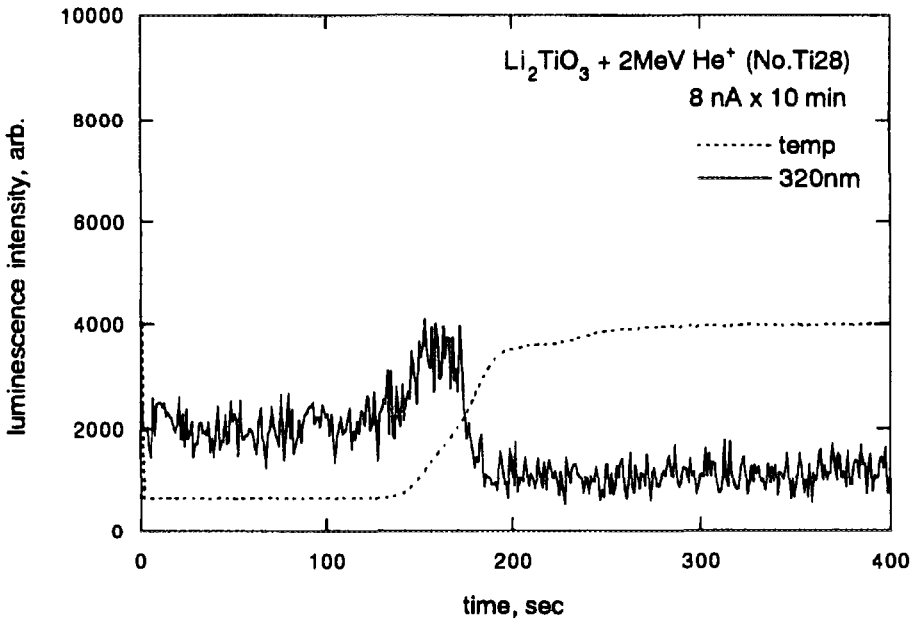

Fig. 3. Temperature-transient behavior of luminescence intensity at 320nm for Li_2TiO_3 irradiated with 2 MeV He^+ ions[4].

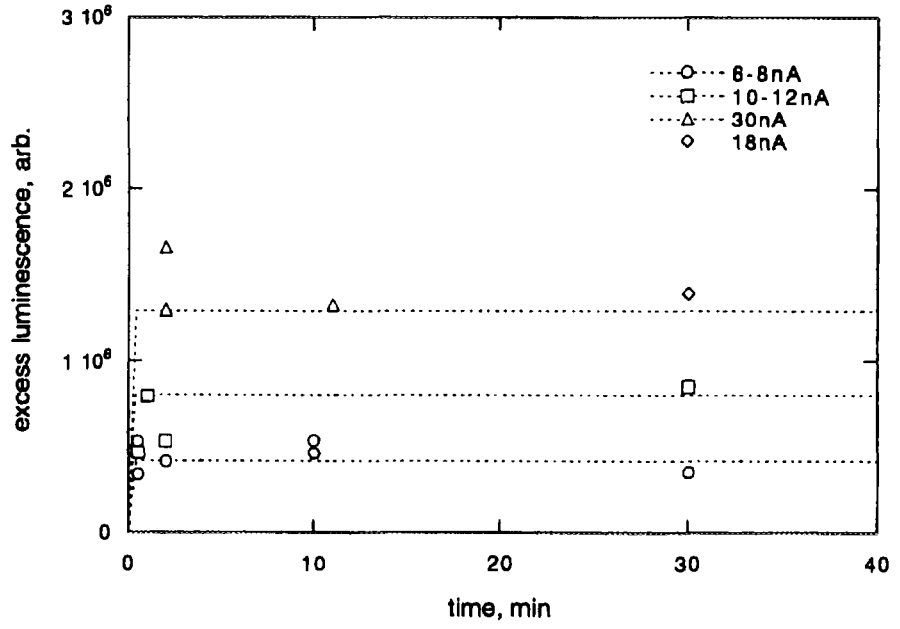

Fig. 4. Dependence of excess luminescence on irradiation time for Li_2TiO_3 irradiated with 2 MeV He^+ ions[4].

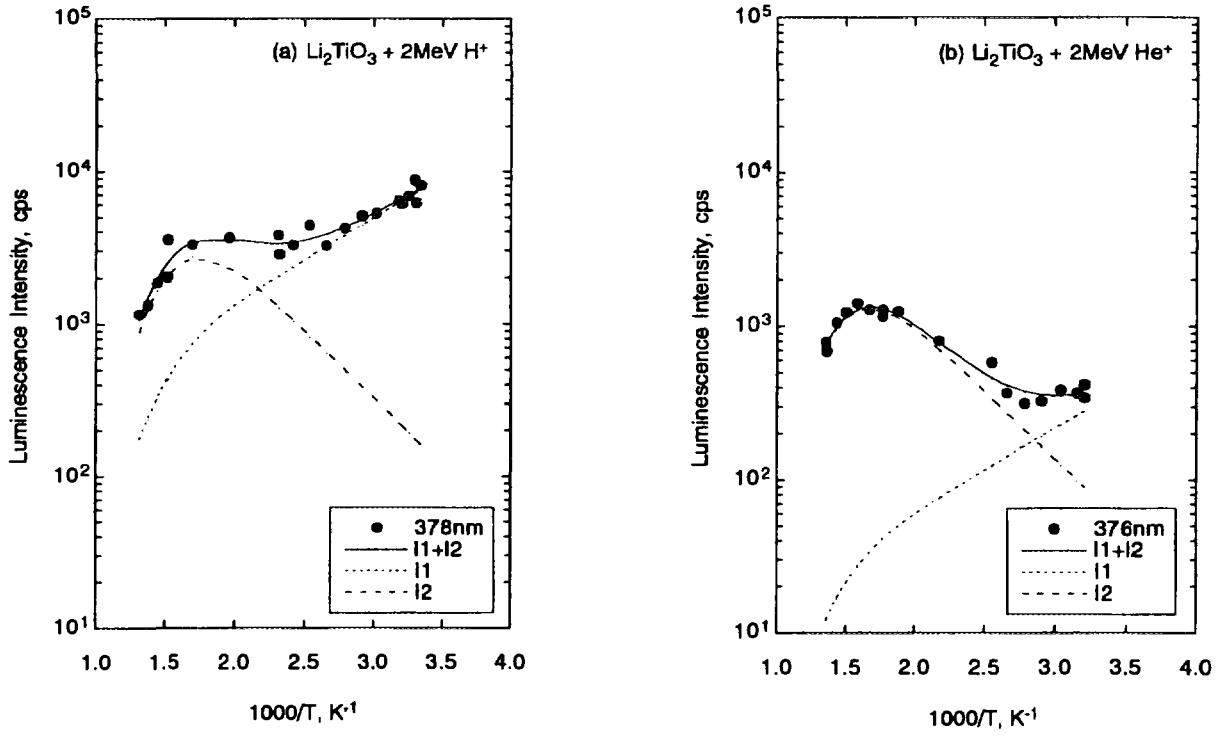

Fig. 5. Arrhenius plots of luminscence intensity of Li_2TiO_3 under (a) H^+ and (b) He^+ irradiation[4]. Marks are experimental[6] and curves represents the least-squares fits of the data to eqs. (9) and (10).

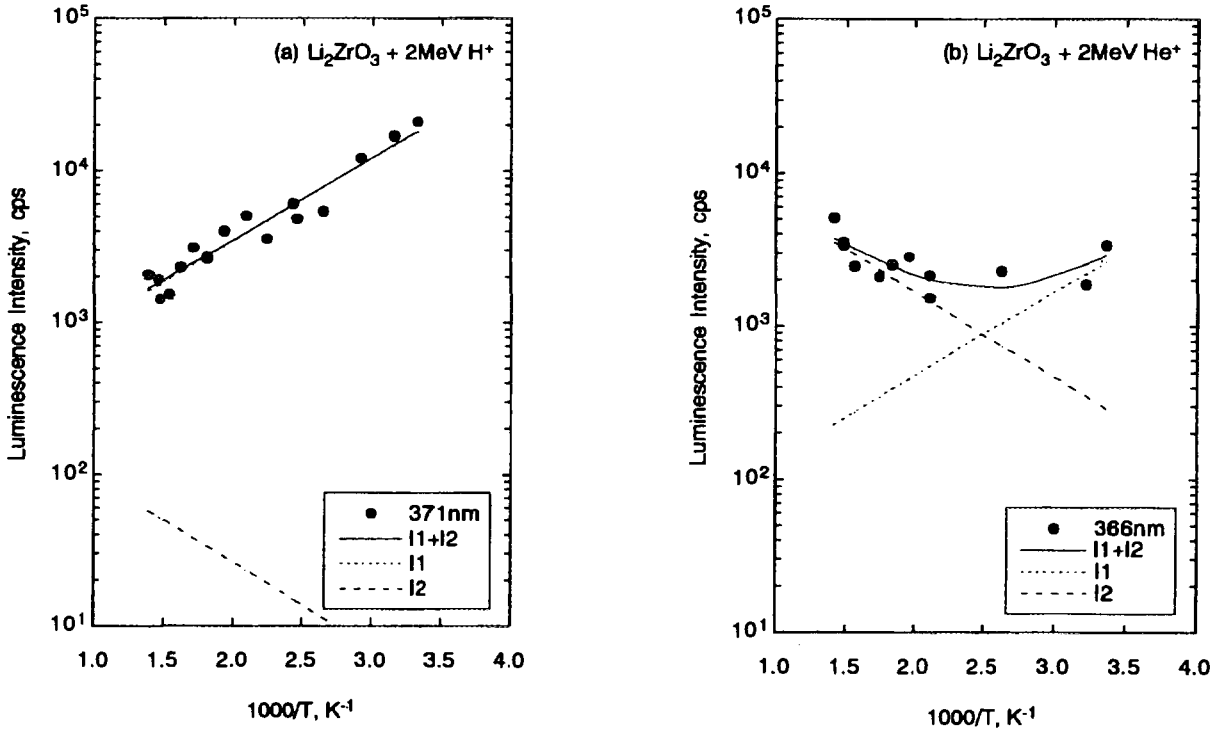

Fig. 6. Arrhenius plots of luminscence intensity of Li_2ZrO_3 under (a) H^+ and (b) He^+ irradiation[4]. Marks are experimental[6] and curves represents the least-squares fits of the data to eqs. (9) and (10).

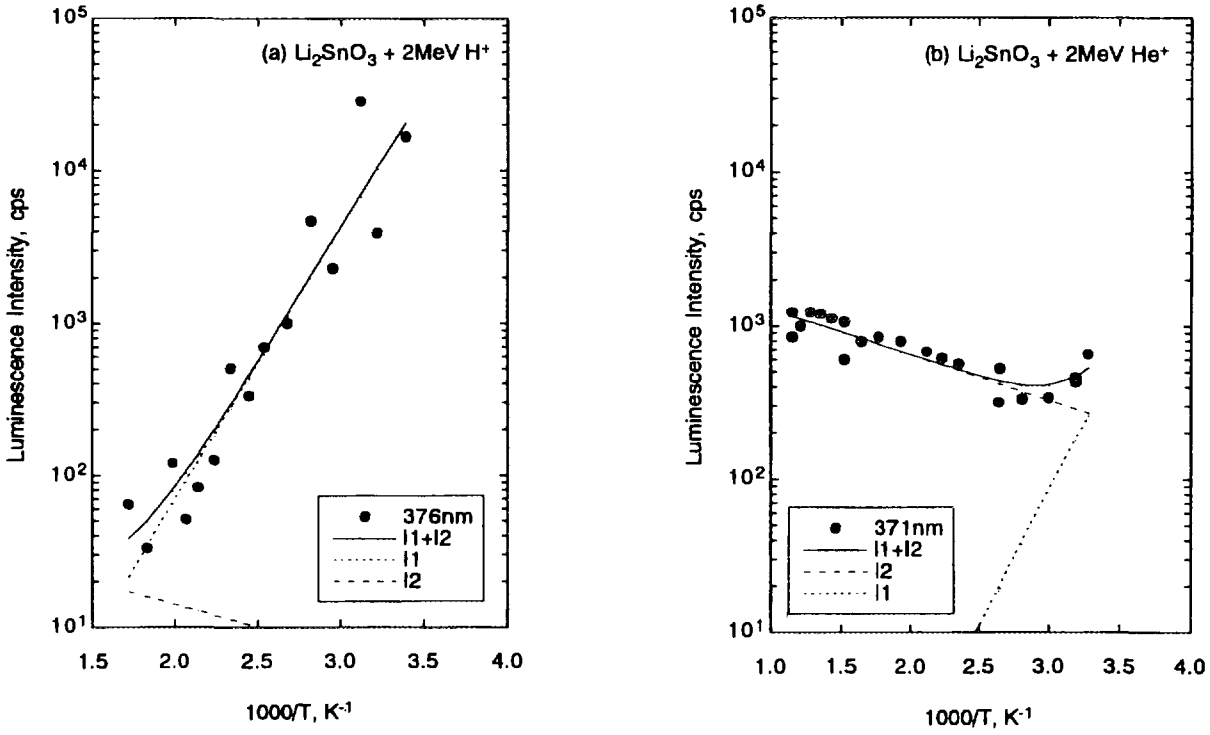

Fig. 7. Arrhenius plots of luminscence intensity of Li_2SnO_3 under (a) H^+ and (b) He^+ irradiation[4]. Marks are experimental[6] and curves represents the least-squares fits of the data to eqs. (9) and (10).

Helium Release from Neutron-Irradiated Li_2O Single Crystals

Daiju Yamaki, Takaaki Tanifuji and Kenji Noda

Japan Atomic Energy Research Institute, Tokai-mura, Ibaraki, Japan.

1. Introduction

Lithium oxide (Li_2O) is one of the prime candidates of tritium breeding materials for fusion reactors. In the fusion reactor blanket environment, irradiation damage is introduced in Li_2O by energetic helium and tritium ions generated with $^6Li(n,\alpha)^3H$ reactions as well as high energy neutrons themselves. In the irradiation damage process, it is known that helium generated forms helium bubbles in Li_2O. In the post-irradiation tests in BEATRIX-II[1] and irradiation experiments using EBR-II[2], it was suggested that the link-up of the helium bubbles forms the open pores in Li_2O and causes the large swelling. In addition, the tritium generated is considered to be trapped in the helium bubbles. Therefore, behavior of helium in Li_2O is a very important R&D issue from the standpoint of the tritium release performance and the irradiation durability which are critical for tritium breeding material. In the previous studies, the helium bubble formation in the bulk[1-3] and helium retention in the Li_2O[4,5] were investigated, however, the helium release behavior, which can provide information on helium migration behavior in Li_2O, has not been investigated. Recently, in the previous study[6], helium release measurements from Li_2O sintered pellets were carried out, and it provided some knowledge on influence of porosity and neutron irradiation on helium release behavior from sintered Li_2O with various bulk densities. In the present paper, the helium release behavior from Li_2O single crystals was investigated, and the results were discussed in the comparison with that for sintered pellets.

2. Experimental

The specimens used were Li_2O single crystals (^6Li enrichment; 0.07 and 7.4 at%) of approximately 0.15-5mm OD. The preparation method and properties of the single crystals were described elsewhere in detail [7,8].

Two kinds of specimens were used. One was the Li_2O single crystals (^6Li: 7.4%) which were irradiated to $2x10^{17}$, $2x10^{18}$ and $2x10^{19}$ n/cm^2 with thermal neutrons in JRR-4 and JRR-2, and the irradiation temperature was in the range of 50 - 100°C. Other was the Li_2O single crystals (^6Li: 0.07%) which were irradiated by using FFTF in BEATRIX-II Phase I irradiation test. The thermal and fast neutron (>0.1MeV) fluence were $1x10^{16}$ and $4x10^{22}$ n/cm^2, respectively, and the irradiation temperature was estimated to be about 650K.

To avoid the tritium contamination of the helium measuring system, the generated tritium in the irradiated specimens was entirely removed in the following process. The irradiated specimens were heated up to 823K (crystal diameter below 590μm) or 873K (crystal diameter over 590μm) in the ammonia sweep gas by a constant heating rate of 2 or 5K/min, and further heated at 823K (crystal diameter below 590μm) or 873K (crystal diameter over 590μm) for two hours to confirm no retention of tritium in the specimens.

The measuring system for helium release is schematically illustrated in figure 1. After removing the tritium, the specimens were loaded in a quartz tube of 20mm in diameter and heated from 823K (crystal diameter below 590μm) or 873K (crystal diameter over 590μm) to 1600K by a constant heating rate of 2K/min. in vacuum (10^{-5}-10^{-6} Pa). During the heating, released helium was continuously measured by pulse-counting method using quadrupole mass spectrometer. Calibration of helium release rate was carried out using helium standard leak and spinning rotor gauge.

3. Results and Discussion.

3.1. Helium release from Li_2O single crystal irradiated with thermal neutrons

Figure 2 shows the typical helium release curves from thermal neutron-irradiated Li_2O specimens in the constant heating rate tests. For all specimens irradiated with thermal neutrons, the helium release curves show only one broad peak in the range of 1100-1300K. It suggests that the helium release process from Li_2O single crystals irradiated with thermal neutrons consists of only one process.

It has been clarified that the tritium release process from Li_2O single crystal irradiated with thermal neutron consists of the bulk diffusion and surface desorption process in the previous study[9]. The helium release process are thought to consist of the bulk diffusion and surface processes by analogy from tritium release processes. However, the surface process may be neglected, since helium atom is inert for Li_2O and sweep gas components. Thus, only the bulk diffusion process could be taken into account.

Figure 3 shows the crystal diameter dependence of the temperature of the helium release peaks. The crystal diameter in fig. 3 is the average diameter of the specimens. It depicts that the temperature of the peaks increase with the crystal diameter. It is considered to show that the diffusion path of the helium released is longer in the larger diameter specimens, and the bulk diffusion process is the rate determining step of the helium release process from Li_2O single crystal irradiated with thermal neutrons.

In the previous study, the helium release behavior from Li_2O sintered pellets was investigated [6]. In the helium release curves from the Li_2O sintered pellets, four kinds of peaks were observed as shown in fig. 4. From the dependencies of the temperature of the peaks on the grain diameter, bulk density and the thermal neutron fluence, and the activation energy of the peaks, it is considered that the helium migration process for peak A in fig. 4 is the diffusion process along the grain boundary, that for peak B is the bulk diffusion process, and that for peak C and D is the diffusion process with

trapping at closed pores in the grains.

Figure 5 shows the grain diameter dependence of the temperature of the peak B in fig. 4 which is considered to be the peak of the bulk diffusion process, and the crystal diameter dependence of the temperature of the peak from single crystal irradiated with thermal neutrons. It is clearly shown that the temperature of the both peaks shows the similar dependence on the grain and crystal diameter. It is considered to suggest that the migration process for peak B in the helium release curves of Li_2O sintered pellets and for the peak in that of Li_2O single crystal are the same process, that is, the diffusion process in the bulk.

Figure 6 shows the relationship between the thermal neutron fluence and the temperature of the peaks in the helium release curves from Li_2O single crystals irradiated with thermal neutrons. It indicates that the temperature of the peaks increase with the thermal neutron fluence. For example, the temperature of the peaks for 150-297μm specimen irradiated with $2x10^{17}$ n/cm^2 of thermal neutrons was 1134K, and that for same diameter specimen irradiated with $2x10^{19}$ n/cm^2 of thermal neutrons was 1304K. From the relationship between the temperature of the peaks and the grain or crystal diameter shown in fig. 5, the peak temparature of 1304K for 150-297μm specimen irradiated with $2x10^{19}$ n/cm^2 of thermal neutron is calculated to be equal to the 3080μm of crystal diameter specimen irradiated with $2x10^{17}$ n/cm^2 of thermal neutrons. It means that the apparent helium diffusion path for the 150-297μm specimen irradiated with $2x10^{19}$ n/cm^2 thermal neutron is about fourteen times of that for the specimen irradiated with $2x10^{17}$ n/cm^2 thermal neutron. It seems to indicate that the helium diffusing in the Li_2O crystal is trapped at defects introduced in the crystals by the energetic helium and tritium generated by the reaction of $^6Li(n,\alpha)^3H$. Radiation damage studies performed so far showed that F+ centers (an oxygen vacancy trapping an electron), F-aggregate centers and Li colloidal centers, etc. introduced by irradiation. Although such irradiation defects are annealed out at the temperatures lower than 900K[10], the irradiation effects on the peaks are still observed above 900K, as shown in figs. 6. Thus, the irradiation defects as the trapping sites are considered to be not the above-

mentioned irradiation defects such as F^+ centers and Li colloidal centers but some defects clusters such as dislocation loops etc. which are not completely annealed out even at 1400K.

3.2. Helium release from Li_2O single crystal irradiated with fast neutrons

Figure 7 shows the typical helium release curve from Li_2O single crystals (^6Li enrichment 0.07%) irradiated with fast neutrons in FFTF in the constant heating rate tests. Although the helium release curves from thermal neutron irradiated Li_2O single crystals have only one peak as shown in fig. 2, that from the Li_2O single crystals irradiated in FFTF seems to consist of two broad peaks which are superimposed by many sharp peaks as shown in fig. 7. It is considered to show that the helium release process from Li_2O single crystals irradiated in FFTF consists of some different processes. From the comparison with the results of the helium release curves from Li_2O single crystal irradiated with thermal neutrons, it is considered that the larger broad peak in fig. 7 (peak F) is for the bulk diffusion process.

Since helium atom is inert for Li_2O and sweep gas components as mentioned previously, the existence of the two broad peaks in the helium release curve suggests that the two different diffusion processes exist in the helium release. Although investigations of microstructure of the specimen using SEM, etc., there is a possibility that the diffusion through the micro crack due to heavy irradiation in FFTF with fast neutrons may be the process for the peak E.

In the helium release curves, many sharp peaks superimposed on the broad two peaks as shown in fig. 7. In the PIE of BEATRIX-II phase I, no helium bubble formation was observed in the specimens[11]. Baldwin et al. indicated that the retained helium in Li_2O sintered pellets irradiated with fast neutrons in EBR-II are 12-25% of the generated helium at the irradiation temperature of 773 and 973K, while 5-10% at 1173K[5]. In the PIE of BEATRIX- II Phase II irradiation tests, it was found that helium bubbles were grown-up in the irradiation temperatures range of 803-913K for Li_2O

sintered ring specimens[1]. In addition, extensive bubble formation was observed after heating in an inert atmosphere to 1223K for 1 hour by Verrall et al.[3]. Therefore, it is considered that the temperature of the FFTF specimen examined in the PIE of BEATRIX-II phase I is not enough high to form helium bubbles in the grain since the temperature of the specimen during and after irradiation was kept below 650K[11]. Since the specimens used in this study had been heated up to over 800K before this study to remove the generated tritium in the specimen, it is considered that the helium bubble could be formed during the tritium removal process. Thus it is considered that the superimposed sharp peaks may due to the burst of the trapped helium in the bubbles through the crack which induced by high heating of temperatures during the measurement of helium release.

4. Conclusion

Helium release behavior in post-irradiation heating tests was investigated for Li_2O single crystals which had been irradiated with thermal neutrons in JRR-4 and JRR-2, and fast neutrons in FFTF. It is clarified that the helium release curves from JRR-4 and JRR-2 specimens consists of only one broad peak. From the dependence of the peak temperatures on the neutron fluence and the crystal diameter, and the comparison with the results obtained for sintered pellets, it is considered that the helium generated in the specimen is released through the process of bulk diffusion with trapping by irradiation defects such as some defect clusters. For the helium release from FFTF specimens, two broad peaks were observed in the release curves. It is considered to suggest that two different diffusion paths exist for helium migration in the specimen, that is, bulk diffusion and diffusion through the micro-crack due to the heavy irradiation. In addition, helium bubble formation after irradiation due to the high temperature over 800K is suggested.

<References>

[1] T. Takahashi, K.Noda, O.D.Slagle and F.D.Hobbs, Microstructure and density changes of Li_2O

during irradiation in BEATRIX-II, Phase I and II, J.Nucl.Mater. 233-237(1996)1457.

[2] Y.Y.Liu, R.F.Mattas, D.L.Smith and D.L.Porter, Microstructural examination of fast-neutron irradiated Li_2O, J.Nucl.Mater. 133&134(1985)209.

[3] R.A.Verrall, D.H.Rose, J.M.Miller, I.J.Hastings and D.S.MacDonald, Bubble formation in irradiated Li_2O, J.Nucl.Mater. 179-181(1991)855.

[4] O.D.Slagle and G.W.Hollenberg, BEATRIX-II, Phase II: Data Summary Report, PNNL Report, Pacific Northwest National Laboratory, PNNL-11148(May 1996).

[5] D.L.Baldwin and G.W.Hollenberg, Measurements of tritium and helium in fast neutron irradiated lithium ceramics using high temperature vacuum extraction, J.Nucl.Mater. 141-143(1986)305.

[6] T . Tanifuji, D . Y amaki a nd K . N oda, Helium Release from Neutron-Irradiated Li_2O Sintered Pellets, presented at the 4th International Symposium on Fusion Nuclear Technology (ISFNT-4), April 1997, Tokyo, Japan, to be published in Fusion Eng. and Des.

[7] T.Tanifuji, K. Noda, T. Takahashi and H. Watanabe, Tritium release from neutron-irradiated Li_2O: Diffusion in single crystal, J.Nucl.Mater. 149(1987)227.

[8] I.Shindo, S. Kimura, K. Noda, T. Kurasawa and S. Nasu, Growth of Li_2O single crystals by the floating zone method, J.Nucl.Mater. 79(1979)418.

[9] T.Tanifuji, D.Yamaki, K.Noda, O.D.Slagle, F.D.Hobbs and G.W.Hollenberg, Tritium release from Li_2O single crystals irradiated with fast neutrons, Fusion Technology 1996(1997)pp.1455.

[10] K. Noda, Radiation damage and irradiation effects in solid breeders, J. Nucl. Mater. 179-181 (1991)37.

[11] T. Takahashi, K. Noda, O.D. Slagle and F.D. Hobbs, Microstructure and density changes of Li2O during irradiation in BEATRIX-II, Phase I and II, J. Nucl. Mater 233-237(1996)1457.

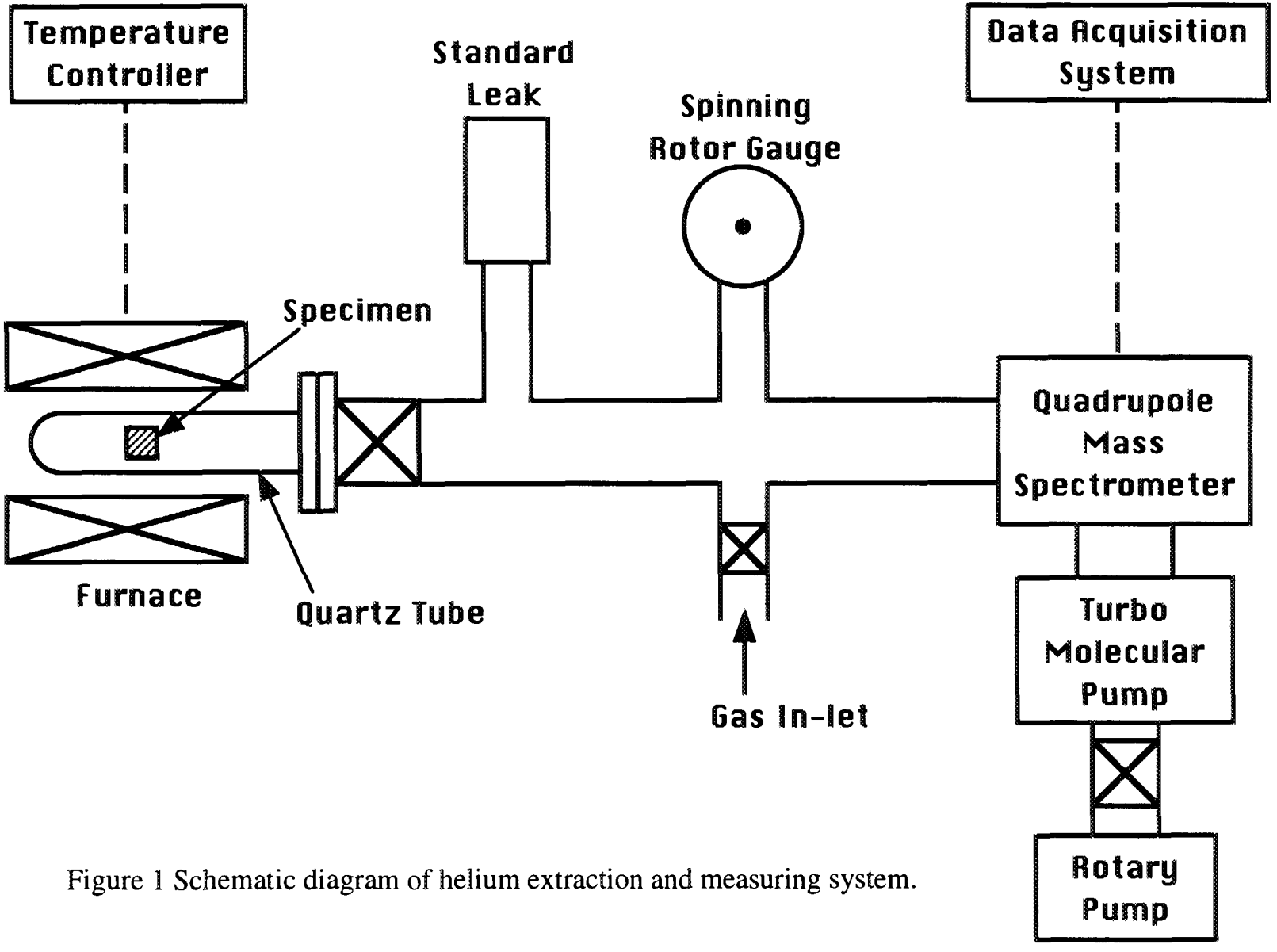

Figure 1 Schematic diagram of helium extraction and measuring system.

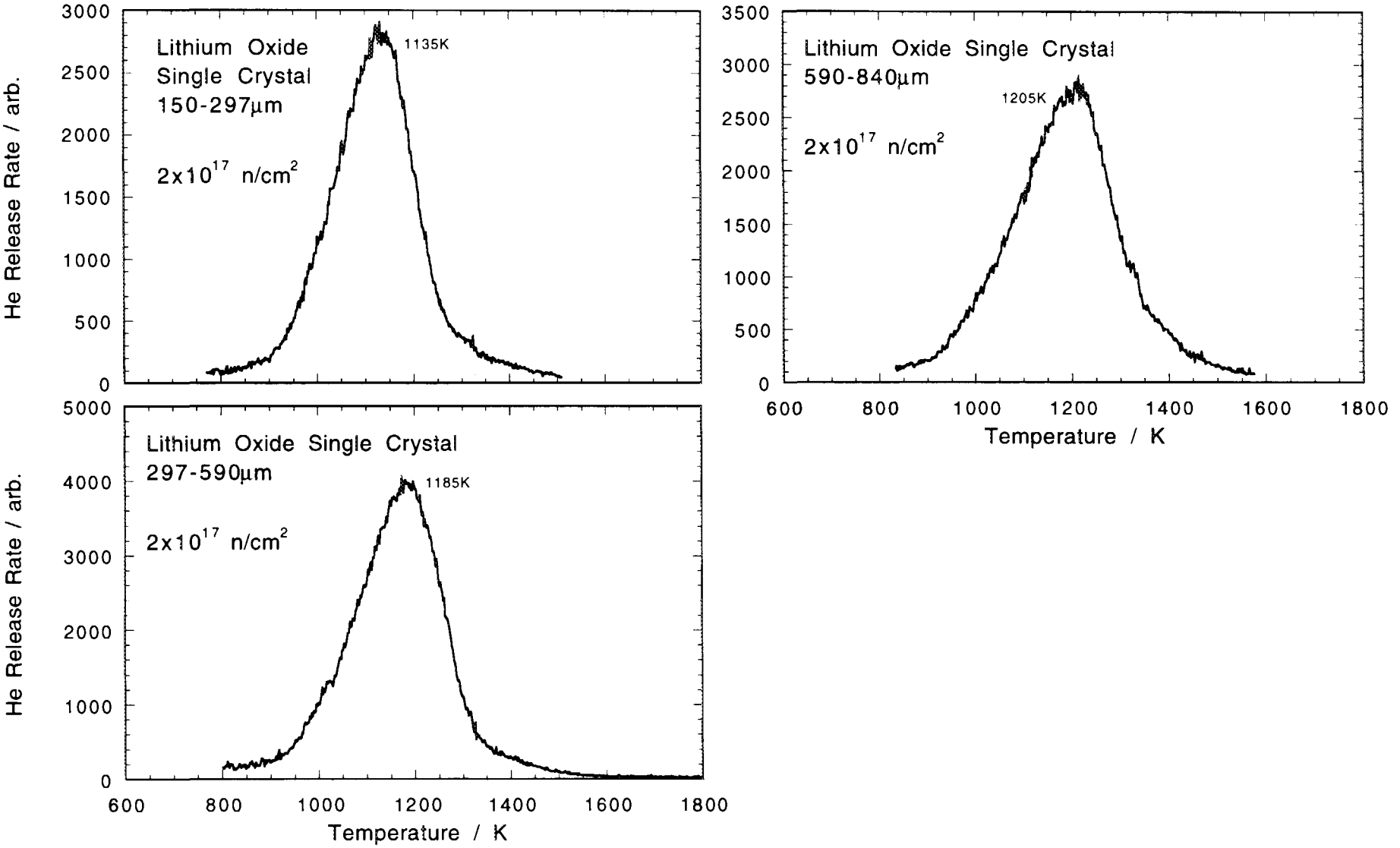

Figure 2 Typical helium release curves from Li2O single crystals irradiated with thermal neutrons.

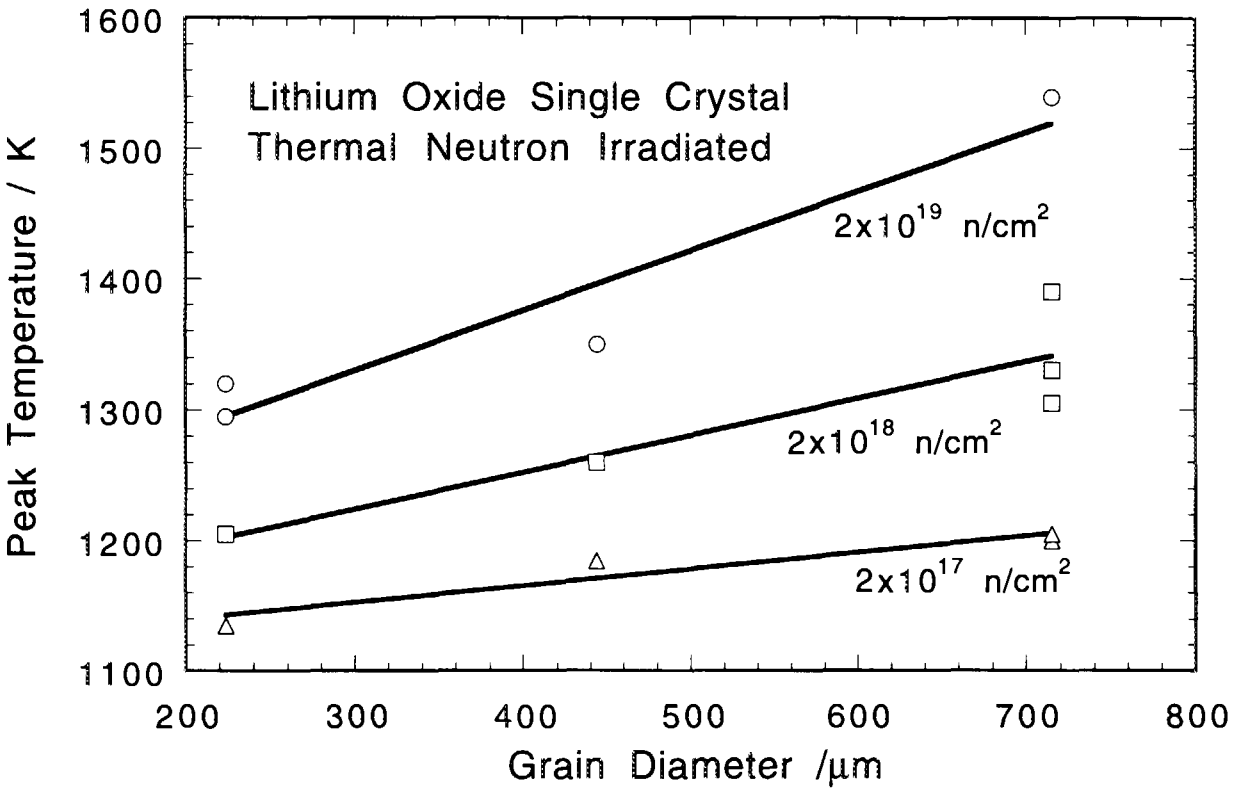

Figure 3 The grain diameter dependence of the temperature of the helium release peaks from Li2O single crystals irradiated with thermal neutrons.

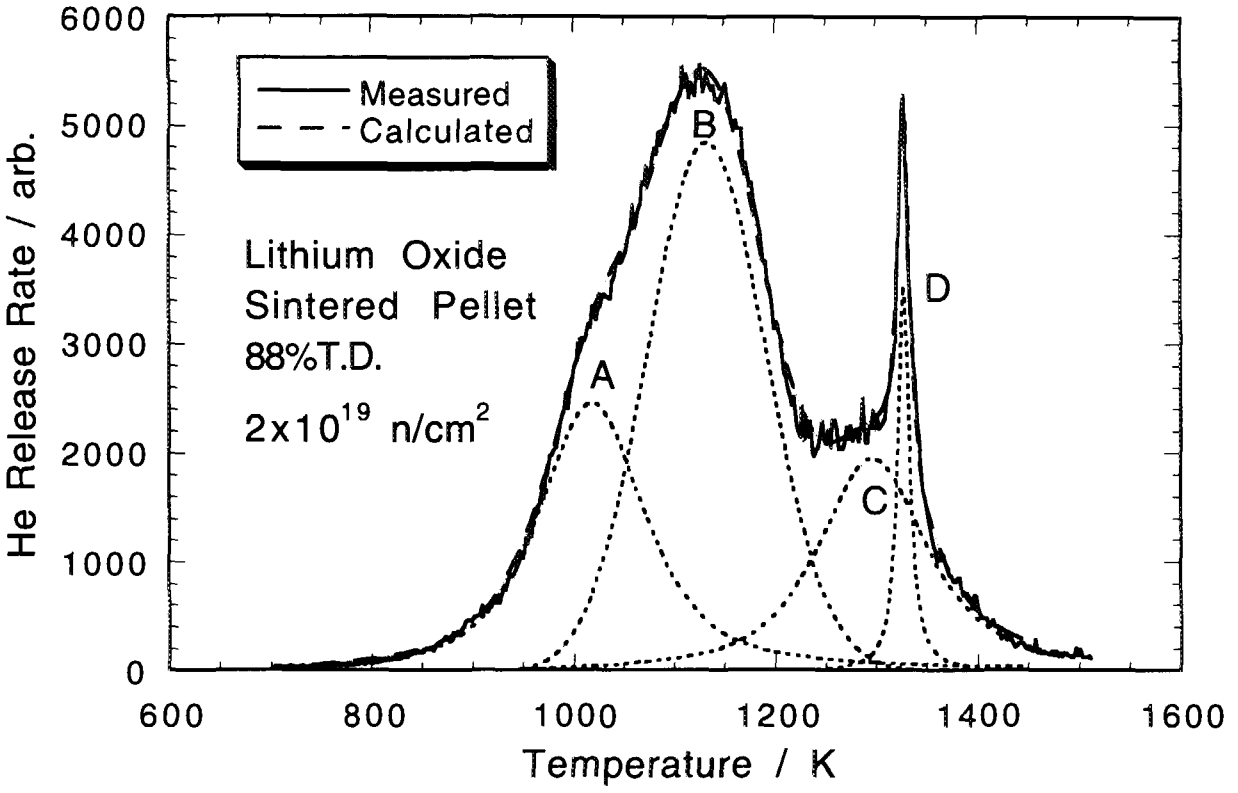

Figure 4 The typical helium release curves from sintered Li2O irradiated with thermal neutrons [6].

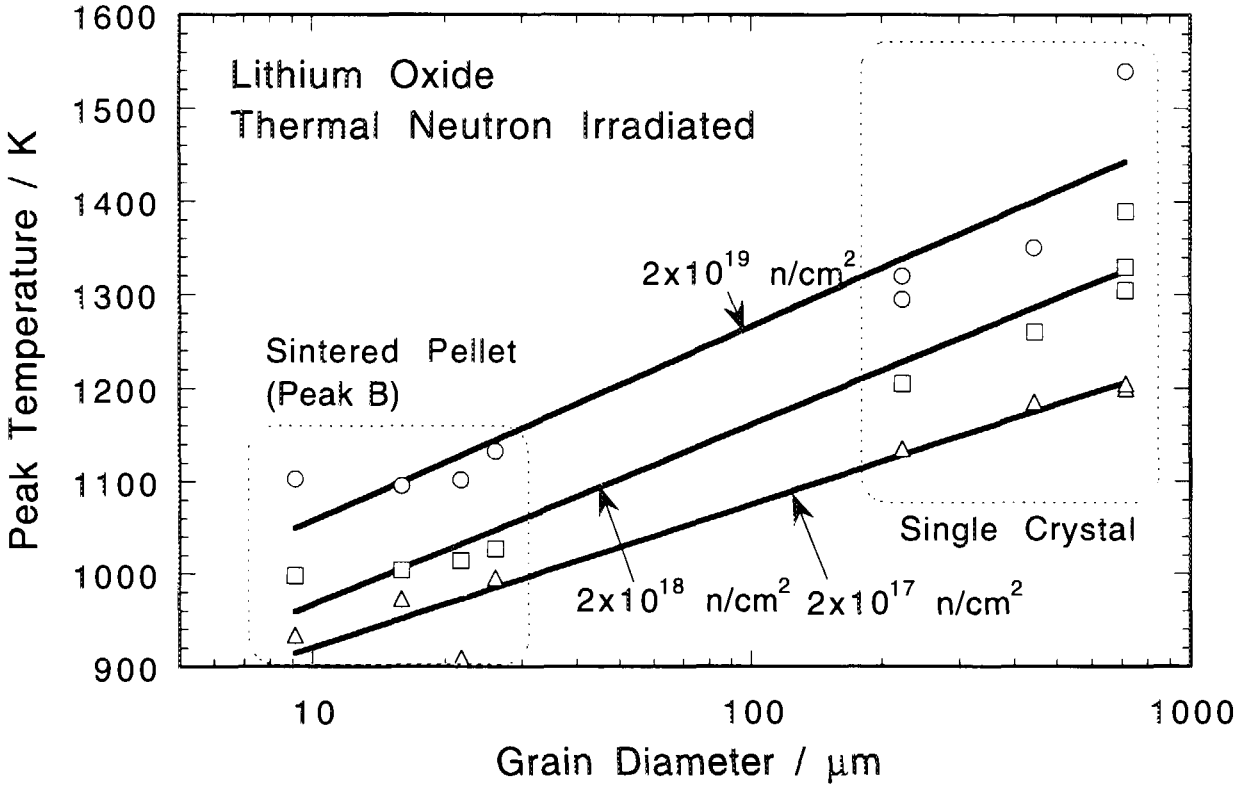

Figure 5 The grain diameter dependence of the temperature of the peak B in fig.4 and that of the peak in the helium release from Li2O single crystal irradiated with thermal neutrons.

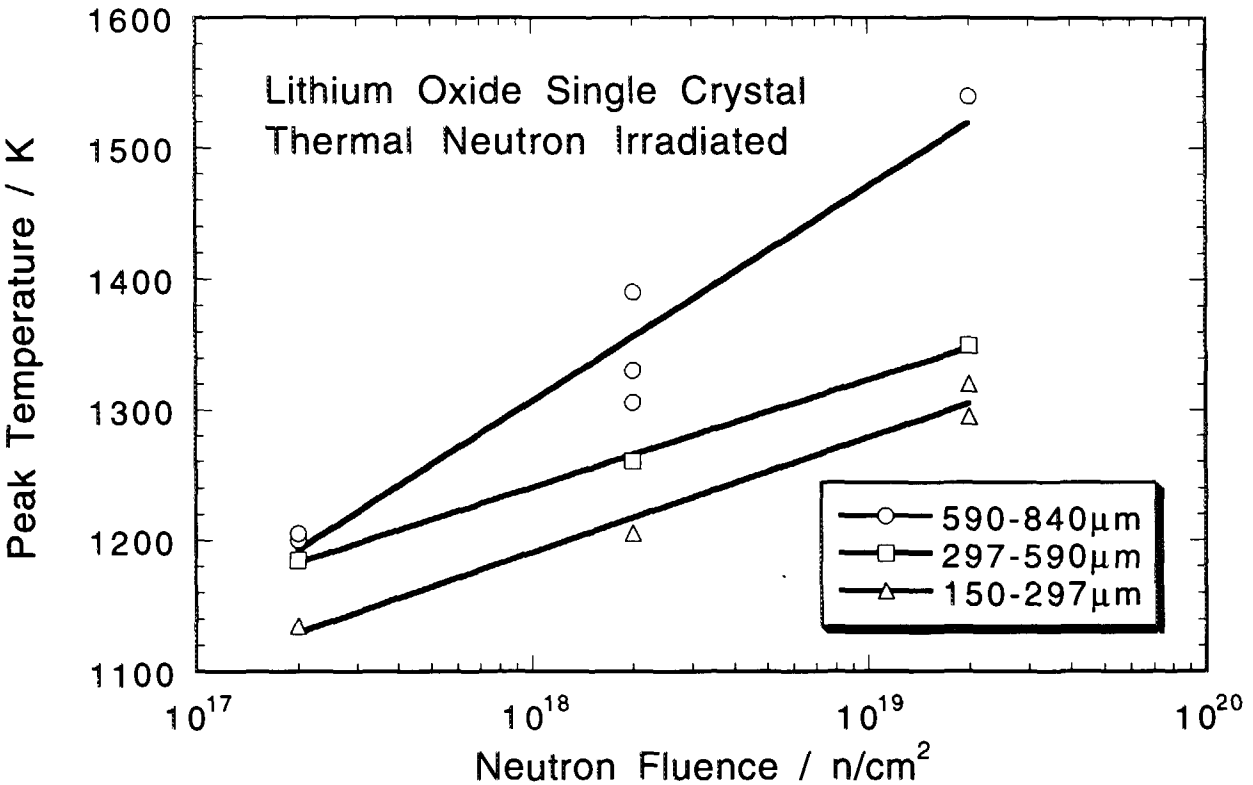

Figure 6 The relationship between the thermal neutron fluence and the temperature of the peaks in the helium release curves from Li2O single crystals irradiated with thermal neutrons.

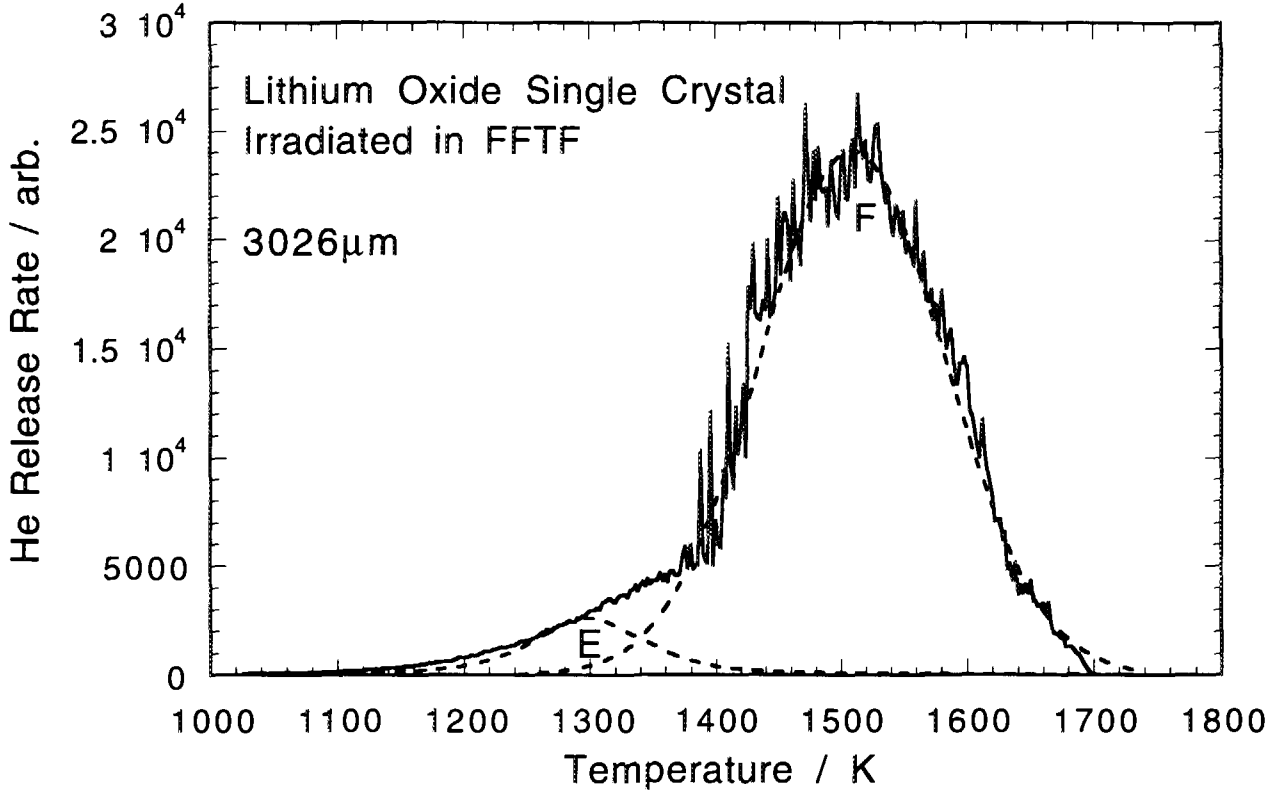

Figure 7 The typical helium release curve from Li2O single crystal irradiated with fast neutrons in FFTF.

SESSION 9

Fabrication of Ceramic Breeders

Density Improvement of Li_2TiO_3 Pebbles Fabricated by Wet Process

K.Tsuchiya*, H.Kawamura*, K.Fuchinoue**, H.Sawada** and K.Watarumi**

*Oarai Research Establishment, JAERI,
Oarai-machi, Higashi-ibaraki-gun Ibaraki 311-13, Japan
**Nuclear Fuel Industries. LTD.,
Tokai-mura, Naka-gun, Ibaraki 319-11, Japan

ABSTRACT

Lithium titanate (Li_2TiO_3) has attracted the attention of many researchers from a point of tritium recovery at low temperature, chemical stability, etc.. The application of small Li_2TiO_3 sphere has been proposed in some designs of fusion blanket. On the other hand, the wet process is most advantageous as the fabrication method of Li_2TiO_3 pebbles from a point of mass production, and of reprocessing necessary for effective use of resources and reduction of radioactive wastes. In the preliminary fabrication test, density of Li_2TiO_3 pebbles was about 40%T.D.. Therefore, in this study, density improvement tests and preliminary characterization of Li_2TiO_3 pebbles by wet process were performed, noting the aging condition and sintering condition in the fabrication process of the gel-spheres. This study yielded Li_2TiO_3 pebbles in target range of 80-85 %T.D..

1. INTRODUCTION

In the development of tritium breeding blankets for fusion reactors, lithium-containing ceramics such as Li_2O, $LiAlO_2$, Li_2ZrO_3, Li_2TiO_3 and Li_4SiO_4 were quickly recognized as promising tritium breeding materials[1-2].

Particularly, Li_2TiO_3 has attracted the attention of many researchers from a point of easy tritium recovery at low temperature, chemical stability, etc. [3-5]. The application of small Li_2TiO_3 pebble was proposed in some designs of fusion blanket in order to reduce thermal stress, etc. [6-9]. Status of fabrication of ceramic tritium breeder pebbles is shown in Table 1. Fabrication development of Li_2TiO_3 pebble is performed in each research.

Recently, reprocessing technology on irradiated ceramic tritium breeders was developed from a point of effective use of resources and reduction of radioactive wastes [10-11]. The basic concept of lithium reprocessing for tritium breeding materials is shown in Fig.1. The sol-gel method and/or wet process [12-15] are the most advantageous for fabricating small Li_2TiO_3 pebbles from the reprocessing lithium-bearing solution. In fusion blanket, tritium is produced and recovered from ceramic breeders. After, used ceramic breeders are taken out from the blanket and reprocessed.

In the preliminary fabrication test, density of Li_2TiO_3 pebbles fabricated by wet process was about 40%T.D.. Therefore, in this study, density improvement tests of Li_2TiO_3 pebbles were carried out by the wet process and characterization of Li_2TiO_3 pebbles were estimated. Especially, aging condition and sintering condition were optimized in order to raise density of Li_2TiO_3 pebbles by wet process.

Table 1 Status of fabrication of ceramic tritium breeder pebbles

	Group	Material	Diameter (mm)	Fabrication Process
Japan	JAERI	Li_2O	1	Melting Granulation
			1	Rotating Granulation
			1	Wet Process
		γ-$LiAlO_2$	1	Rotating Granulation
		Li_4SiO_4	1	Rotating Granulation
		Li_2ZrO_3	1	Rotating Granulation
		Li_2TiO_3	1	Rotating Granulation
			0.5~3	Wet Process
Canada	AECL	γ-$LiAlO_2$	0.8, 1.2, 3	Sol-Gel
			1.2, 3	Extrude/Tumble
		Li_2ZrO_3	1.2, 3	Extrude/Tumble
		Li_2TiO_3	1.2	Extrude/Tumble
EU	CEA	Li_2ZrO_3	1	Extrude/Tumble
			3	Granule/Mechanical Press
		Li_2TiO_3	?	?
	KIK	Li_4SiO_4	0.1~0.2, 0.3~0.6	Melt/Spray
			0.5	Extrude/Tumble
	ECN	Li_2TiO_3	1	Wet Process

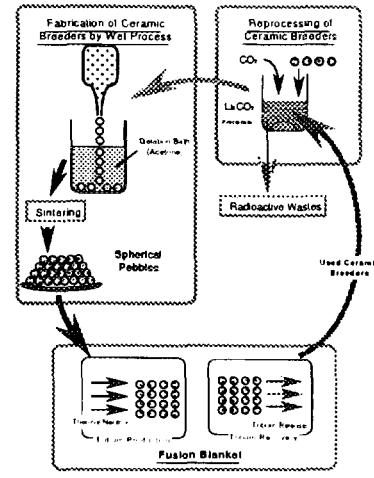

Fig.1 Concept of lithium reprocessing for tritium breeding materials.

2. EXPERIMENTAL

2.1. Materials

Li_2TiO_3 powder, which is starting material, was prepared with purity of 99.9%. This powder was manufactured by Cerac Inc.. The main impurities of Li_2TiO_3 powder were as follows: Na, 95; Ca, 140; Mg, 39; Al, 130; Si, 190; Co, 3; B, <25 (in ppm). The size of Li_2TiO_3 powder was in the region of 0.3-70 μm and 10 μm on an average. Polyvinylalcohol (PVA) manufactured by Kuraray Co., Inc. was used as the binder of Li_2TiO_3 powder.

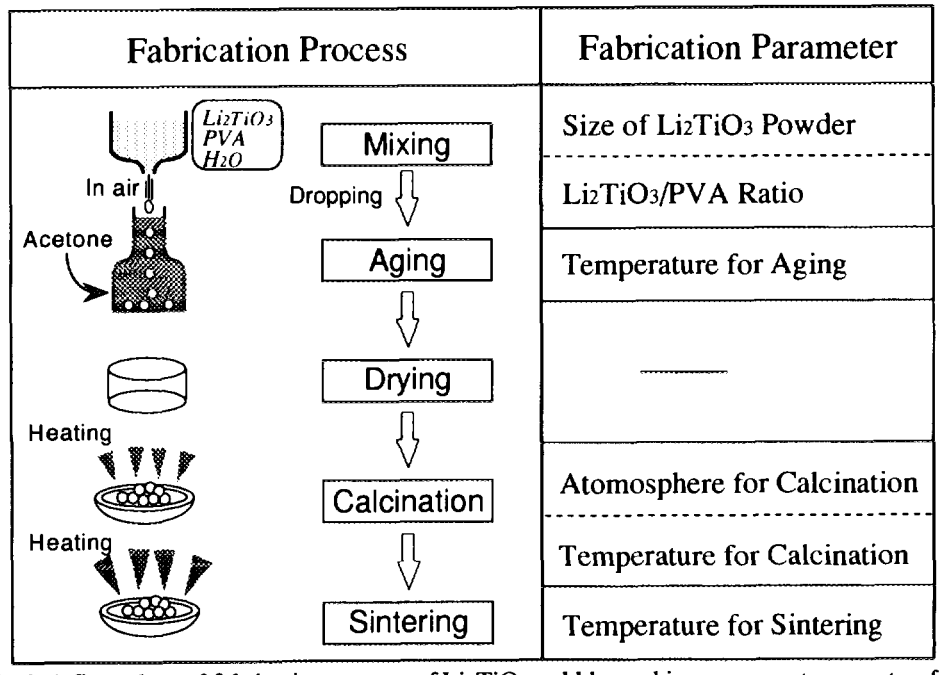

Fig.2 A flow chart of fabrication process of Li_2TiO_3 pebbles and improvement parameters for increasing Li_2TiO_3 pebble density.

2.2. Fabrication Process

The most important feature of the wet process is that Li_2TiO_3 powder is used as starting material to produce Li_2TiO_3 pebbles. A flow chart of fabrication process of Li_2TiO_3 pebbles and improvement parameters for increasing Li_2TiO_3 pebble density are shown in Fig.2. The wet process is shown as follows:

1) Fabrication of gel-spheres; The liquid mixture of Li_2TiO_3 and PVA solution is dropped in cooled acetone through a nozzle, and the gel-spheres is fabricated.
2) Calcination of gel-spheres; PVA in the gel-spheres is removed, and the Li_2TiO_3 spheres with low density are fabricated.
3) Sintering; The Li_2TiO_3 spheres are sintered in air, and Li_2TiO_3 pebbles with high density are fabricated.

2.3. Improvement Tests

In the preliminary fabrication test, the gel-spheres were fabricated under the mixing condition of the Li_2TiO_3 (43 wt%), PVA (4 wt%) and water (53 wt%). These gel-spheres were calcinated and sintered, and then characteristics of Li_2TiO_3 pebbles, i.e. density, sphericity, etc., were evaluated.

In the first fabrication test, a dropping test of the gel-spheres was carried out to decide the optimum mixing ratio between Li_2TiO_3 powder and PVA solution. Sintering conditions (temperature and time of sintering) were changed.

In the second fabrication test, aging condition was changed and relationship between the aging temperature and cracking rate, i.e. rate of the number of cracked gel-spheres to the number of total gel-spheres, was evaluated. The gel-spheres were heated at 650°C for 6 h in air and sintered at 1400°C for 4 h.

In the third fabrication test, sintering tests were conducted in the sintering temperature range from 1100 to 1430°C for 4 h in air. Aging condition was selected at -30°C for 1 h.

2.4. Characterization method of Li_2TiO_3 pebbles

The Li_2TiO_3 pebbles were characterized by following. Density of Li_2TiO_3 pebbles was measured by mercury porosimetry. Microstructure and crystal form were measured by a scanning electron microscope (SEM) and an X-ray diffractmetry (XRD), respectively. The collapse loads were measured by unconfined compression tester with the compression indenter made of SiC. The impurities in Li_2TiO_3 pebbles were measured by an atomic emission spectrometry with inductively coupled plasma (ICP-AES) and an atomic absorption spectorometry (AAS), and content of carbon in Li_2TiO_3 pebbles was measured by infrared absorptiometric method.

3. RESULTS AND DISCUSSIONS

3.1. Optimization on fabrication method of Li_2TiO_3 pebbles

Optimized conditions obtained by each fabrication test of Li_2TiO_3 pebbles is shown in Table 2. Fabrication tests were conducted four times. On the basis of the results obtained from these tests, optimization of fabrication method is discussed as follows in detail.

Table 2 Optimized conditions obtained by each fabrication test of Li_2TiO_3 pebbles

Process / Fabrication Test	Mixture Ratio	Aging Temperature	Calcination Condition	Sintering Time	Sintering Temperature	Density
Preliminary Test	Li_2TiO_3:43wt% PVA :4wt%	0°C	650°C 6 h	10 h	1000°C	40%T.D.
1st Improvement	Li_2TiO_3:46wt% PVA :4wt%	0°C	650°C 6 h	4 h	1150°C	60%T.D.
2nd Improvement	Li_2TiO_3:46wt% PVA :4wt%	-20°C	650°C 6 h	4 h	1400°C	76%T.D.
3rd Improvement	Li_2TiO_3:46wt% PVA :4wt%	-30°C	650°C 6 h	4 h	1400°C	81%T.D.

Remark : The aging temperature and sintering temperature were effective to increase the density of Li_2TiO_3 pebbles

1) *Decision of Li_2TiO_3/PVA ratios*

In the preliminary fabrication test, density of Li_2TiO_3 pebbles was 40 %T.D.. Therefore, fabrication tests were additionally performed three times in order to raise sintering density of Li_2TiO_3 pebble fabricated by wet process.

In the first fabrication test, the fabrication of gel-spheres was performed under various conditions on mixing ratio between Li_2TiO_3 powder and PVA solution. Relationship between content of PVA solution and content of Li_2TiO_3 powder for gel-spheres fabrication is shown in Fig.3. Shape of the gel-sphere in region A, that is the Li_2TiO_3 and PVA ratio of 62 wt% and 3 wt%, was not sphere. In this region, viscosity of liquid mixture was high because of high content of Li_2TiO_3 powder. Therefore, liquid mixture was difficult to leave from the nozzle. On the other hand, shapes of gel-sphere in region B and C, that are the Li_2TiO_3/PVA ratios of 46/4 wt% and 47/3 wt%, respectively, were almost sphere. Especially, the gel-spheres in region B had high sphericity. From these results, Li_2TiO_3 and PVA ratio of the region B was chosen as the optimum condition. The sphericity of gel-spheres fabricated with the pulverized Li_2TiO_3 powder were also better than that of gel-spheres fabricated with the Li_2TiO_3 powder before pulverization. The gel-spheres were heated at 650°C for 6 h in air and sintered at 1150°C for 4 h. In this experiment, density of Li_2TiO_3 pebbles was 60 %T.D..

2) *Aging condition*

Aging temperature dependence on content density of Li_2TiO_3 in gel-spheres and on cracking rate of gel-spheres is shown in Fig.4. The aging time was selected for 1 h. In Fig.3, the Li_2TiO_3 content in the gel-spheres increased with decreasing the aging temperature. It seems that the contraction of gel-spheres increased with decreasing the aging temperature.

On the other hand, gelation of PVA solution occurs at less than -10°C in air. In this test, gelation of liquid mixture occurred at less than 0°C in acetone. It seems that dehyrdration of gel-sphere was hastened by acetone. However, when the aging temperature was lower than -40°C, cracking rate of the gel-spheres was more than 90%. It can be considered that freezing point of the liquid mixture affects the cracking rate of the gel-sphere.

From evaluation results of aging temperature, aging condition was selected between -20°C and -30°C for 1 h. The gel-spheres were heated at 650°C for 6 h and sintered at 1400°C for 4 h. In this test, density of Li_2TiO_3 pebbles was 76 %T.D..

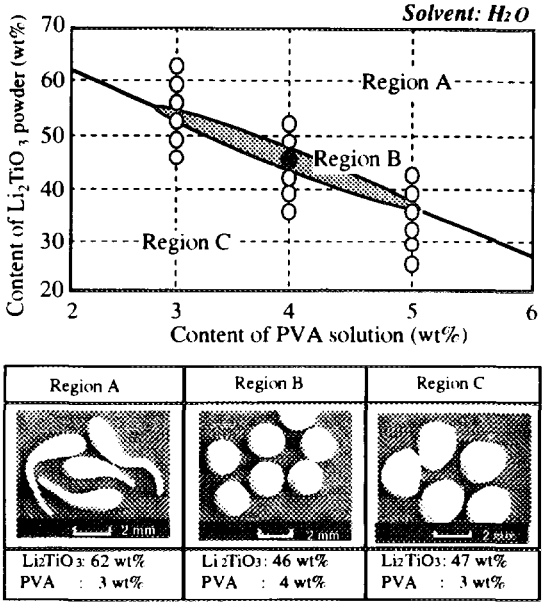

Fig.3 Relationship between content of PVA solution and content of Li_2TiO_3 powder for gel-spheres fabrication.

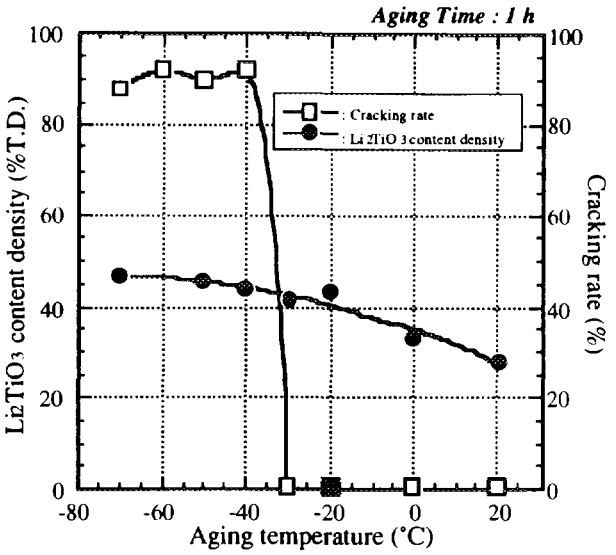

Fig.4 Aging temperature dependence on content density of Li_2TiO_3 in gel-spheres and on cracking rate of gel-spheres.

3) *Sintering condition*

Relationship between sintering temperature and Li_2TiO_3 pebble density is shown in Fig.5. At the sintering condition of 1000°C for 4 h, Li_2TiO_3 pebble density was 54 %T.D. and the grain size of Li_2TiO_3 pebbles was about 4 μm. The microstructure of the Li_2TiO_3 pebbles was altered and grain coarsening was seen. Typical sintering effects such as neck growth, particle coalescence and pore growth were observed in the microstructure. At the sintering condition of 1200°C for 4 h, Li_2TiO_3 pebble density was 64 %T.D. and grain size was about 10 μm. The microstructure showed further evidence of sintering such as grain growth and fewer but larger pores. Particles bridged by necks, are well bonded together by diffusion. The sintering temperatures above 1400°C yielded completely different microstructural features. The grains cannot be distinguished in the fracture surface. They grew extensively (over 20 μm) with no remnants of the initial boundaries. Li_2TiO_3 pebble density was more than 80 %T.D..

The grain size and density of Li_2TiO_3 pebbles increased with increasing sintering temperature. The extent of grain coarsening and achievable final density depend on the rate-controlling mechanism in the coarsening and densification kinetics.

3.2. Characterization of Li_2TiO_3 pebbles

The characterization of Li_2TiO_3 pebbles fabricated in the 3rd fabrication test was carried out. Summary on characterization of Li_2TiO_3 pebbles is shown in Table 3. The main features are discussed below.

The density of Li_2TiO_3 pebbles fabricated by this method was 81 %T.D.. The size of Li_2TiO_3 pebbles was 1.52±0.05 mm (av.). Sphericity of Li_2TiO_3 pebbles, which is the rate of long diameter and short diameter, was measured by the photographic analysis method. Sphericity of Li_2TiO_3 pebbles fabricated by this method was very high at 1.11±0.07. Distribution on collapse load of Li_2TiO_3 pebbles fabricated by wet process is shown in Fig.6. The collapse loads were measured with the above Li_2TiO_3 pebbles. The average collapse load

was 46.1±8.8 N. The crystal form of Li_2TiO_3 pebbles was observed by XRD and only X-ray peak of Li_2TiO_3 was detected. The main impurities of Li_2TiO_3 pebbles were shown in Table 4. From this analysis, it is shown that impurities was not mixed in Li_2TiO_3 pebbles by this process.

From the results of these tests, bright prospects were obtained concerning the fabrication method of Li_2TiO_3 pebbles by wet process.

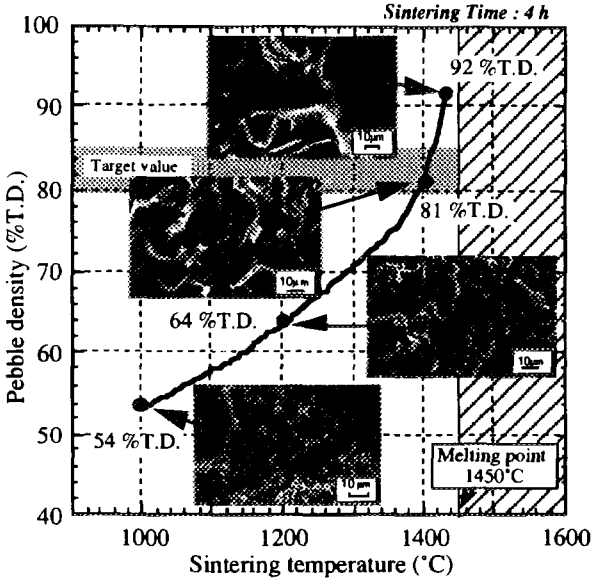

Fig.5 Relationship between sintering temperature and Li_2TiO_3 pebble density.

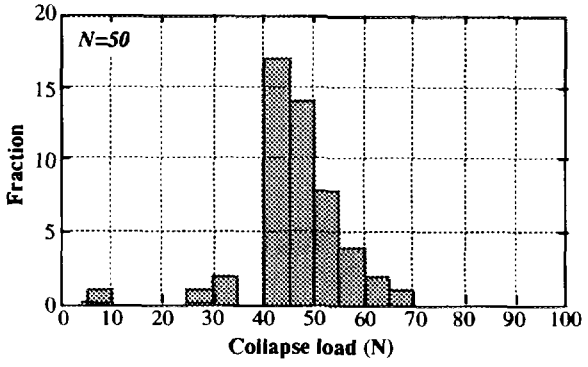

Fig.6 Distribution on collapse load of Li_2TiO_3 pebbles fabricated by wet process.

Table 3 Summary on characterization of Li_2TiO_3 pebbles

Properties	Measuring Methods	Measuring Values
Density	Liquid Immersion Method (Hg)	81.3 %T.D.
Sphericity	Photographic Analysis	1.11 (av.)
Pebble Diameter	Sieve Classification	1.52 mm (av.)
Grain SIze	SEM Observation	50 μm (av.)
Crystal Structure	XD Analysis	XD Pattern
Impurity Content	ICP Analysis	Content (see Table 4)
Collapse Load	Autograph	46.1 N (av.) (see Fig.6)

Table 4 Main impurities of Li_2TiO_3 pebbles

Elements	Contents (ppm)
Na	120
Mg	33
Ca	150
Zr	120
Al	140
Si	170
C	48
Co	1
U	<0.1
B	5

4. CONCLUSION

Density improvement tests of small Li_2TiO_3 pebbles were carried out four times by the wet process and the following can be concluded.

1) It was obvious that density of Li_2TiO_3 pebbles was susceptible to aging temperature and sintering temperature. The aging temperature was selected the values at -30°C for 1 h.
2) The grain size and density of Li_2TiO_3 pebbles increased with increasing sintering temperature. The extent of grain coarsening and achievable final density depend on the rate-controlling mechanism in the coarsening and densification kinetics.
3) When the gel-spheres obtained at the 3rd improvement test were heated at 650°C for 6 h and sintered at 1400°C for 4 h, density of Li_2TiO_3 pebbles was raised up to the target values. As the characteristics of the Li_2TiO_3 pebbles, the diameter was 1.5 mm and sphericity was resulted less than 1.2.

From these tests, bright prospects were obtained concerning the fabrication process of Li_2TiO_3 pebbles by wet process. In the future plan, automatic-control dropping system of gel-spheres will be designed and developed for mass production.

REFERENCES

1. C.E. Johnson, K.R. Kummerer and E. Roth, J. Nucl. Mater., 155-157(1988)188.
2. C.E. Johnson, G.W. Hollenberg, N. Roux, and H. Watanabe, Fusion Eng. Des.,8(1989)145.
3. K. Kurasawa, S. Nasu, K. Noda, T. Takahashi, H. Takeshita, T. Tanifuji and H. Watanabe, Proc. IEEE 9th Symp. on Engineering Problems of Fusion Research, Vol.II, (1981)1200.
4. J.M. Miller, H.B. Hamilton and J.D. Sullivan, J. Nucl. Mater., 212-215(1994)877.
5. P. Gierszewski, CFFTP G-9703(1997).
6. T. Suzuki, O. Murata and S. Hirata, Ceram. Trans., 27(1991)37.
7. N. Asami, K. Nagashima, et al., Ceram. Trans., 27(1991)17.
8. P. Gierszewski, M.D. Donne, H. Kawamura and M. Tillack, Fusion Eng. Des.,27(1995)167.
9. K. Tsuchiya, H. Kawamura, M. Nakamichi, H. Imaizumi, M. Saito, T. Kanzawa and M. Nagakura, J. Nucl. Mater., 219(1995)240.
10. K. Tsuchiya, H. Kawamura, M. Saito, K. Tatenuma and M. Kainose, J. Nucl. Mater., 219(1995)246.
11. K. Tsuchiya, H. Kawamura and T. Takeuchi, ISNFT-4, (Tokyo, 1997).
12. K. Tsuchiya, H. Kawamura, R. Oyamada, K. Nishimura, H. Yoshimuta and K. Watarumi, SOFE-'95, 16th IEEE/NPSS Symposium on Fusion Engineering (1995)1123.
13. K. Tsuchiya, K. Watarumi, S. Saito, K. Fuchinoue, T. Furuya and H. Kawamura, Proceedings of the Fifth International Workshop on Ceramic Breeder Blanket Interactions, (Roma, 1996).
14. R.P. Muis, and J.G. Laan, Proceedings of the Fifth International Workshop on Ceramic Breeder Blanket Interactions, (Roma, 1996).
15. K. Tsuchiya, K. Fuchinoue, S. Saito, K. Watarumi, T. Furuya and H. Kawamura, ACerS 99th Annual Meeting & Exposition (Cincinnati, 1997), to be published in J. Nucl. Mater..

SESSION 10

Blanket System Technology and Structural Materials

Tritium Recovery from Helium Purge Stream of Solid Breeder Blanket by Cryogenic Molecular Sieve Bed (II)
- Regeneration Operation of Cryogenic Molecular Sieve Bed -

Yoshinori KAWAMURA, Mikio ENOEDA and Masataka NISHI

Tritium Engineering Laboratory, Japan Atomic Energy Research Institute
,Shirakata Shirane 2-4, Tokai-mura, Naka-gun, Ibaraki-ken 319-11, Japan
TEL/FAX: +81-29-282-6205/5917 e-mail: kawamura@tpl.tokai.jaeri.go.jp

Abstract

Regeneration operation is a very important operation, because it is the most influential factor for deciding the net operation cycle time and the minimum dimension of Cryogenic Molecular Sieve Bed (CMSB). However, the experimental data of CMSB regeneration operation was not so sufficient that even the optimum regeneration procedure could not be decided yet. This work was focused on getting the primary information about various regeneration procedures.

1. Introduction

Important regeneration parameters are temperature, pressure and flow type. The regeneration procedure can be defined by these parameters and necessary regeneration time is affected by these parameters. The major regeneration procedures are listed in Table 1. Each procedure have their own merit and demerit, which are derived from these parameters. In case of the isothermal regeneration, it is not necessary to empty liquid nitrogen coolant. So, extra time to heat up and cool down the CMSB can be eliminated. On the other hand, it is not clear what temperature will give enough regeneration performance. If the isothermal regeneration performance is not sufficient, the optimum temperature and necessary time should be clarified. The flow type of regeneration affects the amount and composition of regeneration gas and the time for purification of the regeneration gas. If the vacuum regeneration is applied, it can be expected that helium content of the regeneration gas is smaller than the purge regeneration and results less load to the purification process of the regeneration gas. However, it is not clear that if it is applicable practically. In case of the purge regeneration, it is not clear what flow rate and total pressure is optimum and how long will it take. It is necessary to obtain these information for decide optimum regeneration procedure and optimum dimension of the CMSB.

2. Experimental

The experiments on regeneration were performed with the bench-scale experimental apparatus and 60 SLM Test Loop. Figure 1 shows the flow sheet of 60 SLM Test Loop. The test loop consists of mass flow meters, measurement instruments (Gas Chromatography (GC), ionization chamber (IC)), circulation pump, test section (CMSB) and so on. The gas composition of He gas stream was measured by GC and IC at the inlet and outlet of the CMSB. Tritium (HT) was supplied by the metal bed ($LaNi_5Mn_2$). The following are the procedures for the pre-loading adsorption.

A-1. Regeneration of the CMSB in 250°C He flow for more than 4 hours.

A-2. Cool down of the CMSB by immersing into liquid N_2.

A-3. Equalize the He pressure in the CMSB by opening the valves and isolate it.

A-4. Start supplying HT and H_2 from the metal bed.

A-5. Measure the inlet gas concentration by ionization chamber and gas chromatography.

A-6. Establish the gas flow in the CMSB.

A-7. Keep measuring the inlet and outlet gas composition by ionization chamber and gas chromatography for about 30 minutes.

The adsorption operation was terminated before the outlet concentration increase. In this work, both of the vacuum regeneration and the purge regeneration were performed. The regeneration should take place in reverse direction flow, so that the regeneration time become minimum. The following are the procedure by which both of vacuum and purge regeneration experiments were performed.

D-1. After the pre-loading of the CMSB, adjust the total pressure to the experimental condition of the run.

D-2. Establish the flow path to the reverse direction.

D-3. Begin the regeneration experiment, Keep measuring the outlet concentration until the detection limit. (In case of the vacuum regeneration, keep measuring the pressure of recovery tank, to which the regeneration gas is recovered and stored.)

Major specification of the test loop and the typical adsorption condition of the CMSB performed in this work as the part of Q_2 pre-loading before regeneration experiments were summarized in Table 2.

3. Theoretical Discussion on Data Analysis

In the previous work, the overall mass transfer coefficient was applied to simplify the calculation of the mass balance equation in which the axial dispersion term was neglected [1]. In our recent report and other investigator's report, however, it was conclude that there are the influence of mass transfer resistance of gas film and the axial dispersion [2],[3]. Also, the consideration of the analysis of vacuum regeneration made the necessity to incorporate the diffusion in/on adsorbent solid and the axial dispersion term in the mass balance equation.

3.1 Purge Regeneration

The purge regeneration is an effective way to regenerate the saturated CMSB because it doesn't need extra vacuum pumping system. On the other hand, it requires He as the carrier gas, that causes more load to the regeneration gas purification process. Bulk mass balance equation in the CMSB incorporated the axial dispersion is expressed as

$$u\frac{\partial c_i}{\partial z}+\varepsilon\frac{\partial c_i}{\partial t}+\gamma\frac{\partial Q_i}{\partial t}=D_L^i\frac{\partial^2 c_i}{\partial z^2}. \tag{1}$$

The axial dispersion diffusively is represented by Edwards and Richardson Correlation [4].

$$D_L^i=\frac{ud_p}{Pe}, \tag{2}$$

$$\frac{1}{Pe}=\frac{0.73\varepsilon}{ReSc}+\frac{1}{Pe_\infty(1+9.49\varepsilon/ReSc)}\quad\left(\because Pe_\infty=\begin{cases}6.7d_p & (d_p\le 0.3cm)\\ 2.0 & (d_p\ge 0.3cm)\end{cases}\right). \tag{3}$$

The mass balance equation in the solid phase is expressed as

$$\frac{\partial q_i}{\partial t}=D_S^i\left(\frac{\partial^2 q_i}{\partial r^2}+\frac{2}{r}\frac{\partial q_i}{\partial r}\right), \tag{4}$$

and the mass transfer rate equation is expressed as

$$\gamma\frac{\partial Q_i}{\partial t}=k_g^i a_v\left(c_i-c_i^g\right)=-\gamma D_S\left(\frac{\partial q_i}{\partial r}\right)_{r=R}. \tag{5}$$

The mass transfer coefficient of the gas film diffusion is expressed by Carrberry's correlation [5] as

$$k_g^i=\frac{D_{i,He}Sh}{d_p}\qquad(\because Sh=1.15Re^{1/2}Sc^{1/3}). \tag{6}$$

The rest of mass transfer factor are possibly the surface reaction, the pore diffusion and surface diffusion. In this work, the surface reaction can be negligible in such low temperature as liquid nitrogen. By applying the surface diffusion expression as the overall diffusion in solid phase, the term can be written as eq.(4).

Adsorption isotherms of hydrogen isotopes on MS5A at 77K are proposed by Nishikawa et al[6]. They applied summention of two Markham-Benton's equation [7] (Langmuir equation extended for multiple component) and expressed as

$$\left(q_i\right)_{r=R}=\frac{a_1^i c_i^g}{1+\sum_i b_1^i c_i^g}+\frac{a_2^i c_i^g}{1+\sum_i b_2^i c_i^g}. \tag{7}$$

The equations (1)-(7) can be solved numerically by various methods.

3.2 Vacuum Regeneration

The vacuum regeneration is one of possible regeneration procedure which has the advantage of less helium content in the regeneration gas. This advantage give the possibility of elimination of palladium diffuser for the final purification of the regeneration gas. The vacuum regeneration is also described by the similar mass balance equation as in the purge regeneration case. However, the role of axial dispersion term become more important in lower pressure. In lower pressure than 0.1-1.0Pa, the bulk flow become molecular flow. In such condition, it is not possible to define the bulk gas superficial gas velocity and its contribution to the bulk mass balance equation. The axial dispersion diffusively is regarded as the gaseous diffusion coefficient of each gas molecule. Thus, the first term of the left hand side of eq.(1) is neglected as the following equation.

$$\varepsilon\frac{\partial c_i}{\partial t}+\gamma\frac{\partial Q_i}{\partial t}=D_L^i\frac{\partial^2 c_i}{\partial z^2}. \tag{8}$$

The gas film mass transfer coefficient should be replaced to the conductance of vacuum pumping rate analysis and give the rewritten equation of eq.(5) as the following equation.

$$\gamma\frac{\partial Q_i}{\partial t}=k_{cond}^i\left(c_i-c_i^g\right)=-\gamma D_S\left(\frac{\partial q_i}{\partial r}\right)_{r=R}. \tag{9}$$

The mass balance equations for the vacuum regeneration are expected to be solved by the similar methods as the purge regeneration.

3.3 Non-isothermal Adsorption and Desorption

The adsorption isotherm can be modified to simple Markham-Benton's equation to simplify calculation of isotherm for Q_2 and other impurity gas mixture in various temperature with sacrifice of accuracy for about 10%. The simplified isotherm is expressed as

$$\left(q_i\right)_{r=R}=\frac{a_1^i c_i^g}{1+\sum_i b_1^i c_i^g}. \tag{10}$$

Markham-Benton isotherm can be extended to non-isothermal sorption equation with the value of heat of adsorption each adsorbent gas species and expressed using eq.(10) as

$$\left(q_i\right)_{r=R}=\frac{c_i^g a_0^i \exp\left(-\Delta H_0^i/RT\right)}{1+\sum_i c_i^g b_0^i \exp\left(-\Delta H_0^i/RT\right)}, \tag{11}$$

where ΔH_0^i is the heat of adsorption of i gas molecule. The heat of adsorption have been already reported on some limited gas molecules in 5A Zeolite in conjunction with molecule

radius, polarizability and so on [4]. The polarizability of H_2 is a known physical property. Thus, this work applied the interpolation of the polarizability, and then the heat of adsorption for other hydrogen isotopes. Figure2 shows the estimated polarizability of hydrogen isotopes [4]. Polarizability represents the volume of electron orbit of molecule and related to the mass number of molecule. In this work, the primary estimation values of polarizability were interpolated by the reduced mass of each hydrogen isotope molecule because detailed discussion on the polarizability is not the main issue. The heat of adsorption is generated by the potential difference between gaseous molecule and adsorbed molecule, which is related to the polarizability of gas molecule and the potential energy of the adsorbent molecules. Thus, the heat of adsorption is affected by the type of the adsorbent and adsorbate gas molecule. Figure3 shows the heat of adsorption for various gas molecules on MS5A [4]. The values of polarizability, heat of adsorption, Langmuir coefficients at liquid nitrogen temperature and pre-exponential factor of eq.(11) are listed in Table3. Non isothermal operation dynamics can be described by applying heat balance equations with mass balance equations. The theoretical analysis of such case is time-consuming work, as well as the experimental observation. This work is a preliminary step for non-isothermal operation of CMSB, thus, non-isothermal dynamics should be discussed in further discussion.

4. Results and Discussions

4.1 Diffusion coefficient in solid phase

In the previous work, the experimental correlation of the overall mass transfer coefficients were reported and it was concluded that the gas film mass transfer resistance influences on the overall mass transfer process and the diffusion in the solid (pore diffusion and /or surface diffusion) is to be in the same order of magnitude as the gas film mass transfer coefficient [2]. The most important issue is to evaluate each mass transfer resistance in such condition as relevant dimension of CMSB for operation of fusion machine like ITER. Thus, it is necessary to confirm relevancy of the correlation equations of gas film mass transfer coefficient and axial dispersion diffusively proposed so far [4, 5]. And, the diffusion coefficient in adsorbent solid should be obtained experimentally. Eqs.(1)-(7) gives the breakthrough curves as the solution by using experimental condition data as the initial and boundary condition on the assumption of certain value of the diffusion coefficient in the solid.

Figure 4 shows the velocity dependence of obtained diffusion coefficient in solid phase. It can be seen that diffusion coefficient in solid phase have no velocity dependence. Thus, the gas film mass transfer coefficient and the axial dispersion diffusively were properly done in this work by the correlation equation. Figure 5 shows the diffusion coefficients of H_2 and HT in solid phase obtained in this work. The estimated value of H_2 and D_2 by Nishikawa et al. are also shown in Fig.5 Nishikawa et al. estimated the diffusion coefficient in the solid by

transforming of the solid phase mass transfer resistance, which was calculated by reducing the gas film mass transfer resistance and the axial dispersion effect from the overall mass transfer resistance. As can be seen from this figure, the diffusion coefficients of H_2 and HT in solid are related with the total concentration of hydrogen isotopes. Both of experimental observation and estimated values are in the same order of magnitude, that implies the evaluation of gas film resistance and axial dispersion effect are consistent. The observation clarified detailed dependency on concentration compared with the estimation, because this work applied direct fitting calculation of diffusion coefficient in solid and the obtained values of diffusion coefficient represents direct values corresponding to the experimental results. The key issues of this figure is that the isotope effect on diffusion coefficient appears obviously in lower concentration range and become unclear in higher concentration range of total hydrogen isotope concentration. This fact implies that there are multiple diffusion mechanism, one having large isotope effect, the other having less isotope effect. Nishikawa et al. applied the assumption of two different energy state adsorption, which causes two different isotherm characteristics and corresponding diffusion coefficient [3, 6]. The detailed mechanism of diffusion in solid phase should not be concluded only by this work, because the detailed experiments from the view point of status and property of adsorbed molecules on MS5A surface are necessary. The obtained diffusion coefficient in this work is available to describe the mass transfer rate only on the diffusion in solid phase in the wide range of the operation condition. The applicable condition range is the same as that of correlation equation applied to describe the gas film mass transfer and axial dispersion effect. In this way, the design and performance prediction of CMSB became available to wide range of CMSB dimension and operation condition. Also, it was certified that the calculation method proposed in this report was applicable to the regeneration performance prediction.

4.2 Purge Regeneration

The key criteria is the efficiency of the regeneration (regenerated gas amount per adsorbed amount) in limited regeneration time. The influential parameter on the regeneration efficiency are supposed to be the flow rate of He carrier gas, total pressure and regeneration temperature. The effect of the flow rate was already clarified With respect to the regeneration temperature, it will be discussed later. Thus, the experiments were performed on the pressure effect in this work. Basically, the less the total pressure is, the more the hydrogen isotope fraction is, in regeneration compared with adsorption operation, because the partial pressure of hydrogen isotopes in early time of regeneration is reserved as it was in adsorption operation. This implies the effectiveness of negative pressure purge regeneration. Table4 shows the experimental condition of the purge regeneration. The regeneration efficiency and regeneration time were observed in this experiment. In the course of experiment, the outlet Q_2 concentration was measured as frequently as possible. Figure6 shows the observed concentration change in

time. The lines are the calculated values with assumption of 772 torr and 200torr of total pressure. The calculated values and the observed values shows approximately good agreement. Thus, the basic data of the diffusion coefficient in solid phase are supposed to be applicable for primary estimation of the regeneration performance as well as the evaluation method of gas film resistance and the axial dispersion effect. The estimation for case of 200torr in Fig.6 shows that large fraction of hydrogen isotopes can be expected in short time after regeneration operation take place and gives more efficiency of regeneration in same regeneration time. This tendency will last to the pressure as low as the flow of the bulk gas become transient and molecular flow out of viscous flow. Figure7 shows the comparison of the regeneration ratio observed and calculated. This figure was generated for the same system condition as described above. Observed regeneration efficiency was about 70% for H_2 and 60% for HT. The difference between observed and calculated value is supposed to be due to the measurement error of gas chromatography and ionization chamber, since the calibration was performed in atmospheric pressure. However, approximate estimation of the regeneration condition is possible by the similar graph by same analysis method. Fig.7 may give the conclusion that the lower the total pressure is, the better the molecular flow corresponds to the Vacuum regeneration.

4.3 Vacuum Regeneration

With respect to the vacuum regeneration, the experiments of the simple pumping down of saturated CMSB could not recover meaningful amount of hydrogen isotope gas. The vacuum regeneration operation is supposed to be very difficult, because once the bulk flow becomes the molecular flow, the limiting process of the mass transfer governed by pumping capacity at the outlet nozzle of the CMSB. The partial pressure of hydrogen isotopes is fairly low and the fairly big pumping speed is required to establish effective performance of regeneration operation. This work applied the turbo-molecular pump, whose pumping speed is nominally 180 *l* (H_2)/min. Thus, further modification of the outlet nozzle and piping connected to the vacuum pumping system is necessary to minimize the evacuation conductance. This means the necessity of big outlet nozzle and piping between the CMSB and the vacuum pumping system. In this work, such kind of modification of the test loop was not done from the view point of the total system as the tritium system. Careful experiments on the vacuum regeneration performance should be done for the final decision of the vacuum regeneration application.

4.4 Non-isothermal Regeneration

The theoretical investigation performed in section 3.3 enabled the estimation of the isotherm at various temperature. Figure 8 shows the estimated isotherm in various temperature. Equilibrium partial pressure of hydrogen isotopes decreases by a factor of one order of magnitude if temperature changes from liquid N_2 temperature to 100K. The equilibrium partial pressure in ambient temperature (300K) is estimated three order of magnitude small

than liquid N_2 temperature. From the view point of the expected partial pressure, small temperature increase from liquid N_2 temperature will result big partial pressure increase. If the temperature increase to 300 K, four order of magnitude higher partial pressure can be expected. The effort to achieve the shorter regeneration time is equivalent to increase the partial pressure in regeneration operation. Thus, heating of CMSB is a very effective procedure to shorter the regeneration time. Figure 9 shows the estimated isobars of H_2 on MS5A, which is essentially pressure clearer. Assuming the regeneration rate criteria as 99% to the inlet concentration of 1ppm (partial pressure 0.1Pa), 170K of regeneration temperature may give the chance to achieve enough high regeneration efficiency. From the basis of those discussion above, heating CMSB is a very effective method to achieve higher and quicker regeneration operation. However, the careful structure design of the CMSB might be required to protect CMSB from the thermal cycle, because the operation is a frequent thermal cycle. In addition to the careful design, the demonstration test of the prototype CMSB is necessary to prove the effectiveness and relevancy of thermal cycle regeneration of CMSB.

5. Conclusion

This work focused on the regeneration procedure for Cryogenic Molecular Sieve Bed which is used to recover tritium from Breeding Blanket sweep gas. Theoretical and experimental approach were performed and concluded as follows.

(1) Experiments on Vacuum Regeneration did not work because of too low partial pressure of Q_2 inside the CMSB. Thus, very careful design is necessary so that pressure inside the CMSB can reach to enough low pressure. This may cause complicated structure. Purge Regeneration is better.

(2) Lower the pressure is, the faster regeneration can be. By the purge regeneration experiments in this work, 75% of H_2 and 60% of HT were regenerated in 75 min after 35 min CMSB operation. The calculation by the method proposed in this work was available for the simulation of regeneration performance fairly well.

(3) Temperature dependence of isotherm is estimated by using experimental data and reference data. In case of Vacuum Regeneration, CMSB should be heated to higher than room temperature. In case of Purge Regeneration, 100-200 K may give good regeneration performance.

The order of effectiveness of each regeneration procedure option is summarized in Table 5. The effectiveness order in Table 5 is an apparent result which is most likely right by the R&D result obtained in this work. Further discussion will give better and precise decision of procedure selection.

References

[1] M.Enoeda et al., "Recovery of Tritium by Cryogenic Molecular Sieve Bed in Breeding Blanket Interface Condition", Fusion Technol., 26 (1994) 664.

[2] M.Enoeda et al., "Recovery of Hydrogen Isotopes and Impurity Mixture by Cryogenic Molecular Sieve Bed for GDC Gas Cleanup", Fusion Technol., 28 (1995) 591.

[3] M.Nishikawa et al., "Mass Transfer Coefficients in Cryosorption of Hydrogen Isotopes on Molecular Sieves and Activated Carbon at 77K", Fusion Technol., 28 (1995) 717.

[4] D.M.Ruthven, "Principles of Adsorption and Adsorption Processes", John Wiley & Sons, Inc., (1984).

[5] J.J.Carberry et al., "A boundary - layer model of fluid - particle mass transfer in fixed bed", AIChe.J., 6 (1960) 460.

[6] M.Nishikawa et al., "Adsqrption Isotherm and Separation Factor for Multicomponent Hydrogen Isotopes in Cryosorption Method for Recovery of Tritium from Blanket", Fusion Technol., 28 (1995) 711.

[7] E.C.Markham and A.F.Benton, J. Amer. Chem. Soc., 53 (1931) 497.

Nomenclature

a_v : surface area of packed bed [cm^2/cm^3]

c_i : H_2, HT concentration in bulk He purge gas flow [mol/cm^3]

c_i^g : Equilibrium gas concentration with Q_i [mol/cm^3]

D_s : Diffusion coefficient of hydrogen in /on adsorbent solid [cm^2/s]

D_L^i : Axial dispersion diffusivity [cm^2/s]

D_g^i : Molecular diffusion coefficient of hydrogen isotopes [cm^2/s]

k_{cond}^i : Vacuum conductance in CMSB [1/s]

k_g^i : Gas film mass transfer coefficient of hydrogen isotopes [cm/s]

q_i : Local loading distribution of hydrogen isotopes in MS5A equivalent spheric pellet [mol/g-MS5A]

Q_i : H_2, HT loading on MS5A [mol/g-MS5A]

r : Radial direction location in MS5A equivalent spheric pellet [cm]

R : Equivallent sphere radius of MS5A pellet [cm]

R : Gas constant [J/mol•K]

t : Operation time [s]

u : Superficial gas velocity [cm/s]

z : Bed height location [cm]

γ : Bed density [g/cm^3]

ε : Void fraction of bed[-]

ΔH_0^i : Heat of adsorption of hydrogen isotopes on MS5A [kJ/mol]

a_0^i, b_0^i : Pre-exponential factor of non-isothermal Markham-Benton equation

$a_1^i, b_1^i, a_2^i, b_2^i$: Coefficients of Markham-Benton equation of hydrogen isotopes

i : Index for hydrogen isotopes molecules

Table 1 The major regeneration procedures.

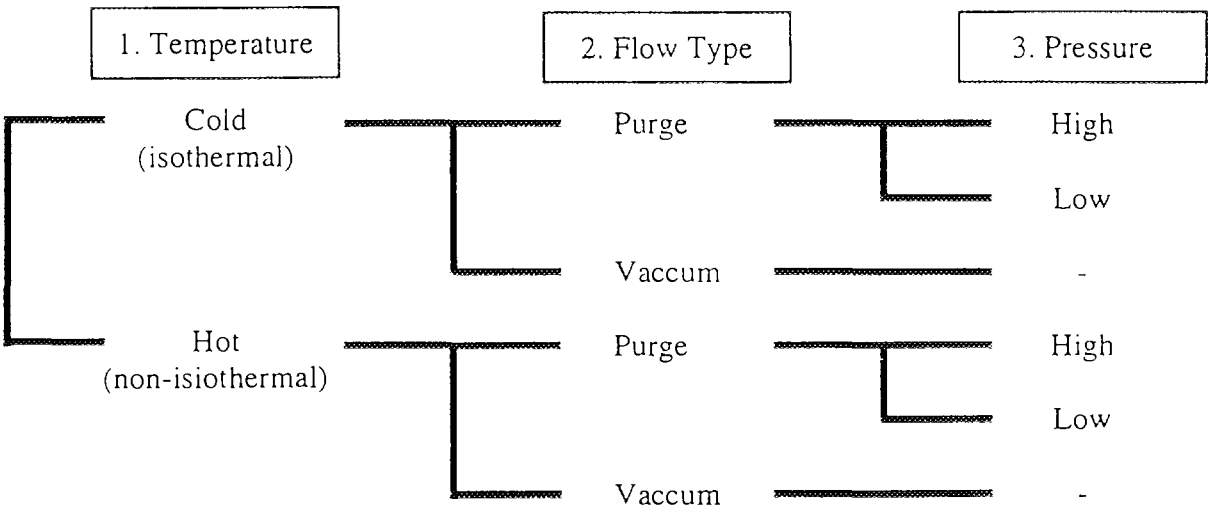

Table 2 Experimental specification.

CMSB Dimension	10.9 cm $\phi \times$ 8.0 cm h (760 cm^3)
Adsorbent	Molecular Sieve 5A 1/8 inch pellet
Density	1.16 g/cm^3
Packing Weight	500 g
Packing Density	0.672 g/cm^3
Packing Fraction	0.58
Surface Area of Packed Bed	15.84 cm^2/cm^3
Purge Gas	Helium
Transfer Pump	Metal Bellow Pump (nominal 60 l (STP)/min.)
Flow Rate	~ 59 l/min
H_2 Concentration	250 - 500 ppm in Atmospheric Pressure
Tritium Supply	Metal Bed ($LaNi_3Mn_2$)
Throughput	7 Ci
H/T Ratio	570
Measurement	Gas Chromatograph , Ionization Chamber

Table 3 Estimated isotherm parameters for temperature dependence.

$$(q_i)_{r=R} = \frac{a_1^i c_i^g}{1 + \sum_i b_1^i c_i^g} \qquad (q_i)_{r=R} = \frac{c_i^g a_0^i \exp(-\Delta H_0^i / RT)}{1 + \sum_i c_i^g b_0^i \exp(-\Delta H_0^i / RT)}$$

q_i : [mol/g-MS5A], c_i : [Pa], T : [K], R : [kJ/mol•K]

Species	Polarizability	Heat of adsorption	Langmuir Coefficient at LN_2 temp.		Pre-exponential Factor	
	α	$-\Delta H_0$	a_1	b_1	a_0	b_0
	$10^{25}cm^3$/molec.	kJ/mol	--	--	--	--
H_2	8.04	5.3126	3.995×10^{-6}	2.136×10^{-3}	1.033×10^{-9}	5.521×10^{-7}
HD	8.741	5.7882	6.036×10^{-6}	3.388×10^{-3}	1.560×10^{-9}	8.757×10^{-7}
HT	9.148	6.0549	7.295×10^{-6}	4.070×10^{-3}	1.885×10^{-9}	1.053×10^{-6}
D_2	10.02	6.651	1.057×10^{-5}	5.912×10^{-3}	2.732×10^{-9}	1.528×10^{-6}
DT	10.61	7.0431	1.16×10^{-5}	6.26×10^{-3}	2.998×10^{-9}	1.618×10^{-6}
T_2	11.361	7.5451	1.44×10^{-5}	7.68×10^{-3}	3.722×10^{-9}	1.985×10^{-6}
N_2	17.56	11.323	4.237×10^{-4}	8.250×10^{-2}	9.563×10^{-12}	1.862×10^{-9}
O_2	14.88	9.9426	5.0×10^{-4}	9.0×10^{-2}	9.654×10^{-11}	1.738×10^{-8}
CH_4	26.04	16.4060	1.281×10^{-3}	2.050×10^{-1}	1.068×10^{-14}	1.709×10^{-12}

Table 4 Experimental condition of the purge regeneration.

	adsorption operation	regeneration operation
Carrier Gas	He	He
Flow Rate	13 SLM	13 SLM
Q_2 concentration	H_2 : 350 ppm HT : 0.65 ppm	
Pressure	760 Torr	380 Torr
Operation Cycle	35 min.	

Table 5 Quantification of regeneration procedure in this work.

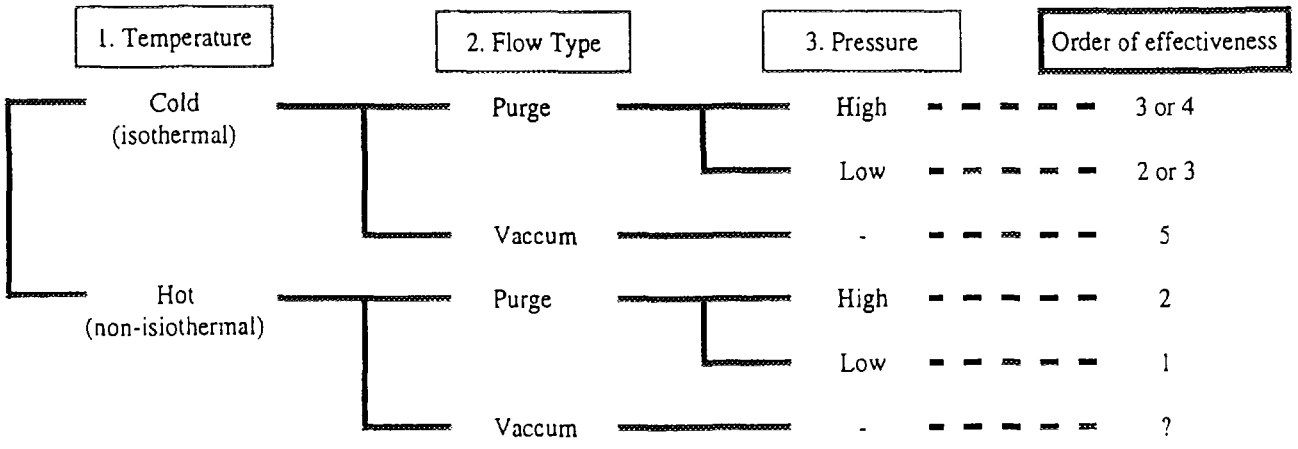

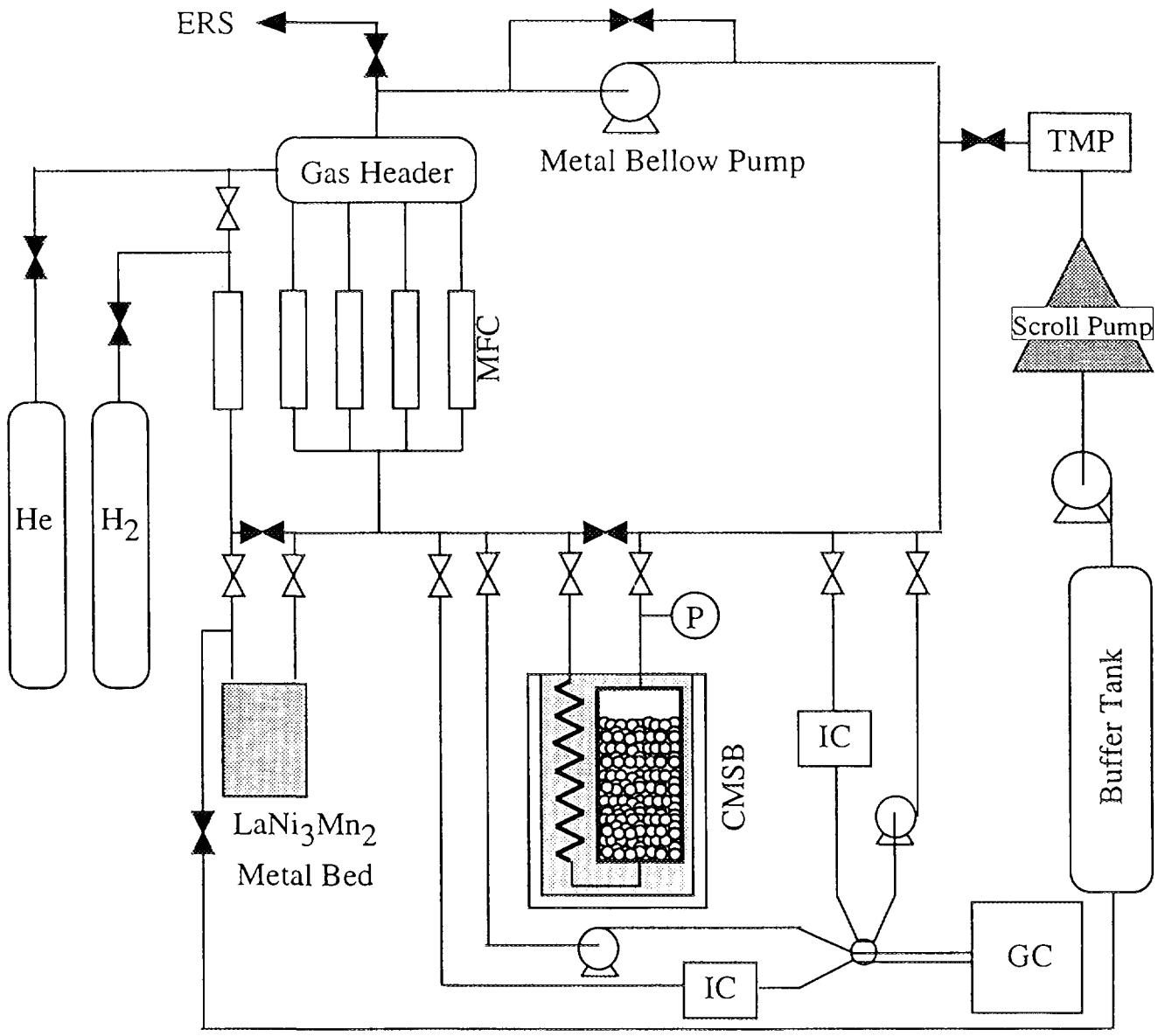

Fig.1 A schematic flow pass of 60 SLM test loop.

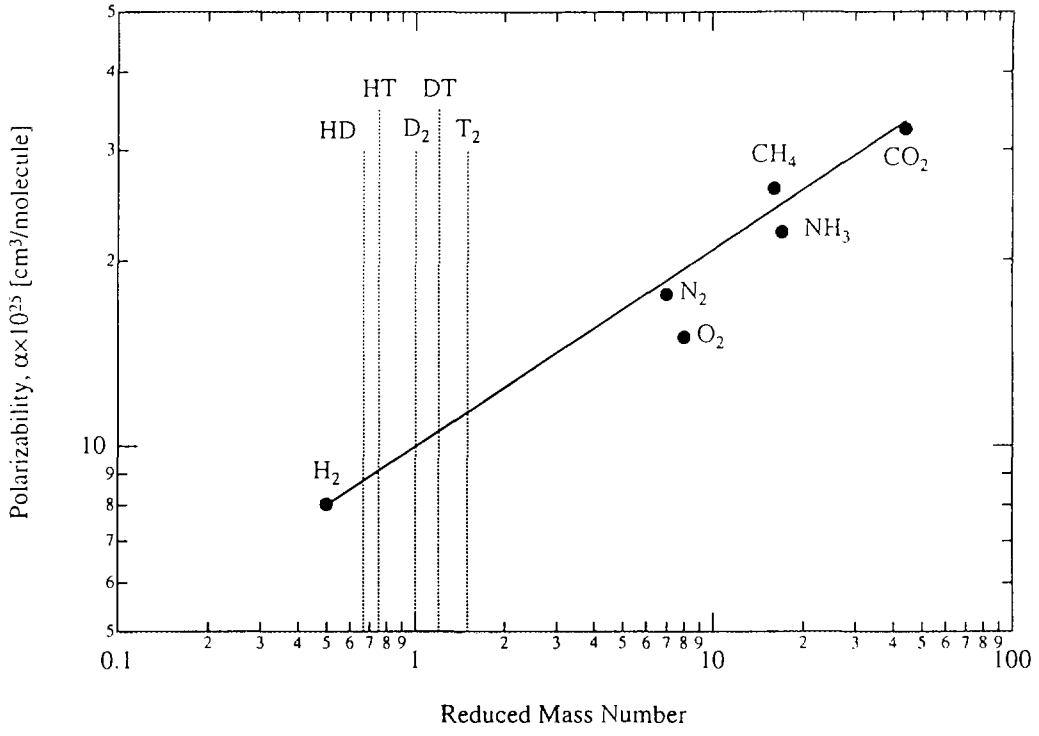

Fig.2 Estimated polarizability of hydrogen isotopes.

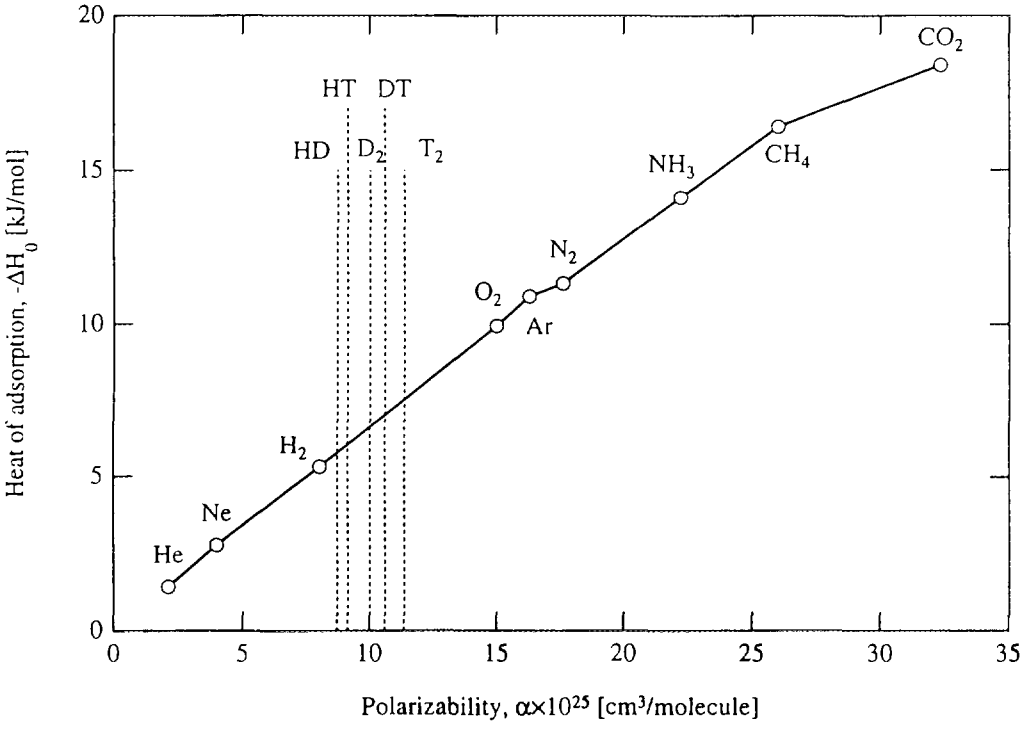

Fig.3 Estimation of the heat of adsorption of hydrogen isotopes on MS5A.

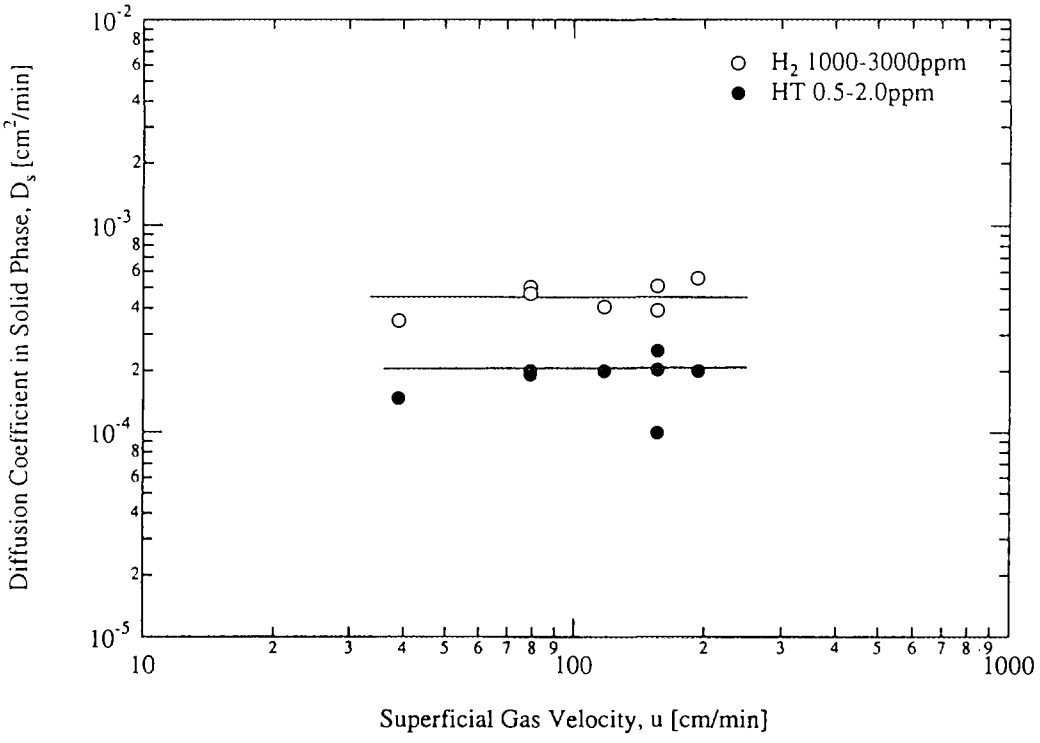

Fig.4 Velocity dependence of observed diffusion coefficient in solid phase.

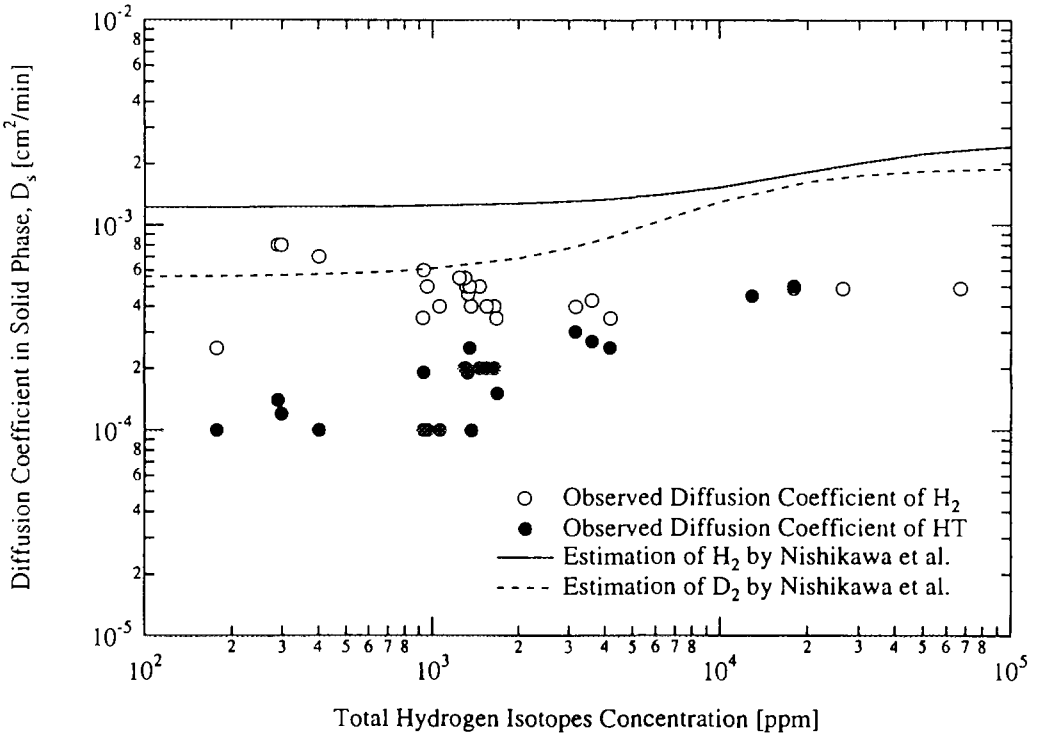

Fig.5 Dependence of Diffusion Coefficient in Sloid Phase on Hydrogen Isotope Concentration.

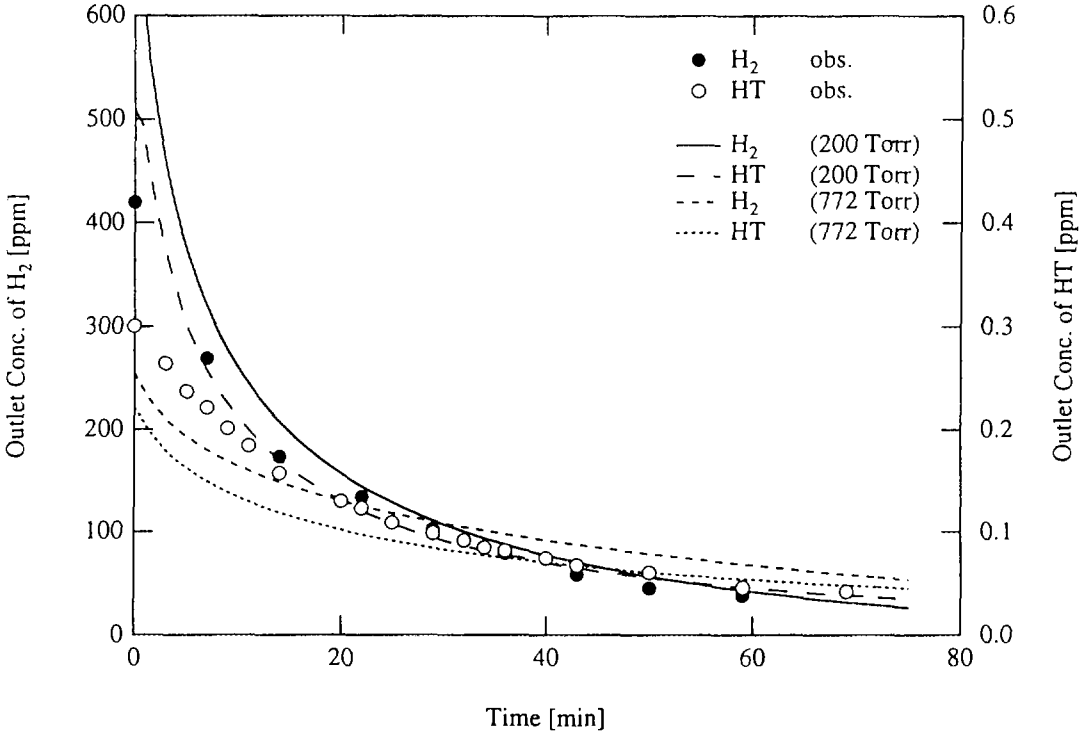

Fig.6 Pressure effect in isothermal purge regeneration.

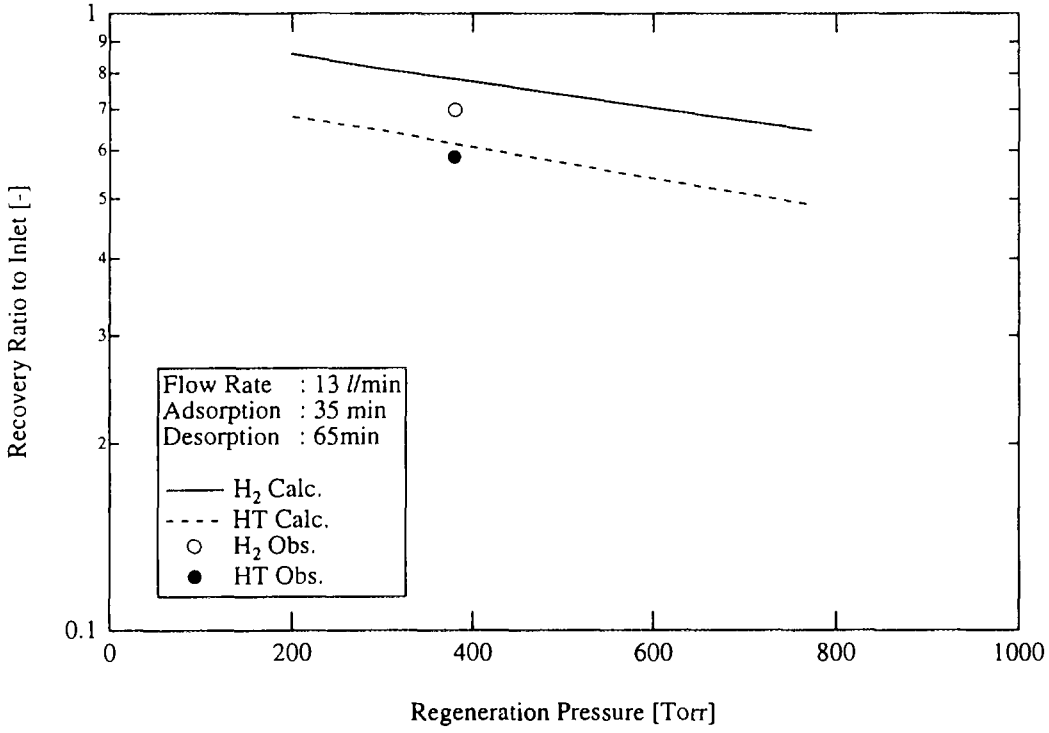

Fig.7 Recovery Ratio Estimation in VariousRegeneration Pressure.

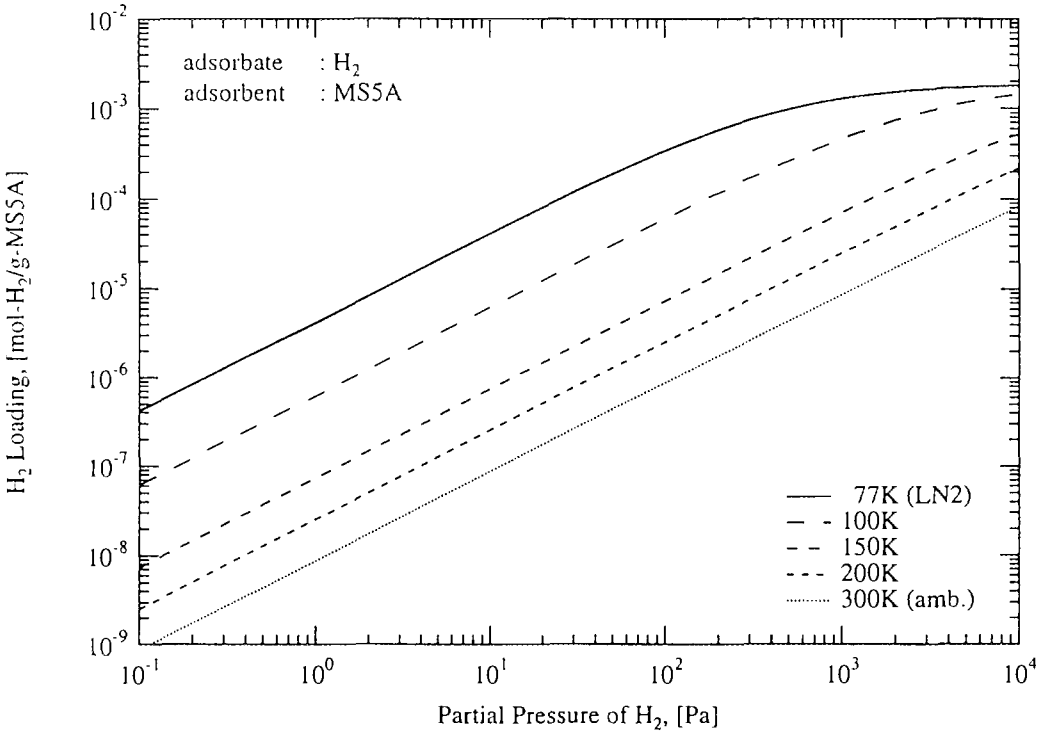

Fig.8 Estimated adsorption isotherm for various temperature.

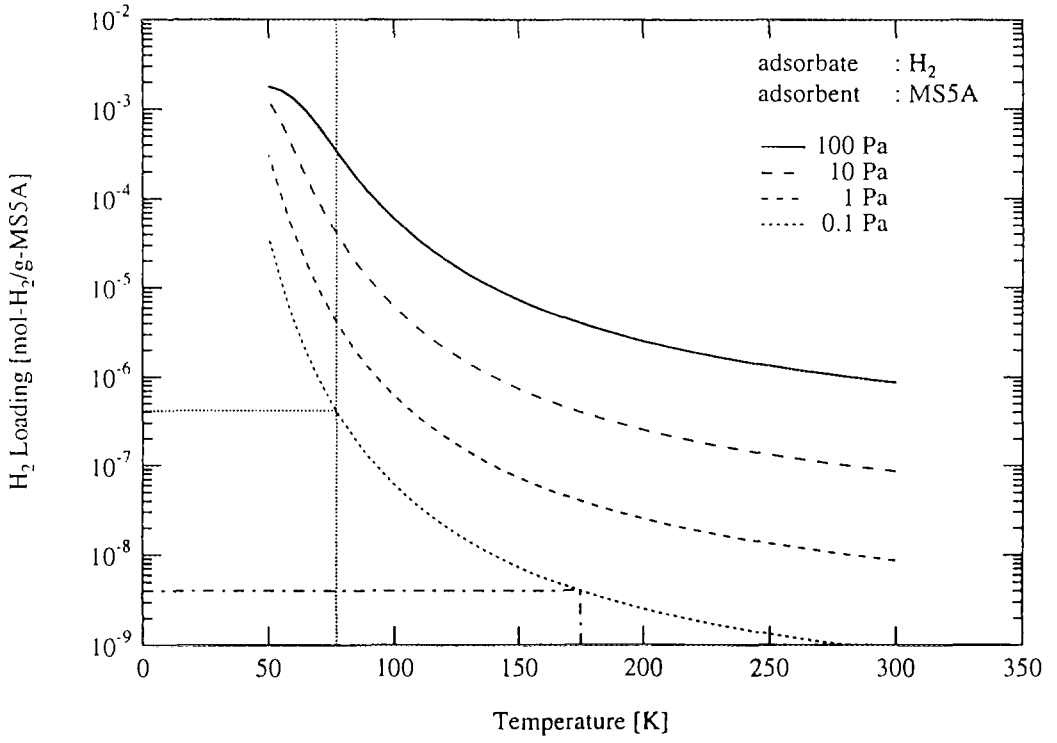

Fig.9 Estimated adsorption isobar for various puressure.

CORROSION FATIGUE STUDIES ON F82H MOD. MARTENSITIC STEEL IN REDUCING WATER COOLANT ENVIRONMENTS.

Marie Françoise Maday, Amedeo Masci

ENEA-CRE Casaccia, Dipartimento Innovazione, Divisione Nuovi Materiali
P.B.2400, 00100, Rome Italy.

Abstract

Load-controlled low cycle fatigue tests have been carried out on F82H martensitic steel in 240°C oxygen-free water with and without dissolved hydrogen, in order to simulate realistic coolant boundary conditions to be approached in DEMO. It was found that water independently of its hydrogen content, determined the same fatigue life reduction compared to the base-line air results. Water cracks exhibited in their first propagation stages similar fracture morphologies which were completely missing on the air cracks, and were attributed to the action of an environment related component. Lowering frequency gave rise to an increase in F82H fatigue lifetimes without any change in cracking mode in air, and to fatigue life reduction by microvoid coalescence alone in water. The data were discussed in terms of i) frequency dependent concurrent processes for crack initiation and ii) frequency-dependent competitive mechanisms for crack propagation induced by cathodic hydrogen from F82H corrosion.

1-Introduction

The current international qualification test Programme on the low activation martensitic steels (LAMS) has the main objective to verify within 1998 the feasability of using such alloys for structural applications in the future fusion devices. In this context, the question of LAMS compatibility with the water coolant option and in the presence of complex time-dependent stresses has been addressed as one of the priority Tasks. The experimental activities still in progress about this argument are performed on the Japanese F82H mod steel, the actual reference LAMS for its availability, and in high temperature water environments, mainly selected in relation to the experience gained in fission reactors and on the basis of theoretical predictions.

In a previous paper, the low cycle fatigue tests run on F82H mod. steel in oxygen-free, low conductivity (pH neutral) water, either without or with dissolved hydrogen were presented[1]. Such a steady-state water quality, the so-called reducing or hydrogen water chemistry (HWC), where radiolytic oxidant production is completely suppressed by hydrogen addition, is strictly specified in light water reactors (LWRs) for steel corrosion cracking mitigation, but will be perhaps difficult to meet in fusion coolants for the harder neutron spectrum[2]. HWC represents nevertheless a boundary condition to be approached. Other water radiolysis scenarios, including those where oxygen and hydrogen peroxide cannot be eliminated, are under study in the continuing part of the explorative work. Finally, based on the LWR specifications which recommend also to keep water slightly alkaline (pH around 7 at 300°C) for minimizing magnetite solubility and therefore contamination, possible pH controlling agents among those used in LWRs have been identified (namely, ^{7}LiOH, KOH) and considered in some tests, even though the argument of employing additives for alkalination in fusion reactor coolants is actually the subject of significant controversy.

The purpose of the present paper is to discuss the implemented LCF study on F82H in reducing water condition, with the support of complementary tests run in an attempt to clarify the underlying fatigue cracking processes.

2-Experimental details

The fully martensitic F82H mod. steel, produced by NKK-Japan with the chemical composition (in wt%): C 0.086, Si 0.1, Mn 0.2, Cr 7.39, W 1.97, S 0.02, P 0.01, Ni 0.02, V 0.14, As<0.005, Sn,Ta<0.002, Ti, Al, Nb < 0.001, N_2:0.006, has been delivered, via JAERI, in its as-received state (normalized at 1040°C/30 min.; tempered at 760°C/60 min.) in the form of 25mm thick plates. Microstructural studies performed by scanning electron microscopy (SEM) and energy dispersive X-ray analysis (EDX) on the longitudinal (parallel to rolling) section of coupons opportunately polished and etched [1], revealed the presence of a martensite lath structure inside prior austenite grains of 90μm average size. The inclusions present in the matrix consisted mainly in Al, Ti, Ta rich, type-B oxides, and globular Al,-Ti, Ta rich, type-D oxides. Thin carbide precipitates (probably $Cr_{23}C_6$) around grain boundaries (GB) and martensite laths, and fine carbide dispersion in the matrix were also observed.
The LCF specimens with a hourglass geometry (7.5mm minimum diameter) and their longitudinal axis in the rolling direction, were mounted on the load frame of a 100kN capacity testing machine, through insulating ZrO_2 pieces, inside an autoclave vessel lined with Teflon. The testing section was part of the high temperature pressurized circuit of a recirculating system, connected to a low temperature loop for water chemistry make-up and control.
The testing environments were prepared at room temperature in a storage tank, and consisted in de-ionized, un-buffered water (conductivity<0.1μS.cm^{-1}; pH=6.9), either only de-aerated (DWC, O_2<1ppb) or de-aerated and with 2ppm dissolved hydrogen (HWC). The water quality was maintained by continuous flowing through ion-exchange resins and filters, and by automatically controlled bubbling with the appropriate gas.
The fatigue experiments were performed under load control according to the ASTM E606 Practice, by using fully reversed triangular wave-forms of 23, 18. and 16kN amplitudes (nominal stresses in the 7.5mm gauge length: 521, 408, and 362 MPa respectively). The loading rate was principally 2.2kN.sec^{-1} (frequencies f in the range: 0.024÷0.035Hz), but was occasionally reduced at 18kN to 0.7kN.sec^{-1} (f ≈ 0.01Hz) for specific assessments. The tests were conducted at 240°C, in static air for base-line data, and in the flowing aqueous environments (flow-rate: 9l/hour; pressure = 45atm.); they were run at least in duplicate for each mechanical/environmental combination, and stopped at complete specimen rupture.
The fracture surfaces were observed by SEM after descaling with Clarke's solution when necessary.

3- Experimental results and discussion

The number of cycles to rupture Nf of the F82H specimens fatigued at 240°C in air and in aqueous media are reported in table 1. The data indicated that water environments, compared to air, determined, independently of their hydrogen content, F82H fatigue life reduction with an increasingly damaging effect as stress and frequency decreased.

Test conditions	Nf
Air-2.2kN.s^{-1}	
18kN	4300±200
16kN	36000±2000
Air- 0.7kN.s^{-1}	
18kN	6400±200
DWC-2.2kN.s^{-1}	
23kN	25±3
18kN	3400±100
16kN	20000±1500
DWC-0.7kN.s^{-1}	
18kN	2550±50
HWC-2.2kN.s^{-1}	
23kN	23±2
18kN	3300±100
16kN	22500±1500
HWC-0.7kN.s^{-1}	
18kN	2600±100

Table 1: F82H fatigue life results in air and water environments at 240°C

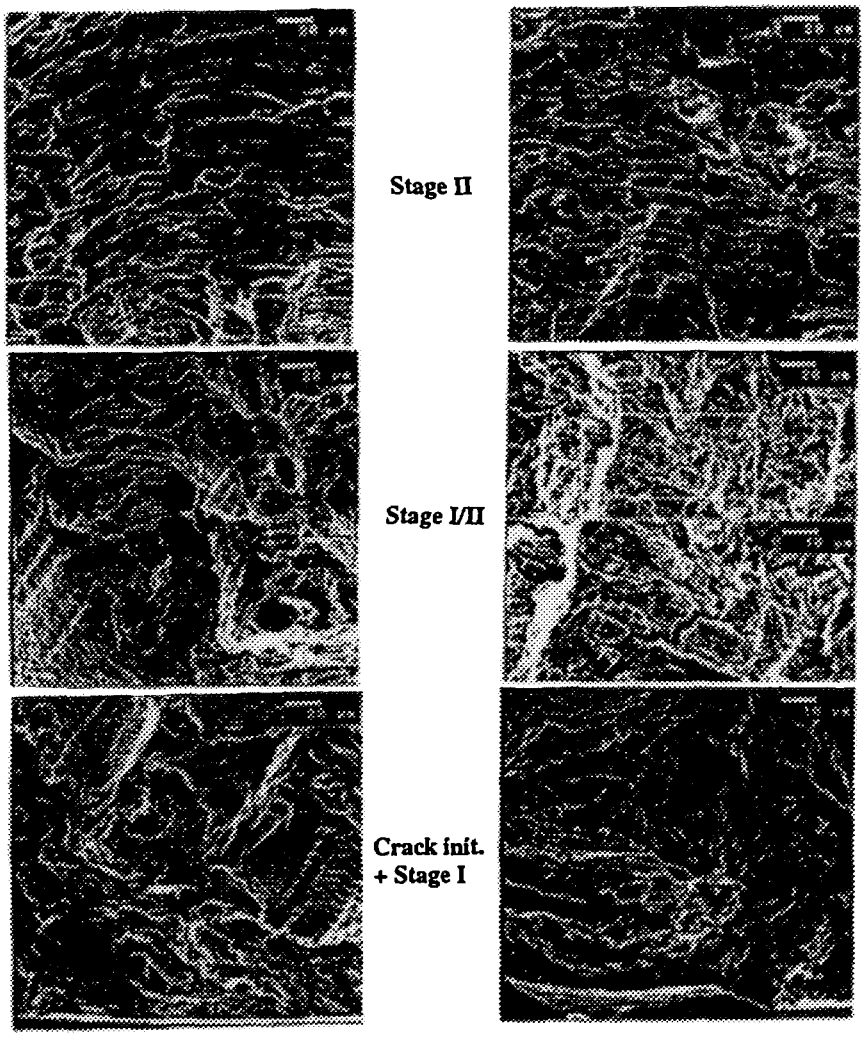

Figure 1: Effect of environment on fatigue crack morphologies
(Load amplitude: 16kN; load rate: 2.2kN/sec)

Fracture surface examination, on a macroscopic scale, of the specimen set tested at 2.2kN/sec. showed that the 23kN cyclic loading caused, in all cases, a cup-cone, dimpled rupture typical of plastic collapse, while the lower stressing conditions led to a sub-critical fatigue crack growth regime, followed by the overload instability region induced by microvoid coalescence (MVC).

Further inspection at higher magnification on the air and water fatigue cracks revealed the following sequence of events as penetration, and therefore stress intensity factor K, increased (fig.1):

- crack initiation started in air always uniformly from specimen periphery, but appeared somewhat related to grain boundary at some sub-surface sites in water.
- The transgranular (TG) elongated and striated features observed in the Stage I of the air cracks, coexisted subsequently with more regular striations on cleavage planes. Water cracks followed initially an un-striated path with evidences of the martensite lath morphologies inside the grains, which changed progressively into a striated TG mode where crack branching between striations appeared associated with grain and lath boundaries.
- In the final stage of fatigue crack propagation before overloading, the fracture surfaces, in all cases, became progressively TG, with smooth ordered striations on cleavage planes without evidence of any branching.

The experimental results showed clearly that an environmental factor contributed to cracking acceleration during the LCF process of F82H in water, with an increasingly enhancing effect as stress amplitude decreased.

It is generally proposed [3-5] that the environment-based component for crack growth enhancement acts in superposition to to pure mechanical fatigue (MF) operating alone in air, and determines different types of cracking mechanisms, currently described in terms of "true corrosion fatigue" (TCF), "stress corrosion fatigue" (SCF) and "hydrogen assisted cracking" (HAC). In the TCF.process, corrosion adds sequentially to pure fatigue without producing any change in the fracture appearence compared to the air crack. Conversely, either SCF or HAC, which occur under specific stress/environment/material conditions, compete with TCF or MF in a completely independent way. The former is essentially controlled by the sequence of slip/anodic dissolution/passivation processes, and occurs in conditions leading to the the most favourable kinetics of these competitive events, while the latter is induced ahead of the crack tip in the point of maximum triaxial stress (fracture process zone) by cathodic atomic hydrogen (H). The primary source of H-supply to the crack-tip region is water reduction inside the local crack cell, which balances metal anodic dissolution after film rupture, in the absence of oxygen. It should be emphisized nevertheless that in steels/high temperatue, oxygen-free water systems, another H-uptake phenomenon occurs as a result of the corrosion/deposition schemes and relative electrochemical processes described in figure 3. This model [6-8] was proposed for explaining the experimentally observed diffusion controlled kinetics of duplex oxide film formation on steels, and for suiting the finding that up to 90% of atomic hydrogen, produced from the cathodic half-cell reaction was liberated at the metal/oxide interface. Cathodic hydrogen was estimated to diffuse 330 times more quickly through the steel than through the oxide, which works as a very effective H permeation barrier [7]. H diffusivity data [9] for alloys of the same class as F82H allow to estimate a tridimensional random H diffusion rate at 240°C of about 0.3mm/sec, so that 10 sec are sufficient for H to reach the center of the specimen. Eventhough the amount of H gained in the fracture process region from specimen surface is probably far less than that collected directly from crack-tip reaction, its contribution cannot be ignored.

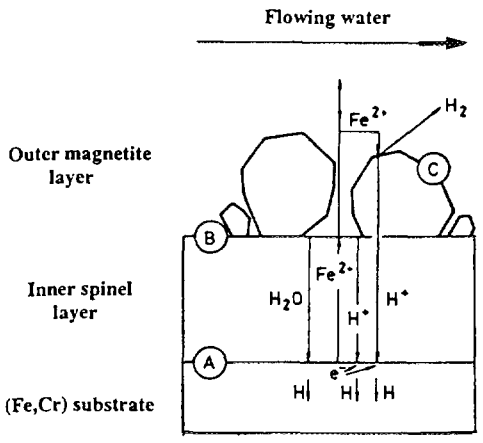

At A : Formation of inner spinel layer:

$(Fe,Cr)_{subs.} + 4\ O^{2-} = Fe_xCr_{3-x}O_4 + 8e^-$
$8H^+ + 8e^- = 8H_{ads}$

$3Fe\ (in\ Fe,Cr)_{subs} = 3Fe^{2+} + 6e^-$
$6H^+ + 6e^- = 6H_{ads}$

Through spinel (microporosity):

outwards diffusion of Fe^{2+}
inwards diffusion of H_2O, O^{2-}
inwards migration of H^+

At B : Fe^{2+} hydrolysis:

$3Fe^{2+} + 3\ H_2O = 3FeOH^+ + 3H^+$

At C : magnetite deposition:

$3FeOH^+ + H_2O = Fe_3O_4 + 2H^+ + 3H^+ + 2e^-$
$2H^+ + 2e^- = 2\ H_{ads} = H_2$

Figure 2: Model for Fe-Cr steel corrosion in high temperature, oxygen free water[7]

SCF and HAC mechanisms determines their proper "brittle"-like features in addition to the so-called "ductile-fatigue" ones (essentially striated cleavage) from MF (or TCF) process, on essentially adjacent areas of the fracture surface.
Correlation between the above theory and the experimental findings from this first group of tests allowed reasonably to conclude as follows:
i) the morphologies found in the outermost region of the water cracks and completely missing in the corresponding zone of the air cracks, resulted from either SCF or HAC, which prevailed over TCF (or only MF) in the initial stage of propagation;
ii) the similar fatigue features found in the inner region of the air and water cracks suggested that TCF (or only MF) was in control in the final propagation regime, because the crack growth rate is too fast for allowing environmental effects;
iii) even though difficulty emerged in differenciating between SCF and HAC, fractographic features such as grain and lath boundaries decohesion, favoured most likely the HAC process: cathodic hydrogen H, quite insoluble in bcc martensitic materials, interacted dynamically with the mobile dislocations created at the crack-tip under cyclic stressing, and was collected in the process zone to stronger traps (carbides at lath and grain boundaries, matrix/inclusion-precipitate interfaces), where it concentrated, decreasing in this manner the bonding energy at these sites. The fracture surfaces showed clear evidences of embrittement at grain and lath boundaries, probably because their cohesive strength were reduced well below that of the other interfaces[10] under the H concentration reached in the fracture process, and the rapid debonding which followed did not leave sufficient time for growth and coalescence of eventually nucleated voids.
v) the potential indirect effect of dissolved molecular hydrogen (H_2) in aiding such process could only occur by inhibiting the recombination in gas molecules of the atomic species[11]. The absence of such effect could be ascribed to the fact that H absorption onto the fresh metal was highly favoured, so that recombination did not need to be counteracted.

v) crack initiation in water just as in air, appeared most likely stress related rather than induced by a local corrosion process, but it followed the most congenial path as soon as oxide film penetration by slip steps under dislocation pile-up, has occurred.

In view of the well-known time-dependence of the environmentally assisted cracking EAC processes, subsequent tests were run under 18kN load amplitude in DWC/HWC and in air for comparism, at a lower loading frequency of 0.01Hz, in an attempt to emphisize the environment sensitive component and get further insight about its nature.
Even though longer times to failure were observed in all cases, the numbers of cycles to rupture was reduced from almost one third in water environments, independently of the dissolved hydrogen content, but suffered a 50% increase in air, if compared to their corresponding higher cyclic frequency test results.

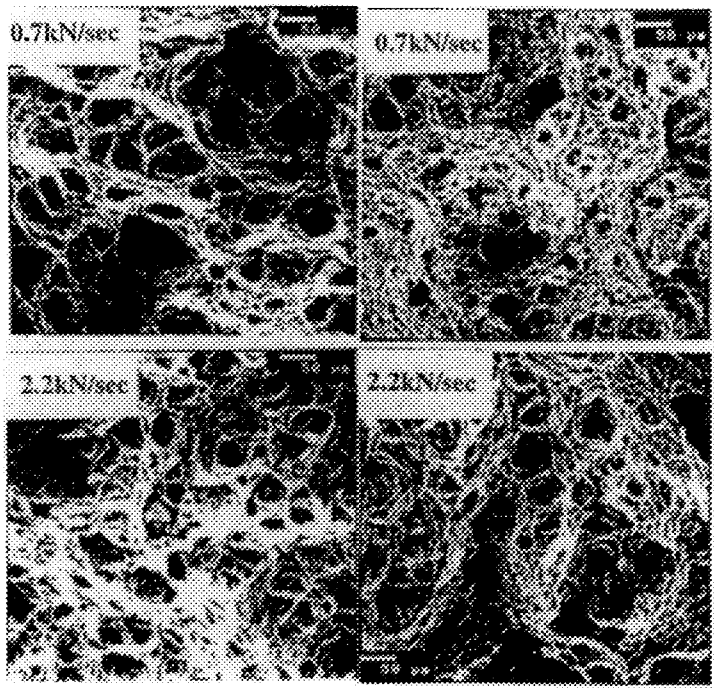

Figure 3: Effect of environment and load rate on the dimple morphologies (load amplitude: 18kN)

The main fractographic feature was the total absence of any fatigue process on the water fracture surfaces, contrarily to the air ones. In fact, except for the presence of few incipient cracks around part of the symetrically deformed periphery, the fracture surfaces appeared almost entirely dimpled, and characterized by more numerous and smaller microvoids compared to those obtained, throughout the overload region, in air at both frequencies and in water environments at higher frequency, even though to a lesser extent (fig.2). The transition from HAC related failure to a completely MVC fracture mode as frequency decreased

suggested that different underlying micromechanisms might be in control in water environments. A possible interpretation of the data could be attempted as follows:
i) the substantial longer F82H fatigue lifetime observed at lower frequency in air which is not inert, might be ascribed to an increasing delaying effect of oxidation on crack initiation (film formation faster compared to the slip step growth rate), and on crack propagation (closure by oxidation products due to the longer crack opening time).
ii) The development of a crack embryo in water environments implied that once oxide film has been penetrated by a slip step, sufficient anodic activity developed at bare metal before repassivation, as well as after each subsequent film disruption, for allowing also H-entry to some extent. This initial step which occurred at the higher frequency value for the favourable kinetics of the synergistic and competitive slip/dissolution/passivation events, appeared blunted at the lower frequency, where the rate of fresh metal production was too slow compared to repassivation. In the absence of any notch feature, the only source of H resulted from the corrosion process at the external specimen surface, which diffused randomly inwards to any potential trapping site. It is possible that, as time elapsed, sufficient H-concentration was increasingly reached at the matrix/particle interfaces to produce their debonding in correspondence to the higher stressed region (minor specimen radius), but resulted fairly lower than the critical value required at such stresses to produce the dramatic drop of the grain and lath boundary cohesion strengths [10]. In the absence of any other embrittling mechanism, the increase in microvoid population induced by H, was followed by their free growth and coalescence up to rupture. Conversely, in the presence of a concurrent HAC component, the MVC process eventhough aided by H in its initial void nucleation stage (fig 2), was too slow compared to the crack tip velocity for controlling the rupture rate, but might contribute to fatigue lifetime reduction by anticipating the plastic collapse.

4- Conclusions

Load controlled LCF tests have been run on F82H mod.martensitic steel at 240°C, in reducing water environments simulating some boundary coolant conditions for DEMO, and in static air for reference data. The main conclusions drawn from the integrated fatigue life and fractographic results can be summarized as follows:
- Water environments compared to air produced, independently of the dissolved hydrogen content, a reduction of F82H fatigue lives, with an increasingly damaging effect as stress and frequency decreased.
- Crack initiation by slip step emergence at specimen surface was probably delayed by oxidation in air and inhibited by repassivation in water environments as frequency was lowered.
- In the higher frequency range, crack growth enhancement in water appeared related to an EAC mechanism, probably HAC from cathodic hydrogen, which acted in competition with a MF (or TCF) process; the former component prevailed in the initial stage of fatigue cracking while the the latter one dominated in the final propagation stage, before the overload rupture.
- The transition in fracture mode from HAC to MVC observed in water by lowering frequency indicated that two time-dependent, rate-determining processes might be in control: HAC and MVC governed F82H cracking response above and below some critical frequency value. The reduction in fatigue lives from MVC alone was ascribed to cathodic hydrogen influence on the void nucleation process.

Acknowledgements

- The contribution of G.Filacchioni*, E.Casagrande* and U.De Angelis* in conducting the LCF experiments in air at 250°C are gratefully acknowledged.
* ENEA- Dip. Innovazione, Div. Tecnologie e Qualificazione dei Materiali.

References

1- M.F. Maday, "Low cycle fatigue and electrochemical behaviour of F82H martensitic steel in water coolant environments", presented at the 19th SOFT, Lisboa, September 16-21 (1996).

2- P. Lorenzetto et al, ITER Task T50, T330 Report, Studsvik Meeting (1996).

3- A. Turnbull, Corros. Science, 34, 6 (1993), 921-960.

4- R.P. Wei, Fatigue Mechanisms (ed. J.T. Fong), ASTM STP 675 (1979), 816-840.

5- R.P. Gangloff, Corrion Fatigue Crack Propagation in Metals, Environment-Induced Cracking in Metals, (eds. R.P. Gangloff and M.B. Ives) (1990), 55-109, NACE, Houston.

6- L.Tomlinson et al., Corr. Sci.,21 N.5 (1981), 369-380.

7- L.Tomlinson et al., Corrosion-NACE, 37 N.10 (1981), 591-596.

8- J.Robertson, Corr.Sci., 29 N.11-12 (1989), 1275-1292.

9- S. Pyun et al, Metall. Trans. A, 21 A (1990), 2577-2583.

10- K.S. Forcey et al, J. Nucl. Mater., 160 (1988), 117-124.

11- P.Skeldon et al., Corrosion-NACE, 48 N.7 (1992), 553-568.

Appendix 1

AGENDA

Wednesday October 22

9:30～9:45 Opening Remarks

Session 1: Ceramic Breeder Properties (1)
Chairperson: M.C. Billone

9:45～10:10 Thermodynamic Description of the H_2O-Li_4SiO_4 System
C. Alvani, S. Casadio, C. E. Johnson

10:10～10:35 Study on the Sweep Gas Effect on the Surface of Li_4SiO_4 by means of Work Function Measurement
A. Suzuki, K. Yamaguchi, M. Yamawaki

10:35～11:00 Coffee Break

11:00～11:25 Progress in the Development of Li_2ZrO_3 and Li_2TiO_3 Pebbles
J. D. Lulewic, N. Roux

11:25～11:50 Study on the surface electronic properties of Li-containing solids
F. Matsuura, A. Suzuki, K. Yamaguchi, M. Yamawaki

11:50～13:20 Lunch

Session 2: Modeling of Tritium Release Behavior
Chairperson: N. Roux

13:20～13:45 Modeling Tritium Behavior in Li_2ZrO_3
M. C. Billone

13:45～14:10 Ab-initio Hartree-Fock Study of Tritium Desorption from Li_2O
M. Taniguchi, S. Tanaka

Session 3: Irradiation Effects on Tritium Release Behavior
Chairperson: K. Morita

14:10～14:35 Tritium Release Kinetics of Li_2O with Radiation Defects
V. Grishmanov, S. Tanaka

14:35～15:00 Status of the EXOTIC-8 programme and first in-pile results for lithium titanate pebbles
J. G. van der Laan, M.P. Stijkel, R. Conrad

15:00～15:30 Coffee Break

Session 4: Hydrogen Behavior in Materials
Chairperson: S. Tanaka

15:30～15:55 Counter-diffusion and Permeation of Deuterium and Hydrogen through Metals
K. Kizu, T. Tanabe

15:55～16:20 Dynamic Behaviors of Protium and Deuterium Implanted into an Oxide Ceramic Studied by Means of Elastic Recoil Detection Technique
E. Iiduka, B. Tsuchiya, K. Soda, K. Morita, H. Iwakura

16:20～16:45 Experimental loop at ENEA for compatibility and hydrogen permeation studies relevant to fusion reactors
M.F. Maday, L. Bimbi, A. Iasonna, A. Mariani, V. Pietrelli, B. Tranchina, G. Zummo

19:00～21:00 Reception (Mito Keisei Hotel)

Thursday October 23

Session 5: Blanket Design
Chairperson: C.E. Johnson

9:00～9:25 Breeding Blanket Designs for ITER and Prototype (DEMO) Fusion Reactors and Breeding Materials Issues
H. Takatsu

Session 6: Ceramic Breeder Properties (2)
Chairperson: C.E. Johnson

9:25～9:50 Compilation of Properties Data for Li_2TiO_3
N. Roux

9:50～10:15 Effect of deuterium addition on the vaporization of Li_2ZrO_3
M. Tonegawa, A. Suzuki, M. Yasumoto, K. Yamaguchi, M. Yamawaki

10:15～10:45 Coffee Break

Session 7: Tritium Release from Solid Breeder Materials
Chairperson: T. Terai

10:45～11:10 Tritium Release from EXOTIC7 Orthosilicate Pebbles: Effect of Burnup and Contact with Beryllium during Irradiation
F. Scaffidi-Argentina, H. Werle

11:10～11:35 Isotope Exchange Reactions on Ceramic Breeder Materials and Their Effect on Tritium Inventory
M. Nishikawa, A. Baba, Y. Kawamura, M. Nishi

11:35～12:00 Description of Tritium Release from Lithium Titanate at Constant Temperature
L. Pena, S. Lagos, J. Jimenez, E. Saravia

12:00～12:25 Tritium Release Behavior from Neutron-irradiated Li_2TiO_3 Single Crystals
T. Tanifuji, D. Yamaki, K. Noda

12:25～12:40 Photo Session

12:40～14:10 Lunch

Session 8: Irradiation Behavior of Ceramic Breeders
Chairperson: M. Yamawaki

14:10～14:35 The Radiolysis of Lithium Oxide Ceramics
J. Tiliks, A. Supe, G. Kizane, J. Tiliks Jr., A. Ozols, S. Tanaka, V. Grishmanov

14:35～15:00 Production Behavior of Irradiation Defects in Solid Breeder Materials
H. Moriyama, K. Moritani

15:00～15:30 Coffee Break

15:30～15:55 Helium Release from Neutron-irradiated Li_2O Single Crystals
D. Yamaki, T. Tanifuji, K. Noda

Session 9: Fabrication of Ceramic Breeders
Chairperson: M. Yamawaki

15:55～16:20 Density Improvement of Li_2TiO_3 Pebbles Fabricated by Sol-gel Method
K. Tsuchiya, H. Kawamura, K. Fuchinoue, H. Sawada, K. Watarumi

Friday October 24

Session 10: Blanket System Technology and Structural Materials
Chairperson: K. Noda

9:00～9:25 Tritium Recovery from Helium Purge Stream of Solid Breeder Blanket by Cryogenic Molecular Sieve Bed (II) - Regeneration Operation of Cryogenic Molecular Sieve Bed -
Y. Kawamura, M. Enoeda, M. Nishi

9:25～9:50 Corrosion fatigue studies on F82H mod. martensitic steel in reducing water coolant environments
M. F. Maday, A. Masci

9:50～10:20 Coffee Break

10:20～11:30 Summary

Appendix 2

List of Workshop Participants		
Name	***Affiliation***	***Country***
Baba A.	Kyusyu Univ.	Japan
Billone M. C.	ANL	U.S.A.
Dalle Donne M.	FZK	EU
Enoeda M.	JAERI	Japan
Franconi E.	ENEA	EU
Futamura Y.	Toyama Univ.	Japan
Grishmanov V.	JAERI	Japan
Hu Q.	Univ. of Tokyo	Japan
Iizuka E.	Nagoya Univ.	Japan
Johnson C. E.	ANL	U.S.A.
Kawamura Y.	JAERI	Japan
Kizu K .	Nagoya Univ.	Japan
Kuroda T.	JAERI	Japan
Malang S.	FZK	EU
Matsuura F.	Univ. Tokyo	Japan
Morita K.	Nagoya Univ.	Japan
Moriyama H.	Kyoto Univ.	Japan
Noda K.	JAERI	Japan
Okamoto M.	Tohoku Univ.	Japan
Okuno K.	Shizuoka Univ.	Japan
Palmer A. J.	INEEL	U.S.A.
Pena L.	CCHEN	Chile
Roux N.	CEA	EU
Saravia E.	CCHEN	Chile
Scaffidi-Argentina F.	FZK	EU
Suzuki A.	Univ. Tokyo	Japan
Suzuki T.	KHI	Japan
Takatsu H.	JAERI	Japan
Tanabe T.	Nagoya Univ.	Japan
Tanaka S.	Univ. Tokyo	Japan
Tanifuji T.	JAERI	Japan
Taniguchi T.	Univ. Tokyo	Japan
Terai T.	Univ. Tokyo	Japan
Tonegawa M.	Univ. Tokyo	Japan
Tsai H.	ANL	U.S.A.
Tsuchiya K.	JAERI	Japan
Watarumi K.	NFI	Japan
Yamaguchi K.	Univ. Tokyo	Japan
Yamaki D.	JAERI	Japan
Ying A.	UCLA	U.S.A.

国際単位系 (SI) と換算表

表 1　SI 基本単位および補助単位

量	名称	記号
長さ	メートル	m
質量	キログラム	kg
時間	秒	s
電流	アンペア	A
熱力学温度	ケルビン	K
物質量	モル	mol
光度	カンデラ	cd
平面角	ラジアン	rad
立体角	ステラジアン	sr

表 2　SI と併用される単位

名称	記号
分，時，日	min, h, d
度，分，秒	°, ′, ″
リットル	l, L
トン	t
電子ボルト	eV
原子質量単位	u

1 eV = 1.60218 × 10^{-19} J

1 u = 1.66054 × 10^{-27} kg

表 5　SI 接頭語

倍数	接頭語	記号
10^{18}	エクサ	E
10^{15}	ペタ	P
10^{12}	テラ	T
10^{9}	ギガ	G
10^{6}	メガ	M
10^{3}	キロ	k
10^{2}	ヘクト	h
10^{1}	デカ	da
10^{-1}	デシ	d
10^{-2}	センチ	c
10^{-3}	ミリ	m
10^{-6}	マイクロ	μ
10^{-9}	ナノ	n
10^{-12}	ピコ	p
10^{-15}	フェムト	f
10^{-18}	アト	a

表 3　固有の名称をもつ SI 組立単位

量	名称	記号	他の SI 単位による表現
周波数	ヘルツ	Hz	s^{-1}
力	ニュートン	N	$m \cdot kg/s^2$
圧力，応力	パスカル	Pa	N/m^2
エネルギー，仕事，熱量	ジュール	J	N·m
工率，放射束	ワット	W	J/s
電気量，電荷	クーロン	C	A·s
電位，電圧，起電力	ボルト	V	W/A
静電容量	ファラド	F	C/V
電気抵抗	オーム	Ω	V/A
コンダクタンス	シーメンス	S	A/V
磁束	ウェーバ	Wb	V·s
磁束密度	テスラ	T	Wb/m^2
インダクタンス	ヘンリー	H	Wb/A
セルシウス温度	セルシウス度	℃	
光束	ルーメン	lm	cd·sr
照度	ルクス	lx	lm/m^2
放射能	ベクレル	Bq	s^{-1}
吸収線量	グレイ	Gy	J/kg
線量当量	シーベルト	Sv	J/kg

表 4　SI と共に暫定的に維持される単位

名称	記号
オングストローム	Å
バーン	b
バール	bar
ガル	Gal
キュリー	Ci
レントゲン	R
ラド	rad
レム	rem

1 Å = 0.1 nm = 10^{-10} m

1 b = 100 fm^2 = 10^{-28} m^2

1 bar = 0.1 MPa = 10^5 Pa

1 Gal = 1 cm/s^2 = 10^{-2} m/s^2

1 Ci = 3.7 × 10^{10} Bq

1 R = 2.58 × 10^{-4} C/kg

1 rad = 1 cGy = 10^{-2} Gy

1 rem = 1 cSv = 10^{-2} Sv

(注)

1. 表 1 ～ 5 は「国際単位系」第 5 版，国際度量衡局 1985 年刊行による。ただし，1 eV および 1 u の値は CODATA の 1986 年推奨値によった。
2. 表 4 には海里，ノット，アール，ヘクタールも含まれているが日常の単位なのでここでは省略した。
3. bar は，JIS では流体の圧力を表わす場合に限り表 2 のカテゴリーに分類されている。
4. EC 閣僚理事会指令では bar，barn および「血圧の単位」mmHg を表 2 のカテゴリーに入れている。

換　算　表

力	N(=10^5 dyn)	kgf	lbf
	1	0.101972	0.224809
	9.80665	1	2.20462
	4.44822	0.453592	1

粘度　1 Pa·s(N·s/m^2) = 10 P(ポアズ)(g/(cm·s))

動粘度　1 m^2/s = 10^4 St(ストークス)(cm^2/s)

圧力	MPa(=10 bar)	kgf/cm^2	atm	mmHg(Torr)	lbf/in^2(psi)
	1	10.1972	9.86923	7.50062 × 10^3	145.038
	0.0980665	1	0.967841	735.559	14.2233
	0.101325	1.03323	1	760	14.6959
	1.33322 × 10^{-4}	1.35951 × 10^{-3}	1.31579 × 10^{-3}	1	1.93368 × 10^{-2}
	6.89476 × 10^{-3}	7.03070 × 10^{-2}	6.80460 × 10^{-2}	51.7149	1

エネルギー・仕事・熱量	J(=10^7 erg)	kgf·m	kW·h	cal(計量法)	Btu	ft·lbf	eV
	1	0.101972	2.77778 × 10^{-7}	0.238889	9.47813 × 10^{-4}	0.737562	6.24150 × 10^{18}
	9.80665	1	2.72407 × 10^{-6}	2.34270	9.29487 × 10^{-3}	7.23301	6.12082 × 10^{19}
	3.6 × 10^6	3.67098 × 10^5	1	8.59999 × 10^5	3412.13	2.65522 × 10^6	2.24694 × 10^{25}
	4.18605	0.426858	1.16279 × 10^{-6}	1	3.96759 × 10^{-3}	3.08747	2.61272 × 10^{19}
	1055.06	107.586	2.93072 × 10^{-4}	252.042	1	778.172	6.58515 × 10^{21}
	1.35582	0.138255	3.76616 × 10^{-7}	0.323890	1.28506 × 10^{-3}	1	8.46233 × 10^{18}
	1.60218 × 10^{-19}	1.63377 × 10^{-20}	4.45050 × 10^{-26}	3.82743 × 10^{-20}	1.51857 × 10^{-22}	1.18171 × 10^{-19}	1

1 cal = 4.18605 J (計量法)

= 4.184 J (熱化学)

= 4.1855 J (15 °C)

= 4.1868 J (国際蒸気表)

仕事率　1 PS (仏馬力)

= 75 kgf·m/s

= 735.499 W

放射能	Bq	Ci
	1	2.70270 × 10^{-11}
	3.7 × 10^{10}	1

吸収線量	Gy	rad
	1	100
	0.01	1

照射線量	C/kg	R
	1	3876
	2.58 × 10^{-4}	1

線量当量	Sv	rem
	1	100
	0.01	1

(86 年 12 月 26 日現在)

PROCEEDINGS OF THE SIXTH INTERNATIONAL WORKSHOP ON CERAMIC BREEDER BLANKET INTERACTIONS OCTOBER 22-24, 1997, MITO CITY, JAPAN